STRUCTURE-PROPERTY RELATIONSHIPS IN AMORPHOUS SOLIDS VIA ATOMIC SIMULATIONS AND MACHINE LEARNING

by

Zhao Fan

A dissertation submitted to Johns Hopkins University in conformity with the requirements for the degree of Doctor of Philosophy.

Baltimore, Maryland

December 2020

Abstract

The establishment of structure-property relationships is a central goal of materials science. For amorphous solids or glasses, the disordered nature of their internal structure poses major challenges to building a quantitative correlation between their (local) atomic configurations and their properties. Via atomistic simulations and state-of-the-art machine learning technologies this work reveals that there is indeed strong correlation between both dynamic and static structure information and multiple properties in several distinct model glasses including amorphous silicon, Cu-Zr metallic glasses at different compositions and a two-dimensional binary Lennard-Jones glass model. Firstly, we demonstrate that flexibility volume, which is a structural indicator previously designed for metallic glasses that incorporates both static and dynamic information, correlates well with several important properties in amorphous silicon. This, combined with earlier study for metallic glasses, points out the universality of flexibility volume as an indicator of the structural state, applicable across amorphous materials with different chemical bonding and atomic pack-

ing structures. Secondly, we explain the plastic flow observed in recent experiments on both metallic glasses and covalently bonded network glasses from the standpoint of the flexibility available in the amorphous structure, and we suggest several feasible routes to tune flexibility in glasses. Thirdly, with the help of a simple machine learning model, we show that the degree of flexibility in amorphous solids can be accessed from static structural information, i.e., the local radial density distribution, which is easier to obtain. Fourthly, by designing a new rotation-invariant structure representation, in conjunction with a powerful deep learning model, we achieve unprecedented accuracy in predicting particles with high plastic susceptibility solely from static structure in both two- and three-dimensional model glasses. In addition, we are able to obtain new insight into the critical structural features responsible for the anisotropy of local mechanical response in glasses. Finally, we illustrate that the initiation positions of shear bands can be forecasted from the density distribution of fertile sites predicted by deep learning models. These contributions are anticipated to enhance our understanding of structure-property relationships in amorphous solids and to prove useful in searching for amorphous materials with desired performance characteristics.

Primary Reader and Advisor: Professor Michael Falk

Secondary Reader: Professor Todd Hufnagel

Dedicated to my family

for their eternal

love, trust and support

Acknowledgments

First and foremost, I am so blessed and honored to have Professor Evan Ma as my advisor. I felt so lucky that he accepted me (I used to work on experimental study of thermoelectric materials), to explore a new world - computer simulation of glasses - with him at Hopkins. Working with Professor Ma is really a fruitful experience, as I have learnt a lot from him over the past five years. It is not only about how to find valuable topics, how to conduct research, how to analyze the data, and how to organize a paper, but more importantly, it is his attitude and passion for learning and thinking that impressed me the most. Working with Professor Ma is a pleasant journey as well, since he is always thoughtful and considerate to students. There inevitably are a lot of frustrating moments during my research, his smile and enthusiasm always inspired me to keep going. Besides, I appreciate very much his encouragement for my exploring into the world of machine learning, which turns out to be a powerful tool to achieve our research goals. Needless to say, this thesis would have been impossible without Professor Ma's guidance and support. But I believe what I

gained is far beyond this thesis; it will benefit my future career in the long run.

I am extremely grateful to Professor Michael Falk for his strong support, insightful discussion and precious camaraderie to me during the last half year of my PhD study. After Professor Ma retired in July 2020, Professor Falk accepted me into his group, gave invaluable comments on my previous work, contributed much to Chapter 6, and guided me to finish and defend this thesis.

I thank my thesis committee members, Professor Todd Hufnagel, Professor Mingwei Chen, Professor Paulette Clancy, Professor Somnath Ghosh, Professor Tim Mueller and Professor Jaafar El-Awady, for their service and time.

This thesis work was supported by the U.S. Department of Energy. Computational resource provided from Maryland Advanced Research Computing Center, National Energy Research Scientific Computing Center and Texas Advanced Computing Center are also gratefully acknowledged. I would like to thank the staff of these supercomputer centers for their precious suggestions of installing packages and running and optimizing computing jobs.

I would love to thank Dr. Yongqiang Cheng and Dr. Dong Ma at Oak Ridge National Laboratory and Dr. Yang Ren at Argonne National Laboratory for their support and help with my attempted experiments using neutron and high-energy X-ray scattering, and thank Professor Zhaoping Lu and Dr. Di Cao at University of Science and Technology Beijing for providing metallic glass samples.

ACKNOWLEDGMENTS

I owe many thanks to the former group members, Dr. Qing-Jie Li, Dr. Jun Ding, Dr. Yongqiang Cheng, Dr. Qi Wang, Ms. Qingyang Gao and Professor Falk's group members for the interesting discussion on research with them and their companionship. I learned a huge amount from both Dr. Qing-Jie Li and Dr. Jun Ding about molecular dynamics simulations. As well, I would love to thank my friends at JHU for their help on my work and daily life, and I enjoyed so much the happy time with my friends at Baltimore.

I am thankful to the assistance provided by Jeanine Majewski, Ellen Libao, Tanea Melvin, Ada Simari, Amanda Gursky and Meghan Tully in the administrative issues.

I have really enjoyed the talking on all kinds of topics with Anne Colgan and Amanda Hilliard from the Center for Leadership Education at JHU and appreciate their professional advice on my English pronunciation and presentation for thesis defense.

Last but not least, a huge thank you to my parents for all their eternal love, support, trust all the way. I know both of them miss me, their only child, very much when I am so far away. I am forever indebted to them for their understanding.

Contents

List of Tables

List of Figures

Chapter 1

Introduction

1.1 Background and motivation

The main objective of materials science is to establish concrete structure-property relations [1]. The paradigm of "microstructure determines properties" has been very successful in explaining and predicting the behavior of conventional materials. This success has, in many ways, been possible because these materials are crystals, containing a plethora of property-controlling microstructural features, such as grains, precipitates, interfaces, dislocations, twins and stacking faults, etc., which can all be routinely identified under a microscope and judiciously manipulated during alloy processing [1]. The plastic flow, for example, is carried by well-defined dislocations and can be quantitatively explained

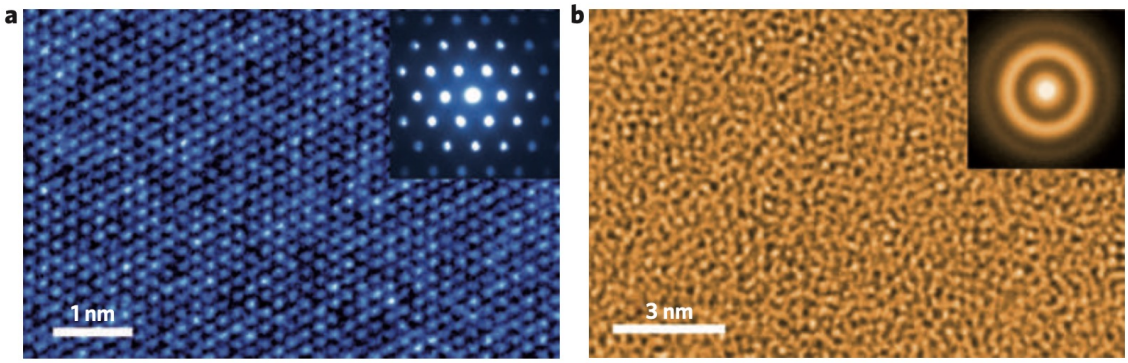

Figure 1.1: Imaging atomic-level structures. a, high-resolution TEM image of a low-carbon steel crystal taken in the [111] direction, showing well-defined lattice fringes. Inset, the corresponding selected-area electron diffraction pattern showing sharp spots. b, high-resolution TEM image of the $Zr_{67}Ni_{33}$ metallic glass, showing a maze-like pattern. Inset, the corresponding selected-area electron diffraction pattern shows diffuse haloes, in stark contrast with the crystalline pattern in a. Taken from Ma and Zhang [6]

by the evolution of these defects [2]. As a result, many predictive structure-property laws have been established, such as the Taylor hardening law based on dislocation density [3] and the Hall-Petch relationship for grain boundary strengthening [4, 5].

In striking contrast, amorphous solids, including metallic glasses (MGs) [7–11] and covalently bonded network glasses (such as amorphous silicon) [12], present no discernible microstructure, invariably displaying a maze-like pattern when examined under a high-resolution transmission electron microscope. For example, The high-resolution transmission electron microscope of a $Zr_{67}Ni_{33}$ metallic glass shown in Fig. 1.1b exhibits the typical maze-like pattern, which is in sharp contrast with the well-defined lattice fringes as shown in Fig. 1.1a.

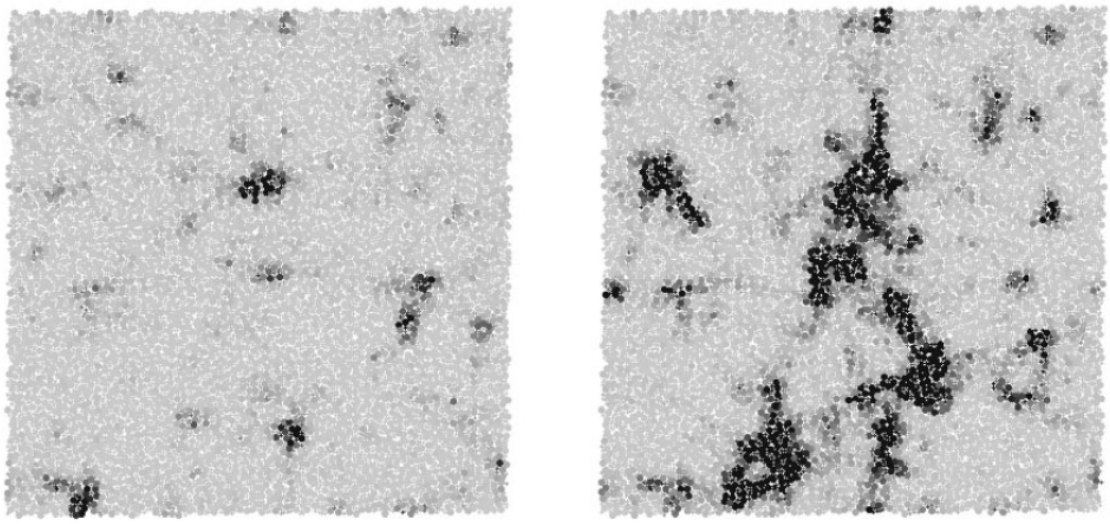

Figure 1.2: The heterogeneity of plastic susceptibility. (a) and (b) shows the field of $D^2_{\min}$, the deviation from affine deformation, in a two-dimensional binary Lennard-Jones model glass under different degrees of strain. Here the dark regions correspond to large $D^2_{\min}$. Adopted from Falk and Langer [16]

In other words, atoms adopt varying local atomic packing configurations and are all potential defects to various degrees. In terms of mechanical rigidity, MGs are more flexible than their crystalline counterparts: a MG typically exhibits a shear modulus $\sim$30% lower [13], with considerable spatial heterogeneity even in a given sample [14, 15]. The plastic susceptibility is variable as well, as nanometer-sized local regions respond to externally applied stresses to various extents [16–25]. For example, Fig. 1.2 shows the typical plastic heterogeneity in a two-dimensional binary Lennard-Jones model glass under different degrees of shear strain. The wide spectrum of local structures in an amorphous solid, i.e., the diverse short-range structures and their medium-

range correlations, as well as the subtle differences between similar local configurations, makes it difficult to identify structural "defects" responsible for the plastic events, even when the static structure (the coordinates or relative distribution of all atoms) is fully known. It remains unclear how to quantitatively bridge the local packing environment with its degree of likelihood for atomic rearrangements when exposed to external stimuli (such as applied stresses and temperature). As a result, explicit structure-property connections have been difficult to come by for amorphous solids, [23, 26–39], let alone robust theoretical equations [40, 41].

However, it has been widely speculated that tell-tale signs about fertile sites, i.e., "defect"-like and responsive flow units or liquid-like regions, ought to be encoded in the structure of glasses. This appealing hypothesis led to a number of plastic theories in in amorphous solids, most notably that of shear transformation zones of Falk and Langer [16], assuming the existence of structurally distinct defects in amorphous materials determine their response to externally applied loading. But these theories are phenomenological in the sense that they contain fitting parameters that one does not know how to extract from first principles, i.e. from the microstructure and interactions between the constituent particles of the materials [42]. Therefore, over the past decades, intensive research along this line of thinking have been conducted to identify structural "defects" similar to dislocations in crystalline solids, from informa-

tion regarding the undeformed structural state in amorphous solids.

The earliest structural parameter most widely quoted in literature is perhaps the free volume [26, 35, 43, 44]. This concept was originally conceived for hard-sphere systems, and is thus deficient for describing bonds characterized by much softer interparticle potentials [45]. Also problematic is that the free volume does not change in large amounts when the composition or processing history of glassy materials is changed, and has recently been shown to be inadequate in correlating with property variations [19, 46]. In addition, free volume is utterly inapplicabe for covalently-bonded network glasses such as amorphous silicon in which the higher the density, the more deformable the open network amorphous structure [47–49].

Subsequent research has suggested a number of parameters, which exhibit some degree of correlation with local properties. However, most of these parameters are not directly determined by the spatial arrangement of atoms alone, but needs to be deduced from the knowledge of interparticle interactions through extensive computations. Examples include atomic-level stresses [45, 50], potential energy [27, 51, 52], local elastic modulus [53], soft modes (quasi-localized low-frequency vibrational modes) [19, 54], local yield stress [55], fictive temperature [56, 57], local thermal energy [31] and activation energy barrier [58, 59].

Some other indicators are more “structural”, in the sense that they spec-

ify and focus on certain features of local atomic packing, such as short-range atomic order (coordination polyhedra) [17, 18], correlated local order [23, 60], degree of local five-fold symmetry (LFFS) [61], bond length deviation [62] and bond-orientational order [63]. But the correlation between these indicators and local properties is not sufficiently strong, partly because these short range order (SRO) indicators each provides only limited information to account for property variations. Unfortunately, the degree of order and coordination in the medium range (e.g., up to 2 nm) is more difficult to decipher and rank for an amorphous solid [23, 32]. Simultaneously accounting for multiple facets of the structural ingredients pertaining to properties is an even more demanding proposition. Recently this challenge was paraphrased as an intellectual puzzle by the authors of a review on MGs [34]: atomic simulations at present, and experiments in future, can reach the point of mapping out the coordinates of each atom in an MG; but "knowing position of every atom; ... then what to do with all that information?" In other words, while it is desirable to be able to predict properties solely from the (local) atomic configuration, current simplified/partial description of this environment does not correlate sufficiently well with properties, especially since the structural features influence the properties in a rather complex way.

These frustrating results have left many to wonder whether the response of amorphous supercooled liquids and glassy solids under external stimulus is

really dependent on initial static structure. For example, Berthier *et. al.* [64] claimed in a review of glassy dynamics that "the distinction between mobile and immobile particles is mostly dynamical in nature, suggesting that the quest for a connection between the static and dynamic properties of glass formers at the particle level is in vain."

Fortunately, motivated by the recent progress in the field of machine learning [65, 66] and the success of constructing empirical interatomic force field by Behler and Parrinello [67], Cubuk *et. al.* [21] attempted to identify structure flow defects in amorphous solids including a two-dimensional jammed system and both two- and three-dimensional binary Lennard-Jones binary models glasses using a support-vector machine (SVM) with a linear kernel, a machine learning algorithm. Subsequently, Wang and and Jain suggested a new machine learning framework with "interstice" distribution as the structure representation, in an effort to make the machine learning model less system-specific [68]. In April 2020, Bapst *et. al.* [69] demonstrated that a graph neural network (GNN) [70] is superior to a linear SVM in establishing relations between static structure and properties/dynamics for both supercooled liquids and gassy solids. Compared to previously used physically-inspired methods, these data-driven approaches can simultaneously take into account multiple aspects of a local configurations beyond the first nearest neighbor shell. Once an optimal machine learning model is hand, all that is required to predict a

given property of local configurations is static structural information, i.e., one would only need to track the relative atomic positions. No extra knowledge needs to be supplied again, for the alloy system in question. However, these successes achieved using machine learning methods are still modest, and do not show sufficiently high accuracy in predicting plastic susceptibility. This is particularly true at large degrees of deformation (close to the yielding point), which renders these methods insufficient to predict some critical behaviors, such as shear banding, the dominant failure mode in metallic glasses [30]. There are a number of issues that have limited the success of these previous machine learning methods. First, subtle but nontrivial structural information appears to be lost during the process of converting atomic coordinates into structure representatives as input to machine learning models. Secondly, these prior machine learning algorithms are incapable of capturing the complex and complicated correlations between initial static structure and the dynamic response upon deformation, particularly at strains very close to the yielding point of amorphous solids. Most importantly, the prediction based on these data-driven approaches or any one of the particular physically-inspired methods mentioned previously is a scalar, i.e. a rotation-invariant quantity, which is inherently inadequate in capturing the anisotropic response of a local configuration. It is well established that a given local material region can respond quite differently when the externally applied global stress is imposed along

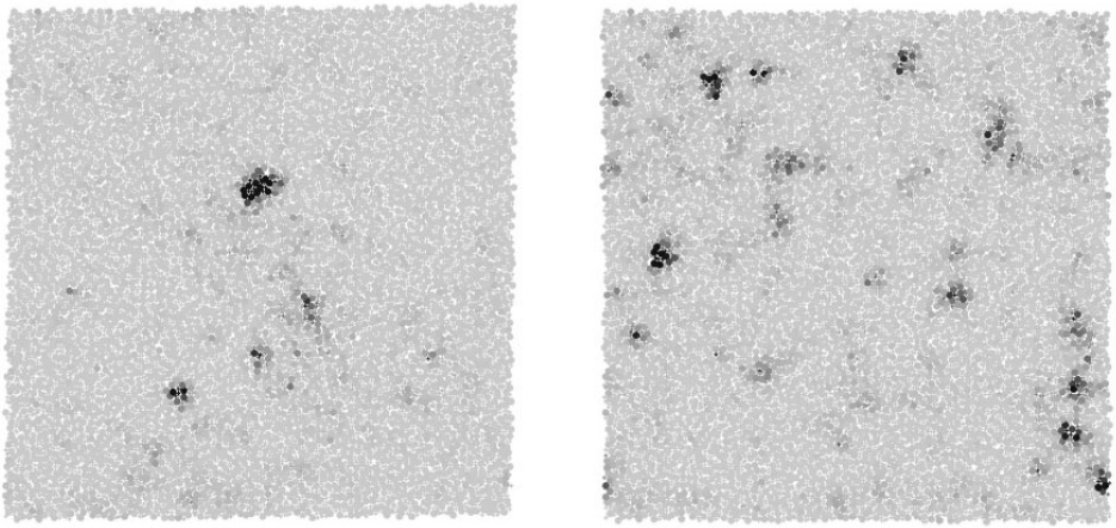

Figure 1.3: The anisotropy of mechanical response of amorphous solids. (a) and (b) show the field of $D^2_{\min}$, the deviation from affine deformation, in an exactly same two-dimensional binary Lennard-Jones model glass at a same strain level after deformation under positive and negative simple shear, respectively. Here the dark regions correspond to large $D^2_{\min}$. Adopted from Falk and Langer [16]

different orientations [16, 71–73], as shown in Fig. 1.3.

In some fairly recent efforts predicting the propensity for plastic activity, the anisotropy of local mechanical behavior has been taken into account. For example, Barbot *et. al.* [71] measured local yield stress [55] obtained by shearing local configurations in different directions to predict plastic events under different loading protocols. In other work Schwartzman-Nowik *et. al.* proposed to use the linear response coupling of local heat capacity [31] to external deformation tensors to predict the orientation-dependent plastic events. Xu *et. al.* [73] also suggested so-called atomic nonaffinity, a metric quantifying the contribu-

tion of an individual atom to the total nonaffine modulus of amorphous solids, as an indicator to forecast the local mechanical response in different loading orientations. Although these new indicators taking into account anisotropy showed enhanced predictive capability in two-dimensional model glasses, it remains unclear how well these new indicators fare in three-dimensional amorphous solids. Furthermore, these indicators are physical quantities that need to be evaluated with known interparticle interactions, every time the structure changes. In other words, one cannot simply monitor the atomic positions alone, to explain property changes. More importantly, it is hard, if not impossible, to use these methods to directly identify the critical structure features (i.e., the atomic environment *per se*) responsible for the anisotropic local mechanical response. This has been a puzzle existing at least more than two decades since Falk and Langer pointed it out in 1998 [16].

1.2 Overview of objectives

This thesis is a computationally investigation on atomic-level structure-property relationships of amorphous solids including covalently-bonded network glasses, metallic glasses and two-dimensional (2D) binary glass models, using classical molecular dynamics simulations [74] and state-of-the-art machine/deep learning technologies [65, 66, 75, 76]. The primary purpose of this thesis is to establish strong and robust atomic-level relationships between an initial structure

state and the resulting dynamic response under various external stimuli for amorphous solids, overcoming the challenges discussed in Section 1.1. This thesis contains five main chapters.

In chapter 2, which is published in Physical Review B [77], we explore the applicability of "flexibility volume," a new structure indicator which was first designed for metallic glasses by Ding *et. al.* [78] in 2016, to covalently-bonded open-network glasses. Flexibility volume incorporates the atomic volume and the vibrational mean-square displacement to combine both static structure and dynamics information. This indicator was shown to quantitatively correlate with the properties of metallic glasses across a very wide range of metallic glass compositions, processing conditions and length scales [78]. However, it remains to be examined if this parameter is useful for other types of glasses with bonding characteristics, atomic packing structures, and properties that are distinctly different from metallic glasses. In chapter 2, we describe systematic molecular-dynamics simulations of amorphous silicon (a-Si) models produced via different cooling rates. As a-Si is a prototypical covalently bonded network glass, its structure and properties cannot be characterized using structural parameters such as free volume used for metallic and polymeric glasses. Specifically, we demonstrate that a quantitative prediction of the shear modulus of a-Si can be derived from the flexibility for atomic motion. This flexibility volume descriptor, when evaluated on the atomic scale, is shown to also corre-

late well with local packing, as well as with the propensity for thermal relaxations and shear transformations. It thus provides a metric to map out and explain the structural and mechanical heterogeneity in the amorphous material. This case study of a model of covalently bonded network a-Si, together with the earlier demonstration for metallic glasses [78], points to the universality of flexibility volume as an indicator of the structure state that can be linked with properties.

In chapter 3, which is published in Materials Research Letters [79], we demonstrate using examples and models that it is the flexibility rather than the excess volume that can be tuned to facilitate plastic flow and ductility in glassy materials. Making glasses ductile at room temperature is a daunting challenge, but has been shown to be feasible in recent years. We explain the plastic flow from the standpoint of the flexibility available in the amorphous structure: imparting flexibility into the structure facilitates bond switching needed to mediate shear transformations to carry strain. This structure-property correlation is demonstrated using molecular dynamics simulation data. The flexibility can be improved via ultrafast quenching or rejuvenation. In particular, the flexibility volume parameter offers a quantitative metric to explain the flexibility and deformability, even for glasses where the commonly cited free volume is not applicable.

The results presented in chapter 2 and 3 as well as in Ref. [78] suggest

that flexibility volume is powerful in correlating with properties and universal for various glass systems with distinct chemical bonding and atomic packing structures. However, flexibility volume has several limitations. First, flexibility volume is *not* just the static structure, which is the normally used and more accessible data from both simulation models and real glassy samples. The vibrational mean-square displacement has to be mapped out to assess flexibility volume every time the sample changes, which is intractable in experimental work. Second, flexibility volume is difficult to define for glasses under high stress (pressure) or temperature, not to mention in liquid state and shear flow, as the contribution of atomic diffusion cannot be easily separated out in those situations. So it is important and necessary to have a structural quantity which can be derived solely from static structural information and yet work as well as flexibility volume. In chapter 4, which is published in Materials Today [80], we show that this goal is achieved via machine learning.

Furthermore, as the previous structure indicators discussed in Section 1.1, flexibility volume is also a scalar or rotation-invariant quantity and thus cannot take into account the anisotropy of local mechanical response in amorphous solids. Consequently, it is not sufficient to use flexibility volume to predict orientation-dependent elementary plastic events, let alone the location of shear band initiation in amorphous solids. To overcome this long-standing challenge, in chapter 5, which is under review for publication, we introduce a rotation-

variant local structure representation that encompasses responses under differently oriented loading. Such a representation essential for high-fidelity prediction of the propensity for stress-driven shear transformations. This novel structure representation, when combined with convolutional neural network (CNN), a powerful deep learning algorithm [75], leads to unprecedented accuracy for predicting atoms with high plastic susceptibility, solely from the static structure in both two- and three-dimensional model glasses. The data-driven models trained on samples at one composition and a given processing history are found to be transferrable to glass samples with different processing history or at different compositions in the same alloy system. Our analysis of the new structure representation also provides valuable insight into key atomic packing features that influence the local mechanical response and its anisotropy in glasses. The deep learning prediction is confirmed to be fully consistent with the expectation based on this structural insight.

In chapter 6, we unveil that the location of shear band initiation in metallic glasses is predictable from initial undeformed static structure state, i.e., the distribution of the density of fertile sites (DFS) predicted using the CNN model established in chapter 5, although shear bands do not always appear at a same region even though deformation simulation is conducted under athermal quasi-static condition, due to some extrinsic variation, such as atom sequence in initial configuration of glassy models. We defined a figure of merit to quan-

tify the correlation strength between CNN-based predicted DFS and the shear band initiation in the MG samples, which is superior to the prediction based on other structural indicators suggested previously. To the best of our knowledge, this is the first time to exhibit that there is strong correlation between the initial static structure and shear banding behavior in MGs and other amorphous solids. The demonstrated correlation may be useful to establishing robust physical model of plastic behavior of amorphous solids in future, and also justified that it is feasible to controlling shear banding behavior and thus optimizing mechanical properties of MGs via tuning their initial structural state before deformation.

The achievements presented in this thesis are expected to improve our understanding of the unusual structural and mechanical heterogeneity inherent to a seemingly homogeneous amorphous solid. For engineering applications, our findings may facilitate the development of amorphous solids with better properties, e.g., through judicious tuning of their internal structure based on what is learnt in this thesis as to how the composition and processing change its response to stimulus and hence the properties. In addition, the new atomic structure representation in conjunction with the powerful deep learning algorithm are anticipated to find use in overcoming other challenges in the field of materials science and engineering, such as constructing both fast and efficient interatomic force fields [81, 82].

Chapter 2

Correlating the properties of amorphous silicon with its flexibility volume

2.1 Introduction

For amorphous solids, quantitative property correlations have been difficult to come by, lagging far behind conventional crystalline materials. An example is the widely used amorphous silicon (a-Si). a-Si can be prepared via a number of processing routes, the most popular being chemical or physical vapor deposition [83–85]. Other routes include ion irradiation [86, 87] or mechanical

deformation [88] of crystalline silicon. The resultant amorphous structures are all different, and so are their shear rigidity and deformability (e.g., some a-Si are brittle while others can be plastically deformed [47, 88, 89]). It remains a challenge to define a parameter that can be used to quantitatively link properties.

For metallic or polymeric glasses, free volume is widely cited as a structural parameter to correlate with properties [44, 90]. For example, a rapidly quenched metallic glass is believed to contain more free volume than a slowly cast one and is thus less rigid and more prone to flow. However, this picture is obviously invalid for a-Si, which is a prototypical covalently bonded network amorphous material. Here faster cooling from liquid actually retains a higher-density glass, containing less open volume (see Refs. [47, 89]), but the resultant structure is more metallic- and liquidlike, making the glass more amenable to shear flow. Conversely, slower cooling leads to a network glass with a relatively open structure, but the material is stronger. More discussion on the inadequacy of excess atomic volume to reflect the deformability of a-Si will be presented later in this chapter.

Fictive temperature [91, 92] is another commonly used concept in the field of glass research for representing the level of disorder in a glassy material. But this parameter is not descriptive of the atomistic origin of a property, and needs to be mapped to some other real physical quantities such as potential energy for

it to be computed or measured. In terms of correlating with properties, a glass with a lower fictive temperature has a lower potential energy, and is usually stronger and has a higher elastic modulus. However, there are also cases where a glass has a higher energy and higher fictive temperature [93, 94] but is more kinetically stable because the glass is in a potential energy valley with a higher curvature, leading to a higher elastic modulus and strength [95]. In other words, fictive temperature is only correlated with thermodynamic stability but not necessarily with kinetic stability and strength/modulus. In the case of a-Si, faster quenching from liquid [47,89] results in an amorphous structure that is higher in energy, more metallic- and liquidlike, and hence more deformable and less stiff. This could perhaps be depicted as corresponding to a higher fictive temperature; nonetheless there is no equation that can directly predict modulus or strength, based on the fictive temperature or potential energy of the a-Si in question.

Simulating the a-Si model employing the Stillinger-Weber (SW) potential [96], Demkowicz and Argon showed that depending on the cooling rate used to quench from liquid silicon, the resultant a-Si models exhibit different elastic moduli, yield-point behavior, and flow stresses [47, 89]. These differences can be attributed to different fractions of liquidlike atomic environments, ϕ, in the amorphous structure [47,89]. The liquidlike atoms were defined based on their nearest-neighbor bond-angle distribution that resembles liquid Si. However,

while this structural descriptor is useful in explaining the property trend from the structural state the a-Si is in, again the challenge remains as to how to quantitatively derive from the descriptor a property such as shear modulus or strength.

Very recently, Ding *et al.* [78] introduced a new indicator of the structural state, termed the "flexibility volume", which is assessed via combining both atomic volume and atomic vibrations that probe local configurational space. This parameter incorporating local structure and local dynamics was developed for metallic glasses (MGs), a class of amorphous materials characterized by metallic bonding. A systematic study on a variety of MGs has demonstrated that the flexibility volume can deterministically predict the shear modulus, and strongly correlate with various properties on both atomic and macroscopic levels. However, it is unclear if the same holds for a-Si, the amorphous material focused on in this chapter. Specifically, the a-Si structure is a covalently bonded continuous random network (CRN), and loosely packed with a coordination number (CN) of $\sim$4-6 [96–99]. This is very different from the densely packed MGs with nondirectional bonds that result in a high CN often of the order of 12 [23]. Moreover, free volume is often cited to characterize MGs, but not applicable to a-Si as discussed earlier. Therefore, it would be interesting and important to examine the validity of applying the flexibility volume parameter to a-Si; this would not only provide a useful indicator for establishing

correlations with properties in a-Si, but also validate the concept of flexibility volume as a universal parameter for different classes of amorphous materials characterized by a variety of electronic bonding and atomic packing structures.

2.2 Methods

Molecular-dynamics (MD) simulations [74] have been employed to prepare and analyze the a-Si samples using the SW potential [96], which has been extensively utilized to model the structure and properties of a-Si (this potential is believed to be adequate to construct a representative model of a-Si for our purposes; we are aware that additional tweaking of the prefactor for the three-body term in the potential can change the degree of bond directionality, which was found to affect the coordination number of local defects and/or their behavior in plastic arrangements in similar network amorphous solids [100]). Our a-Si model contains 85,184 atoms, i.e., 22×22×22 cubic unit cells of the diamond cubic configuration, under periodic boundary conditions (PBCs). The samples were quenched to room temperature (300 K) from equilibrium liquids above the melting point. The quenching was performed using a Nose-Hoover thermostat with zero external pressure, over a range of cooling rates from 5.0×10^{10} to 5.0×10^{13} K/s. The average atomic volume (Ω_a) of those simulated a-Si, increasing with decreasing cooling rate (note that this is opposite to the trend for MGs), is shown in Fig. 2.1.

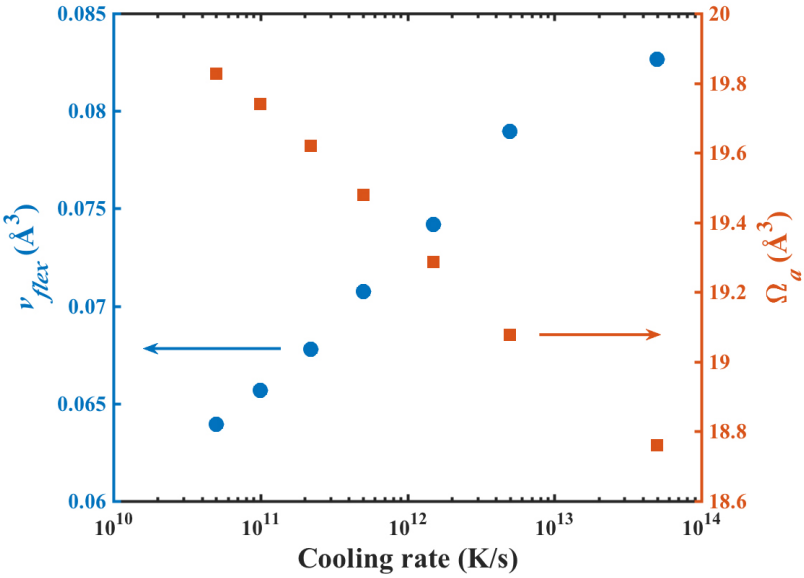

Figure 2.1: The system-averaged flexibility volume v_{flex} and atomic volume Ω_a as a function of cooling rate for a-Si samples prepared using various cooling rates (q, in K/s) from liquid.

Each sample was kept at equilibrium under a microcanonical ensemble (NVE) at room temperature to calculate the atomic vibrational mean-square displacement (MSD). The MSD of the ith atom is defined as $\langle [x_i(t) - \bar{x}_i]^2 \rangle$, where $\bar{x}_i$ is the equilibrium (time-averaged) position of the ith atom, and the MSD is evaluated on short time scales when the MSD is flat with time and thus contains the vibrational but not the diffusional contribution [78] [see Fig. 2.2(a)]. The calculated MSD was taken by averaging over 100 independent runs, all starting from the same configuration but with momenta assigned randomly from the appropriate Maxwell-Boltzmann distribution [78, 101]. Voronoi tessellation [102] was employed to obtain the atomic volume (Ω_a).

The vibrational anisotropy (η_i) of the ith atom is calculated by monitor-

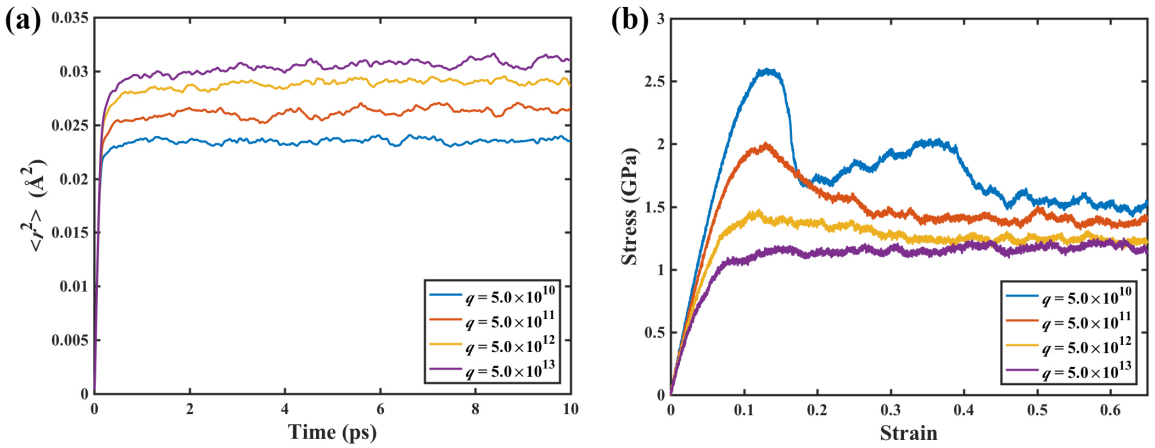

Figure 2.2: For a-Si configurations prepared using various cooling rates (q, in K/s) from liquid. (a) MSD, $\langle r^2 \rangle$, as a function of time. $\langle r^2 \rangle$ is evaluated on these short time scales and thus contains the vibrational but not the diffusional contribution. (b) MD-simulated stress-strain curves under simple shear loading with strain rate of 10^8 s^{-1}.

ing the time-dependent $\eta_i(t) = x_i(t) - \bar{x}_i$, where $\eta_i(t)$ is the Euclidean vector to describe the corresponding atomic vibration. The average of fabric tensor $\langle \eta_i(t) \otimes \eta_i(t) \rangle$ for the ith atom yields three eigenvalues, λ_k $(k = 1, 2, 3)$. Then the vibrational anisotropy can be defined as $\frac{3}{\sqrt{6}} \sqrt{\sum_{k=1}^{3} \left(\lambda_k - \frac{1}{3}\right)^2}$. For the isotropic case, $\lambda_1 = \lambda_2 = \lambda_3 = \frac{1}{3}$, so $\eta_i = 0$. For the extremely anisotropic case, e.g., one-dimensional atomic vibration, $\lambda_1 = 1$ and $\lambda_2 = \lambda_3 = 0$, then $\eta_i = 1$.

Simple shear deformation at a strain rate of 10^8 s^{-1} was applied on a-Si samples prepared at various cooling rates. During the shear deformation, the box was deformed by supercell tilting followed by MD relaxation, with a step length of 1×10^{-7} in shear strain. The shear stress-strain curves are shown in Fig. 2.2(b). The shear modulus G of a-Si models was derived from the shear stress-strain curves at small (0.5%) strain (around which the G value levels off

to a steady value) and averaged over simple shear deformation along different directions (i.e., ±xy, ±xz, ±yz). Our studied *a*-Si samples are large enough (containing 85,184 atoms) to achieve the converged *G* in the calculation.

The activation-relaxation technique (ART nouveau) in MD simulations [20, 78, 103, 104] was used to investigate the energy barrier for thermally activated relaxation events in the *a*-Si sample quenched to room temperature from liquid at 1×10^{11} K/s. To initiate the local excitations of the system, small perturbations in ART were introduced by applying random displacement on a small group of atoms (an atom and its nearest neighbors with a distance cutoff of 3.0 Å). The magnitude of displacement was fixed, while the direction was randomly chosen. The system was pushed toward the saddle point using the Lanczos algorithm, when the curvature of potential energy landscape was found to overcome the chosen threshold. A total of ∼150,000 different activations were identified for that *a*-Si sample, after removing the failed searches and redundant saddle points.

2.3 Results and discussion

2.3.1 The flexibility volume

As introduced before [78], the flexibility volume is defined as $v_{flex} = \langle r^2 \rangle a$, where a is the average atomic spacing, given by $a = \sqrt[3]{\Omega_a}$, Ω_a is the average

atomic volume, and $\langle r^2 \rangle$ is the atomic vibrational mean-square displacement [in the regime where it is flat with time, as shown in Fig. 2.2(a)]. This structure parameter is unlike all other previous ones, as it combines the structural information of both the atomic volume and the space accessed by atomic vibration, the two together quantitatively determining the shear modulus G of a-Si (as shown below in Sec. 2.3.2). The flexibility volume can in fact be evaluated on each and every atom (the ith atom), $v_{flex,i}$, and v_{flex} of the sample (or local region) is then an arithmetic mean of all the $v_{flex,i}$ in the system (region). As shown in Fig. 2.1, the flexibility volume of a-Si undergoes obvious changes with the cooling rate used to prepare the amorphous sample. The trend that v_{flex} decreases with slower cooling rate is consistent with the case for MGs [78]. But, as mentioned earlier, unlike MGs the a-Si with slower cooling rate (equivalently with lower internal energy) exhibits larger volume (or lower density). The opposite trends between the flexibility volume and atomic volume for a-Si (see Fig. 2.1) bring forth an interesting scenario: a larger surrounding elbow room ($\Omega_{a,i}$ or the system average Ω_a) can actually be accompanied by a smaller wiggle space accessed via vibration (smaller MSD, $v_{flex,i}$ and v_{vflex}). To better explain this seemingly anomalous behavior, we also calculated the vibrational anisotropy (η) of the ith atom, by monitoring the time-dependent atomic oscillation (see Sec. 2.2). As shown in Fig. 2.3(a), for a-Si, the larger the flexibility volume, the greater the vibrational anisotropy. The latter is apparently a ma-

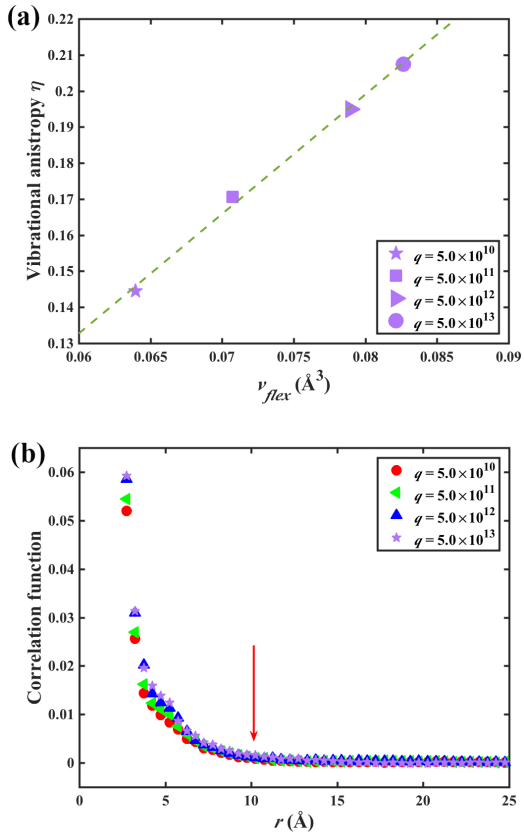

Figure 2.3: Four a-Si configurations prepared uing different cooling rates (q, in K/s) from liquid. (a) System-averaged vibrational anisotropy η versus flexibility volume. (b) Spatial correlation function of atomic flexibility volume for a-Si configurations. The correlation length is around 1 nm, as indicated by the red arrow.

jor contributor to the flexibility volume. For instance, the packing distortion around an atom entails looser directions and an easier pathway for atomic movement, and consequently higher vibrational anisotropy, leading to larger flexibility volume. Conversely, a well-defined and strongly bonded local motif such as tetrahedrally coordinated Si reduces anisotropy, and decreases flexibility, even though the surrounding space is enlarged. This can be confirmed by calculating the average vibrational anisotropy for CN = 4 and CN $>$ 4, which

are 0.151 and 0.218, respectively (in the a-Si sample quenched using a cooling rate of 5×10^{11} K/s).

We note that the flexibility volume evaluated for individual atoms, i.e., $v_{vflex,i}$, is not uniformly and randomly distributed across the a-Si sample. Instead, a spatial correlation is revealed in Fig. 2.3 (b), by employing the spatial correlation function, $C_{flex}(r)$. A similar function of nonaffine displacement was used before to indicate the size of shear transformation zones in MGs [105]. We define $C_{flex}(r)$ as

$$C_{flex}(r) = \frac{\sum_{i \leqslant j} v_{flex,i} v_{flex,j} n(r - r_{ij})}{\sum_{i \leqslant j} n(r - r_{ij})} - \frac{\left[\sum_{i \leqslant j} v_{flex,i} n(r - r_{ij})\right] \left[\sum_{i \leqslant j} v_{flex,j} n(r - r_{ij})\right]}{\left[\sum_{i \leqslant j} n(r - r_{ij})\right]^2} \tag{2.1}$$

where r_{ij} is the distance between the ith and jth atoms, and the function $n(x) = \begin{cases} 1, & |x| \leqslant \frac{1}{2}\Delta \\ 0, & |x| > \frac{1}{2}\Delta \end{cases}$ [Δ is the width of the bins used in calculating and plotting $C_{flex}(r)$; see Fig. 2.3(b)]. The spatial correlation functions of flexibility volume, for a-Si prepared with various cooling rates, decreases with increasing distance r. Following Ref. [105], the corresponding correlation length, as indicated in Fig. 2.3(b), is the distance where spatial correlation vanishes. For all four samples prepared with different cooling rates, this correlation length for a-Si is at $\sim$1 nm, which is consistent with the approximate size of shear trans-

formation zones in a-Si (Refs. [49, 89, 106]. This implies an underlying link between the local structure (in terms of flexibility volume) and shear transformation in a-Si (more discussions in Sec. 2.3.4).

2.3.2 The v_{flex}-G correlation

We probe into the correlations based on flexibility volume, by first quantitatively determining the shear modulus G of a-Si. Here G is taken as our primary target because it is widely regarded as a key baseline property that controls the energy barrier for relaxation and shear flow [52, 107]. G is also known to depend strongly on glass configuration, and hence on processing history [60]: the slower the cooling rates, the higher the G [as reflected by the steeper slope of stress-strain curve in Fig. 2.2(b)]. The connection between G and the atomic MSD, $\langle r^2 \rangle$, was recognized before [108] but has not been quantitatively verified using systematic data, let alone for different types of glasses. Moreover, we have shown recently that MSD alone is actually not universally deterministic of G, but flexibility volume is [78].

For an isotropic Debye solid, the Debye temperature θ_D can be expressed as [107]:

$$\theta_D = \frac{h}{k_B} \left(\frac{4\pi}{9} \right)^{-\frac{1}{3}} (\Omega_a)^{-\frac{1}{3}} \left(\frac{1}{v_l^3} + \frac{2}{v_s^3} \right)^{-\frac{1}{3}} \tag{2.2}$$

where $v_l = \sqrt{\left(B + \frac{4}{3}G\right)/\rho}$ and $v_s = \sqrt{\frac{G}{\rho}}$ are the longitudinal and transverse sound velocities, respectively, B is the bulk modulus, and $\rho = \frac{m}{\Omega_a}$ is the mass density, where m is the average atomic weight. For SW *a*-Si [96], B/G is in the range of 3.21-4.81. Thus the cases we are dealing with are those for which $B = (4.0 \pm 0.8)\,G$. Over this range, approximaiting $B = 4G$ would only involve an error of no more than $\sim$1% in θ_D, because in Eq. 2.2 the second term in the last bracket overrides by far the first term. Hece Eq. 2.2 can be simplified to

$$\theta_D \approx \frac{h}{k_B}\left(\frac{4\pi}{9}\right)^{-\frac{1}{3}}(2.082)^{-\frac{1}{3}}\left(\Omega_a\right)^{-\frac{1}{3}}\sqrt{\frac{G}{\rho}}. \tag{2.3}$$

Now, recall that the Debye temperature is also known to scale with the vibrational MSD, $\langle r^2\rangle$, following [109]

$$\theta_D^2 = \frac{9\hbar^2 T}{m k_B \langle r^2\rangle}. \tag{2.4}$$

Combining Eqs. 2.2, 2.3 and 2.4, we arrive at [78]

$$G = C_{\mathrm{Si}}\frac{k_B T}{\langle r^2\rangle a} = C_{\mathrm{Si}}\frac{k_B T}{v_{flex}}, \tag{2.5}$$

where k_B is the Boltzmann constant and the constant $C_{\mathrm{Si}} = \frac{9}{4\pi^2}\left(\frac{4\pi}{9}\right)^{2/3}(2.082)^{2/3} = 0.464$. Note that *G* in Eq. 2.5 contains no viscoelastic relaxation. This derivation conveys the idea that high-frequency, atomic level vibrations contain a sig-

nature of long-wavelength phonons which depend on G. The equation predicts that at a given temperature T (e.g., room temperature), a single structural parameter v_{flex} can be used to predict the shear modulus (in the current chapter, for a-Si). In other words, once the structural descriptor v_{flex} is quantified via computational or experimental measurement for a-Si samples that have been processed differently to give rise to different v_{flex}, a quantitative correlation is available to gauge and compare the mechanical response G of these various v_{flex}. In the following, we will demonstrate that Eq. 2.5 indeed holds for a-Si.

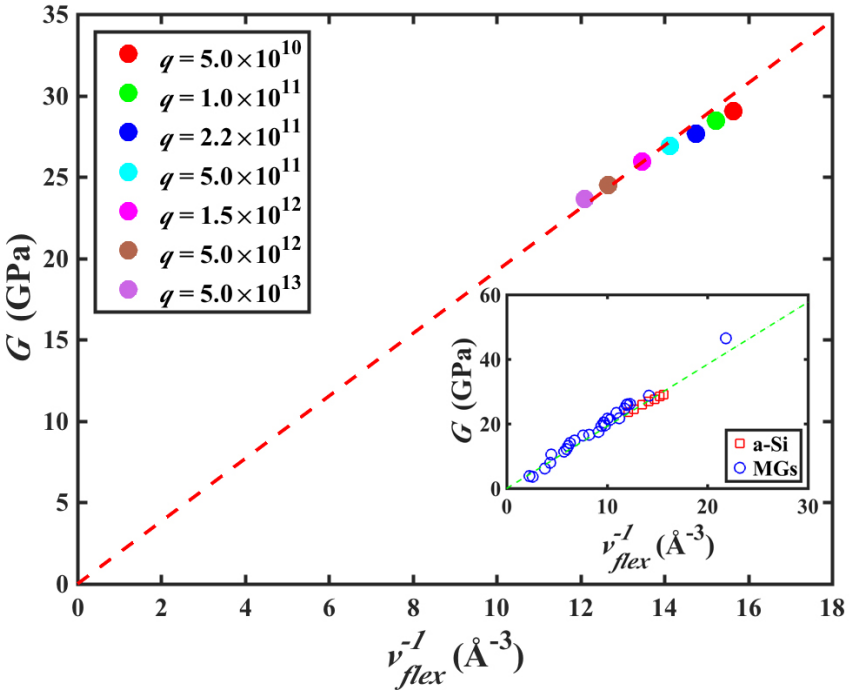

Figure 2.4: Quantitative correlation between the shear modulus G and the flexibility volume v_{flex} for a-Si obtained using different quench rates q, in K/s. The inset includes all the data points for a-Si (present work) and MGs (from Ref. [78]). The dashed red straight line (green in the inset) is the prediction derived in Eq. 2.5.

Figure 2.4 plots G versus v_{flex}. The error bar for the group of data used for averaging is smaller than the size of each data point shown in the plot. The dataset demonstrates a strong correlation, and in fact conforms within $\sim$3% to the linear relationship predicted in Eq. 2.5, which is the straight dashed line in Fig. 2.4 (the slope of this line itself has an error margin of $\sim$2%, from the uncertainty in B/G or v_l/v_s in the approximation used in the derivation of the above equations). The small error in our dataset ($<$3%) may also be partly from the method used to derive G, i.e., taking the slope of the shear stress-strain curve at 0.5% strain. Figure 2.4 establishes that v_{flex} is all that is needed to account for G quantitatively, allowing prediction and comparison for various a-Si prepared under different conditions. This conclusion is consistent with that reported for MGs [78]. As seen in the inset of Fig. 2.4, which includes the dataset for MGs as well as that for the a-Si samples studied here, the prediction given in Eq. 2.5 (dashed line) is an adequate representation of all the data (in other words, $C_{\rm Si}$ here is practically the same as the constant C known for all MGs [78]). This observation of a single flexibility volume parameter to quantitatively correlate with the mechanical response of different amorphous materials is very interesting. In contrast, all other structural metrics used before, even in cases where they themselves are quantifiable (e.g., fraction of liquidlike sites ϕ, or potential energy, or excess volume over a reference such as the corresponding crystal, or even the absolute value of free volume if that

is actually quantifiable by some means), cannot be plugged into an equation to directly calculate a particular property.

2.3.3 Correlating v_{flex} with atomic-level static structure

Next we connect the static atomic-level structure of a-Si with the flexibility volume. Two static structural indicators at the atomic level, the CN and fraction of liquidlike sites, are commonly used for a-Si [48, 96]. Several examples of atomic sites in a-Si with different CN (CN = 3-6) are plotted in Fig. 2.5(a). In comparison, crystal Si (c-Si) has the tetrahedral packing with CN = 4, which is also regarded as the favored local motif in a-Si. Several decades ago, the defects in a-Si were originally hypothesized to be undercoordinated sites (e.g., CN = 3), referred to as "dangling bonds" [110, 111]. But more recent findings have indicated that overcoordinated sites (e.g., CN = 5) are more defectlike and liquidlike [47,48,112]. As presented in Fig. 2.5(b), the atomic flexibility volume in a-Si correlates predominantly with CN = 5 (the fractions of CN=3 and CN=6 are negligible): more CN=5 at the expense of CN = 4 corresponds to larger atomic flexibility volume. The other static atomic-level structural indicator for a-Si is the liquidlike sites. These sites were characterized by Demkowicz and Argon according to the mean bond angle as well as its standard deviations (see details in Refs. [47, 48]. Following this practice, we analyzed the bond angles in our a-Si in Fig. 2.5(c), where liquidlike and solidlike atomic sites can be

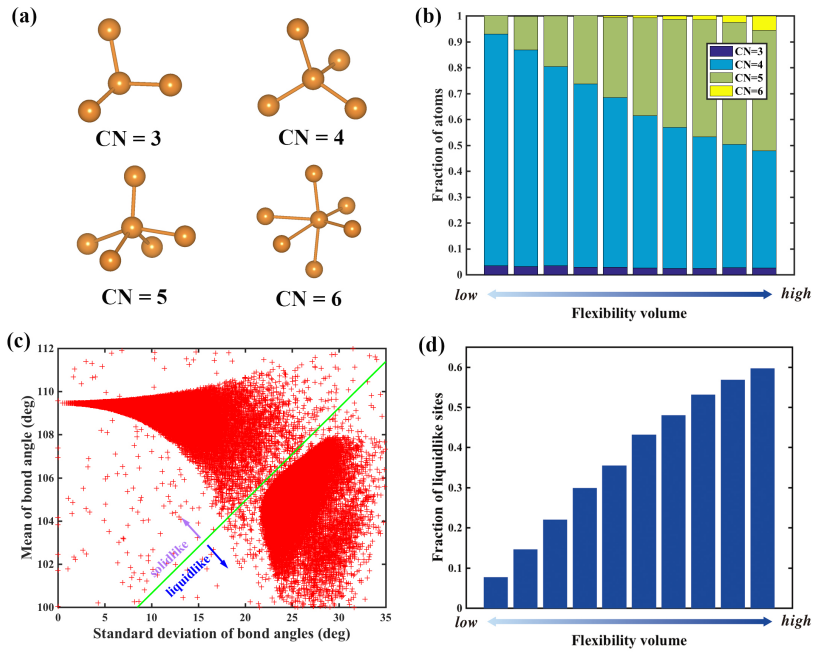

Figure 2.5: Correlation between flexibility volume v_{flex} and static structural indicators for a-Si. For the a-Si with the cooling rate of 5.0×10^{11} K/s, (a) illustration of examples of atomic sites in a-Si with different CN; (b) correlation between the flexibility volume and the fraction of atomic sites with different CN (from CN = 3 to CN = 6). All the atoms are sorted, from left to right, based on flexibility volume $v_{flex,i}$ into bins each containing 10% all of the atoms; (c) mean bond angles and their corresponding standard deviation for all the atomic sites; the solidlike and liquidlike sites can be separated accordingly; (d) correlation between the flexibility volume and the fraction of liquidlike sites. All the atoms are sorted based on flexibility volume $v_{flex,i}$ into bins each containing 10% of all the atoms.

well separated. Interestingly, as shown in Fig. 2.5(d), the flexibility volume exhibits a strong correlation with the fraction of liquidlike sites ϕ: the larger the flexibility volume, the higher the fraction of liquidlike sites. All these analyses indicate that the flexibility volume reflects very well the existing static structural indicators at the atomic level. But the new parameter of flexibility volume brings unprecedented advantages: it offers not only another way to quantita-

tively identify the liquidlike sites (more defectlike sites), but also a descriptor of structure state that can deterministically predict the shear modulus.

2.3.4 Correlating v_{flex} with local relaxation events

We first examine the correlation between flexibility volume and shear transformations, which are the fundamental processes underlying the inelastic deformation [53]. As already revealed in Refs. [47, 48] and Fig. 2.2(b), a-Si samples with different quench rates show different propensity for shear deformation driven by imposed stresses (and flow stress and yield point); a slower cooling rate results in higher resistance to flow, in line with the higher G. Now the latter can be directly linked with a higher v_{flex} (see Fig. 2.4). Moreover, we can use $v_{flex,i}$ as an effective descriptor of local structure to offer a zeroth-order explanation of the different local response to the stress stimulus (longer-range collective effects on atomic motion in amorphous solids are neglected for the time being). Figures 2.6(a)-(d) show that $v_{flex,i}$ is indeed a very effective indicator of the propensity to undergo shear transformations. Specifically, here athermal quasistatic shearing (AQS) [54, 113] was applied to induce atomic rearrangement in a-Si, and the shear transformations were tracked by monitoring the nonaffine displacement $D^2_{\min}$ [54]. The contoured maps of the spatial distribution of $v_{flex,i}$ are then compared/superimposed with the top 5% atoms that have experienced the most accumulative nonaffine strains, after a global

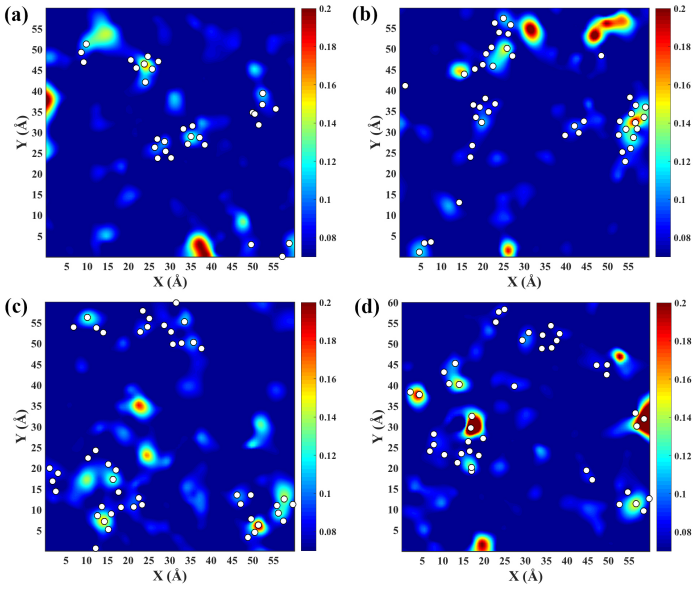

Figure 2.6: Strong correlation between flexibility volume $v_{flex,i}$ and the propensity for shear transformations. Contoured color maps show the spatial distribution of $v_{flex,i}$ (see sidebar) in the a-Si quenched using a cooling rate of 5.0×10^{11} K/s. Four representative slabs [(a)-(d)] are sampled for illustration purposes and each has a thickness of 2.5 Å. White spots superimposed in the maps mark the locations of atoms that have experienced the most (top 5%) accumulative nonaffine displacement (D^2_{min}), upon athermal quasistatic shear of the simulation box to a min global strain of 5%. Note that not all such regions would undergo shear transformation for a particular loading. This is reasonable because apart from the intrinsic flexibility of the local configurations, the stress field (tensor) is another (extrinsic) factor that will influence the response of the atoms.

strain (e.g., 5%). The clear correlation in Figs. 2.6(a)-(d) establishes that under externally imposed stresses, shear transformations have a high propensity to originate from those regions with the highest flexibility volume [78]. Note that not all such regions would undergo shear transformation for a particular loading. This is reasonable because apart from the intrinsic flexibility of the local configurations, the stress field (tensor) is another (extrinsic) factor that will influence the response of the atoms. As presented in Fig. 2.7, such

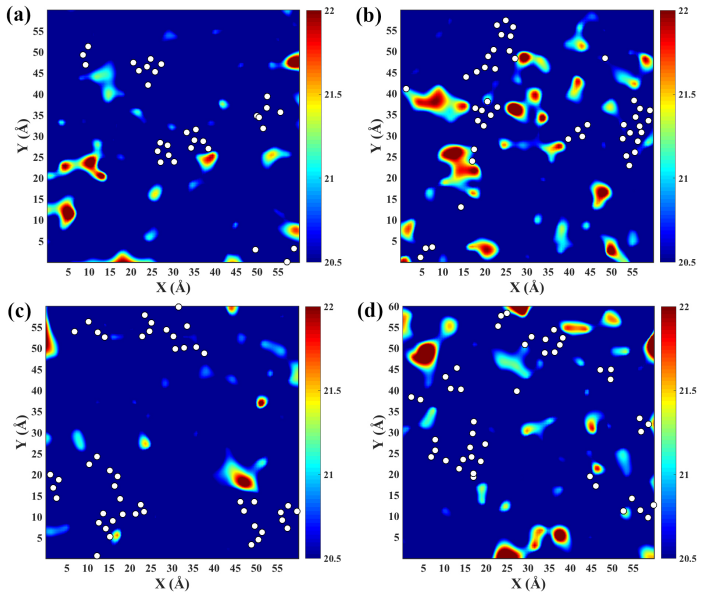

Figure 2.7: Contour color maps showing the spatial distribution of local atomic volume ($\Omega_{a,i}$) (see colored sidebar for the magnitude) in the a-Si quenched using a cooling rate of 5.0×10^{11} K/s. Four representative slabs [(a)-(d)] are sampled for illustration purposes and each has a thickness of 2.5 Å. White spots superimposed in the maps mark the locations of atoms that have experienced the most (top 5%) accumulative nonaffine displacement (D^2_{min}), upon athermal quasistatic shear of the simulation box to a global strain of 5%. There appears to be no clear correlation with the locations with the highest local atomic volume.

a correspondence with shear transformations is clearly absent, when a similar contour map is made to correlate with local atomic volume. This lack of correlation echoes our earlier statement that atomic volume is not a telltale structure parameter that connects well with the properties of a-Si.

In addition, it was found that the flexibility volume is also strongly correlated with the activation energy barrier for thermally activated relaxation events for a-Si, which can be monitored using the ART nouveau in MD simulations [20, 78, 103, 104] (see Sec. 2.2). The distribution of activation energy

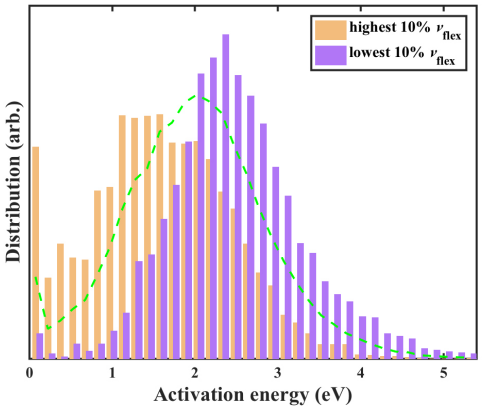

Figure 2.8: Correlation between flexibility volume and thermally activated relaxation events. Distribution of activation energy in the a-Si (quenched with the cooling rate of 1.0×10^{11} K/s) characterized using ART nouveau. The activated relaxation events are for atoms in the center of their coordination polyhedra. This plot shows the distribution of activation energy for the two groups with the highest and lowest 10% flexibility volume ($v_{flex,i}$) and the green line is for the entire sample. Here each curve is normalized by the total number of activated events sampled by the entire group of atoms involved in the distribution.

for all the atoms in the a-Si is shown as the dashed line in Fig. 2.8 (consistent with previous literature [114]). Then the atoms with the lowest 10% and highest 10% $v_{flex,i}$ are identified, and the distribution of activation energy for thermally activated events surrounding these atoms (as illustrated in Sec. 2.2, small perturbations in ART were initially introduced on the designated atom and its nearest neighbors) is plotted. We observe in Fig. 2.8 that there is an obvious gap (a difference as large as $\sim$1.1 eV) between the two peak positions for the two groups with the lowest 10% and highest 10% $v_{flex,i}$: the sites with larger flexibility volume are found to exhibit lower-energy barriers, and the lowest flexibility volume sites correspond to high-energy barriers. This clear

bifurcation for thermally activated relaxation, based on $v_{flex,i}$ is also what was observed in the case of MGs [78].

2.3.5 General applicability of v_{flex} for amorphous materials

Our results above have demonstrated the successful application of the new flexibility volume parameter for network-forming amorphous solids, using an a-Si model as the representative. Flexibility volume not only deterministically predicts the macroscopic shear modulus (Sec. 2.3.2), but also strongly correlates with the local relaxation events activated by shear stress or thermal agitation (Sec. 2.3.4). These findings, together with our previous work on MGs, point to the generality of the flexibility volume parameter for different amorphous materials, irrespective of their distinct structure and bonding characteristics. Therefore, flexibility volume as a descriptor of the structure state is projected to be universally useful for other amorphous materials, such as glassy polymers [115] and oxide glasses [116], to build a bridge between the structure and properties.

This general applicability is not possible with any previous indicator of the amorphous configuration. For example, one can again compare with previous parameters based on the magnitude of the local volume, such as the two-order-parameter (TOP) model proposed by Tanaka [117]. In this model, (i) there exist

distinct locally favored structures (LFSs) as state F and (ii) such structures are formed in a "sea" of normal liquid structures (L). Each state is associated with a different value of energy (U), specific (or atomic) volume (V), and entropy (S). For amorphous or liquid Si [117], $U_F<U_L$, $V_F>V_L$ (LFS with tetrahedral order has a higher specific volume) and $S_F < S_L$. For metallic glasses/liquids, however, $U_F < U_L$, $V_F < V_L$, $S_F < S_L$, because in this case the LFS is efficiently packed motifs with smaller volume. In both cases, the fraction of the LFS increases upon cooling, with lowered U and S. But V goes in the opposite direction between a-Si and MGs. Now, using flexibility volume rather than V, in both cases v_{flex} consistently decreases with increasing undercooling and with decreasing cooling rate. As such, flexibility volume can act as a universal and quantitative descriptor of the LFS, or the structure state in general, in lieu of the static volume. In other words, specific LFSs can be vastly different for different glasses, such as tetrahedral order for a-Si versus icosahedral order for some MGs, but all LFSs inherently entail lower flexibility volume. This brings forth a unified description of atomic-level structure state for amorphous materials, despite their differences in chemical bonding and atomic packing.

2.4 Summary

We conclude by highlighting several salient features of our results. First of all, the correlation we have demonstrated above is an advance over relying solely

on the static configuration (often merely a single aspect of the structure) to correlate with properties. Instead, our v_{flex} purposely incorporates dynamics information via MSD and reflects the overall flexibility that is actually available in the glass internal structure. For a-Si, this descriptor implicitly covers information such as the nature of atomic bonding and how liquidlike the environment is. Although v_{flex} does not directly describe anisotropy, it does reflect the effects of the latter on atomic flexibility. Second, the new flexibility parameter here arises from Debye theory and enables a quantitative calculation of G directly from Eq. 2.5. Currently none of the existing structural parameters for glasses incorporates dynamics and has one-to-one correspondence with key properties. Third, which is an important point of this work, the success with a-Si lends support to the universality of Eq. 2.5 for various types of glasses, beyond the demonstration earlier for metallic glasses [78]. In fact, the material we are modeling here is different in nearly all respects from the metallic glasses for which the formalism was initially developed: different from metallic glasses, a-Si is a network glass with directional covalent (rather than metallic) bonding, and importantly, does not show the correlation of properties with free volume that we have grown to expect in metallic glasses. We have confirmed again that indeed excess volume is not of fundamental importance in governing the fertile sites where shear transformations tend to take place (see Fig. 2.7). Fourth, v_{flex} is a good candidate as a single internal variable

characterizing the state of the glass in a possible continuum description of mechanical rigidity. In the meantime, we also see that for this open-structure glass, high $v_{flex,i}$ and its local average remain as a telltale indicator of regions most amenable to imposed local shape change via stress-driven shear transformations, as demonstrated by the correlation in Figs. 2.6(a)-(d). $v_{flex,i}$ is thus a prognostic parameter in monitoring the deformability distribution inside a-Si, to explain the spatial heterogeneity of the mechanical response in an amorphous solid [25, 35, 118]. Finally, our current approach of incorporating dynamics information overcomes some shortcomings associated with the earlier approach using the vibrational modes [19, 54, 119, 120], where the soft spots were identified based on a preselected cut-off vibrational frequency (for example, arbitrarily choosing the 1% lowest frequency), and the participation of atoms in these soft modes is evaluated on a relative basis. This makes it difficult to decide which soft spots are truly eventful, in terms of being actually activated in relaxation. There is also no quantified measure of their contributions to the overall glass properties. Moreover, it is not feasible to directly compare the soft spots in different samples and in different glasses. In comparison, flexibility volume is universal and easier to use, and it quantitatively scales with G. One can now use this parameter to directly calculate and compare for different amorphous solids, and explain the spatial heterogeneity of mechanical properties mapped out for different local regions. Taken together,

the new points made in this chapter constitute a step forward in developing (mathematically) verifiable correlations that link the amorphous configuration with properties.

Chapter 3

Making glassy solids ductile at room temperature by imparting flexibility into their amorphous structure

3.1 Introduction

Glassy or amorphous materials are ubiquitous, offering many useful properties in our daily lives [8, 29, 121–125]. But for glasses with a glass transition temperature greater than room temperature (RT), they suffer from one major

drawback, being usually brittle at RT [28, 30, 34, 126–128]; their shape change relies upon viscous flow near or above the glass transition temperature. This poses a challenge to both engineers and scientists. In terms of engineering applications, amorphous solids lack the capability of plastic deformation without fracture under ambient conditions, severely limiting the manufacture and utility of glasses. For example, there is currently a relentless push to make metallic glasses (MGs) ductile at RT so that their use in structural applications can be widened [30]. From the standpoint of materials science, an interesting question to explore is how to facilitate bond breaking and re-forming in the amorphous structure, to mimic viscous flow at elevated temperatures (or the action of dislocations in crystalline solids). Our current understanding with regard to how to tailor the amorphous structure of glassy materials to enable flow under applied loads is so far in its rudimentary stage, especially when compared with the well-established microstructure-plasticity relations in crystalline materials.

In this chapter, we draw the attention of the community to recent experimental observations of glassy solids that have been made ductile at RT; we will cite one example (Cu-Zr) as a representative for metallic glasses (MGs), and one (amorphous silica) for covalent network glasses. While the examples may be extreme cases, we use them to advocate our perspective that if the amorphous structure can be made unusually flexible to facilitate bond switching in

shear transformations, glasses can all be rendered to flow at RT. The focus of this chapter is molecular dynamics (MD) simulation results, which, coupled with these experimental examples, reveal the origin of the ductility achieved. Our argument is that the flexibility affordable by the atomic bonding and local configurational environment, rather than the sheer magnitude of excess spatial volume (local free volume), quantitatively determines the shear modulus, which scales with the energy barrier for relaxation [52], and hence controls the (local) propensity for shear transformations. This causal correlation will be demonstrated to be universal for both metallic glasses and covalently bonded glasses. The case studies we discuss in the following also suggest processing strategies that can enhance the flexibility in the amorphous structure, in particular through the retention of, or structural rejuvenation to restore, sufficient heterogeneous liquid-like regions with high flexibility.

3.2 Glasses made ductile at room temperature

To set the stage for our discussion of the relationship between structural flexibility and deformability, we first cite experimental examples of glasses made ductile at RT. This is only for brief demonstration purposes, since our emphasis is on the structural origin underlying the flow.

3.2.1 Metallic glasses

There have been a number of recent experimental observations of MGs exhibiting tensile ductility at RT [25]. Fig. 3.1 is a representative case, demonstrating that "normal-metal-like" behavior is indeed possible for an MG at RT [129, 130]. This engineering stress-strain curve of $Cu_{49}Zr_{51}$ MG is fully quantitative, showing an apparent elastic regime, followed by yielding and some uniform elongation accompanying apparent strain hardening, to a rather high tensile strength of $\sim$2.5 GPa (at a strain around 4.6%), where progressive necking starts. The total elongation is 10%. This tensile strain to failure, and the eventual cone-like shape of the fractured region, is typical of conventional ductile alloys that experience necking in a uniaxial tensile test. Such a ductile behavior is achieved because the glass sample size is very small (see inset of Fig. 3.1), such that it contains no pre-existing nuclei or easy nucleation sites for shear bands. Also, the small sample volume stores limited elastic strain energy and provides only a short runway, such that strain fluctuation across the sample does not get to develop into severe shear localization that evolves into a mature shear band [129,130]. We note that in this particular case, the $Cu_{49}Zr_{51}$ MG sample was prepared using melt spinning, such that rapid quenching was involved, and the glass structure was further rejuvenated during the cutting of the test specimen using focused ion beam [129, 130].

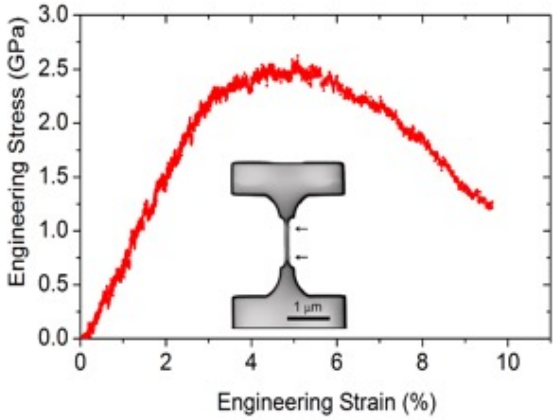

Figure 3.1: Engineering stress-strain curve of $Cu_{49}Zr_{51}$ MG. The inset shows the sample used in the *in situ* test. The arrows point to the gauge section. The high strength (∼2.5 GPa) observed indicates that the temperature cannot be much higher than RT. Adapted from Ref. [130]

Irradiation of MGs using ion beam was also used recently by several other groups [131–134], and found to promote ductility. As will be discussed later, this is an effective approach to impart flexibility into the glass structure. One can also use rapid quenching to retain flexibility from the parent phase, such as vapor-quenching via sputter deposition, to produce Zr-Cu-Al thin films that are ductile in tension [135]. Our discussions later will cover both routes, rapid quenching (from the liquid) as well as irradiation (by disposing extra energy to atoms), in our MD models.

3.2.2 Covalently bonded network glasses

Covalently bonded network glasses are well known to be completely brittle at RT. It is therefore somewhat surprising to observe in Fig. 3.2 that an amor-

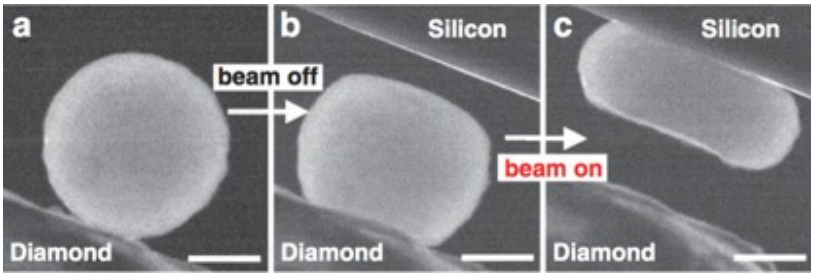

Figure 3.2: Compression of a-SiO_2 ball inside an electron microscope. Panels (a)–(c) show the centered dark-field images. In (a), the ball is adhered to the diamond punch and the silicon punch has not moved into the picture. In (b), the ball, after irradiation in (a), is imaged after it has been pressed with the beam off. Subsequently in (c), with the beam on, the ball can be compressed into a pancake without fracture or severe shear localization (shear banding) under a moderate force. The scale bar is 200 nm. Adapted from Ref. [136].

phous silica (a-SiO_2) ball can be compressed into a pancake without fracture or severe strain localization. This homogenous shape change clearly involves extensive plastic deformation. Nanowires of normally brittle amorphous silica in fact appeared superplastic in a tensile test inside a TEM [136]. Note that with the imaging e-beam on, the flow stress is a factor of three lower [136] than when the beam is blanked off, producing the pancake-shaped disk within two minutes. This shows that the e-beam dynamic rejuvenation during compression is more effective in making the silica flow than post-irradiation deformation.

We only briefly mention these two examples, one for metallic glasses and one for covalent glasses, because they suffice to motivate the focused discussions in this chapter on the understanding as to what is happening in the amorphous structure that could make these glassy materials flow at RT. For a survey of making glasses ductile at RT, the readers are referred to Ref. [25],

where it is seen that rapid quench and irradiation rejuvenation are often involved. We will, therefore, use modeling in Sections 3.3 and 3.4 to shed light on the changes in the glass structure processed via these two processing routes. In general, the overarching mechanism is the same: it is the retention of, or the rejuvenation to restore, flexibility in the glass structure that makes glass flow at RT upon loading.

3.3 Origin of ductility: flexibility versus excess volume

Glasses gain the ability of viscous flow at temperatures near or above the glass transition temperature, due to thermally activated bond switching that reposition and rearrange the atoms [137]. Then what does it take to make the same happen at RT? To answer this question, it is tempting to simply invoke the well-known concept of free volume, v_f [26], which is a widely cited structural parameter in the literature on glasses. On a per atom basis, v_f is the "critical excess" [43] relative to a critical atomic volume corresponding to a reference glass state that has zero free volume. A popular answer to the question we posed above, in numerous papers over the years, is to add more free volume into the glass. v_f increases the extra space needed for dilatation during shear transformation, and as a result renders the glass more deformable [138].

However, this free volume concept is more appropriate for hard sphere models and polymeric glasses, but deficient for describing much softer interatomic potentials [45]. The latter also leads to ambiguous or inaccessible reference state [139], making v_f difficult to identify and quantify. In the literature, the more easily measurable average atomic volume Ω_a (or Voronoi cell volume, or the volume/density difference from the corresponding crystal) is often used to reflect the free volume content, because the Ω_a is expected to scale with the v_f. In the following, we will use case studies related to our examples in Section 3.2, to illustrate the inadequacy of the free volume picture and advocate a flexibility concept that can explain all the ductility trends observed.

3.3.1 Elevating flexibility to make MGs ductile

We begin our discussion with the MGs, as it is a case for which the origin of ductility has often been perceived to be well known. Different from covalent network glasses characterized by localized directional bonds, where the free volume idea is obviously not applicable (see Section 3.3.2), so far most publications in the MG community have embraced the free volume idea, often using Ω_a as the indicator. A rapidly quenched MG is believed to contain more free volume than a slowly cast one and is thus less rigid and more prone to flow [44,90]. An often-mentioned reason to resort to the volume-centric Ω_a is that MGs have densely packed amorphous structure, so the presence of excess spatial volume

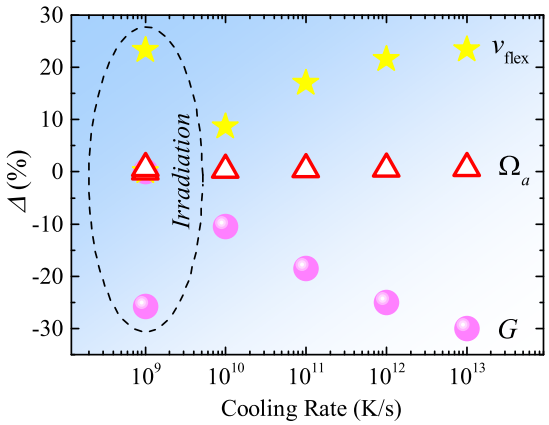

Figure 3.3: Percent change (Δ) of modulus (G), atomic volume (Ω_a) and flexibility volume (v_{flex}) for $Cu_{64}Zr_{36}$ MGs with various processing history (cooling rates and irradiation), relative to the corresponding values for the sample quenched at cooling rate of 1×10^9 K/s. Note that G decreases while v_{flex} increases with faster cooling rates or after irradiation. The increase in Ω_a is too small to be meaningful.

would be important to allow dilatation to instigate shear transformation [138].

However, despite of the frequent citing of v_f (Ω_a), most researchers in the community are aware of the drawbacks with this parameter. This is because v_f is not quantifiable as the reference zero-v_f state is not well defined [19, 46]. Even the measurable Ω_a is not user-friendly, as it is insensitive to composition and processing history of MGs. Here we use MD simulations employing the LAMMPS code [140] and EAM potential [141], to compare MGs at the same $Cu_{64}Zr_{36}$ composition. Even when the shear modulus (G) differs by 30% due to different processing history (cooling from the liquid with rates of 1×10^9 to 1×10^{13} K/s), the difference in Ω_a is miniscule (15.9043 versus 16.0159 Å^3, 0.7%) [78], as shown in Fig. 3.3. Also, in correlating with deformation kinetics,

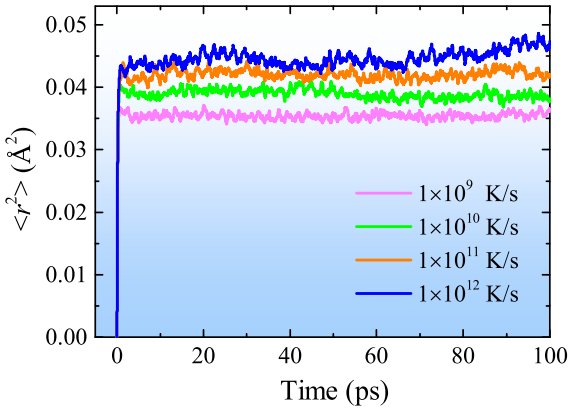

Figure 3.4: Evaluation of the vibrational mean squared displacement (MSD), i.e. $\langle r^2 \rangle$, for $Cu_{64}Zr_{36}$ MGs prepared using various cooling rates. The magnitude of MSD is dependent on processing (cooling rate)

Ω_a does not quantitatively determine any activation parameter. Moreover, even if we assume one can figure out how much change of v_f has happened in the sample, e.g. it has increased by 1%, it is still not possible to predict how much change in properties would be induced. It is therefore difficult to use Ω_a to explain the MG ductility seen in Figure 3.1.

This calls for a new parameter, one that can be quantitatively determined and sensitive to processing. We recently defined such a parameter, termed flexibility volume [78],

$$v_{flex} = \frac{\langle r^2 \rangle}{a^2} \cdot a^3 = \langle r^2 \rangle \cdot a, \tag{3.1}$$

where $\langle r^2 \rangle$ is the vibrational mean squared displacement (MSD) and a is the average atomic spacing. Both are temperature dependent so Equation (3.1) is a

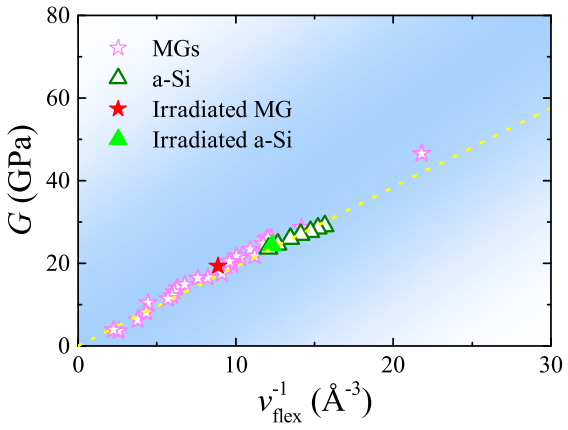

Figure 3.5: Correlation between shear modulus (G) and flexibility volume (v_{flex}) for both MGs and a-Si, including after experienced irradiation. Data of non-irradiated MGs and a-Si were adopted from Ref. [78] and [77], respectively.

quasi-harmonic approximation. v_{flex} can be viewed as an effective free volume, by modifying local atomic volume with the Lindemann ratio. Specifically, v_{flex} combines static atomic volume with dynamics information, through the MSD, which is readily evaluated in the MD model, see an example in Figure 3.4. In other words, v_{flex} uses vibration-assessed wiggle room as a probe to "test the water", to gauge how flexible the local configuration is, under the particular geometrical and bonding environment.

Importantly, v_{flex} quantitatively correlates with G [77, 78], as shown in Figure 3.5. It is significant that this correlation is deterministic, because G is known to scale with the activation energy for thermally activated relaxation and the propensity for stress-driven shear transformations [52]. G also scales with the yield strength [27].

As seen in Figure 3.3, the absolute percent change of v_{flex} is comparable to

that of G, a clear advantage over the indistinguishable Ω_a in the same figure. From the shift of the sample-average v_{flex} by $\sim$25%, one expects a similar percent change in G and a corresponding change in strength. This quantitative correlation is a clear advantage over other previously used parameters such as free volume, fictive temperature [91, 92], topological disorder (GUMs [24, 54], soft spots [142–144], or liquid-like flow defects [47, 48]. Figure 3.6 displays the stress-strain curves in uniaxial tension at 50 K for $Cu_{64}Zr_{36}$ MG obtained by cooling at 1×10^{10} and 1×10^{13} K/s form the liquid. The 1×10^{10} K/s sample shows an overshoot stress to rejuvenate the structure for initial yielding, followed by a major stress drop on the curve, which is often a signature of strain localization [145, 146]. This is in contrast with the 1×10^{13} K/s sample, showing no overshoot and sustainable plastic flow.

As such, v_{flex} gets around several shortcomings with free volume, particularly its vague and non-quantitative nature. In particular, v_{flex} allows a direct comparison of the structural flexibility after different processing, making it very useful to explaining the strength/ductility behavior such as the prediction of the corresponding change in modulus, strength and uniformity of flow. For the latter, the higher the v_{flex}, the lower the local G, the lower the activation barrier for shear transformations, and hence an easier and more spread-out flow. This can be rationalized by assuming that the plastic flow is proportional to the propensity for (or the rate of) shear flow, P, which in turn is controlled

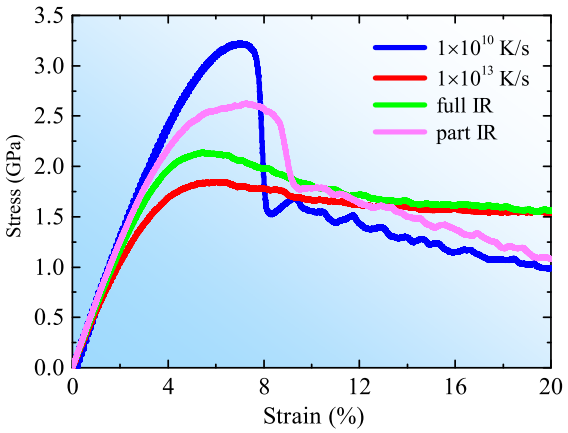

Figure 3.6: Stress-strain curves in uniaxial tension (along Z-direction) loaded at 50 K with constant strain rate of 4×10^7 s^{-1} for $Cu_{64}Zr_{36}$ MGs with various processing history (full IR: irradiated entire sample; part IR: irradiated X surfaces of the sample). Those samples have dimensions of 40.1 (X) $\times$ 8.0 (Y) $\times$ 79.5 (Z) nm^3, containing 1.6 million atoms. Periodic boundary condition (PBC) was imposed in the Y- and Z-directions, while free surface was used in the X-direction to allow shear offset on the free surfaces.

by G ($= Ck_BT/v_{flex}$) [78] in the energy barrier for shear flow,

$$P = P_0 \exp\left(-\frac{\alpha C}{v_{flex}}\right), \tag{3.2}$$

where α scales with an activation volume and is composition dependent. With v_{flex} increasing via rapid quench and/or irradiation, the probability for shear transformation increases, assuming the prefactor and activation volume remain similar for samples at the same composition.

Indeed, there is almost no stress overshoot in the curve of the 1×10^{13} K/s sample. The glass structure is ready to flow, and after yielding the smooth flow stress plateau suggests stable homogeneous plastic deformation. A direct com-

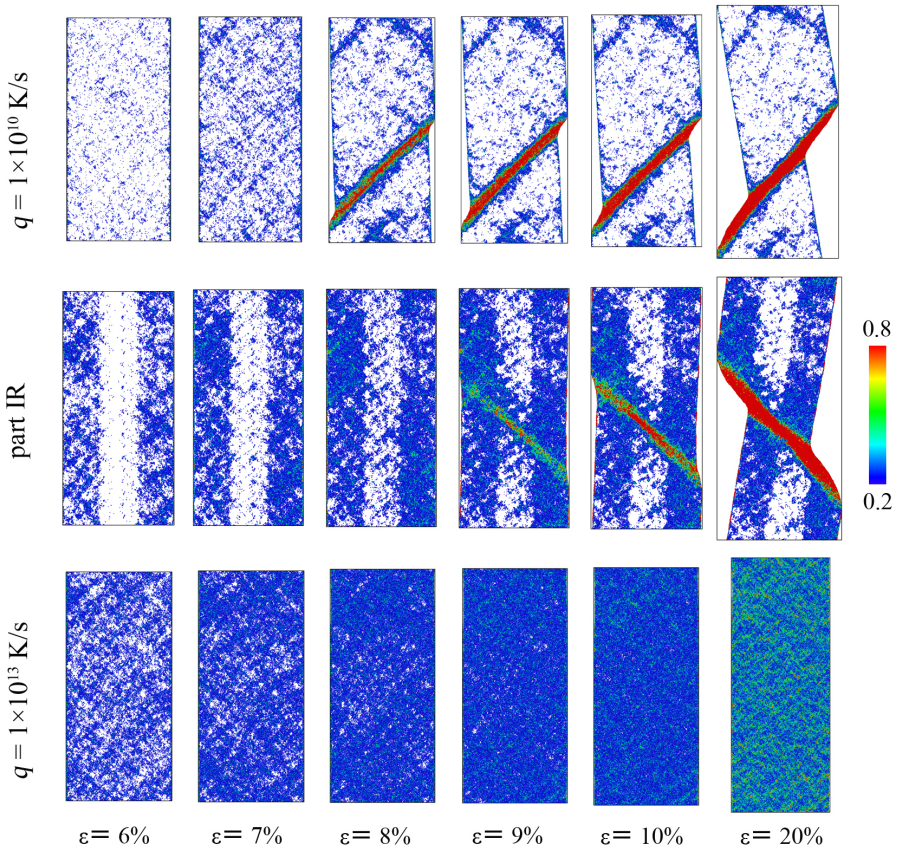

Figure 3.7: Projected views of the atomic configurations, showing the deformation process corresponding to Fig. 3.6, by monitoring local shear strain of each atom for $Cu_{64}Zr_{36}$ MGs quenched at cooling rate (q) of 1×10^{10} K/s (upper panel), 1×10^{9} K/s followed by surface irradiation (middle panel), and 1×10^{13} K/s (lower panel), respectively. Only atoms with a local shear strain above 0.2 are shown.

parison showing the strain distribution in the sample is presented in Figure 3.7 for the samples strained to 20% in uniaxial tension. The contrasting behavior of the two MGs is evident. In contrast to the high v_{flex} case of the 1×10^{13} K/s sample, where shear transformations spread out uniformly throughout the sample, v_{flex} is inadequate in the 1×10^{10} K/s sample, exhibiting inhomogenous deformation. Strains localize into a single dominant shear band quickly as a

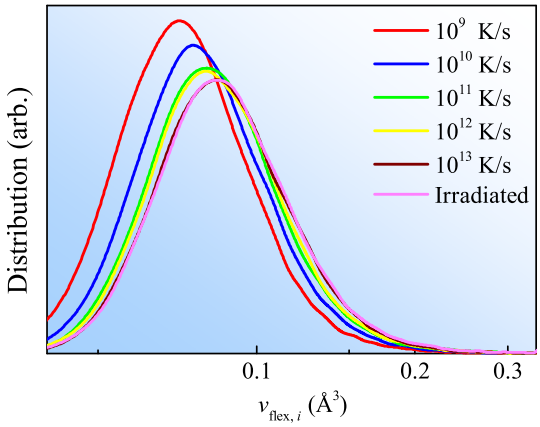

Figure 3.8: Probability distribution of the atomic flexibility volume ($v_{flex,i}$) of $Cu_{64}Zr_{36}$ MGs with various processing history (cooling rates and irradiation).

result, as contrasted in Figure 3.7 (upper panel vs. lower panel), and in Movies 1(a, b, c) and 2 [1].

Again the drastic difference in plastic flow is attributable to the difference in v_{flex} after cooling at the two different rates: this can be seen by comparing the atomic $v_{flex,i}$ in the probability distribution compared in Figure 3.8 for the two cooling rates. The sample with a faster cooling rate has much more local regions with larger v_{flex} compared to the sample with the slower cooling rate. These local regions are fertile sites where shear transformation zones (STZs) prefer to emerge (see Section 3.4 for further evidence). Such spread-out fertile sites help to distribute the strain to avoid localization into a single severe shear band, as shown in Figure 3.7.

Another way to elevate the v_{flex} of an MG is to irradiate the sample with the energetic beam. Note that Ω_a remained almost unchanged (15.9043 vs.

[1] see: https://www.tandfonline.com/doi/suppl/10.1080/21663831.2018.1503198?scroll=top

16.0104 Å^3, 0.67%) even after full irradiation of the 1×10^9 K/s sample. The sample-average v_{flex}, on the other hand, increased by 23%, to the level equivalent to the 1×10^{13} K/s sample, as shown in Figure 3.3. And the distribution also approaches that of the latter, see Figure 3.8. The stress-strain curve (included in Figure 3.6) and the distribution of local strain (not shown) also become similar to that of the 1×10^{13} K/s sample. Similar irradiation effects on MG ductility were reported by Shi *et. al.* [147] and Albe *et. al.* [148].

In addition to fully irradiating the MG samples as did by Albe *et. al.* [148], we also irradiated the free surface normal to the X-direction of $Cu_{64}Zr_{36}$ MG sample, similar to the simulation of Shi *et. al.* [147] on cylindrical MG samples with a small radius of 3.9 nm. Our work used much larger samples containing 1.6 million atoms: for saving computing time, we first duplicated small cubic sample quenched at cooling rate of 1×10^9 K/s containing 32,000 atoms and cell length of $\sim$8 nm (5$\times$ along the X-direction), and then opened free surfaces (PBCs for the other two). To simulate the irradiation, on each X free surface a randomly chosen atom $<$ 12 nm from the free surface was taken as the primary knock-on atom (PKA). A velocity parallel to the X-direction is assigned to this atom: the corresponding recoil energy (kinetic energy) is 10,000 eV when the PKA is at the open surface, linearly decreasing to 100 eV at 12 nm. The collision cascade process is similar to that in Ref. [147]. After enough cascade loops when the energy and v_{flex} become steady, the sample was duplicated along the

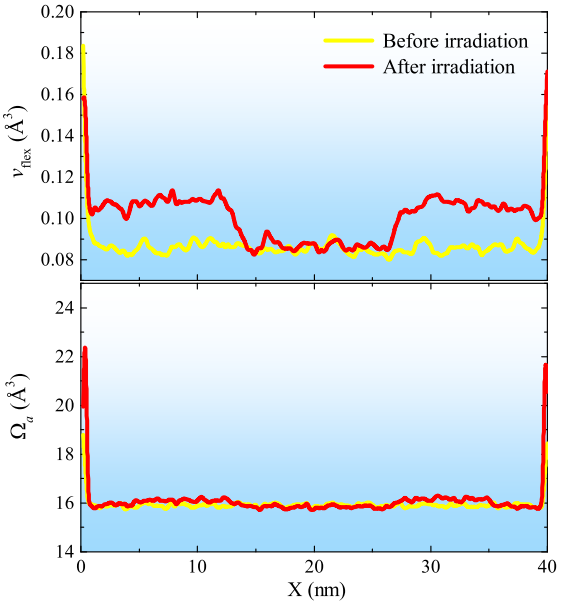

Figure 3.9: Contrast of the distribution of flexibility volume (v_{flex}) (upper panel) and atomic volume (Ω_a) (lower panel) along the X-direction of $Cu_{64}Zr_{36}$ MG before and after irradiation on the X-free surfaces.

Z-direction by a factor of 10 and relaxed for 1 ns at RT before the final quench to 50 K. Its stress-strain curve in Figure 3.6 shows apparent work-hardening (bending of the curve after yielding), very similar to that observed in Figure 3.1 (the evolution can be seen in Figure 3.7 and Movie 3 [2]). From the contrast shown in Figure 3.9, it appears that the gradual exhaustion of the rejuvenated v_{flex} in the irradiated layer, rather than the annihilation of Ω_a, is responsible for the work-hardening observed.

In sum, flexibility volume can be retained via faster quench, and a similar level can also be reached via rejuvenation (irradiation) of a slower cooled (or relaxed) sample (Figures 3.3 and 3.8). These explain the evenly distributed

[2]see: https://www.tandfonline.com/doi/full/10.1080/21663831.2018.1503198

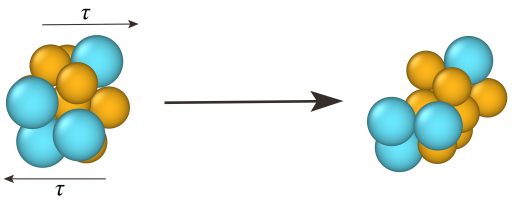

Figure 3.10: A schematic of the local shear transformation of a group of atoms.

flow observed in Figure 3.7, and the experimental observation in Figure 3.1.

3.3.2 Flexibility makes covalent network glasses ductile

We next explain the ductile flow of amorphous silica in Figure 3.2, again from the flexibility perspective. Such a covalently bonded glass is in fact an example for which the "free volume" concept is utterly inapplicable. To make our point, in this section we will discuss MD-simulated models of amorphous silicon (a-Si), as a general case study of covalently bonded network glasses (for which amorphous silica and a-Si are typical examples). a-Si has a coordination number $\sim$4 and an open structure to begin with. But the ample "empty space" is apparently not tantamount to easy flow, and introducing even more spatial volume into the structure makes little difference.

This brings us to the following question: other than spatial volume for dilatation, what else is essential to enable bond switching to mediate shear transformations? As seen in the schematic in Figure 3.10, the relocation of the atoms in the shear transformation requires bond breaking and re-forming, so the formation of dangling bonds and weakening of the rigid covalent bonds would be a

particularly important pre-requisite for bond switching. Without this bonding flexibility, shear transformation does not happen readily, despite of the open space surrounding the tetrahedrally bonded motifs. Just like the MG case, MSD can be sent as a "detective" that gets down to near the bottom of the energy basin to sense the curvature, i.e. the flatness of the basin and the bond force constant. In other words, v_{flex} once again serves the purposes of gauging the flexibility available.

Here, the SW a-Si model [77, 96] is used to illustrate our point of view. We are aware that there are other potentials developed to model a-Si (e.g. a modified SW potential with doubled three-body term to increase the degree of bond directionality and thus the stiffness, plus quenching at a constant density with the Tersoff potential [100,106,149]), especially since the SW a-Si model tends to exhibit much more ductility than experimental a-Si in the laboratory [150,151]. For amorphous silica there has also been much potential development, including ongoing efforts [152]. However, we choose to use the simpler SW potential as a model, which suffices to deliver our main point at a low computational budget. Our message would not depend on the potential used, and the model material is only used to show that the ample space or excess volume available in the open glass structure is insufficient to sustain ductility by itself. The difficulty with plastic flow lies instead in the rigid chemical bonds that suppress the flexibility to realize bond switching.

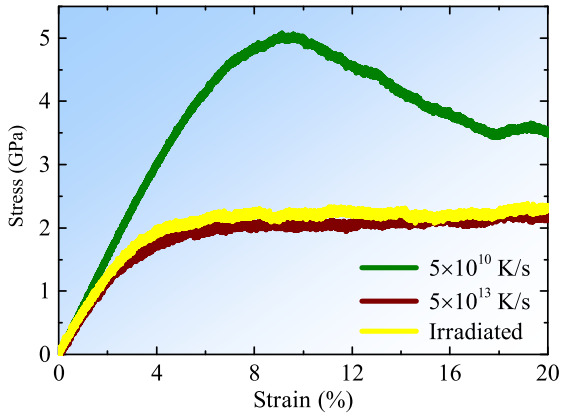

Figure 3.11: Stress-strain curves in uniaxial tension (along Z-direction) loaded at 300 K with constant strain rate of 1×10^8 s^{-1} for a-Si with PBCs in all three directions and quenched at cooling rate of 5×10^{10} and 5×10^{13} K/s and one after irradiation. The stress normal to the loading direction was relaxed to allow for lateral contraction.

Figure 3.11 shows the stress-strain curves in uniaxial (pulling along the Z-direction) tension. We observe that the a-Si cooled at 5×10^{10} K/s requires an overshoot stress of $\sim$5 GPa to initiate flow, followed by obvious localization of plastic strain into very narrow bands as can be seen in Figure 3.12(a) after straining to 20%.

We now show what can be done to make a-Si more amenable to plastic deformation. One way is to quench the liquid at rapid rates, e.g. 5×10^{13} in Figure 3.11 for SW a-Si. The stress overshoot is eliminated, indicating that the as-quenched glass structure becomes ready to flow, and the flow stresses are also cut by more than half when compared with the slower cooled glasses. The strain localization is also replaced by distributed flow, as compared in Figure 3.12(b). In other words, just like MGs, we see that by increasing the quench

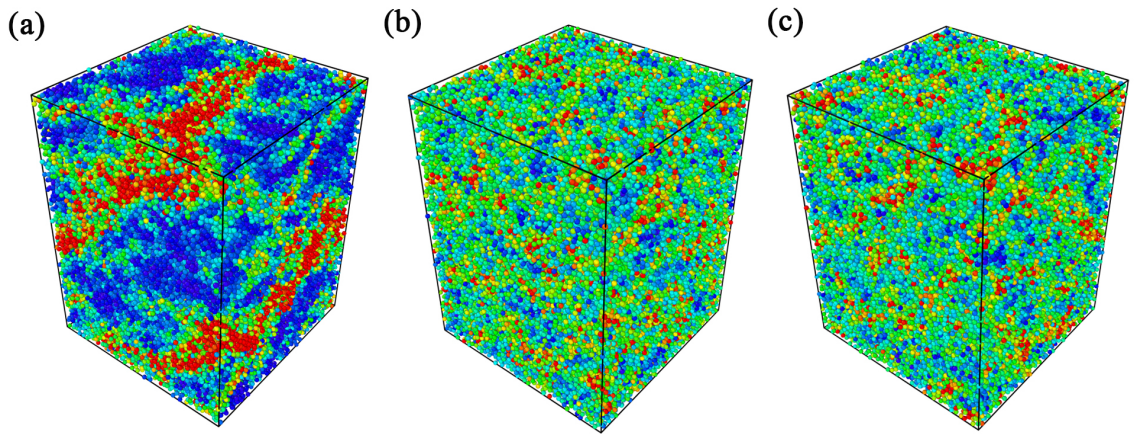

Figure 3.12: Snapshots of SW a-Si with various processing history were strained to 20% in uniaxial tension at 300 K. Color represents the local shear strain of each atom (red and blue represent upper and lower limit, respectively). Panels (a) and (b) are as-quenched samples with cooling rate of 5×10^{10} and 5×10^{13} K/s, respectively; (c) is irradiated as-quenched samples with cooling rate of 5×10^{10} K/s.

speed from the liquid, a-Si can indeed be made easier to flow and in a more uniform manner.

Now, it is important to note that, the Ω_a in the SW a-Si glasses is actually decreasing with increasing quench rate, as demonstrated in Figure 3.13, while the glasses become more amenable to flow. It is thus obvious that more spatial volume is not the enabling condition for easier flow. Rather, the bonding at the higher quench rate contains more metallic character (and therefore higher coordination number and mass density [47, 48]), such that the amorphous structure is more flexible for plastic flow despite of the reduction in average atomic volume.

The second route to make glasses ductile is to rejuvenate the already-relaxed

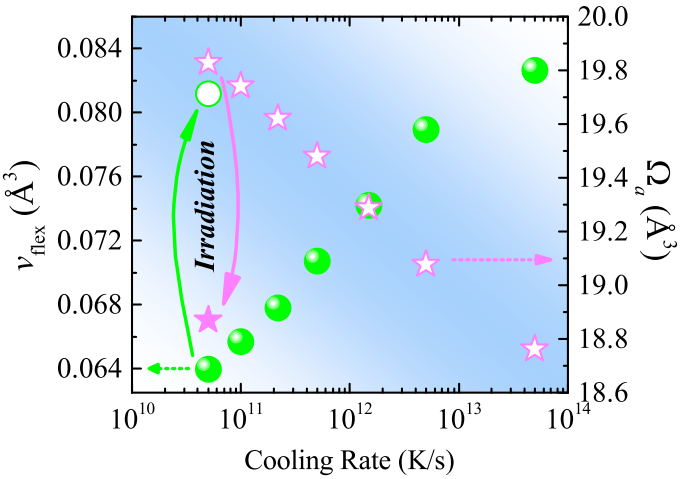

Figure 3.13: Variation of flexibility volume (v_{flex}) and atomic volume (Ω_a) of SW a-Si due to different processing history (cooling rates and irradiation).

amorphous structure. We model this by irradiating the "slowly" (5×10^{10} K/s) cooled SW a-Si sample. In simulating the irradiation, the short-range repulsion of the SW potential was modified with the Ziegler-Biersack-Littmark (ZBL) potential [153], with a spline function joining with SW [154]. Each cascade was initiated by giving a random primary knock-on atom (PKA) a recoil energy of 4 KeV in a random direction. The simulation time for each cascade run was 20 ps under an NVE ensemble. Following each cascade run, a relaxation run was carried out under an NPT ensemble with the cooling rate of 1×10^{13} K/s, decreasing the system's temperature and pressure to 300K and 0 bar, respectively. After 150 such loops, we observe in Figure 3.11 that the irradiated glass shows a stress-strain curve very close to the 1×10^{13} K/s quenched sample. The strain localization in Figure 3.12(a) is also alleviated, as seen in Figure 3.12(c). Interestingly, as shown in Figure 3.13, the Ω_a is actually reduced after

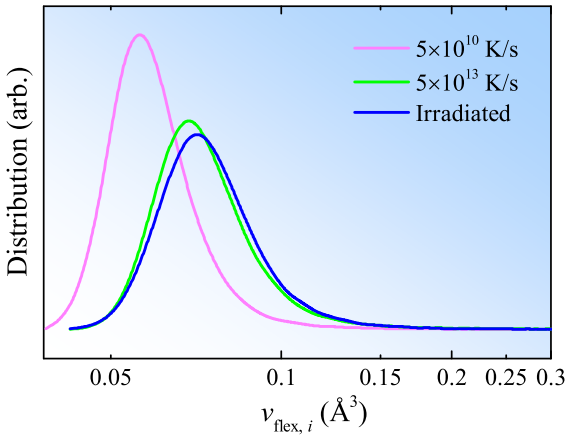

Figure 3.14: The probability distribution of the atomic flexibility volume ($v_{flex,i}$) in SW a-Si with different processing history.).

irradiation, consistent with the densification reported in previous irradiation studies on amorphous silicon and silica [154]. This demonstrates once again that the spatial free volume picture is not generally applicable as a universal explanation to making glasses ductile.

Next, we show that in this case the flexibility in the amorphous structure remains a powerful indicator to rationalize the deformation readiness. We first note that, even though our a-Si model is a covalently bonded network amorphous material qualitatively different from the metallically bonded and densely packed MGs for which v_{flex} was first demonstrated, the v_{flex}-G correlation in Figure 3.5 remains valid. This shows v_{flex} is a universally applicable indicator of the rigidity for different types of glasses, even for the "denser is more deformable" cases.

The faster the quench from liquid, the larger the v_{flex}, as shown in Fig-

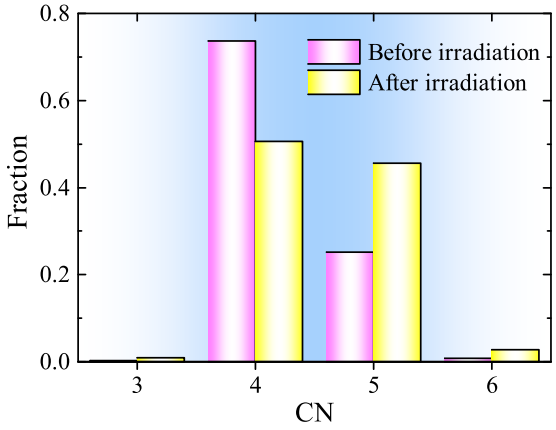

Figure 3.15: The change of coordination number (CN) of a-Si due to irradiation.

ure 3.13. This signals a smaller G as seen in Figure 3.5 and reduced energy barrier for inelastic relaxation. The irradiated SW a-Si, while denser with Ω_a decreased (Figure 3.13), also arrives at an elevated v_{flex} (Figure 3.13) and in turn a reduced G (Figure 3.5), both similar to that in the fastest quenched glass (including an obvious shift of the distribution of v_{flex}, Figure 3.14). So we again conclude that it is the higher flexibility retained or rejuvenated in the amorphous structure that renders the resultant glass more amenable to shear flow [47, 89]. The excess volume or open structure is inconsequential in determining the deformability.

The increased flexibility with reduced atomic volume (or increased density) is due to the more metallic-like bonding retained from liquid Si via the rapid quench [47,48]. Figure 3.15 shows that after irradiation, the coordination number of Si shifts from CN = 4 dominated to CN = 5, suggesting the increased

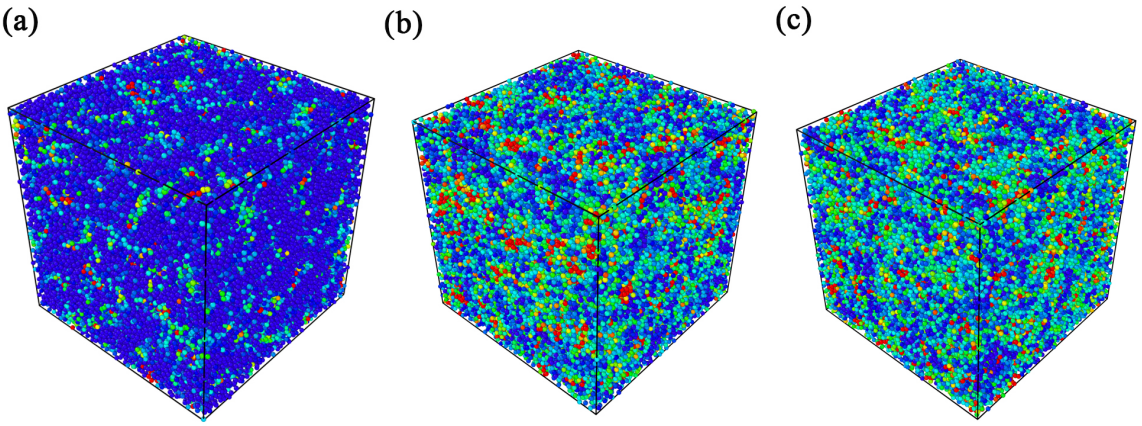

Figure 3.16: Spatial distribution of the atomic flexibility volume ($v_{flex,i}$) before tension of SW a-Si with various processing history. (a) and (b) are as-quenched samples with cooling rate of 5×10^{10} and 5×10^{13} K/s, respectively; (c) is the as-quenched samples with cooling rate of 5×10^{10} K/s after irradiation.

population of more liquid-like regions. This latter term was used by Demkowicz and Argon [47, 48]; now "liquid-like" region would mean a higher v_{flex} and lower G, both of which are quantifiable. These heterogeneities are shown in Figure 3.16. In the next section, we will confirm that the v_{flex} correlates well with the local atomic shear strain, as defined in Ref. [155] and calculated using the OVITO program [156].

We started in Section 3.2 with the example that the normally brittle amorphous silica turned very ductile (Figure 3.2) inside a TEM [136]. The arguments for a-Si above can also be used for amorphous silica, which behaves in many ways similar to a-Si, as another typical covalently bonded network glass. It belongs to the category where the free volume concept is not applicable. The high deformability that the a-SiO_2 ball can be compressed into a pancake is

again due to the flexibility imparted into the structure, in this glass enabled by the electron beam irradiating on the sample, as it is being deformed inside an electron microscope. The e-beam illuminating on a-silica dynamically rejuvenates the glass structure, particularly effective when the deformation is carried out *in situ* when the sample is continuously imaged to monitor its deformation. The weakened bonds due to energy input under ionization irradiation have been found to be akin to ultrafast quench [154].

SiO_2 is highly susceptible to electron beam softening, such that the entire sample undergoing plastic deformation is constantly rejuvenated by e-beam irradiation, producing many simultaneous bond switching events to contribute to flow. We point out, however, that the exact mechanisms on the electron level that imparts flexibility may be more complicated than, what we have discussed above. For example, our simulation is about the direct breaking of bonds when the incident electrons transfer energy to Si, with a magnitude comparable to their displacement threshold energy, causing knock-on displacement and subsequent collision cascade. But there can also be other effects: e-beam with energies in the 0-100 eV range can cause radiolysis. Let us look at the silicon oxide case. Since all the valence electrons of Si are bound with O, there would be no spare ones left available to fill the Si core hole created by the electron irradiation (via intra-atomic Auger decay). Instead, O would have to return the electron lent from Si to accomplish an inter-atomic Auger process [157].

In any case, both mechanisms sever or weaken the bonding between O and Si and dynamically rejuvenate the silica glass structure, allowing bond breaking all over the sample volume under applied stresses [136]. Meanwhile, the strong and directional covalent bonds would quickly re-form with other neighbors. This bond switching is then akin to thermally activated bond breaking and re-forming in viscous flow at elevated temperatures. It provides the mechanism needed for shear transformations to produce strain and heal incipient damage, as the bond switching reconnects, reorients and relocates the SiO_4 motifs. The brittle silica glass is therefore made not only malleable in compression (Figure 3.2), but also ductile in tension at room temperature [96].

To recapitulate, in this section we have demonstrated three reasons as to why flexibility is the deciding factor towards plastic flow. First, flexibility is shown to explain the deformability trend, when the free volume is not appropriate to use at all, as seen for *a*-Si. Second, we also showed that at a glass composition, while Ω_a changes little with the different processing history of samples, v_{flex} spans an appreciable range that can be tuned using different processing conditions. The third advantage is that v_{flex} scales with G quantitatively (Figure 3.5), so one can directly connect it with the ease of inelastic relaxation (Equation 3.2) and compare glasses processed differently.

Note here that so far the discussion is, for the most part, about the sample-average v_{flex}, correlating with the overall strength/ductility of a glass. One can

in fact go one step further, to correlate with local atomic-level strains. Such details about local correlations will be discussed in the next section.

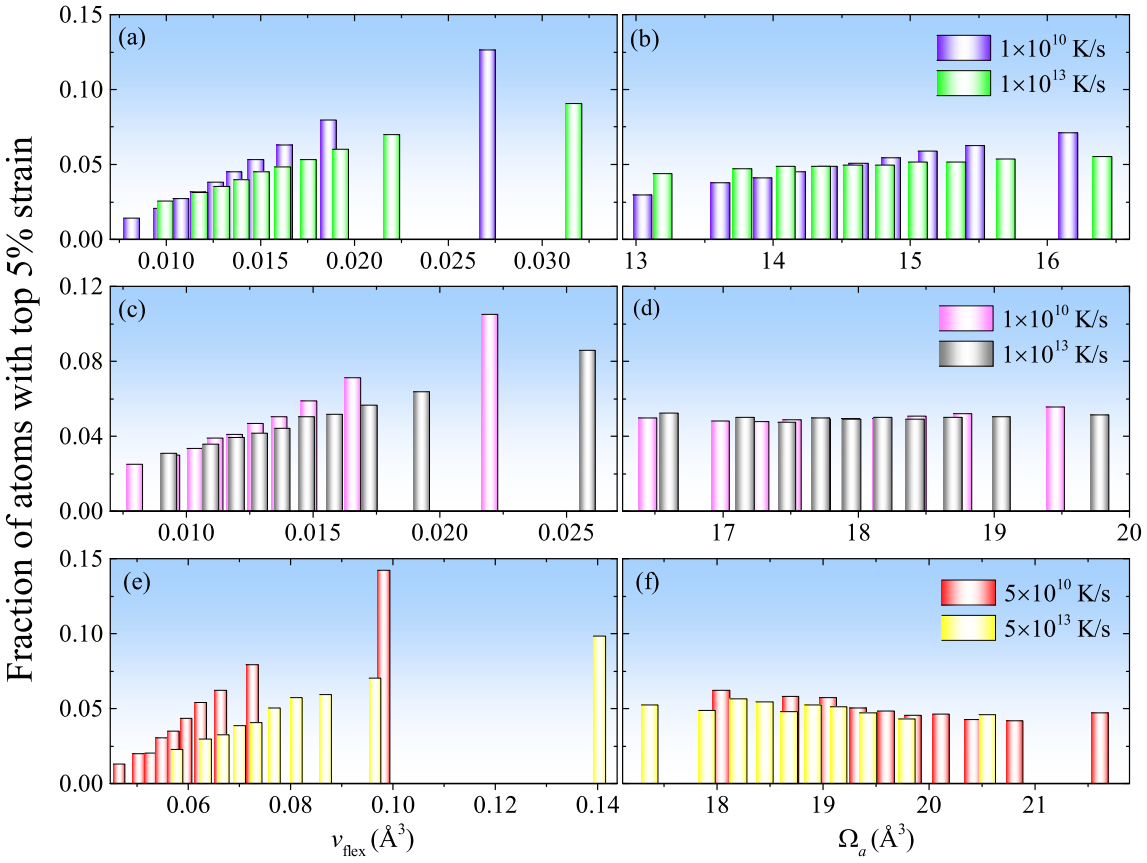

Figure 3.17: Correlating the flexibility volume (v_{flex}) or atomic volume (Ω_a) with the propensity for shear transformations of atoms (fraction of atoms with top 5% atomic strain in each group when each sample was strain to 3% under uniaxial tensile deformation with PBCs along all three directions at 300 K). All the atoms of each atom species in each sample are sorted based on flexibility volume ($v_{flex,i}$) or atomic volume ($\Omega_{a,i}$) into bins each containing 10% of all the atoms of each atom species. Panels (a) and (c) show the correlation with v_{flex} for Cu and Zr atoms in $Cu_{64}Zr_{36}$ MG, respectively, and (e) shows the correlation with v_{flex} in SW a-Si. (b), (d) and (f) show that there is no observable correlation with Ω_a.

3.4 Correlating local flexibility with spatially heterogeneous shear transformations

Then, on the level of local atomic strain in glasses, does the local (coarse-grained on nanometer scale) v_{flex} indeed indicate the propensity for shear transformations, which are expected to be heterogeneous and on the nanometer scale in the glass? In this section, we will confirm this heterogeneity and correlation, which is the fourth advantage of using flexibility, an important merit that Ω_a again fails to have. A strong correlation of atomic strains with local v_{flex} but not with Ω_a will nail down our assertion in the preceding section that flexibility indeed has the ability to account for the readiness of shear transformation, and for the mechanical heterogeneities. We will also confirm that the correlation with local Ω_a is very weak. In fact, dense regions can be prone to shear transformations if their v_{flex} is high.

It was shown in Ref. [77, 78] that the magnitude of v_{flex} correlates well with the fertile sites where shear transformations tend to take place in glassy materials under athermal quasistatic shearing [157]. Here we demonstrate that even under uniaxial tensile deformation at 300 K, which is typical in laboratory experiments, it is the v_{flex}, and not the Ω_a, that is the meaningful marker of the propensity for shear transformations. To evaluate this correlation, we

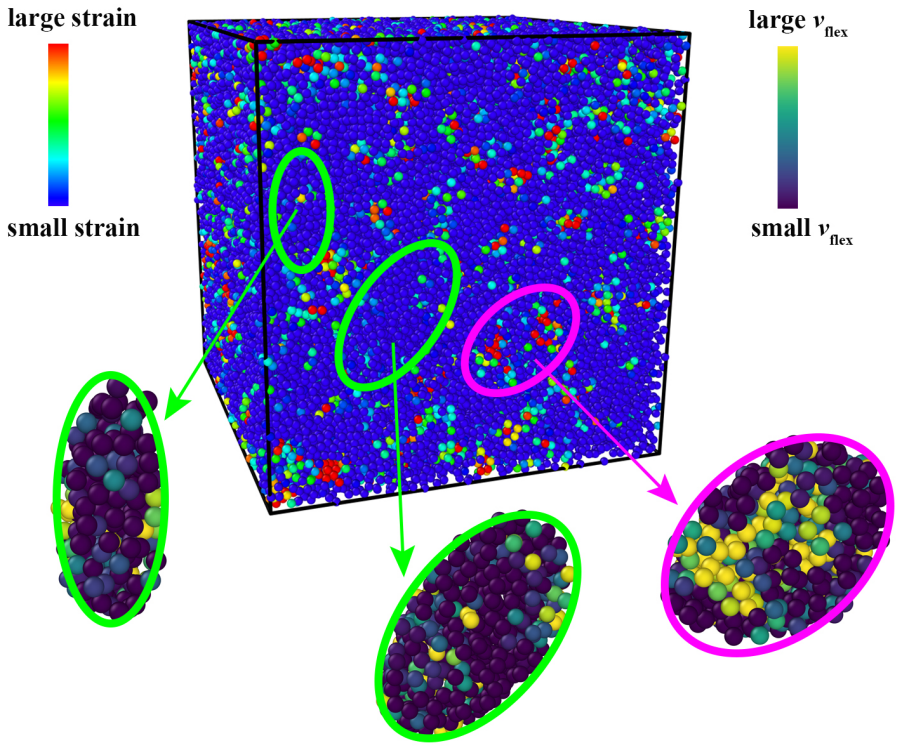

Figure 3.18: Atomic strain map when a SW a-Si with cooling rate of 5×10^{10} K/s was strained to 3% under uniaxial tensile deformation. The three insets show the corresponding flexibility volume (v_{flex}) distribution before deformation of three local regions.

sort all atoms for each atom species in each sample ($Cu_{64}Zr_{36}$ and SW a-Si with various cooling history) into bins each containing 10% of all the atoms of that species, based on escalating flexibility volume ($v_{flex,i}$) or atomic volume ($\Omega_{a,i}$), and then count in each bin the fraction of atoms that have experienced the top 5% atomic strain when the overall uniaxial tensile strain was 3% (with PBCs along all three directions to eliminate the effect from atoms on free surfaces). The trend is clear in Figure 3.17(a, c and e) that the larger the coarse-grained v_{flex} in a region, the larger the fraction of atoms with top 5% atomic strain, for

both Cu and Zr atoms, respectively, in $Cu_{64}Zr_{36}$ MG, and for all the Si atoms in SW a-Si. In contrast, the propensity for shear transformation is almost the same for all bins sorted based on increasing $\Omega_{a,i}$, see Figure 3.17(b, d and f). In other words, atomic volume offers no useful information with regard to the likelihood of shear transformation. We also found that even at 20% overall sample strain, most atoms having relatively large atomic strain are still those with larger initial v_{flex}. Figure 3.18 shows a map of Si atoms colored according to atomic strain in the 5×10^{10} K/s cooled SW a-Si at 3% overall tensile strain. The three insets show the corresponding initial v_{flex} distribution in the three local regions circled. As clearly shown in the figure, the initial v_{flex} is larger in the region with more shear strain but smaller in the region with less shear strain, which confirms the correlation in Figure 3.17. These illustrate that flexibility volume can indeed serve as a tell-tale indicator to reflect the mechanical heterogeneity of amorphous materials, but local atomic volume cannot.

The flexibility is distributed heterogeneously in the glass [25, 37, 158]. So the flexibility imparted into the glass structure is consistent with the idea we advocated earlier [25], i.e. tailoring the amorphous structure to embed more heterogeneities and soft spots that are enriched with geometrically unfavored motifs (GUMs) [24, 54]. Indeed, fast quench or irradiation are expected to retain more disorder and GUMs, which promote v_{flex} and aggregate into patches as structural heterogeneities that in turn produce spatial variations in v_{flex}

and mechanical properties.

3.5 Concluding remarks on strategies to make glasses ductile

It follows from Section 3.4 that a higher population and density of high flexibility regions helps to carry imposed deformation and relieve strain localization. Although the cooling rates and strain rates used in our modeling are much faster than that in laboratory experiments due to the spatiotemporal scale limitation in current MD simulations, the trend discussed above should hold. That is, the more local regions with larger flexibility volume in a glass, the more ductile it would be. Glassy solids can all be made ductile at RT, if the amorphous structure is made sufficiently flexible.

Flexibility is about the propensity for bond switching upon loading and a high structural flexibility encourages spread-out shear transformations for plastic flow. For glasses a commonly used descriptor about structural flexibility is “free volume”, and glasses are likely to be more deformable if the free volume content is higher. This concept is, however, neither quantitative nor universal. There are several take-home messages from our discussions above. First, flexibility reigns, and an indicator of flexibility is the flexibility volume, not the local excess spatial volume, as shown above with an extreme case of open structure

glasses such as amorphous Si and silica. They are made deformable only if the bonding is weakened to afford more flexibility, even though excess volume or elbow room for bond switching is always available. In other words, open space is a given but does not imply deformability. Second, flexibility volume v_{flex} can be quantified, and it quantitatively scales with shear modulus G to influence the relaxation energy barrier. Third, for MGs the variation is miniscule for Ω_a, but v_{flex} exhibits pronounced changes for different preparation history and for different compositions. With such a quantitative measure of flexibility, one can now compare glasses at a glass composition but processed differently, or different regions in a given glass (as a local measure of heterogeneous flexibility). Fourth, v_{flex}, easily obtained in MD simulations, provides a quantitative measure to reflect the overall effects of other indicators previously used in the glass community to correlate with deformation, such as fictive temperature, GUMs, liquid-like flow defects, soft spots, etc., each of which focusing on a certain aspect of the glass state/structure. Fifth and finally, the flexibility is non-uniform in glasses, able to account for mechanical heterogeneity. Of course, free volume is also heterogeneous, but shear transformation happens preferentially where flexibility is high, with no meaningful correlation with local atomic volume. This chapter summarizes these major merits of using flexibility to describe the glass structure and its deformability; other advantages over Ω_a have been discussed before in Ref. [78] .

We conclude that if adequate flexibility is activated throughout the sample, the deformation mode can become “homogeneous”. To that end, one should retain flexibility from the parent phase to begin with, for example by rapid quench from liquid or vapor, or by using “nanoglass”, which consolidates glass nanoparticles together [146, 159–161]. The other route we demonstrated is to rejuvenate an already-relaxed amorphous structure—irradiation appears to be an effective method in that regard. Other rejuvenation routes including plastic deformation under triaxial stress state [162], elastoplastic loading [163] and cryogenic thermal cycling [164]; but they have yet to be shown to be effective in producing large deformability and tensile ductility. Generally speaking, the spread-out heterogeneities with high flexibility avoid the localization of plastic strains. The spatially distributed plastic events can then make glasses flow in a ductile manner at RT.

Chapter 4

Machine learning bridges local static structure with multiple properties in metallic glasses

4.1 Introduction

In the preceding two chapters and Ref. [78], it was demonstrated that the performance of flexibility volume (v_{flex}) is excellent in quantitatively determining the shear modulus and correlating with multiple properties of both metallic glasses (MGs) and covalently-bonded open network glasses. This lays the groundwork for significant progress in the course of establishing robust rela-

tionships between structure and property for amorphous solids.

However, v_{flex} is *not* solely based upon the static structure, which is the normally used and more accessible data from both simulation models and real glassy samples. As defined in Ref. [78], the $v_{flex,i}$ of atom i is:

$$v_{flex,i} = a_i \cdot \langle r^2 \rangle_i \tag{4.1}$$

where a_i and $\langle r^2 \rangle_i$ are the interatomic distance and vibrational mean-square displacement of atom i, respectively. Obviously, the $\langle r^2 \rangle_i$ cannot be extracted directly from initial static structural state of amorphous solids. Instead, $\langle r^2 \rangle_i$ has to be mapped out to assess v_{flex} every time the sample changes, which is intractable in experimental work. In addition, v_{flex} is hard to define for solid amorphous solids under high stress (pressure) or temperature, not to mention in the liquid state or during shear flow as the contribution of atomic diffusion cannot be as easily separated out in those situations. These limitations in using v_{flex} suggest that it is more desirable to have a structural quantity which can be derived solely from static structural information and yet work as well as v_{flex}.

The goal of this chapter is to resolve the issue above. We now move the starting block to the static local structure in the amorphous solids. From this initial input we set out to establish a single quantity that represents the struc-

ture sufficiently well to predict its adaptation to stimuli. We then use this new structural quantity, which will be termed structural flexibility (*SF*), to correlate with multiple properties, including vibrational and diffusional relaxation properties, as well as propensity for temperature- or stress-induced rearrangements in response to external stimuli (thermal, mechanical, etc.). These structure-property relations should also be applicable to (i.e., can be coarse-grained to) various scales, all the way to a global average for the entire sample volume. Note that the initial input used in correlating with properties will be the static structure, and our goal is to "convert" this complex local atomic environment into a single descriptor, *SF*. This conversion is made possible by machine-learning methods, and the translation takes advantage of the established structure parameter v_{flex}. This strategy will be illustrated in detail in the following, using results in the Cu_xZr_{100-x} model system.

4.2 Machine learning to link the static structure to structural flexibility

As stated above, in correlating with properties our mandate in this chapter is not to start from $v_{flex,i}$ as the structural input, but instead from square one, the static structure. But, $v_{flex,i}$ remains our vehicle to map the static structure to a new indicator, *SF*. The $v_{flex,i}$ response of a local configuration is of course

influenced by the atomic distribution surrounding atom i, but in a complex way. This makes it challenging to simplify the inter-relation between the two quantitatively. However, the advent of machine learning (ML) brings a new tool box that may help push the boundary of materials science. In fact, ML methods are particularly suited for establishing relations where simple theory has previously been intractable.

Before discussing step by step the structural representation, supervisory signal, and ML protocol in the sub-sections that follow, we first briefly comment on the recent use of ML to address structure-property relations in glasses and supercooled liquids [21, 22, 68, 165]. Cubuk *et. al.* was the first to apply ML in the context of amorphous solids using Lennard-Jones model glasses and jammed systems, showing that local radial- and bond-angle- distribution information can be used to separate atoms with high (versus low) susceptibility to displacement [21]. Wang and Jain used instead "interstice" distribution as the structural representation, in an effort to make the ML model less system-specific [68]. A separate attempt was made by Schoenholz *et. al.* at the correlation with dynamics: they used the magnitude of p_{hop} [166, 167], as the supervisory signals in ML to separate out atoms with very large hopping rates. All these previous ML attempts, however, have left much to be desired for. First, they undertook training on a binary classification task but used the result as in a regression problem [168]. They had to rely on the distance to

the separating hyperplane, or a class probability estimate, in describing the "softness" [165] (or quench-in softness [68]), to evaluate each atom's susceptibility to rearrangement. It is more desirable to construct a structural flexibility quantity through direct ML regression, as will be done in this chapter. Second, the (local) softness defined was property-specific, i.e., it is trained on how "soft" the local environment is, with respect to a particular excitation. For example, the magnitudes of non-affinity, $D^2_{\min}$, when subjected to shearing was directly used as supervisory signals in training the ML model. The result is then already aligned with local plastic susceptibility under that specific loading condition. In other words, it is trained on one specific behavior, tested and meant for recognizing that particular behavior for the most part. Every other property (such as hopping rate in diffusion) may require a different ML model for the same MG structure. So for a MG alloy system it is not the goal of this prior work to produce a ML product that can establish correlations with all essential properties. Third, the above suggests that when the MG structure is changed, e.g. via shear deformation under one loading condition, to predict the response under a different (loading) condition we may need to re-train the ML model. As a result, each property (e.g. $D^2_{\min}$) may need to be reevaluated, as the input variable for repeated training. This means that we cannot input static structural information only, but have to perform expensive atomistic computations accounting for all the interactions (a computational cost comparable to or

exceeding that of directly using $v_{flex,i}$). These shortcomings point to a pressing need for advances in ML tactics to increase and broaden the resulting predictive power while requiring less non-structural input.

4.2.1 Structural representation

As mentioned earlier, the properties of a local configuration are affected by the intricate and often collective physical and chemical interactions of atoms over a medium-range distance. So far, no single simple structure parameter provides robust predictivity capable of correlating with a diverse array of properties. However, the spatial distribution of the atoms in the initial, undisturbed structure is the most straightforward and accessible structural information and, hence, that which one would prefer to use to correlate with properties. We, therefore, construct structure-property relations with this "local static structure" as the baseline input. Accordingly, we represent the structural state based on the widely used pair distribution function (PDF).

PDF represents the probability of finding atoms as a function of radial distance r from an average center atom [23]. The partial PDF (i.e., the element-specific PDF) for any α-β in the MG (such as Cu-Zr in our model system) is defined as [169]

$$g_{\alpha\beta}(r) = \frac{N}{4\pi r^2 \Delta r d N_\alpha N_\beta} \sum_{i=1}^{N_\alpha} \sum_{j=1}^{N_\beta} \delta(r - r_{ij}) \tag{4.2}$$

where d is the number density of atoms in the sample of N atoms, N_α and N_β are the number of atoms of species α and species β, respectively. r_{ij} is the distance between atom i (of α) and atom j (of β). The α-β partial PDF of a sample is an average of the partial PDF of each single atom, over all α atoms in the sample. If we consider the local configuration around each individual atom, we compute the partial PDF of a single atom i as:

$$g\left(r\right)_{i,\beta} = \frac{1}{4\pi r^2 \Delta r d f_\beta} \sum_{j=1}^{N_\beta} \delta\left(r - r_{ij}\right) \tag{4.3}$$

where $f_\beta = \frac{N_\beta}{N}$ is the composition fraction of species β in a sample. In fact, $g\left(r\right)_{i,\beta}$ of a single atom i specifies the density of atoms (or number of atoms) of species β in the shell a distance r from the center atom i. Once the surrounding atoms across several neighboring shells within a cut-off distance are fixed, the local packing around the center atom i is defined. Thus the partial PDF of a single atom includes details on local environment across several shells, in addition to SRO, atomic volume (Ω_a) and coordination number (*CN*). The chemical order around a center atom is included as well, when all partial PDFs of the center atom are combined together. Therefore, we expect that the radial distribution of atoms surrounding atom i, embodied by all the partial PDFs, can adequately describe the local static structure. This purely structural information will comprise a multi-dimensional vector $\boldsymbol{x}_i$ as our structural representation.

4.2.2 A new structural quantity

The next challenge is, as discussed earlier, how to convert the comprehensive static structure $\boldsymbol{x}_i$ into a more property-oriented and user-friendly structural quantity. We will need to i) re-cast the "structure" in terms of the degree of flexibility of the local configuration, and ii) do so in a way that simplifies this "structure" into a single quantity. As outlined earlier, this is achieved by defining a 'structural flexibility' (*SF*). The *SF* of atom i is

$$\boldsymbol{SF}_i = \boldsymbol{\omega}^T \cdot \boldsymbol{x}_i \tag{4.4}$$

Here the superscript T represents the transpose of another vector ($\boldsymbol{\omega}$) that contains all the weighting factors reflecting the influence of the various aspects in $\boldsymbol{x}_i$ to flexibility. Mathematically, $\boldsymbol{SF}_i$ is the dot product of two column vectors, the static structural vector $\boldsymbol{x}_i$ and the weighting vector $\boldsymbol{\omega}$, resulting in a dimensionless scalar that can be utilized to rank property differences. Our next task is to solve, via machine learning (ML), for the complex $\boldsymbol{\omega}$ that links $\boldsymbol{x}_i$ and $\boldsymbol{SF}_i$.

4.2.3 Supervisory signal

The suitable supervisory signal to be used for ML, y_i, needs to reflect the flexibility of a local configuration. v_{flex} comes in handy in this regard, as it contains relevant dynamic information that depends on the static local configuration to

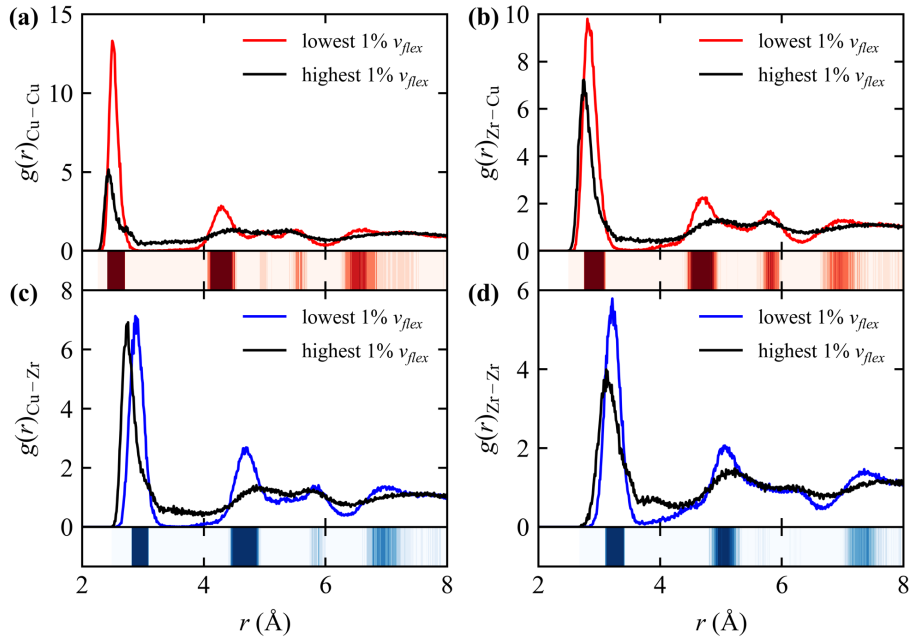

Figure 4.1: Partial pair distribution functions, $g(r)$, for Cu (a and c) and Zr (b and d) atoms with the lowest and the highest 1% $v_{flex,i}$ in a $Cu_{50}Zr_{50}$ MG. The model contains 1,024,000 atoms and quenched at an effective cooling rate of 1×10^{10} K/s. The upper and lower panels represent $g(r)_{\alpha-\mathrm{Cu}}$ and $g(r)_{\alpha-\mathrm{Zr}}$, respectively. The colored contour maps below $g(r)$ highlight the difference in $g(r)$ between atoms with the lowest and the highest 1% v_{flex}. The dark red (or blue) regions are where the radial density of Cu (or Zr) atoms in the most inflexible group is much higher than those belonging to the most flexible group.

a large degree. Also importantly, $v_{flex,i}$ has strong correlation with multiple MG properties [78].

We now demonstrate that there is a strong inter-relation between local radial distribution and $v_{flex,i}$. The purpose of this exercise is to justify that by carrying out ML regression on these two, we can expect to determine the ω that best transforms $\boldsymbol{x}_i$ into the flexibility-oriented *SF*. Our analysis can also shed light on what components/regions of the PDF really matter for flexibility. To this end, we sort the Cu (or Zr) atoms in our $Cu_{50}Zr_{50}$ MG model (see

Methods in Section 4.5.1) into 100 groups based on their $v_{flex,i}$ and computed the partial PDFs, $g(r)$, for each group. The partial PDFs of the 100 groups gradually evolve with increasing average v_{flex}; but for clarity, here we only contrast the extreme cases to gain some insight: in Fig. 4.1 we compare the $g(r)$ for the group of atoms having the lowest 1% v_{flex} (inflexible atoms) with that of the group of the highest 1% v_{flex} (flexible). We observe that i) both the intensity and the position of the first peak are clearly different between these two groups of atoms; ii) besides the first peak, there is no other pronounced peak on $g(r)$ for the most flexible atoms, while there are more than three visible peaks for the most inflexible atoms; iii) for the inflexible atoms, almost no atoms fall in between the first and second peaks (wide trough with intensity close to 0). The colored contour maps below $g(r)$ show the difference in $g(r)$ between atoms with the lowest and the highest 1% v_{flex}. The dark red regions are where the radial density of Cu atoms is high, corresponding to the most inflexible group (dark blue regions for Zr). This is to be contrasted with the light red regions in between that correspond to the most flexible group (light blue for Zr). iv) For Cu atoms, the first peak intensity ratio of Cu-Cu to Cu-Zr is greater than 1 for inflexible atoms, while that for flexible atoms is less than 1. For Zr center atoms, the first peak intensity ratio of Zr-Cu to Zr-Zr is greater than 1 in general, deviating from the global composition ratio of Cu to Zr ($Cu_{50}Zr_{50}$). This indicates that chemical order also plays a role in v_{flex}, together with topological

arrangement.

The findings in Fig. 4.1 suggest that, for atoms to be inflexible, they tend to require more surrounding Cu (Zr) atoms to appear in dark red (blue) regions, see the contour maps below $g(r)$ in Fig. 4.1, and fewer atoms to reside in other regions. In other words, the larger the ratio of neighboring atoms in the dark regions (peaks) to those in the light/bright regions (troughs), the more inflexible the central atom will be. Our results are consistent with, but much more convincing than, the hint mentioned in Ref. [21], where the authors contemplated that "soft" particles would have environments with fewer particles in their nearest neighbor shells but more in the troughs in between the shells.

Again, Fig. 4.1 helps to establish that the local flexibility ($v_{flex,i}$) is intimately connected with the local static structure ($\boldsymbol{x}_i$) around an atom. The next question is to what degree is this the case, and how might this be quantified. To answer these questions we deploy ML regression to pinpoint an optimized $\boldsymbol{\omega}$. We reiterate that while $v_{flex,i}$-property correlations have been established [78], $v_{flex,i}$ is not derived purely from static structural information. At the same time, we also note that because of the universality and versatility of $v_{flex,i}$, a single ML model based on it would allow *SF* to correlate with multiple properties. In this context, $v_{flex,i}$ serves as an physically motivated ML supervisory signal.

4.2.4 The machine learning model

We now proceed to develop a ML model to assess the flexibility of each atom from purely structural information embedded in $\boldsymbol{x}_i$. We will specify the exact forms of $\boldsymbol{x}_i$, y_i and $\boldsymbol{\omega}$ to be used. Given that the $g(r)$ of a single atom is actually zero for the majority of the radial distance r, and, thus, contains much redundant information, instead of using the discrete PDF of each atom, we use Gaussian functions to weight the radial density at various distances $r \pm \sigma$ from the central atom i. The resultant structure function of each atom [21, 165] is approximated as

$$G_i^{\beta}(\bar{r}) = \sum_{j \in \beta, \bar{r}_{ij} \leqslant \bar{r}_c} \exp\left[-\frac{(\bar{r} - \bar{r}_{ij})^2}{2\sigma^2}\right] \tag{4.5}$$

where $\bar{r}_{ij}$ the distance between the central atom i and the neighboring atom j of species β (Cu or Zr, here), within a cutoff $\bar{r}_c = 3.0$. Here $\bar{r}_{ij} = r_{ij}/r_p$, where r_p is the position of the first peak in the corresponding $g(r)$ of atoms with the lowest 1% $v_{flex,i}$ as shown in Fig. 4.1. The purpose of using this reduced distance is to facilitate the transfer of the resulting ML model trained on one MG system to other MG systems, a proposition we will check later in this chapter. For various $\bar{r}$ within the range between 0.6 and $\bar{r}_c$, in increments of the bin width $\sigma = 0.05$, and for various choices of β, $G_i^{\beta}(\bar{r})$ measures the density of atoms of each species β at distance $\bar{r} \pm \sigma$ from the central atom i [165] and contains

similar structural information as that in Eq. 4.3. A set of $G_i^{\beta}(\bar{r})$ at different distances $\bar{r}$ for species β can be viewed as a Gaussian weighted partial radial distribution function for β atoms surrounding each reference atom i. All $G_i^{\beta}(\bar{r})$ sets for different β and a constant bias term $b = 1$, (the trainable parameter corresponding to the bias term is contained in the weight vector $\boldsymbol{\omega}$) are then assembled into a vector $\boldsymbol{x}_i$ as

$$\boldsymbol{x}_i = \left[G_i^{\mathrm{Cu}}(\bar{r}_1), G_i^{\mathrm{Cu}}(\bar{r}_2), \ldots G_i^{\mathrm{Cu}}(\bar{r}_m), G_i^{\mathrm{Zr}}(\bar{r}_1), G_i^{\mathrm{Zr}}(\bar{r}_2), \ldots G_i^{\mathrm{Zr}}(\bar{r}_m), b = 1\right], \quad (4.6)$$

this represents the static structure description of the local environment of atom i for ML as well as in the structure-property relations we establish later.

We use $y_i = \ln(v_{flex,i})$ as the supervisory signal or target value. The use of natural logarithm makes training easier, when the distribution of the target value is close to a normal distribution. Through direct ML regression, we "fit" $\boldsymbol{x}_i$ and our actual y_i data to obtain the best weighting vector $\boldsymbol{\omega}$. In the context of Eq. 4.4, this means that the predicted dimensionless SF_i targets and approximates $\ln(v_{flex,i})$, keeping/reflecting the same ranking order as that of $v_{flex,i}$. The regression was carried out using L2-regularized L2-loss support vector regression (SVR), which is a linear algorithm, through minimizing the

following loss function via adjusting $\boldsymbol{\omega}$:

$$\mathcal{L} = \frac{1}{2}\boldsymbol{\omega}^T\boldsymbol{\omega} + C\sum_{i=1}^{l}\left[\max\left(0, |y_i - \boldsymbol{\omega}^T\boldsymbol{x}_i| - \epsilon\right)\right]^2. \tag{4.7}$$

Here C is a regularization parameter and $\epsilon \geqslant 0$ is a parameter used to specify the sensitiveness of the loss $\mathcal{L}$ [170]. Again, with this weighting (scaling) function established through ML, we arrive at a single SF_i, which, being a scalar flexibility indicator, offers a power similar to $v_{flex,i}$ in correlating with various (other) properties in MGs. Moreover, now that we have finished feeding the $v_{flex,i}$ information into $\boldsymbol{\omega}$, from here on the SF can be computed solely from $\boldsymbol{x}_i$. In other words, the static information about atomic positions is our initial and only structural input.

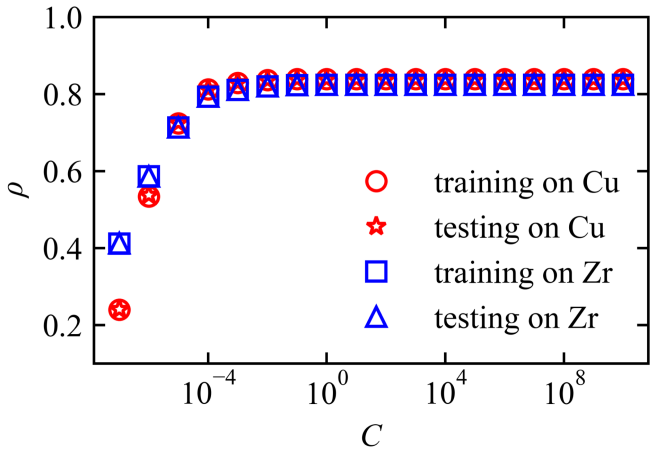

Figure 4.2: Pearson correlation coefficient (ρ) achieved on the training and testing data set for Cu and Zr species from all nine Cu_xZr_{100-x} metallic glasses (MGs), at different value of regularization parameter C.

In the regression tasks, a high Pearson correlation coefficient ρ of 0.84 (and

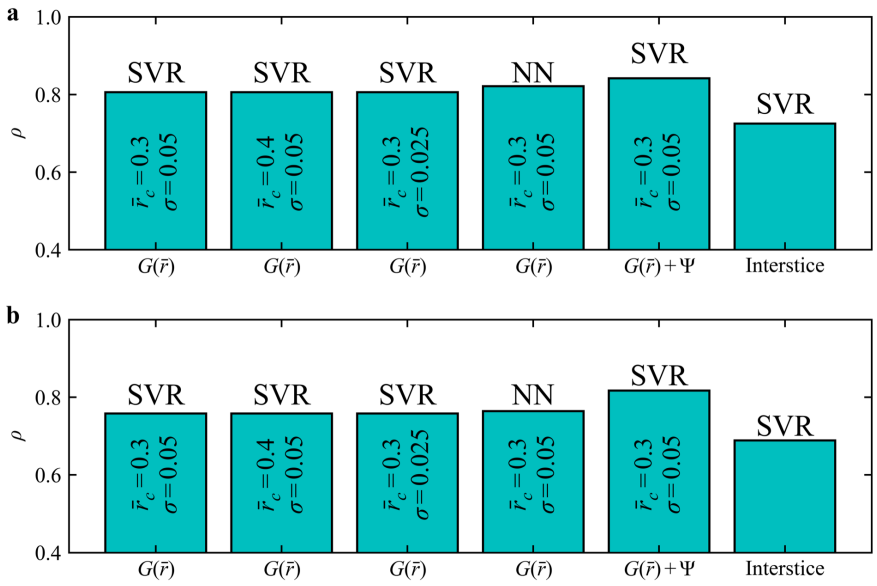

Figure 4.3: Other structural representations or ML algorithms. We also tried other structural representations or ML algorithms, to see if the current results can be further improved. This figure shows the Pearson correlation coefficient (ρ) achieved on the same testing data set of Cu (a) and Zr (b) species in $Cu_{50}Zr_{50}$ metallic glass (MGs) using different structural representations (radial structure functions ($G(\bar{r})$)) with different parameters adding/not adding angular structure functions (Ψ) or interstice distribution) or machine learning algorithms (support vector regression (SVR) or neural network (NN)). Note that all the testing results are almost the same as their corresponding training results and thus here only testing results are shown. The observation that adding bond-angle distribution information into input vector x_i can slightly improve both the training and test accuracy also suggests the training results could be further improved, if one finds and incorporates more and more relevant structural information into the input. The neural network (NN) model presented here has two hidden layers with rectified linear units (ReLU) nonlinearity, and the number of hidden units in each hidden layer is the same. Many different number of hidden units in each hidden layer (3, 5, 10, 20, 30, 40, 50, 60, 70, 80, 90, 96 (length of our input vector)) have been tried, but it does not have big influence on training results. In the plots, we used 50 hidden units in each hidden layer, corresponding to the highest Pearson correlation coefficient on test dataset, and chose the learning rate of 0.0001 and RMSprop optimizer. The training of NN model is implemented in KERAS backend with Tensorflow.

0.82) between predicted and true values of y_i was achieved for the test set for Cu (and Zr). This makes quantitative the relation between the local packing environment and flexibility observed in Fig. 4.1. As shown in the Appendix (section 4.6.1), in undertaking a classification task to separate out the least flexible atoms, our accuracy is as high as 98.4%. Because the data sets used in ML are sufficiently large, there is no over-fitting issue, and the ML result is not sensitive to the regularization parameter C when C is larger than 1, as shown in Fig. 4.2.

To ensure that our ML model can be applied across a large composition range in a MG system where glassy states can be obtained in experiments, our training and testing data sets are composed of atoms from Cu_xZr_{100-x} MGs at 9 compositions ($x = 30, 35, \ldots, 70$, in step of 5). We have also confirmed that the ML model trained on the data set composed of atoms from a single composition has the same efficacy as that from 9 compositions, and can thus be transferred to other compositions in the same MG system. This is because the former data set was sufficiently large that it already covers the majority of the possible variations of local environment Cu (or Zr) atoms would see in the Cu-Zr system (see more discussion in Appendix, section 4.6.2). As shown in Fig. 4.3, adjusting the value of $\bar{r}_c$ and σ in $G_i^\beta(\bar{r})$, or using neural network regression, did not yield visible improvement. Using interstice distribution [68] as the structural representation lowered ρ slightly. Combining bond-angle

structural functions with radial structural functions improved ρ only slightly, which is consistent with the observation in Ref. [165]. This further justifies the use of the local radial distribution alone, which is clear and simple in its physical meaning, as our structural representation $\boldsymbol{x}_i$.

The high ρ achieved through SVR between $\boldsymbol{\omega}^T\boldsymbol{x}_i$ and $\ln(v_{flex,i})$ indicates a successful regression producing an optimized $\boldsymbol{\omega}$. As such, the evaluation of $\boldsymbol{SF}_i$ from here on no longer requires the computation of $v_{flex,i}$. Purely structural information embedded in $\boldsymbol{x}_i$ would suffice. In other words, once the machine-learned $\boldsymbol{\omega}$ is in hand, this same weighting vector ω will be used as the designated machinery to convert static structural information into the flexibility for this entire given MG alloy system. As can be seen from Equation 4.4, all that is needed to calculate $\boldsymbol{SF}_i$ is $\boldsymbol{x}_i$, which comes from the static atomic positions in a sample. We stress here that even though we have involved, through $v_{flex,i}$, the dynamics of atoms in the training to construct $\boldsymbol{\omega}$, the latter is not a dynamical quantity but a structural one: it reflects the important aspects of the structural environment $\boldsymbol{x}_i$ that matter to the atomic flexibility in its dynamic response. The same can also be said for $\boldsymbol{SF}_i$, which builds upon but goes beyond the static $\boldsymbol{x}_i$.

In what follows, we will demonstrate using the Cu_xZr_{100-x} MG models the ability of a single *SF* quantity to strongly correlate the (local) structure with multiple (at least five) microscopic/macroscopic properties, including shear mod-

ulus, soft vibrational modes, the Boson peak, as well as the barriers for thermally activated rearrangements and stress-driven shear transformations. This represents a broad range of MG responses, from vibrational to diffusional to elastic/plastic relaxation events.

4.3 Correlations between *SF* and MG properties

4.3.1 Strong SF_i-$v_{flex,i}$ correlation for all MGs

As the ML model was trained and tested on $v_{flex,i}$, we first anticipate a strong correlation between the SF_i and $v_{flex,i}$, in other Cu-Zr MGs quenched at different cooling rates and at different compositions, those that were never involved in our ML training or testing. This is indeed seen in Fig. 4.4 for Cu atoms (and Fig. 4.5 for Zr). The ρ (displayed on these maps) between SF_i and $\ln(v_{flex,i})$ for Cu (Zr) atoms in these samples is almost the same as that in previous ML testing (shown in Fig. 4.6), confirming the generalizability of our ML models. The ρ is much higher than the corresponding ρ between $\Omega_{a,i}$ (or LFFS_i) and $\ln(v_{flex,i})$, shown in Figs. 4.7, 4.8, 4.9 and 4.10. As can be seen from Fig. 4.4 and Fig. 4.5, the largest scatter/deviation is mainly for atoms with extremely large $v_{flex,i}$ which are most sensitive to thermal fluctuation. If plotted against

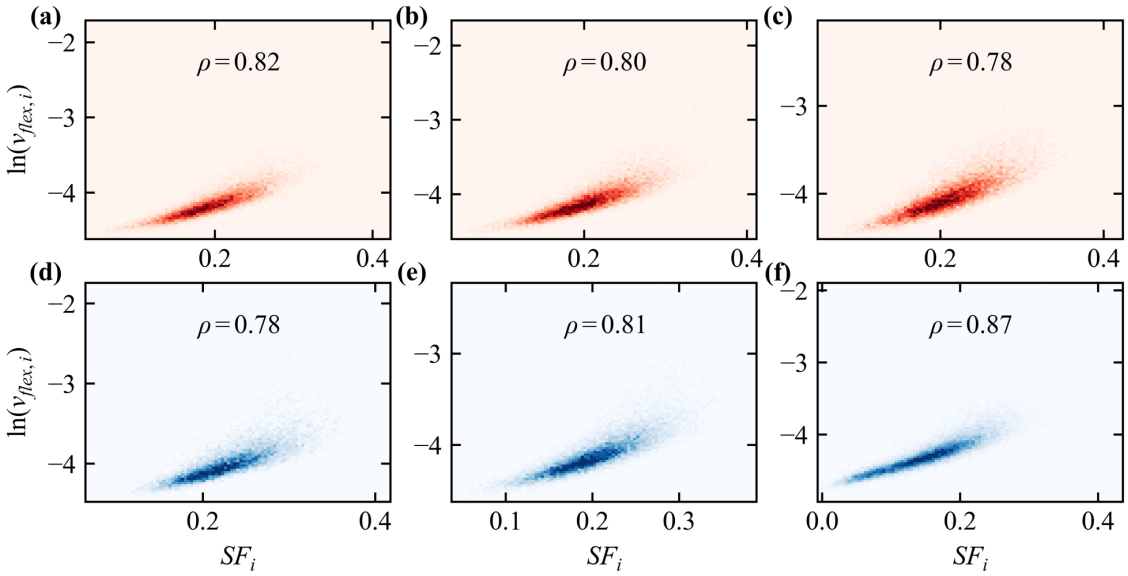

Figure 4.4: Correlation between structural flexibility SF_i and flexibility volume $v_{flex,i}$ of Cu atoms in Cu-Zr metallic glasses (MGs). The color in each plot scales with the density of atoms, dark (bright) corresponding to high (low) density of atoms. The Pearson correlation coefficient ρ between SF_i and $\ln(v_{flex,i})$ for each sample was shown in each figure. (a-c) Correspond to $Cu_{50}Zr_{50}$ MGs (31,250 atoms) quenched at cooling rates of 1×10^9, 1×10^{11} and 1×10^{13} K/s, respectively. (d-f) Correspond to $Cu_{30}Zr_{70}$, $Cu_{50}Zr_{50}$ and $Cu_{70}Zr_{30}$ MGs (32,000 atoms), respectively, quenched at the same effective cooling rate of 1×10^{10} K/s. The corresponding plots for the Zr atoms are shown in Fig. 4.5.

sample-averaged v_{flex}, the sample-averaged *SF* for Cu (or Zr) atoms scales linearly with it, as seen in Fig. 4.11a and b (or Fig. 4.12a and b). This is expected, as *SF* represents the flexibility-centric "structure", a dimensionless manifestation of v_{flex}. Fig. 4.13 shows that the sample-averaged *SF* for Cu (or Zr) atoms increases with increasing cooling rate or Zr concentration, which is the same trend that v_{flex} is known to exhibit [78].

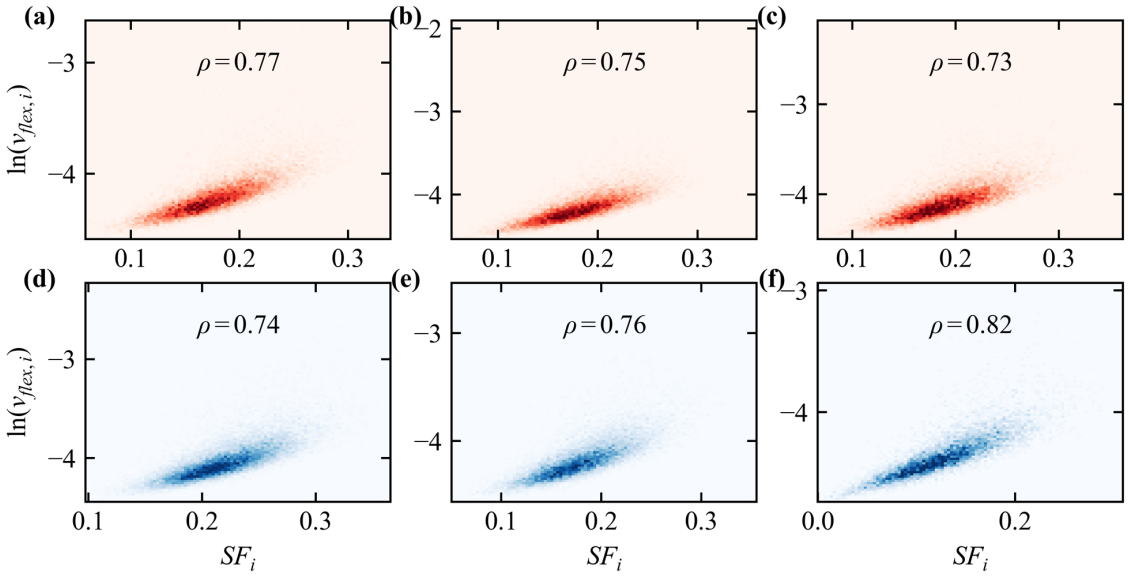

Figure 4.5: Correlation between structural flexibility SF_i and flexibility volume $v_{flex,i}$ of Zr atoms in Cu-Zr metallic glasses (MGs). The color in each plot scales with the density of atoms, dark (bright) corresponding to high (low) density of atoms. The Pearson correlation coefficient ρ between SF_i and $\ln(v_{flex,i})$ for each sample was shown in each figure. (a-c) Correspond to $Cu_{50}Zr_{50}$ MGs (31,250 atoms) quenched at cooling rates of 1×10^9, 1×10^{11} and 1×10^{13} K/s, respectively. (d-f) Correspond to $Cu_{30}Zr_{70}$, $Cu_{50}Zr_{50}$ and $Cu_{70}Zr_{30}$ MGs (32,000 atoms), respectively, quenched at the same effective cooling rate of 1×10^{10} K/s.

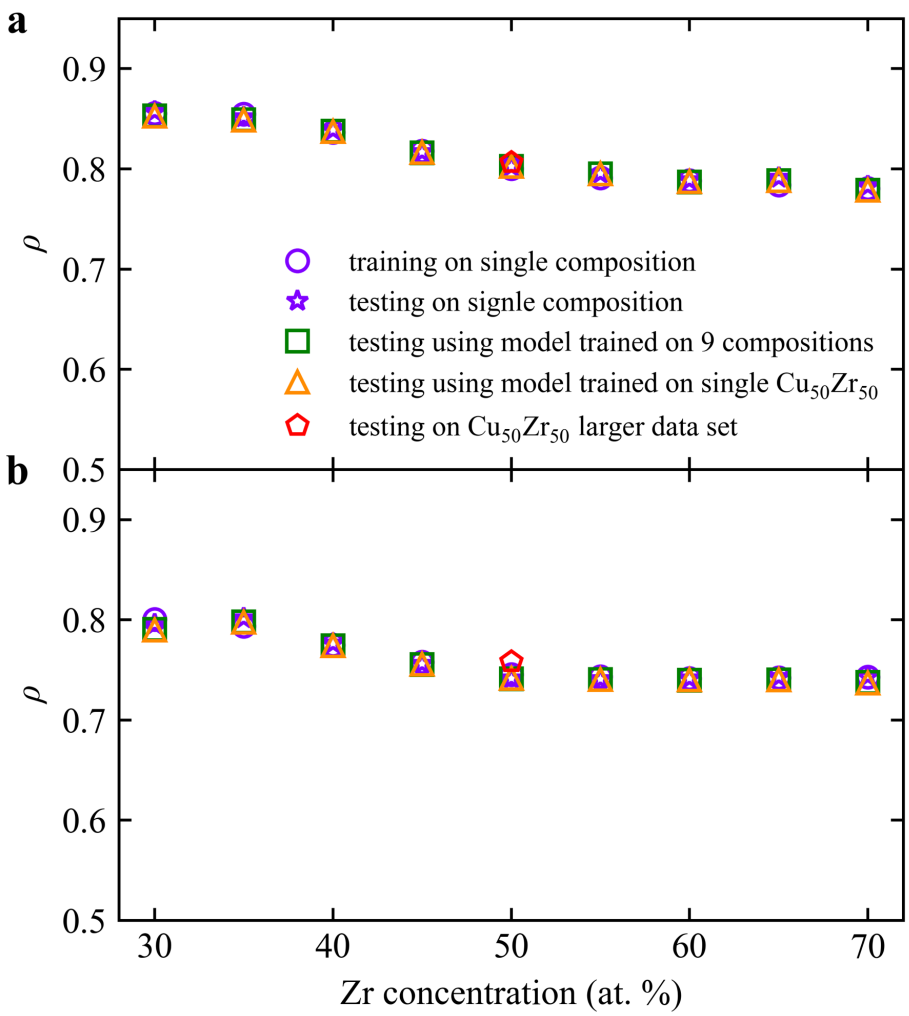

Figure 4.6: Pearson correlation coefficient (ρ) achieved on the training (purple circle) and testing (purple star) data sets, for Cu (a) and Zr (b) species in Cu_xZr_{100-x} MGs. There is no difference in ρ between the training and testing sets, suggesting there is no over-fitting issue in these ML tasks. The ML task for each composition was performed on data sets composed of atoms from that single composition/sample containing 500,000 atoms. To compare ML models trained on different data sets, the ML model trained on date set composed of atoms from 9 compositions or more atoms from a single composition of $Cu_{50}Zr_{50}$ was used to compute ρ on the testing data set of each composition (same data sets used to obtain purple stars in this figure) and corresponding results are shown using green squares or orange triangles. The ρ on the large testing data set of $Cu_{50}Zr_{50}$ is shown as red pentagon. (The ρ on corresponding training data set is almost the same and thus is not shown).

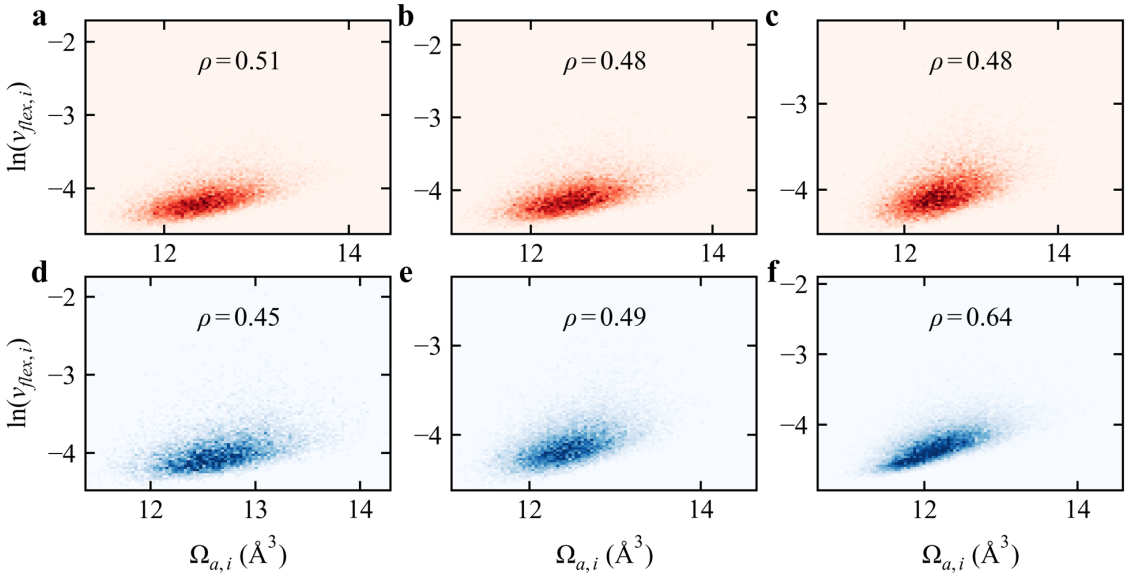

Figure 4.7: Weak correlation between atomic volume $\Omega_{a,i}$ and flexibility volume $v_{flex,i}$ of Cu in Cu-Zr metallic glasses (MGs). The color in each figure represents atom density in the map of $\Omega_{a,i}$ against natural logarithm of $v_{flex,i}$. Dark (bright) corresponds to high (low) density of atoms. The Pearson correlation coefficient ρ between $\Omega_{a,i}$ and $\ln(v_{flex,i})$ for each sample is shown in each figure. (a-c) Correspond to $Cu_{50}Zr_{50}$ MGs (31,250 atoms) quenched at cooling rates of 1×10^9, 1×10^{11} and 1×10^{13} K/s, respectively. (d-f) Correspond to $Cu_{30}Zr_{70}$, $Cu_{50}Zr_{50}$ and $Cu_{70}Zr_{30}$ MGs (32,000 atoms), respectively, quenched at the same effective cooling rate of 1×10^{10} K/s.

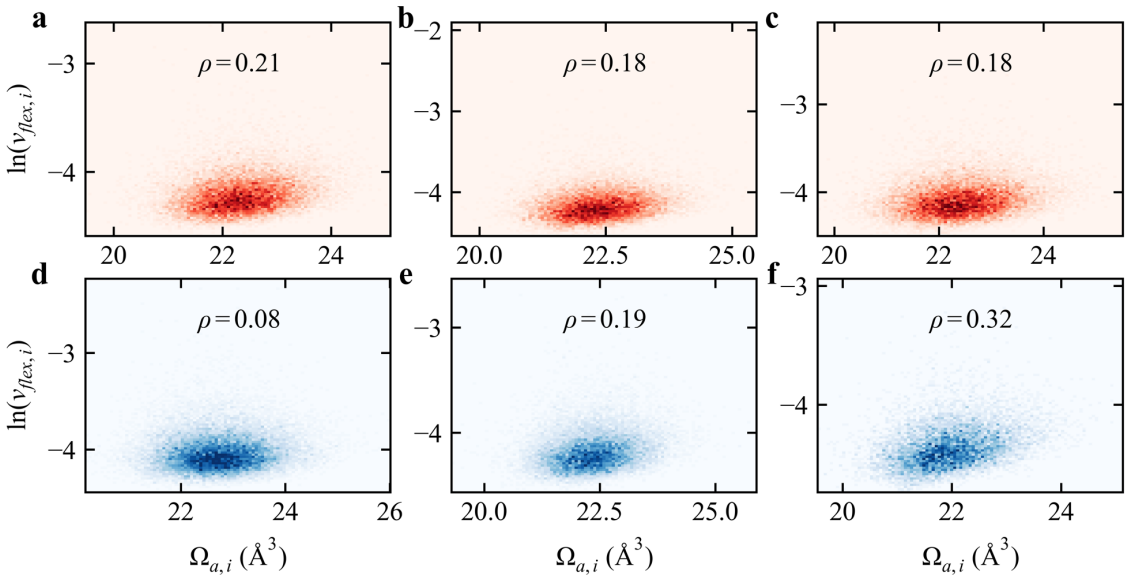

Figure 4.8: Poor correlation between atomic volume $\Omega_{a,i}$ and flexibility volume $v_{flex,i}$ of Zr in Cu-Zr metallic glasses (MGs). The color in each figure represents atom density in the map of $\Omega_{a,i}$ against natural logarithm of $v_{flex,i}$. Dark (bright) corresponds to high (low) density of atoms. The Pearson correlation coefficient ρ between $\Omega_{a,i}$ and $\ln(v_{flex,i})$ for each sample is shown in each figure. (a-c) Correspond to $Cu_{50}Zr_{50}$ MGs (31,250 atoms) quenched at cooling rates of 1×10^9, 1×10^{11} and 1×10^{13} K/s, respectively. (d-f) Correspond to $Cu_{30}Zr_{70}$, $Cu_{50}Zr_{50}$ and $Cu_{70}Zr_{30}$ MGs (32,000 atoms), respectively, quenched at the same effective cooling rate of 1×10^{10} K/s.

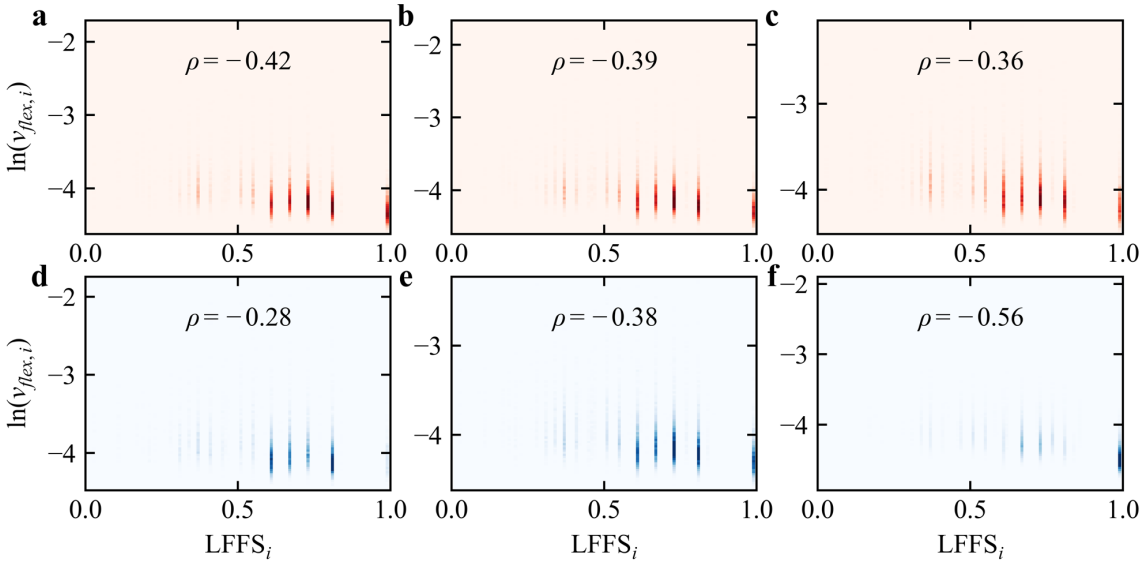

Figure 4.9: Absence of correlation between the degree of local five-fold symmetry (LFFS_i) and flexibility volume $v_{flex,i}$ of Cu in Cu-Zr MGs. The color in each figure represents atom density in the map of LFFS_i against natural logarithm of $v_{flex,i}$. Dark (bright) corresponds to high (low) density of atoms. The Pearson correlation coefficient ρ between LFFS_i and $\ln(v_{flex,i})$ for each sample was shown in each figure. (a-c) Correspond to $Cu_{50}Zr_{50}$ MGs (31,250 atoms) quenched at cooling rates of 1×10^9, 1×10^{11} and 1×10^{13} K/s, respectively. (d-f) Correspond to $Cu_{30}Zr_{70}$, $Cu_{50}Zr_{50}$ and $Cu_{70}Zr_{30}$ MGs (32,000 atoms), respectively, quenched at the same effective cooling rate of 1×10^{10} K/s.

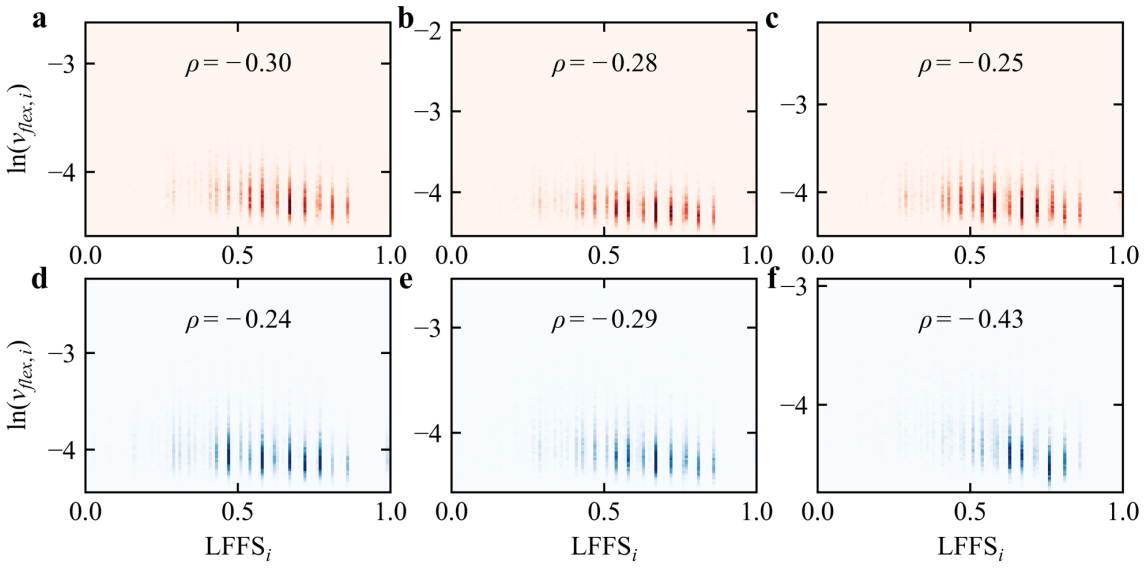

Figure 4.10: Absence of correlation between the degree of local five-fold symmetry (LFFS$_i$) and flexibility volume $v_{flex,i}$ of Zr in Cu-Zr MGs. The color in each figure represents atom density in the map of LFFS$_i$ against natural logarithm of $v_{flex,i}$. Dark (bright) corresponds to high (low) density of atoms. The Pearson correlation coefficient ρ between LFFS$_i$ and $\ln(v_{flex,i})$ for each sample was shown in each figure. (a-c) Correspond to $Cu_{50}Zr_{50}$ MGs (31,250 atoms) quenched at cooling rates of 1×10^9, 1×10^{11} and 1×10^{13} K/s, respectively. (d-f) Correspond to $Cu_{30}Zr_{70}$, $Cu_{50}Zr_{50}$ and $Cu_{70}Zr_{30}$ MGs (32,000 atoms), respectively, quenched at the same effective cooling rate of 1×10^{10} K/s.

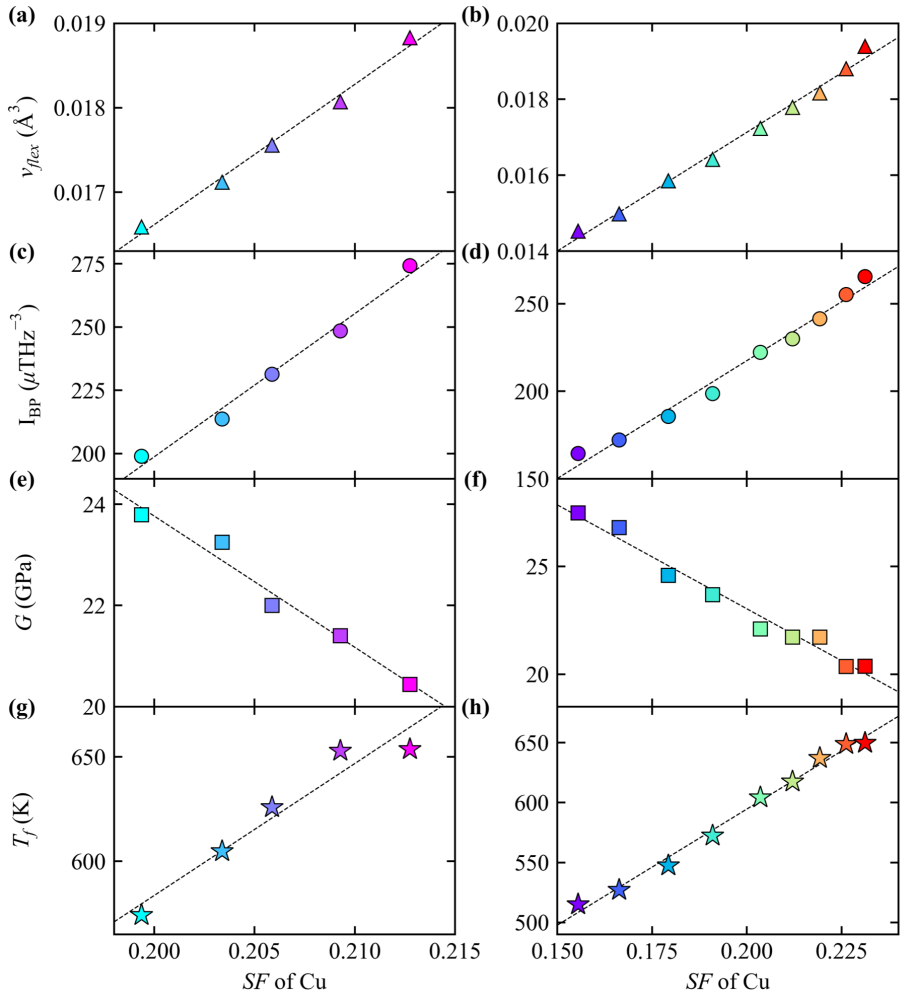

Figure 4.11: Correlation of structural flexibility *SF* averaged over all Cu atoms in a given MG with multiple macroscopic properties, for Cu-Zr MGs quenched at different cooling rates and at different compositions. The left column shows $Cu_{50}Zr_{50}$ MGs (31,250 atoms) quenched at cooling rates of 1×10^9, 1×10^{10}, 1×10^{11}, 1×10^{12} and 1×10^{13} K/s and the right column shows Cu_xZr_{100-x} MGs (where $x = 30, 35, \ldots, 70$) (32,000 atoms) quenched at same effective cooling rate of 1×10^{10} K/s. The four rows, from top to bottom, are for four different sample-averaged properties for Cu atoms: v_{flex}, Boson peak intensity I_{BP}, shear modulus G and fictive temperature T_f. The dash lines serve as a guide to the eye.

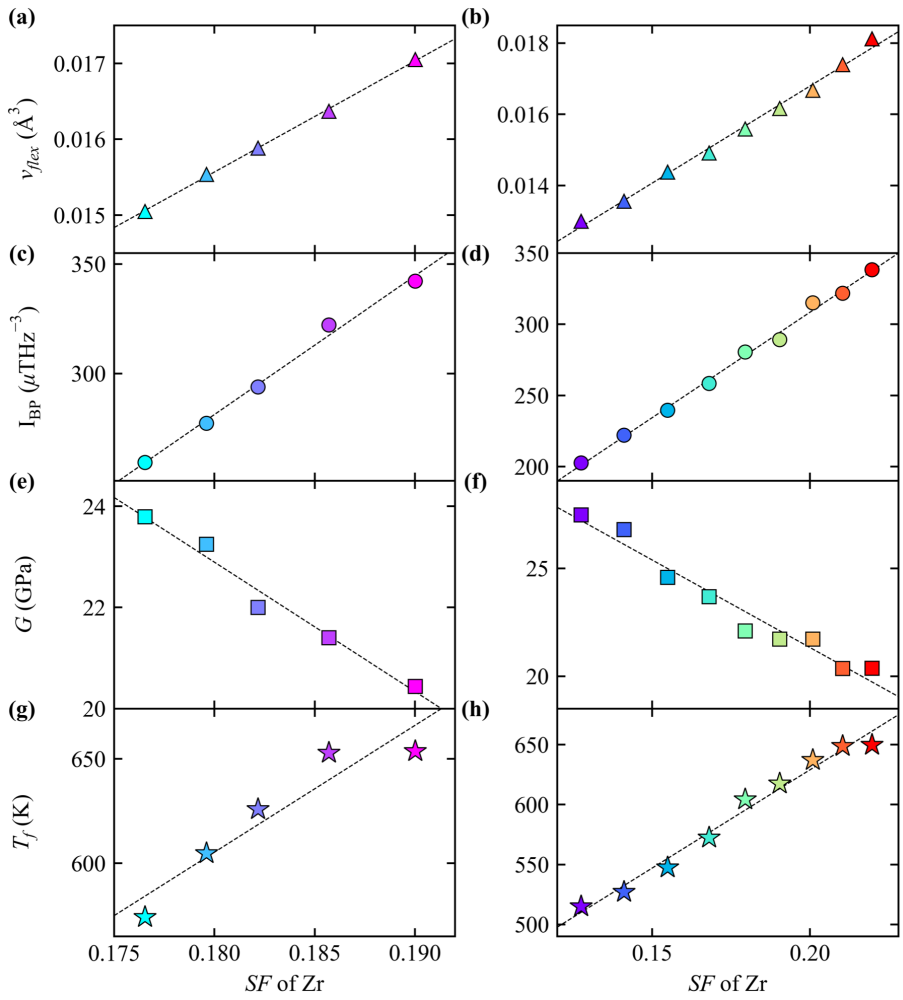

Figure 4.12: Structural flexibility *SF* averaged over all Zr atoms in one MG, correlated with multiple macroscopic properties for Cu-Zr metallic glasses (MGs) quenched at different cooling rates and at different compositions. The left column shows $Cu_{50}Zr_{50}$ MGs (31,250 atoms) quenched at cooling rates of 1×10^9, 1×10^{10}, 1×10^{11}, 1×10^{12} and 1×10^{13} K/s and the right column shows Cu_xZr_{100-x} MGs (where $x = 30, 35, \ldots, 70$) (32,000 atoms) quenched at same effective cooling rate of 1×10^{10} K/s. The four rows, from top to bottom, are for four different sample-averaged properties for Zr atoms: v_{flex}, Boson peak intensity I_{BP}, shear modulus G and fictive temperature T_f. The dash lines serve as a guide to the eye.

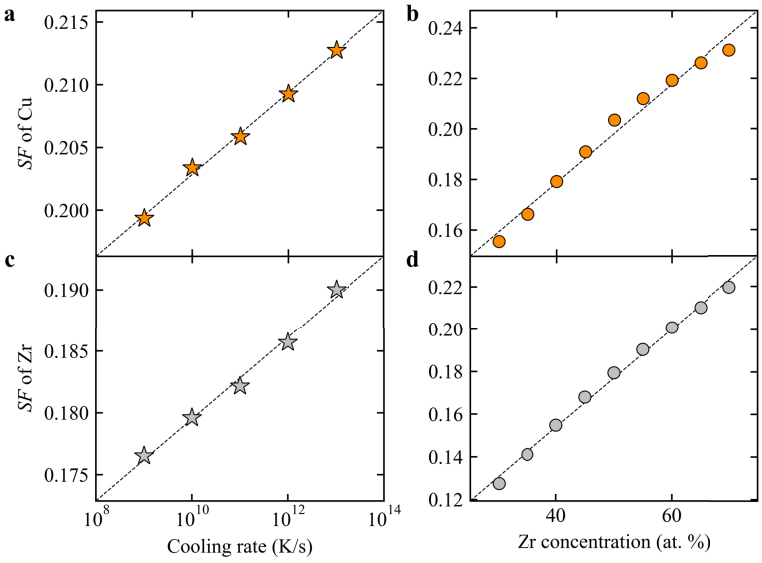

Figure 4.13: Correlation between sample-averaged structural flexibility *SF* and cooling rates (left) and compositions (right) for Cu-Zr MGs. Upper and lower panels correspond to Cu and Zr atoms, respectively. In the left panel, each symbol represents one $Cu_{50}Zr_{50}$ MG (31,250 atoms) quenched at a specific cooling rate; in the right panel, each symbol represents one Cu_xZr_{100-x} MG at a particular composition (32,000 atoms and same effective cooling rate of 1×10^9 K/s). The dash lines are shown as a guide to the eye.

4.3.2 Correlating structural flexibility with quasi-localized soft modes

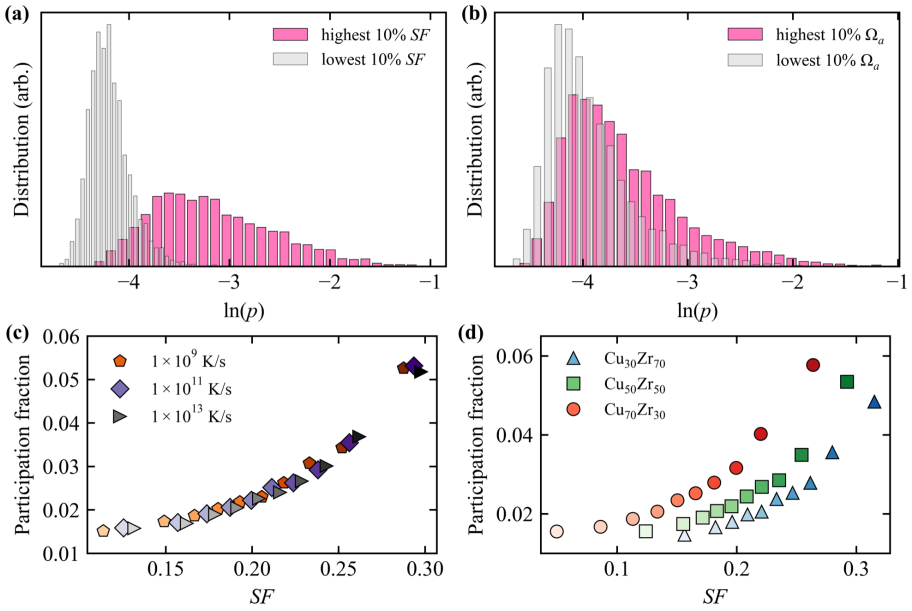

Figure 4.14: Structural flexibility correlates strongly with the participation in quasi-localized soft modes for Cu atoms. (a) Cu atoms with the highest 10% of SF_i show obviously higher participation fraction, p, than those with the lowest 10% SF_i. The same cannot be said when attempting to correlate p with (b) atomic volume $\Omega_{a,i}$. The data are from 10 different $Cu_{50}Zr_{50}$ MGs each containing 10,000 atoms and quenched at the same cooling rate of 1×10^{10} K/s. (c) and (d) All the Cu atoms in a Cu-Zr MG are sorted based on their SF_i value into bins each containing 10% of the atoms. An average participation fraction (p) is then calculated for the atoms in each bin, and plotted to demonstrate the strong correlation with SF. The samples in (c) are $Cu_{50}Zr_{50}$ MGs each containing 10,000 atoms and quenched at three different cooling rates. The samples in (d) are Cu_xZr_{100-x} MGs (x = 30, 50 and 70) each containing 10,000 atoms and quenched at a cooling rate of 1×10^{10} K/s.

The next demonstration is for the correlation between SF and the quasi-localized low-frequency vibrational modes [19, 54]. The correlation between these two is

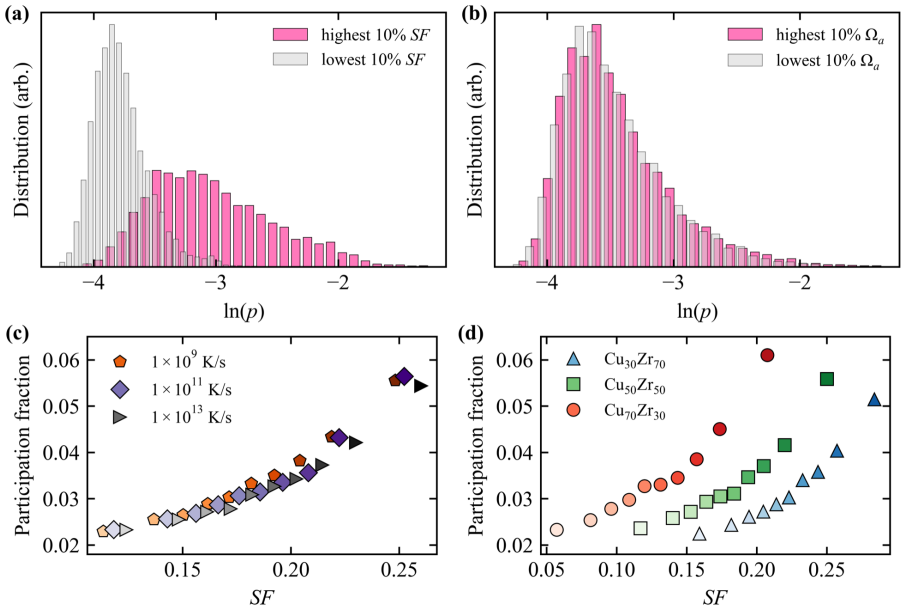

Figure 4.15: Structural flexibility correlates strongly with the participation in quasi-localized soft modes for Zr atoms. Distribution of natural logarithm of participation fraction, p, in soft modes of Zr atoms with the highest/lowest 10% of the value for structural flexibility SF_i (a) or $\Omega_{a,i}$ (b). The data is from 10 different $Cu_{50}Zr_{50}$ MGs each containing 10,000 atoms and quenched at same cooling rate of 1×10^{10} K/s. (c) and (d) All the Zr atoms in a Cu-Zr MG are sorted based on their SF_i value into bins each containing 10% of the atoms. An average participation fraction (p) is then calculated for the atoms in each bin, and plotted to demonstrate the strong correlation with SF. The samples in (c) are $Cu_{50}Zr_{50}$ MGs each containing 10,000 atoms and quenched at three different cooling rates. The samples in (d) are Cu_xZr_{100-x} MGs (x = 30, 50 and 70) each containing 10,000 atoms and quenched at a cooling rate of 1×10^{10} K/s.

expected to be strong, as the latter is known to correlate with the local atomic packing structure [54] and should correlate with v_{flex} [78], both being ingredients fed into SF. In Fig. 4.14a, we plot the distribution of the Cu atoms (the corresponding plot for Zr is in Fig. 4.15a) with the highest and the lowest 10% of SF_i (from 10 different $Cu_{50}Zr_{50}$ MGs) versus the participation fraction in soft modes, p, obtained by normal mode analysis (see details in Methods, sec-

tion 4.5.4). As seen from Fig. 4.14a (and Fig. 4.15a), the maximum, mean and minimum values of p for Cu (Zr) atoms with the highest 10% SF_i are all much higher than the corresponding values of Cu (Zr) atoms with the lowest 10% SF_i. To demonstrate that this correlation is strong, we contrast it with Fig. 4.14b (and Fig. 4.15b) where no obvious correlation is present with atomic volume $\Omega_{a,i}$: the distributions for the highest and the lowest 10% of $\Omega_{a,i}$ overlap on top of each other. The correlation between SF and p also exists for Cu-Zr MGs with other compositions and processing history (cooling rates). We sorted Cu (Zr) atoms in each sample, based on increasing magnitude of SF_i, into bins each containing 10% of all the atoms and then computed the average p for the atoms in each bin. As seen from Fig. 4.14c and d (and Fig. 4.15c and d), there is a clear trend that the higher the SF, the larger the p.

4.3.3 Correlating structural flexibility with the Boson peak

Boson peak (BP) is one of the universal features of glasses and typically ascribed to an excess vibrational density of states (VDOS). The origin of BP is still a matter of ongoing debate [171–177]. It has been shown that there is a strong correlation between the vibrational MSD and BP [173,174]. We thus expect the SF to have a strong correlation with BP. Fig. 4.16a shows the VDOS $g(\omega)$ of a $Cu_{50}Zr_{50}$ MG (containing 1,024,000 atoms and quenched at 1×10^{10} K/s), which

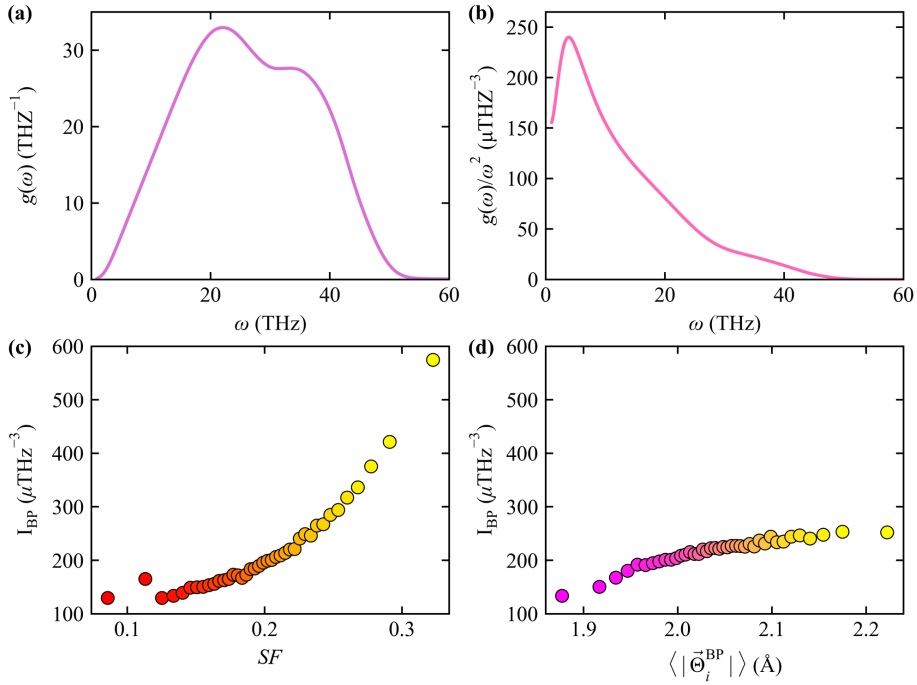

Figure 4.16: Correlation between structural flexibility and Boson peak. (a) and (b) show vibrational density of states (VDOS) $g(\omega)$ and reduced VDOS $g(\omega)/\omega^2$ of a $Cu_{50}Zr_{50}$ MG containing 1,024,000 atoms and quenched at effective cooling rate of 1×10^{10} K/s. In (c) and (d), all the Cu atoms in the MG are sorted based on SF_i and the length parameter $|\bar{\Theta}_i^{BP}|$, into bins each containing 2.5% of the atoms. The intensity of the Boson peak, I_{BP}, is then calculated for each group of the atoms, and plotted against group-averaged *SF* and $\langle|\bar{\Theta}_i^{BP}|\rangle$.

was obtained by the Fourier transform of the velocity auto-correlation function [173, 178] (see details in Methods, section 4.5.6). The BP can be observed easier by plotting reduced VDOS $g(\omega)/\omega^2$ over ω, as shown in Fig. 4.16b. To check the relation between *SF* and BP, we sorted all Cu (and separately Zr) atoms in the MG based on the magnitude of SF_i into groups each containing 2.5% of these atoms and then calculated the BP intensity (I_{BP}) contributed by the group. The I_{BP} of each group was plotted against group-averaged *SF*, as shown in Fig. 4.16c (Fig. 4.17a).

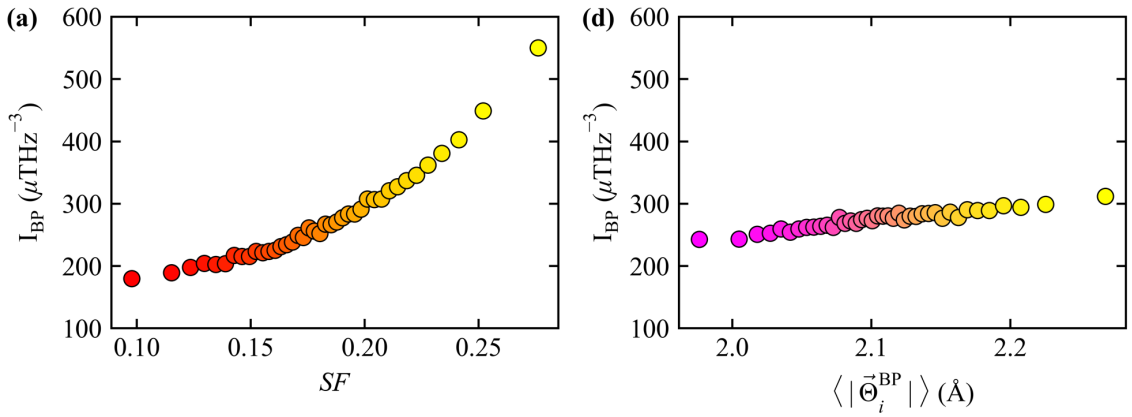

Figure 4.17: Correlation between structural flexibility and Boson peak intensity for Zr atoms. In (a) and (b), all the Zr atoms in the $Cu_{50}Zr_{50}$ MG (containing 1,024,000 atoms and quenched at effective cooling rate of 1×10^{10} K/s) are sorted based on SF_i and length parameter $|\bar{\Theta}_i^{\mathrm{BP}}|$, into bins each containing 2.5% of the atoms. Boson peak intensity I_{BP} is then calculated for each group of the atoms, and plotted against the group-average *SF* or $\langle|\bar{\Theta}_i^{\mathrm{BP}}|\rangle$. The dependence on *SF* is obviously much stronger than the one on $\langle|\bar{\Theta}_i^{\mathrm{BP}}|\rangle$.

A strong correlation between BP intensity and *SF* is apparent in 4.16c (Fig. 4.17a). For comparison, we plotted in 4.16d (Fig. 4.17b) the BP intensity versus a recently introduced orientational order, $|\bar{\Theta}_i^{\mathrm{BP}}|$, which was shown to exhibit good correlation with BP [176]. The difference in I_{BP} between Cu (or Zr) atoms with the highest and the lowest 2.5% *SF* is 445 (370) $\mu\mathrm{THZ}^{-3}$, several times larger than the 119 (69) $\mu\mathrm{THZ}^{-3}$ between the highest and the lowest 2.5% $|\bar{\Theta}_i^{\mathrm{BP}}|$. This much better contrast is not a surprise, given that *SF* contains much more information while $|\bar{\Theta}_i^{\mathrm{BP}}|$ is just a simple topological SRO parameter. The obvious correlation between *SF* and BP also holds for Cu-Zr MGs with different compositions and processing history, as shown in Fig. 4.11c and d (4.12c and d).

The strong correlations so far between *SF* and vibrational behavior are somewhat expected, because vibrational displacements are directly involved in the $v_{flex,i}$ we feed as the target value in working out the machine-learned ω. From here on, we move away from vibrational properties and establish correlations between the *SF* and several other key MG responses upon thermal and mechanical excitation. Note that in our approach relaxation events and shear transformations are not input variables in ML at all. Again, as we remarked earlier, we continue to project strong correlations across the board, because SF_i has been informed by $v_{flex,i}$, which is known to correlate well with (and therefore can "recognize") many MG properties [78].

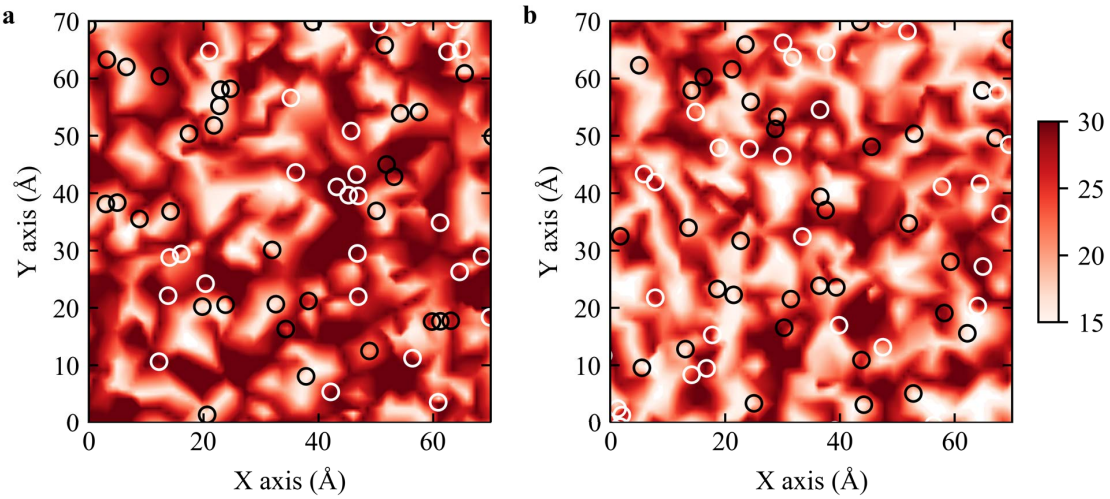

Figure 4.18: Spatial correlation between structural flexibility (SF_i) and local elastic moduli (C_{44}) for Cu (a) and Zr (b) atoms, respectively. The contoured map shows the spatial distribution of local elastic moduli (C_{44}) of Cu or Zr atoms in a slab having a thickness of 4.0 Å cut from a $Cu_{50}Zr_{50}$ MG (31,250 atoms and quenched at a cooling rate of 1×10^9 K/s). The white (black) circles superimposed in the map mark the locations of Cu or Zr atoms with the lowest (highest) 5% SF_i.

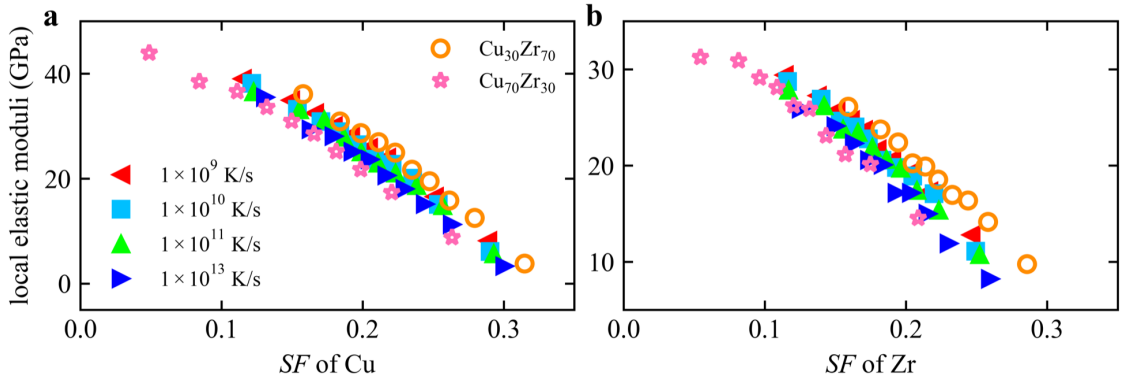

Figure 4.19: Strong correlation between structural flexibility (SF_i) and local elastic moduli (C_{44}) for Cu (a) and Zr (b) atoms. All the Cu (Zr) atoms in a Cu-Zr MG are sorted based on SF_i into bins each containing 10% of the atoms. An average local elastic moduli (C_{44}) is then calculated for the atoms in each bin, and plotted to demonstrate the strong correlation with *SF*. Each solid symbol represents a $Cu_{50}Zr_{50}$ MGs which contains 31,250 atoms and was quenched at a given cooling rate and each empty symbol represents one Cu_xZr_{100-x} MG which contains 32,000 atoms and was quenched at same effective cooling rate of 1×10^{10} K/s.

4.3.4 Correlating structural flexibility with elastic constants

The shear modulus, *G*, a key parameter in MGs. Since *G* has been shown to be deterministically dependent on v_{flex} for all MGs of different compositions and processing history [78], we expect a clear relation between *SF* and *G*. This is indeed observed in Fig. 4.11e and f (Fig. 4.12e and f), for the sample-average. As an example, Fig. 4.18a and b show the spatial correlation between SF_i and local elastic moduli (C_{44}) of Cu and Zr atoms, respectively, in a slab having a thickness of 4.0 Å cut from a $Cu_{50}Zr_{50}$ MG, where most of atoms with the

lowest 5% SF_i (white circles) are located in regions with large (dark red region) local elastic moduli (C_{44}). Correspondingly, the highest 5% SF_i (black circles) coincide mostly with the small (light regions) C_{44} regions. Fig. 4.19 suggests a similar correlation for other Cu-Zr MGs at other compositions or with different cooling rates.

4.3.5 Correlating structural flexibility with stress-driven shear transformation

We next demonstrate the strong correlation of *SF* with stress-driven shear transformations. Athermal quasi-static shear (AQS) was applied to a global strain of 5% (well below their yielding strain) on Cu-Zr MG simulation models with various compositions and processing histories, and then all Cu (or Zr) atoms in each sample were sorted based on the magnitude of SF_i into bins each containing 10% of the total Cu (or Zr) atoms. Each bar chart in Fig. 4.20 (and Fig. 4.21 for Zr) shows the distribution of Cu atoms that have the top 5% non-affinity ($D^2_{\min}$) [16] upon AQS. Here the vertical axis is the fraction of such Cu atoms, out of the total atoms in each bin. These histograms clearly show that the higher the SF_i of atoms, the larger the likelihood of participation in stress-driven shear transformation. The correlation is much stronger than those attempting to relate $D^2_{\min}$ with $\omega_{a,i}$ or LFFS$_i$, as shown in Figs. 4.22, 4.23, 4.24 and 4.25. The contour maps in the row below each bar chart in Fig.

4.20 (Fig. 4.21) show a spatial correlation between SF_i and $D^2_{\min}$ on a slab of thickness of 4.0 Å arbitrarily cut from each sample.

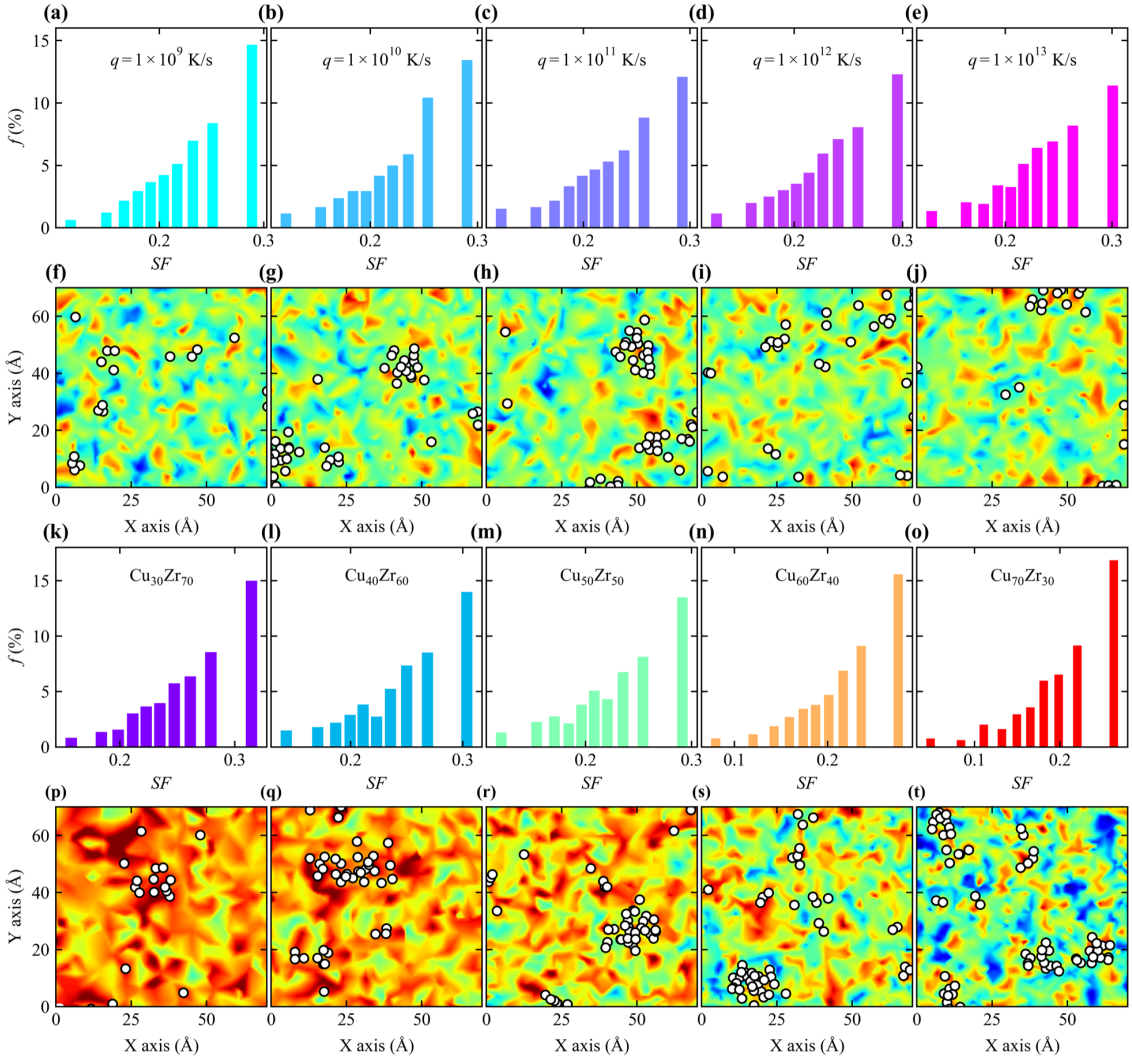

Figure 4.20: Strong correlation between structural flexibility (SF_i) and plastic susceptibility for Cu atoms in Cu-Zr MGs with various compositions and processing history. The simulation box was subjected to athermal quasistatic shear to a global strain of 5%. In the first row, each bar chart corresponds to one $Cu_{50}Zr_{50}$ MG which contains 31,250 atoms and was quenched at a specific cooling rate q labeled on top. In the third row, each bar chart corresponds to one Cu_xZr_{100-x} MG composition, for a model of 32,000 atoms quenched at the same effective cooling rate of 1×10^{10} K/s. Each bar chart shows the faction of

Cu atoms with top 5% non-affine squared displacement ($D^2_{\min}$), distributing the total number of these most-transformed Cu atoms into 10 bins each containing 10% of the total Cu atoms. Each contoured map below the bar chart shows the spatial distribution of $\boldsymbol{SF}_i$ of Cu atoms, in a slab having a thickness of 4.0 Å cut from the corresponding sample. Red (blue) corresponds to high (low) $\boldsymbol{SF}_i$. White spots superimposed in the maps mark the locations of Cu atoms with top 5% $D^2_{\min}$, mostly overlapping with the red regions. The corresponding charts and maps for Zr atoms are shown in Fig. 4.21.

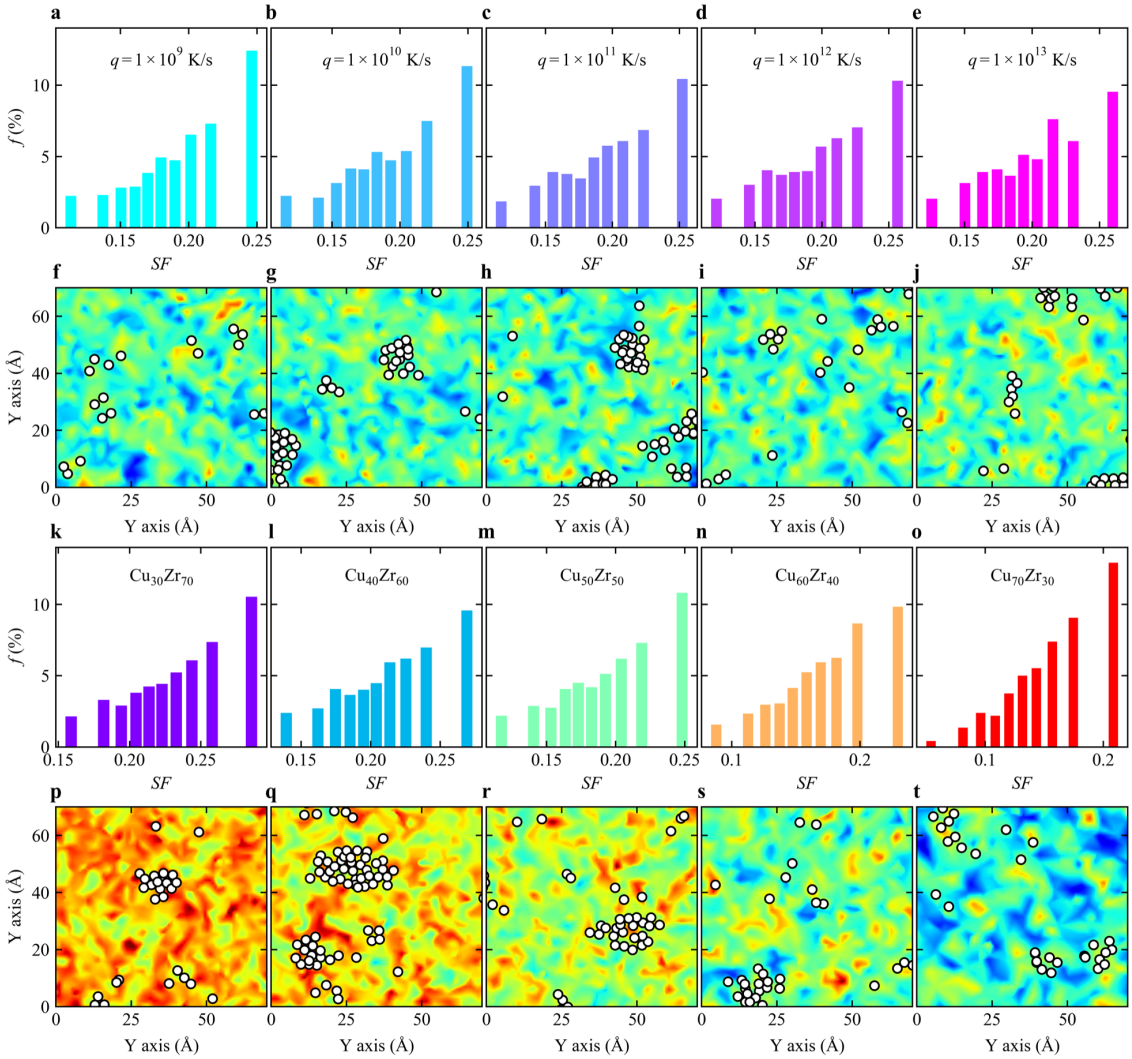

Figure 4.21: Strong correlation between structural flexibility (SF_i) and plastic susceptibility for Zr in Cu-Zr metallic glasses (MGs) with various compositions and processing history. In the first row, each bar chart corresponds to one $Cu_{50}Zr_{50}$ MG which contains 31,250 atoms and was quenched at a specific cooling rate labeled on top of each bar chart. In the third row, each bar chart corresponds to one Cu_xZr_{100-x} MG (specific composition was labeled on top of each bar chart) which contains 32,000 atoms and was quenched at same effective cooling rate of 1×10^{10} K/s. Each bar chart shows the faction of atoms with top 5% non-affine squared displacement (D^2_{min}) upon athermal quasistatic shear of the simulation box to a global strain of 5%. All the atoms of Zr in each sample are sorted based on SF_i into bins each containing 10% of all the total Zr atoms. Each contoured map below bar chart shows the spatial distribution

of SF_i of Zr atoms on a slab having a thickness of 4.0 Å cut from corresponding sample. Red (blue) corresponds to high (low) SF_i. White spots superimposed in the maps mark the locations of atoms with top 5% $D^2_{\min}$.

One may notice that only $< 15\%$ atoms out of those with the top 5% $D^2_{\min}$ are in the top 10% of SF_i; this is because shear transformation or $D^2_{\min}$ also depends on loading conditions, such as temperature, strain rate, and loading orientation. For instance, the same local configuration can have very different $D^2_{\min}$ when the shear is performed along different directions [16, 71]. To take this into account, the $D^2_{\min}$ of a $Cu_{50}Zr_{50}$ MG was averaged over 4320 different loading conditions (3 deformation forms [uniaxial tension/compression, simple shear, pure shear] $\times$ 6 strain rate [4×10^6, 1×10^7, 4×10^7, 1×10^8, 4×10^8 and 1×10^9 s-1] $\times$ 40 temperatures [10, 20, 30, . . . , 400 K] $\times$ 6 loading directions). As seen in Fig. 4.26, now when we examine Cu atoms having the top 5% average $D^2_{\min}$, their fraction in the bin of the highest 10% SF_i almost doubles that in Fig. 4.20 (Fig. 4.21), with almost none residing in the bins for the lowest 20% SF_i. This more convincingly establishes that SF_i correlates strongly with $D^2_{\min}$.

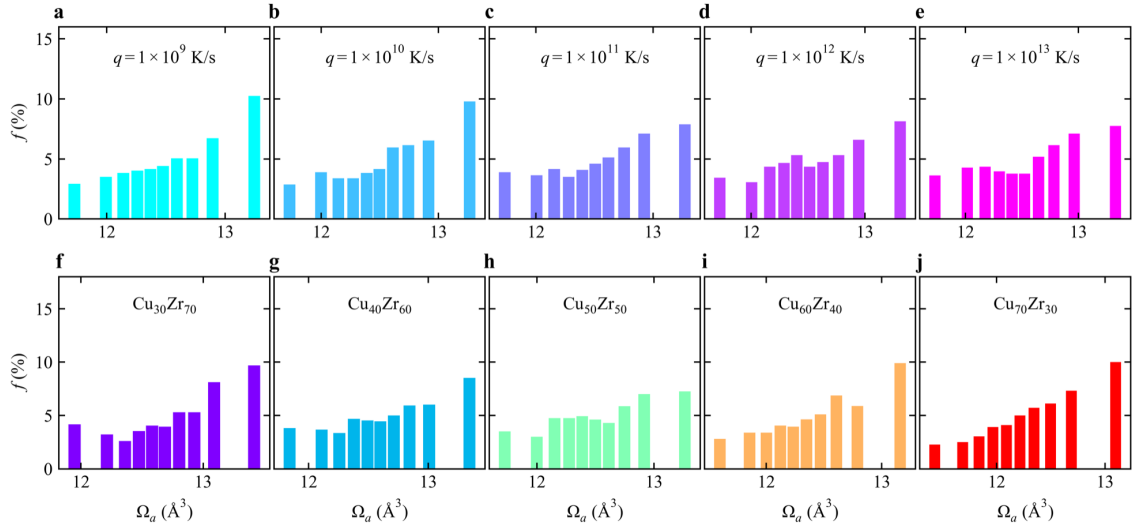

Figure 4.22: Correlation between atomic volume ($\Omega_{a,i}$) and plastic susceptibility for Cu atoms in Cu-Zr metallic glasses (MGs) with various compositions and processing history. In the upper row, each bar chart corresponds to one $Cu_{50}Zr_{50}$ MG which contains 31,250 atoms and was quenched at a specific cooling rate labeled on top of each bar chart. In the lower row, each bar chart corresponds to one Cu_xZr_{100-x} MG (specific composition was labeled on top of each bar chart) which contains 32,000 atoms and was quenched at same effective cooling rate of 1×10^{10} K/s. Each bar chart shows the faction of atoms with top 5% non-affine squared displacement (D^2_{min}) upon athermal quasistatic shear of the simulation box to a global strain of 5%. All the Cu atoms in each sample are sorted based on $\Omega_{a,i}$ into bins each containing 10% of these atoms.

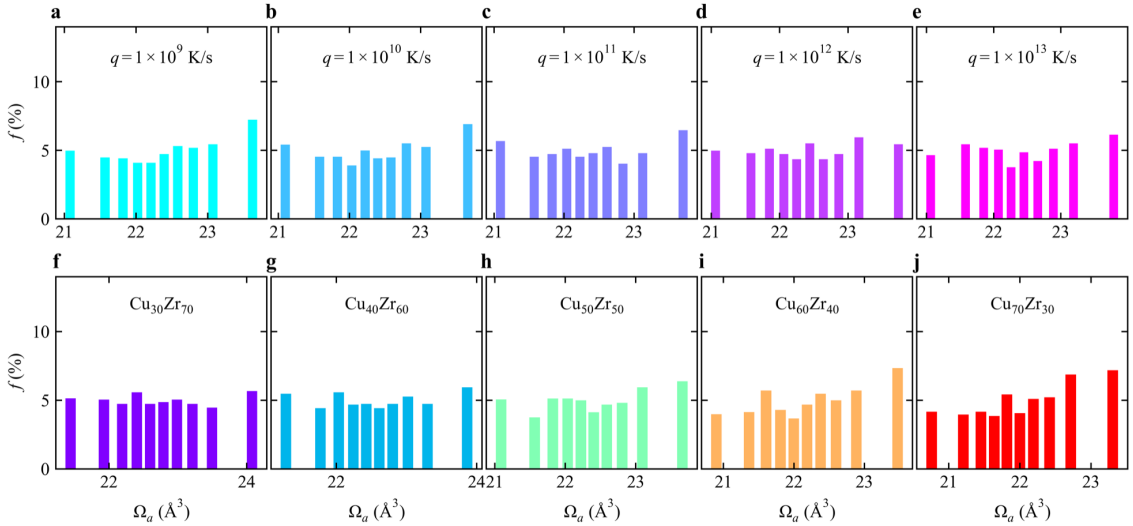

Figure 4.23: No obvious correlation is observed between atomic volume ($\Omega_{a,i}$) and plastic susceptibility for Zr in Cu-Zr metallic glasses (MGs) with various compositions and processing history. In the upper row, each bar chart corresponds to one $Cu_{50}Zr_{50}$ MG which contains 31,250 atoms and was quenched at a specific cooling rate labeled on top of each bar chart. In the lower row, each bar chart corresponds to one Cu_xZr_{100-x} MG (specific composition was labeled on top of each bar chart) which contains 32,000 atoms and was quenched at same effective cooling rate of 1×10^{10} K/s. Each bar chart shows the faction of atoms with top 5% non-affine squared displacement (D^2_{min}) upon athermal quasistatic shear of the simulation box to a global strain of 5%. All the atoms of Zr in each sample are sorted based on $\Omega_{a,i}$ into bins each containing 10% of all the Zr atoms.

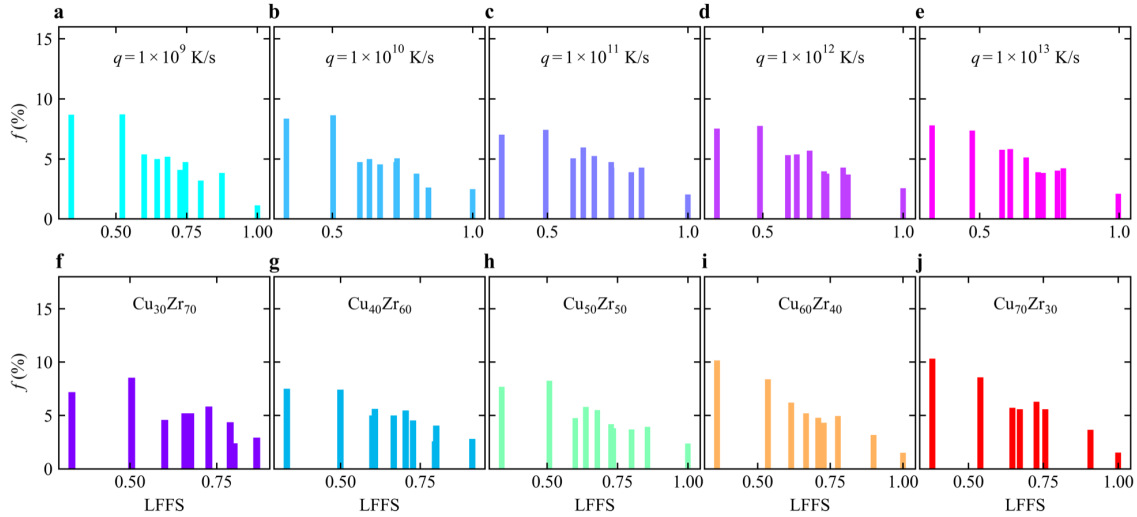

Figure 4.24: Poor correlation between the degree of local five-fold symmetry (LFFS) and plastic susceptibility for Cu in Cu-Zr metallic glasses (MGs) with various compositions and processing history. In the upper row, each bar chart corresponds to one $Cu_{50}Zr_{50}$ MG which contains 31,250 atoms and was quenched at a specific cooling rate labeled on top of each bar chart. In the lower row, each bar chart corresponds to one Cu_xZr_{100-x} MG (specific composition was labeled on top of each bar chart) which contains 32,000 atoms and was quenched at same effective cooling rate of 1×10^{10} K/s. Each bar chart shows the faction of atoms with top 5% non-affine squared displacement (D^2_{min}) upon athermal quasistatic shear of the simulation box to a global strain of 5%. All the Cu atoms in each sample are sorted based on LFFS_i into bins each containing 10% of these atoms.

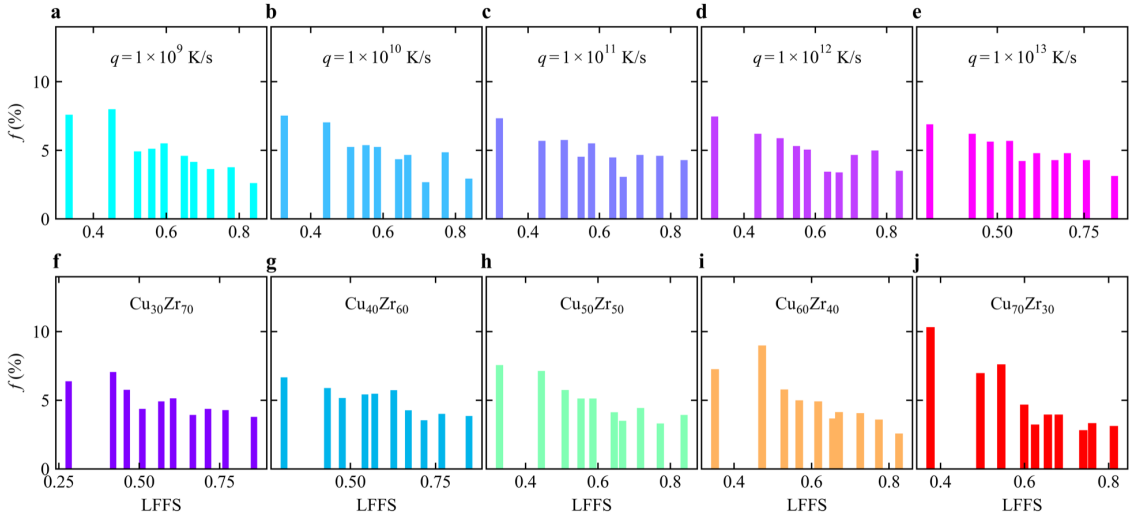

Figure 4.25: Lack of correlation between the degree of local five-fold symmetry (LFFS) and plastic susceptibility for Zr in Cu-Zr metallic glasses (MGs) with various compositions and processing history. In the upper row, each bar chart corresponds to one $Cu_{50}Zr_{50}$ MG which contains 31,250 atoms and was quenched at a specific cooling rate labeled on top of each bar chart. In the lower row, each bar chart corresponds to one Cu_xZr_{100-x} MG (specific composition was labeled on top of each bar chart) which contains 32,000 atoms and was quenched at same effective cooling rate of 1×10^{10} K/s. Each bar chart shows the faction of atoms with top 5% non-affine squared displacement (D^2_{min}) upon athermal quasistatic shear of the simulation box to a global strain of 5%. All the atoms of Zr in each sample are sorted based on LFFS_i into bins each containing 10% of all the Zr atoms.

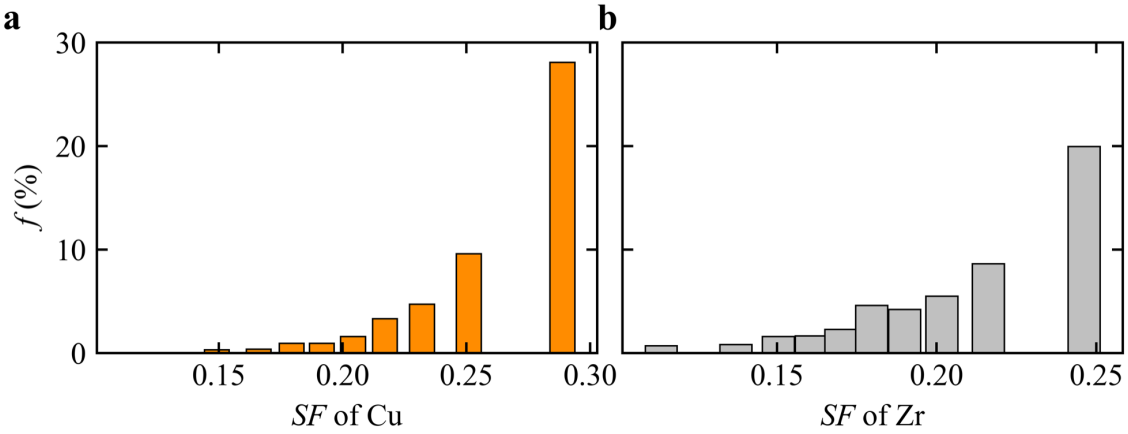

Figure 4.26: Strong correlation between structural flexibility (SF_i) and intrinsic plastic susceptibility for Cu (a) and Zr (b) in $Cu_{50}Zr_{50}$ metallic glasses (MGs) containing 31,250 atoms and quenched at cooling rate of 1×10^9 K/s. To reflect sample's intrinsic plastic susceptibility, here non-affine squared displacement (D^2_{min}) was averaged over 4,320 different loading conditions (3 deformation forms [uniaxial tension/compression, simple shear, pure shear] $\times$ 6 strain rate [4×10^6, 1×10^7, 4×10^7, 1×10^8, 4×10^8 and 1×10^9 s-1] $\times$ 40 temperatures [10, 20, 30, ..., 400 K] $\times$ 6 loading directions). D^2_{min} under each loading condition was normalized, via $[D^2_{\text{min}} - \min(D^2_{\text{min}})] \,/\, [\max(D^2_{\text{min}}) - \min(D^2_{\text{min}})]$, into the range between 0 and 1 before averaging. The bar charts show the distribution of atoms with top 5% D^2_{min} upon athermal quasistatic shear of the simulation box to a global strain of 5%. The vertical axis gives their fraction out of the total number of atoms in each bin. All the atoms of Cu (Zr) in the sample are sorted based on SF_i into bins each containing 10% of all the Cu (Zr) atoms.

4.3.6 Structural flexibility as an order parameter to monitor plastic flow in MGs

Four decades ago, Spaepen [26] developed strain rate equations to describe how deformation parameters (stress, temperature, etc.) affect the plastic flow behavior of MGs, employing free volume as the order parameter. However, as

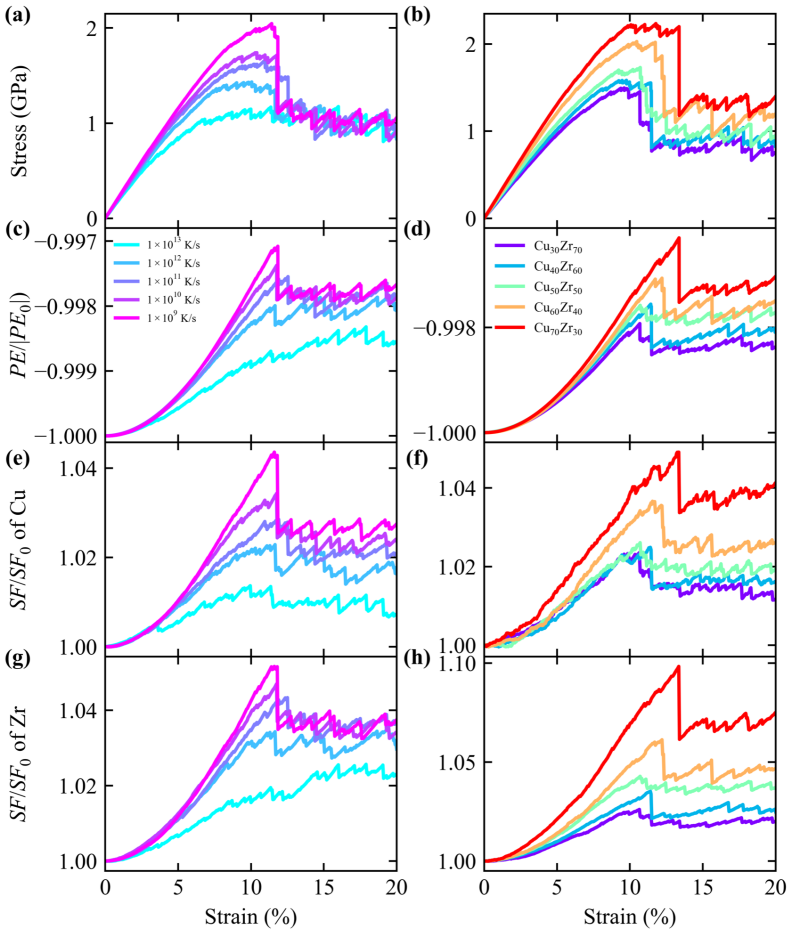

Figure 4.27: Evolution of stress (a and b), potential energy (*PE*) (c and d) and system-averaged *SF* of Cu (e and f) and Zr (g and h) with strain. The corresponding values at strain = 0, before athermal quasi-static shear (AQS), are used as the reference. Left column is for $Cu_{50}Zr_{50}$ MGs each containing 31,250 atoms and quenched over a range of cooling rates from 1×10^9 to 1×10^{13} K/s. Right column is for Cu_xZr_{100-x} MGs each containing 32,000 atoms and quenched at same effective cooling rate of 1×10^{10} K/s.

pointed out by Shi *et. al.* [17,18] and Egami [179], free volume cannot be unambiguously defined for MGs, which are not hard sphere systems. Free volume is also not sensitive to specific atomic scale structures or the thermomechanical history of MGs. It is therefore desirable not to depend solely on the concept

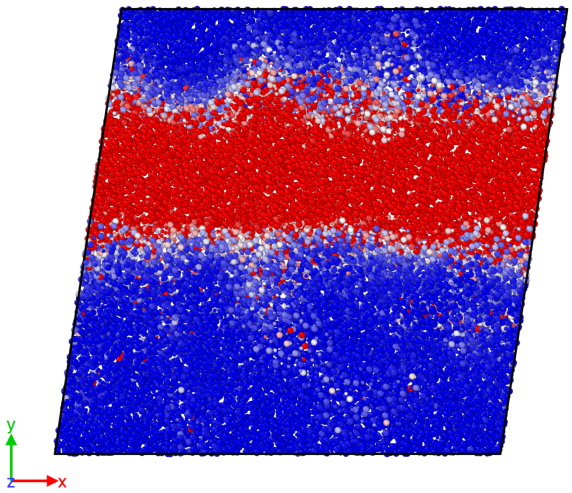

Figure 4.28: The projection of spatial distribution of $D^2_{\min}$ on xy plane when the $Cu_{50}Zr_{50}$ MG (containing 31,250 atoms and quenched at 1×10^9 K/s) was strained to 15% under athermal quasistatic shear (AQS) along +xy direction.

of free volume to model plastic flow for MGs. In the preceding section, we have demonstrated that the machine-learned microscopic structural parameter, *SF*, strongly correlates with local plastic susceptibility in MGs. It is natural to ask if the evolution of *SF* during deformation can be used to predict the change of flow stress with increasing strain. We deformed the system using AQS on Cu-Zr MGs with various compositions and processing histories along the +xy direction and monitored the evolution of stress, potential energy (*PE*) and system-averaged *SF* of both Cu and Zr atoms with strain. Fig. 4.27 confirms that the change of system-averaged *SF* correlates closely with both the flow stress and *PE* during deformation (note that volume is constant during AQS). Fig. 4.28 shows the distribution of $D^2_{\min}$ when a $Cu_{50}Zr_{50}$ MG (quenched

at cooling rate of 1×10^9 K/s) was strained to

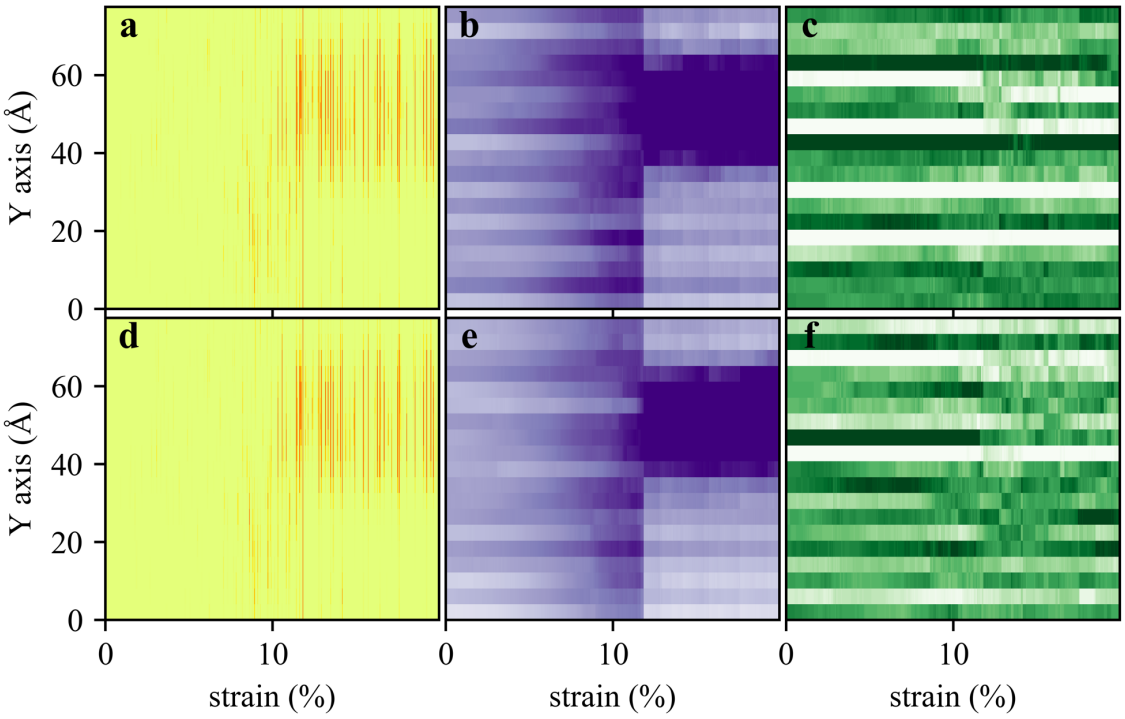

Figure 4.29: Evolution of $D^2_{\min}$ (left panel), structural flexibility (*SF*) (middle panel), and the number of atoms (*N*) (right panel) of Cu atoms along with straining in a $Cu_{50}Zr_{50}$ MG. The Y axis in these three panels represent these three quantities, respective. Here $D^2_{\min}$ was calculated using two snapshots, the current one and another reference one taken at a strain 0.05% earlier. The box contained 31,250 atoms, quenched at a cooling rate of 1×10^9 K/s. The $D^2_{\min}$, *SF* and *N* are each averaged within a layer: the sample was divided into 20 layers with equal thickness of ~ 4 Å parallel to the shear band (or xz) plane. They are monitored as a function of increasing strain, upon AQS on the sample along +xy direction. Red (yellow) corresponds to large (small) $D^2_{\min}$; dark (light) purple corresponds to large (small) *SF*; dark (light) green corresponds to large (small) atom number.

15%. To check if the change of *SF* could reflect the structural disordering in the region of shear localization(shear band), we divided the sample into 20 layers with equal thickness of ~ 4 Å parallel to the shear band plane (xz plane) and

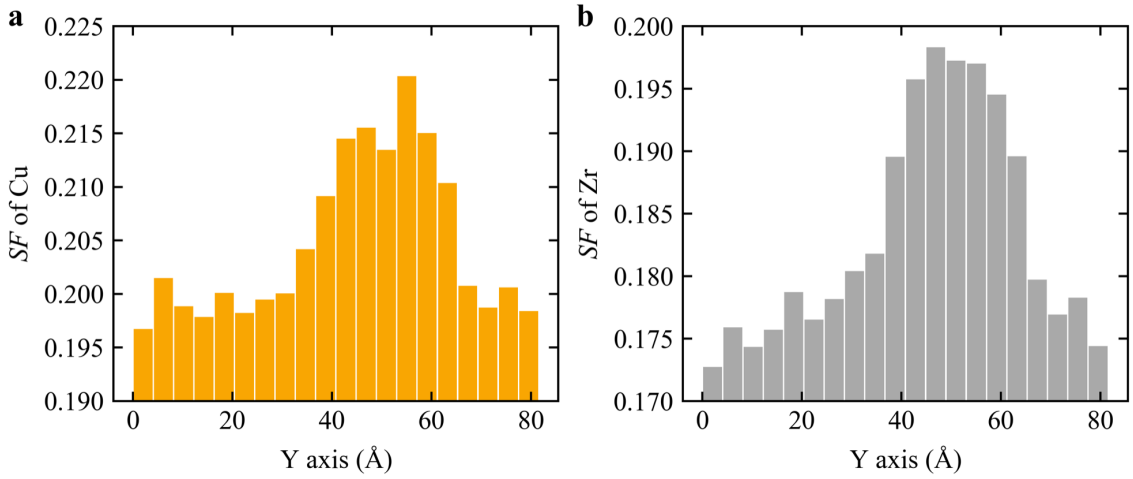

Figure 4.30: The distribution of the structural flexibility (*SF*) of Cu (left) and Zr (right) atoms, along Y axis (the direction perpendicular to shear band)), when the sample was strained to 15%. The *SF* is the average *SF* within each layer after the sample was divided into 20 layers with equal thickness of ~ 4 Å parallel to the shear band (or xz) plane.

monitored the evolution of the average $D^2_{\min}$, *SF*, and the number of atoms (*N*), which scales with the packing density and free volume content, within each layer as they change due to strain. As can be seen from Fig. 4.29, when a single shear band forms at $\sim$12% strain, both $D^2_{\min}$ and *SF* in all layers show a sudden change, and later deformation is mainly concentrated within the single shear band. The *SF* in the band is much higher than other regions. In contrast, the change of *N* in each layer seems random. As a specific example, Fig. 4.30a and b show the pronounced contrast of *SF* in and outside shear band when the sample was strained to 15%. These suggest that *SF* can serve as an order parameter to monitor the structural evolution upon straining and may possibly be incorporated into the formulation of plastic flow in MGs. In this regime, the

SF is actually a more sensible parameter to use than v_{flex} to monitor the degree of structural flexibility of atoms. This is because, after global yielding most of the atoms are involved in the flow and the MSD rises drastically along with straining, reflecting both atomic vibration and also contributions from shear-transformation assisted atomic diffusion. In contrast, *SF* is a simple quantity that requires only static structural information to calculate once an optimum ω is in hand.

4.3.7 Correlating structural flexibility with thermally activated relaxation events

Since v_{flex} is known to have a good correlation with the activation energy barrier, ΔE, for thermally activated β processes including relaxation [78], which are related to glass transition, aging, atomic hopping and other important properties in MGs, we also expect a strong correlation between *SF* and ΔE. We searched 30 relaxation events centered at each Cu (or Zr) atom in a $Cu_{50}Zr_{50}$ MG (31,250 atoms and quenched at 1×10^9 K/s) using the activation-relaxation technique (ART nouveau) [20, 103, 104] (see details in Methods, section 4.5.5). We then compared the distribution of ΔE of these events with the atoms exhibiting the highest and the lowest 10% of values of SF_i. As seen in Fig. 4.31a (Fig. 4.32a), there is a marked difference in average ΔE between the two groups, 0.42 (0.26) eV. In contrast, the distributions for atoms with the high-

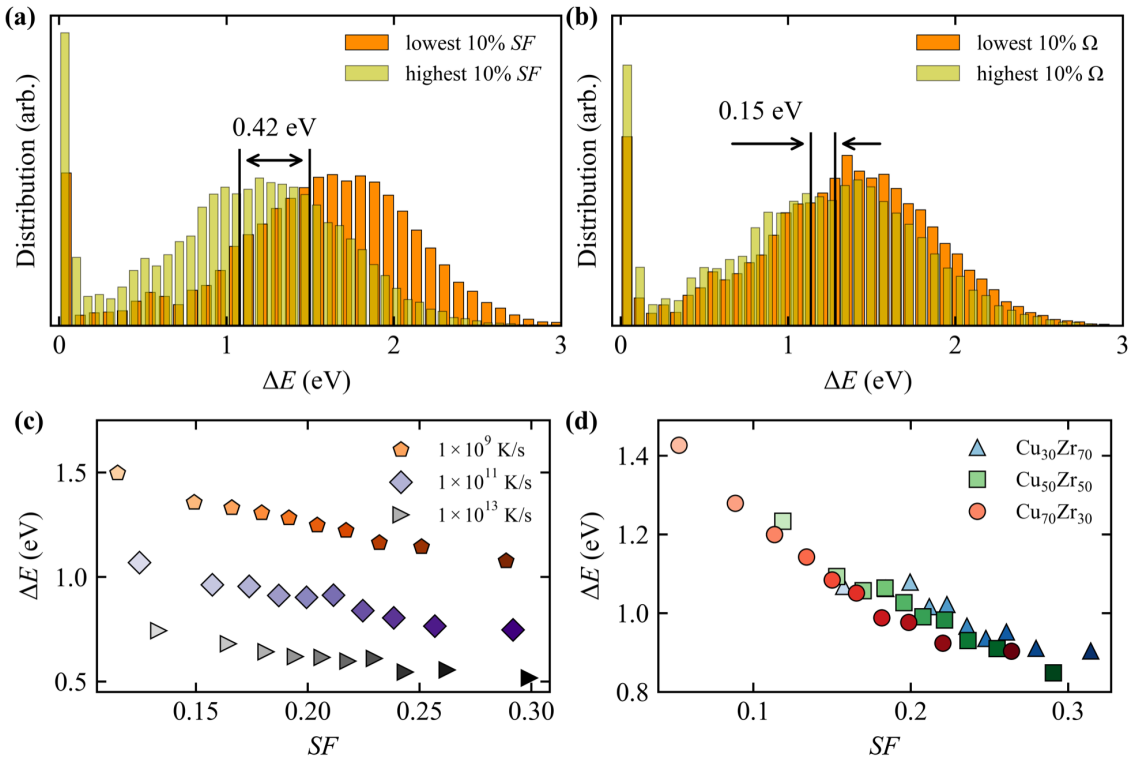

Figure 4.31: Correlation between structural flexibility and thermally activated relaxation events for Cu atoms. Distribution of thermal activation energy (ΔE) of Cu atoms in a $Cu_{50}Zr_{50}$ MG (31,250 atoms and quenched at cooling rate of 1×10^9 K/s) characterized using ART nouveau. (a) Shows the two groups with the highest and lowest 10% of structural flexibility (SF_i), and (b) is for the two groups with the highest and lowest 10% of the values for the atomic volume ($\Omega_{a,i}$). The difference in average ΔE between the two groups in the case of SF_i is 0.42 eV, much larger than 0.15 eV in the case of $\Omega_{a,i}$. In (c) and (d), all the Cu atoms in each composition or cooling rate are sorted based on SF_i, into bins each containing 10% of the atoms. An average activation energy is then calculated for the atoms in each bin, and plotted to demonstrate the correlation with structural flexibility. In (c), all samples are $Cu_{50}Zr_{50}$ MGs and the data for cooling rates of 1×10^{11} and 1×10^{13} K/s are from 5 samples each containing 2000 atoms while data for cooling rate of 1×10^9 K/s is from one sample containing 31,250 atoms. In (d), all samples are quenched at same effective cooling rate of 1×10^{10} K/s and the data for each composition are from 5 samples each containing 2000 atoms.

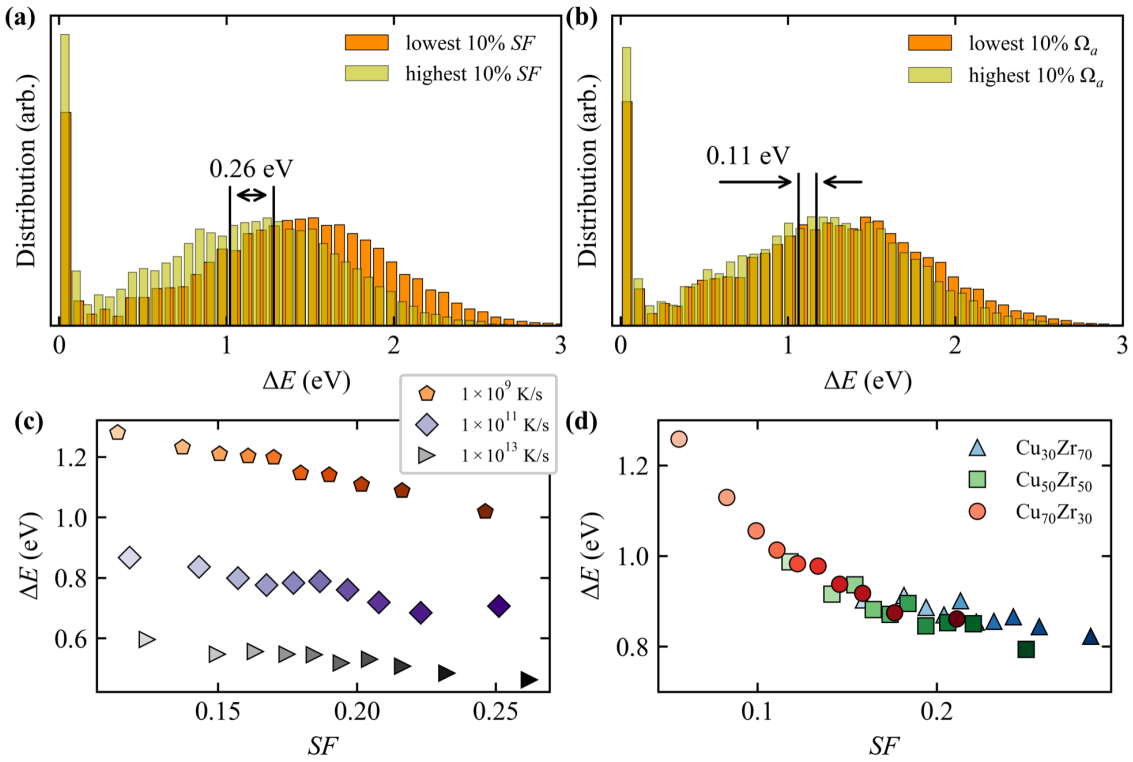

Figure 4.32: Correlation between structural flexibility and thermally activated relaxation events for Zr atoms. Distribution of thermally activation energy (ΔE) of Zr atoms in a $Cu_{50}Zr_{50}$ MG (31,250 atoms and quenched at cooling rate of 1×10^9 K/s) characterized using ART nouveau. (a) Shows the two groups with the highest and lowest 10% of structural flexibility (SF_i), and (b) is for the two groups with the highest and lowest 10% of the values for the atomic volume ($\Omega_{a,i}$). The difference in average ΔE between the two groups in the case of SF_i is 0.26 eV, much larger than 0.11 eV in the case of $\Omega_{a,i}$. In (c) and (d), all the Zr atoms in each composition or cooling rate are sorted based on SF_i, into bins each containing 10% of the atoms. An average activation energy is then calculated for the atoms in each bin, and plotted to demonstrate the correlation with structural flexibility. In (c), all samples are $Cu_{50}Zr_{50}$ MGs and the data for cooling rates of 1×10^{11} and 1×10^{13} K/s are from 5 samples each containing 2000 atoms while data for cooling rate of 1×10^9 K/s is from one sample containing 31,250 atoms. In (d), all samples are quenched at same effective cooling rate of 1×10^{10} K/s and the data for each composition are from 5 samples each containing 2000 atoms.

est and the lowest 10% $\Omega_{a,i}$ almost overlap with each other, and the difference in average ΔE is much smaller, as shown in Fig. 4.31b (Fig. 4.32b). We also sorted Cu (Zr) atoms in Cu-Zr MGs with various cooling rates or compositions based on SF_i into bins each containing 10% of these atoms and calculated the average ΔE for each bin. All these samples show a clear correlation that the higher the group-average SF, the lower its average ΔE, as show in Fig. 4.31c and d (Fig. 4.32c and d).

In addition, fictive/effective temperature (T_f) is another way to represent the average structural state of glassy materials [56, 57, 59]. Previously, Liu *et. al.* [59] showed that for MGs at a fixed composition, the system-average ΔE changes monotonically with cooling rate and thus correlates with T_f. Such a trend is also seen for our $Cu_{50}Zr_{50}$, as shown in Fig. 4.33a, but absent for different compositions (Fig. 4.33b). Thus, a correlation between the system-average SF and T_f is expected. This is indeed observed, as shown in Fig. 4.11g and h (Fig. 4.12g and h).

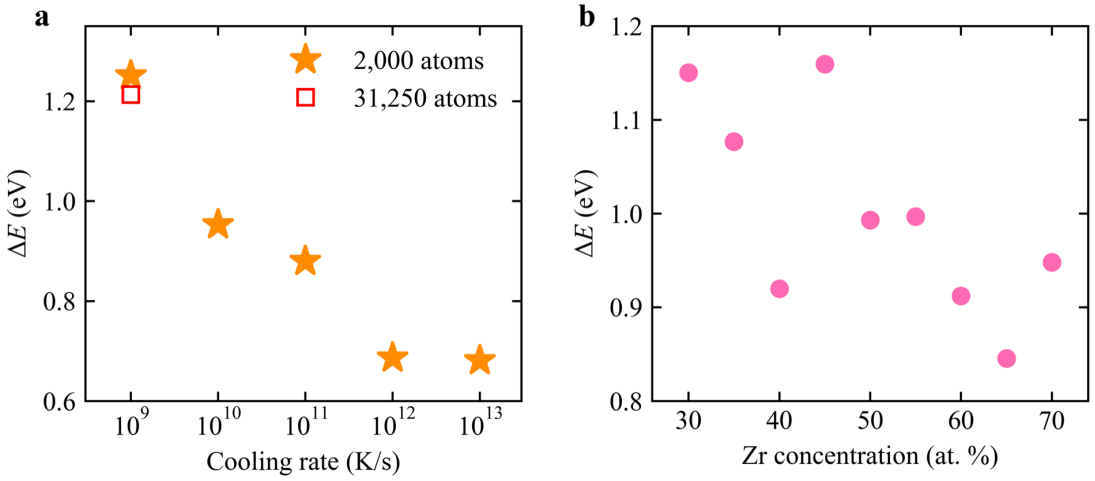

Figure 4.33: System-averaged thermal activation energy (ΔE) as a function of effective cooling rate (left, at the composition of $Cu_{50}Zr_{50}$), and of Zr composition (right, all prepared at an effect cooling rate of 1×10^{10} K/s). 30 relaxation events were searched for each atom.

4.4 Summary

Our results above contribute several advances over previous efforts to establish structure-property relations in MGs, including recent attempts employing ML. To probe into the structural origin of MG behavior, we have taken the perspective that the (local) properties should be controlled by a more property-oriented and flexibility-centric "structure" that combines comprehensive structural attributes including where and how the surrounding atoms are distributed spatially, their (short-to-medium-range) interactions, and the dynamic "wiggle room" indicative of the collective agitation of the (local) atomic configuration. Our approach is to absorb these into a single simple structural quantity. We

did so with *SF*.

This SF_i quantity is still based on x_i, the atomic coordinates across several neighboring shells embedded in the partial radial (atomic) density distributions. In other words, our approach allows the "structure" in the structure-property relations to be assessed from the static packing environment, x_i. Because x_i is too complicated to be permit quantifiable correlation with properties, this initial structural input is translated/converted into a single scale SF_i, which is informed by how responsive the atomic configuration would be upon excitation. Here through ML we have taken advantage of our recently established atomic $v_{flex,i}$ as the supervisory signal. In doing so, we have used ML regression to link the complex local radial density distribution (x_i) and flexibility. This direct linear regression gives us an optimized ω with high Pearson correlation coefficient. The *SF* combining the (x_i, ω) information is a structural metric of each atom's flexibility, beyond the previous classification approach defining "softness" (or "quench-in softness") as the distance to the separation plane in hyperspace [165] (or estimate of class probability [68]).

A single simple quantity, the resultant *SF* is shown to be indeed indicative of "structure" in terms of its behavior, i.e. its degree of responsiveness. Strong correlations with a variety of microscopic and macroscopic properties have been systematically demonstrated, particularly those not involved in the ML training process, including both stress-driven and thermally activated re-

laxation events. That is, we have achieved a wider range of utility with just one ML model, enabling the correlation of *SF* with at least five different properties. Finally, the same weighting function represented by the vector ω in multi-dimensional space is found to be applicable for Cu-Zr MGs with different compositions and processing histories. The same machine-learned bridge remains effective as the avenue to various correlations throughout a MG alloy system. The *SF* can then be evaluated from purely structural information only, requiring no further learning or re-learning when the structure changes upon processing or deformation. This is therefore a useful step towards structure-property relations with minimized non-structural input (note that the latter can be either impossible to acquire, or computationally too expensive). Taken together these investigations have provided a convincing bridge between the structure revealed by the local PDF and all of the key properties investigated here. For instance, one can now use the magnitude of *SF* to gauge whether the changes induced in the static structure via processing would improve the MG towards desired properties such as higher plasticity.

4.5 Methods

4.5.1 Sample preparation

Binary Cu_xZr_{100-x} MG models with different sample sizes at different compositions were constructed through classical molecular dynamic (MD) simulation [180], with an optimized embedded atom method (EAM) potential, adopted from Ref. [141], as implemented in LAMMPS [140]. The largest time step used in this study is 2 fs. After adequate equilibration at 2500 K, the liquids of those samples were quenched to 50 K under conditions of constant zero pressure and steadily varying temperature using a Nose-Hoover thermostat. Periodic boundary condition were applied in all three directions. In this work, to save computation time, some samples were first quenched to 1500 K at a rate of 1×10^{13} K/s, followed by 1×10^{12} K/s to 1000 K, then at the desired rate (effective cooling rate, in the text) to 500 K, and finally at 1×10^{13} to 50 K. This cooling schedule was verified not to cause noticeable difference in properties. All samples were equilibrated for 2 ns at 50 K before calculations of various properties. All atomic coordinates used in structure analysis are extracted from inherent structures obtained via energy minimization with a conjugate gradient (CG) algorithm. Voronoi tessellation analysis [141] was employed to obtain atomic volume, and global shear modulus G was calculated using the fluctuation method [181].

4.5.2 Calculation of vibrational MSD

Each sample was kept in equilibrium under a microcanonical ensemble (NVE) at 50 K to calculate the vibrational MSD. The MSD of atom i is defined as $\langle (x_i(t) - \bar{x}_i)^2 \rangle$, where $\bar{x}_i$ is the equilibrium position of atom i. The MSD was computed on short time scales when the MSD is flat with time, and contains the vibrational but not the diffusional contribution. To reduce the influence from thermal fluctuation, the calculated MSD was averaged over 100 independent runs, all starting from the same configuration but with momenta assigned randomly from the appropriate Maxwell-Boltzmann distribution [101, 182].

4.5.3 Machine learning

In all ML tasks, we treat Cu and Zr separately as two species having different favorite local packings [23]. Both classification and regression were performed and executed in the LIBLINEAR package [170]. In the classification task that separates out atoms with extremely small $v_{flex,i}$ from other atoms in $Cu_{50}Zr_{50}$ MGs, the training and testing data sets were selected from Cu (Zr) atoms with the lowest 0.36% (0.18%) $v_{flex,i}$ in 150 $Cu_{50}Zr_{50}$ MGs, each containing 32,000 atoms and quenched at an effective cooling rate of 1×10^{10} K/s. These inflexible atoms were labeled as $y_i = -1$. The same number of Cu (Zr) atoms randomly selected from the remaining atoms were labeled as $y_i = +1$. The ratio of in-

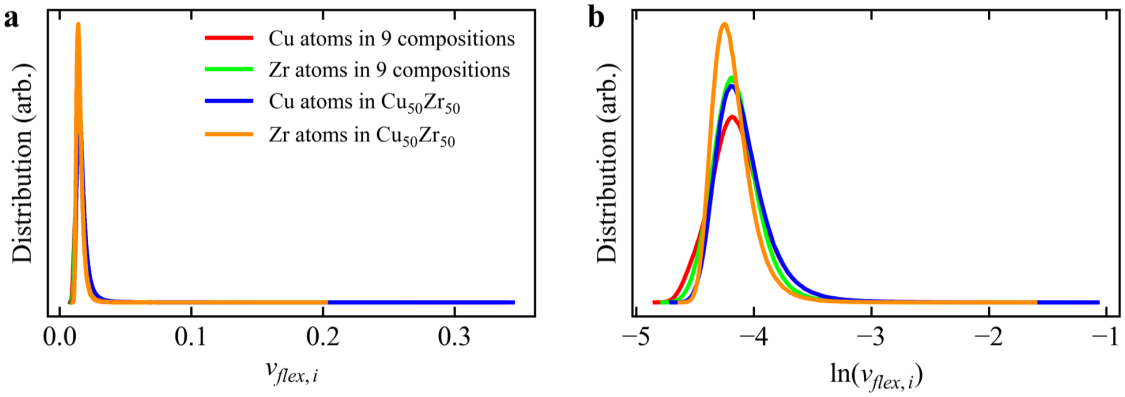

Figure 4.34: The distribution of $v_{flex,i}$ (a) and $\ln(v_{flex,i})$ (b) of both Cu and Zr atoms in Cu-Zr MGs. Data for 9 compositions are from 9 different Cu_xZr_{100-x} MGs (x = 30, 35, ..., 70) each containing 500,000 atoms and quenched at an effective cooling rate of 1×10^{10} K/s. Data for $Cu_{50}Zr_{50}$ MGs are from 150 samples each containing 32,000 atoms and quenched at an effective cooling rate of 1×10^{10} K/s.

stance number, of training set to testing set, is 4:1.

For the regression task, two different types of datasets were used. The first type contained a total of 1.35 million Cu (or Zr) atoms, i.e., 150,000 Cu (or Zr) atoms from each of 9 Cu_xZr_{100-x} samples (x = 30, 35, ..., 70, in step of 5). The nine MGs each contained 500,000 atoms and were quenched at an effective cooling rate of 1×10^{10} K/s. The second type used a single composition, and all Cu (Zr) atoms in the sample (each totaling 500,000 atoms) were used to construct the corresponding training and testing data sets at that composition. In addition, one very large dataset for $Cu_{50}Zr_{50}$ was constructed, using all Cu (Zr) atoms in 150 $Cu_{50}Zr_{50}$ MGs (each containing 32,000 atoms and quenched at an effective cooling rate of 1×10^{10} K/s). The purpose of these various training sets was to confirm that the models trained on those smaller data sets are all

reliable, and the ML model trained on this single composition has similar predictive power to that trained on the data set composed of atoms from 9 various compositions. The comparison confirmed that the ML model trained on this single composition can be transferred to other compositions in the same MG system. For all regression tasks, the ratio of instance number in training and testing data sets is 4:1. We used the natural logarithm of $v_{flex,i}$ as the target value in ML, i.e. $y_i = \ln(v_{flex,i})$, which is close to a normal distribution, as shown in Fig. 4.34b. This is because the distribution of $v_{flex,i}$ is rather heterogeneous, see the very long tail in Fig. 4.34a. To avoid high-bias or under-fitting, we carefully tuned the hyperparameters in ML models, including regularization parameters, sensitivity of the loss function, tolerance of the termination criterion, and both $\bar{r}_c$ and σ in Eq. 4.5, which are used to compute the input attributes ($G(\bar{r}_c)$).

4.5.4 Calculation of participation fraction in soft modes

The normal mode analysis of the glass was carried out by diagonalizing the dynamical matrix of the MG inherent structure obtained using the conjugate-gradient (CG) method. The participation fraction of atom i in eigenmode e_ω is defined by $p_i = |\vec{e}^{\,i}_\omega|^2$, where $\vec{e}^{\,i}_\omega$ is the corresponding polarization vector of atom i [142]. Here, p_i was summed over a small fraction of 1% (same as that in Ref. [54]) of the lowest-frequency normal modes and denoted as the participation

fraction p_i for atom i, which measures the involvement in soft modes for that atom.

4.5.5 Energy barrier of thermally activated events

The local potential energy landscape (PEL) was explored using ART nouveau [20,58,103,104]. For the local excitations, initial perturbations in ART were introduced by applying random displacement on a central atoms and its nearest-neighbors. The magnitude of the displacement was fixed at 0.5 $\mathrm{\AA}$, while the direction was randomly chosen. When the curvature of the PEL was found to be < -0.01 eV/$\mathrm{\AA}^2$, the system was pushed towards the saddle point using the Lanczos algorithm [183]. The saddle point is considered to be found when the overall force of the total system is below 0.05 eV/$\mathrm{\AA}$. The corresponding activation energy is computed as the difference between the saddle point energy and the initial state energy. For each central atom in each sample, 30 relaxation events were searched.

4.5.6 Calculation of the velocity auto-correlation function

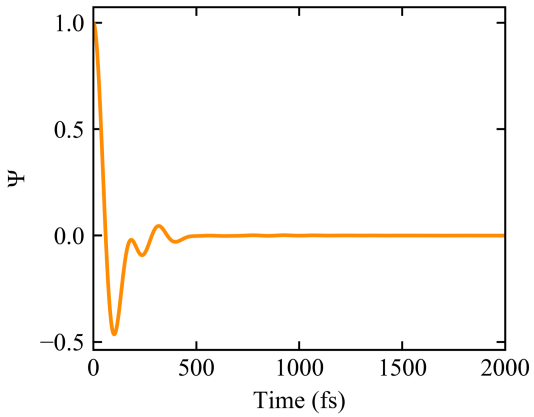

Figure 4.35: Velocity auto-correlation function Ψ at 50 K for the whole $Cu_{50}Zr_{50}$ MG sample containing 1,024,000 atoms and quenched at effective cooling rate of 1×10^{10} K/s.

The velocity auto-correlation function (VACF) describes the correlation of atomic motions in the time evolution of a system. This function is defined as [184]: $\Psi(t) = \langle \bar{v}_i(\tau + t) \cdot \bar{v}_i(t) \rangle / \langle \bar{v}_i(t) \cdot \bar{v}_i(t) \rangle$, where $\bar{v}_i(t)$ is the velocity of atom i, τ is the time origin, and the angular brackets represent the ensemble average. For the samples each containing ~30,000 atoms, the same initial configuration was assigned with 100 different initial velocity fields to reduce thermal noise. For the large sample containing 1,024,000 atoms, we assigned 60 different initial velocity fields to the same initial configurations to calculate VACF for the entire sample and each group of atoms. As an example, Fig. 4.35

shows the VACF at 50K of the whole $Cu_{50}Zr_{50}$ MG (containing 1,024,000 atoms and quenched at effective cooling rate of 1×10^{10} K/s).

4.5.7 Fictive temperature

The fictive temperature (T_f) was determined from the evolution of volume with temperature during heating at a constant rate of 1×10^{10} K/s. The fictive temperature is the temperature where the volume intersects the equilibrium liquid line when extrapolated along the glass line [56]. Fig. 4.36 shows an example.

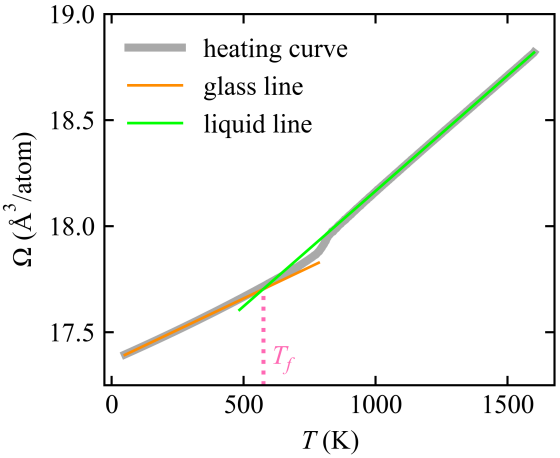

Figure 4.36: Volume as a function of temperature during heating at a constant rate of 1×10^{10} K/s for a $Cu_{50}Zr_{50}$ MG containing 31,250 atoms and quenched at a cooling rate of 1×10^{9} K/s. The fictive temperature (T_f) is the temperature where the equilibrium liquid line intersects the extrapolated glass line.

4.5.8 Calculation of local elastic moduli

Local moduli of MGs were evaluated at 50 K using the fluctuation method as described in detail in Ref. [60]. For a canonical (NVT) ensemble, the local

moduli can be calculated as the sum of three contributions, the fluctuation, kinetic contribution and the Born term, respectively. To reduce the statistical error in our simulated samples, the average local moduli were averaged over 20 different thermal initialization.

4.6 Appendix

4.6.1 Classification tasks

We also performed classification to separate Cu (or Zr) atoms with $v_{flex,i}$ smaller than 0.045 Å, i.e., the lowest 0.36% (or 0.18%) $v_{flex,i}$, from the remaining atoms in $Cu_{50}Zr_{50}$ MGs quenched at an effective cooling rate of 1×10^{10} K/s, using logistic regression (a linear ML classification algorithm). In this classification task, we achieved a testing accuracy of 98.39 % and 97.25 % for Cu and Zr atoms, respectively. This nearly perfect mark indicates a highly successful separation of atoms with the lowest $v_{flex,i}$ (inflexible) from other atoms. Incidentally, this is a feat difficult to achieve using $D^2\mathrm{min}$ as the supervisory signal [21, 68]. While atoms showing large $D^2\mathrm{min}$ are clearly flexible, a small $D^2\mathrm{min}$ seen under a particular loading condition does not necessarily mean the atom is inflexible. The values of $D^2\mathrm{min}$ under loading along different directions can be very different for the same atom in a given local configuration, so that one has to change the loading conditions numerous times, each being destructive to the sample,

making it excessively computationally expensive.

4.6.2 Comparing ML models trained on a single composition vs nine compositions

During ML regression, we first trained a ML model for each single composition and calculated ρ on both the training and testing data sets at each single composition between y_i and $\boldsymbol{\omega}^T \boldsymbol{x}_i$ using $\boldsymbol{\omega}$ trained for each single composition. These ρ were shown as purple circles (training) and stars (testing) in Figure 4.6. There is almost no difference between the purple circles (training) and purple stars (testing), suggesting no over-fitting issue.

We next obtained an optimized $\boldsymbol{\omega}$ for all compositions in the MG system using the data set (1.35 million atoms) composed of atoms from 9 compositions (see Methods, section 4.5.3). The ρ achieved on testing data set of each single composition using this $\boldsymbol{\omega}$ is shown using green squares in Fig. 4.6.

We observe in Fig. 4.6 that there is no visible difference between purple stars and green squares. Both of them were calculated on exactly the same testing data set for each composition, but with $\boldsymbol{\omega}$ from different datasets above. This consistency suggests that the $\boldsymbol{\omega}$ obtained from one composition has the same power as that trained on all the compositions in the Cu-Zr system, and vice versa, although they are not exactly equal in numerical values (this is because the set of scaling parameters used to normalize $\boldsymbol{x}_i$ before ML depends

on the specific training data set).

The next task is to check how much difference can be made to ω if a very large data set at a single composition is used. To answer this, another ω was obtained using a data set containing 2.4 million of Cu (or Zr) atoms from 150 $Cu_{50}Zr_{50}$ MGs (each with 32,000 atoms). The ρ obtained during testing is shown as the red pentagon in Fig. 4.6. It overlaps with the purple star at $Cu_{50}Zr_{50}$, indicating that 250,000 atoms (50% of the 500,000 atoms in $Cu_{50}Zr_{50}$ are Cu or Zr) already make a sufficiently large data set and increasing it to 2.4 million atoms makes no obvious difference. Using the ω trained on this large data set of $Cu_{50}Zr_{50}$, we re-evaluated the ρ values for testing data sets at each individual composition. The results are shown as orange triangles in Fig. 4.6. They fall almost exactly on green squares, suggesting that an ω trained on a single composition can be transferred to other compositions. This broad validity of ω implies that even at one composition the local environment is diverse enough to reflect most of the possibilities in this alloy system. Consequently ω computed at one cooling rate and composition is broadly valid at all cooling rates and compositions.

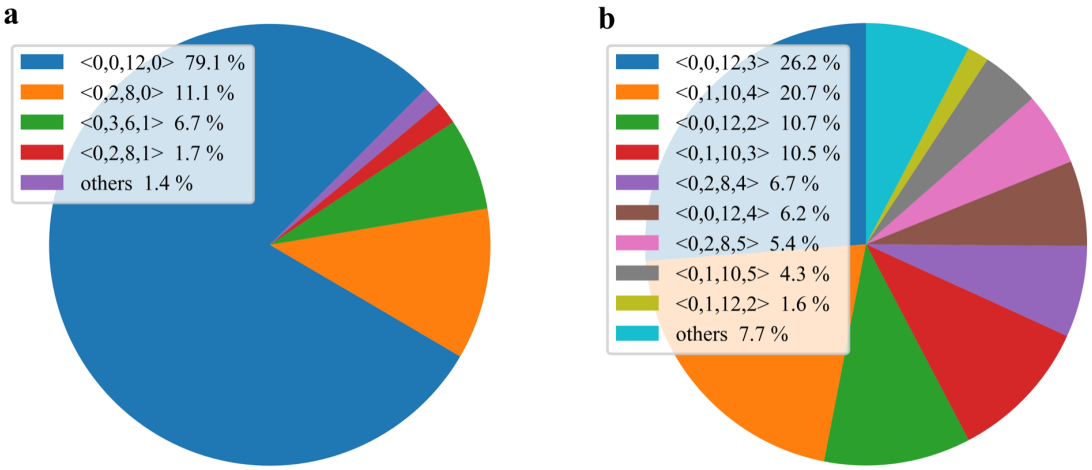

Figure 4.37: The fraction of Cu-centered or Zr-centered Voronoi polyhedra for Cu (a) or Zr atoms (b) that have the lowest 1% v_{flex} in a $Cu_{50}Zr_{50}$ MG containing 1,024,000 atoms and quenched at effective cooling rate of 1×10^{10} K/s.

4.6.3 Simple structural parameters show poor correlation with flexibility volume

To see if $v_{flex,i}$ is correlated with $\Omega_{a,i}$, the two quantities are plotted in Figure 4.7 and 4.8 for Cu and Zr atoms, respectively, using data from Cu-Zr MGs at different compositions and quenched at different cooling rates (see figure captions). The largest Pearson correlation coefficient ρ (the absolute value of ρ reflects the degree of correlation and a negative ρ means anti-correlation) between $\Omega_{a,i}$ and $\ln(v_{flex,i})$, is only 0.64 and 0.32 for Cu and Zr, respectively. The correlation between LFFS_i [61] and $\ln(v_{flex,i})$ is even worse, as shown in Figure 4.9 and 4.10. Ding *et. al.* [78] showed that v_{flex} has some correlation with local coordination polyhedra in a $Cu_{64}Zr_{36}$ MG. But we found that in the

$Cu_{50}Zr_{50}$ MG, even among the Cu atoms with the lowest 1% v_{flex}, only 79% are centers of full icosahedra $\langle 0, 0, 12, 0 \rangle$ and 21% of Cu atoms are the centers of other Voronoi polyhedra. For Zr atoms, there is no dominant type of Voronoi polyhedra at all for Zr atoms with the lowest 1% v_{flex}, as shown in Figure 4.37. It thus appears that Ω_a, LFFS, and local coordination polyhedra each reflects only a certain aspect of the local atomic packing relevant for v_{flex}. Their inadequacy is expected as they are all limited to the packing of atoms in the nearest-neighbor shell, and even for such SRO they are degenerate because different coordination polyhedra, usually with various degrees of distortion, can give the central atom the same Ω_a, LFFS, and Voronoi index.

4.6.4 Transferability to other MG alloys systems

To check if our ML models trained on Cu-Zr MG system can be transferred to other MG systems, we computed SF_i of Al atoms in a $Al_{90}Sm_{10}$ MG (simulated using a potential from Ref. [185], with 32,000 atoms and quenched at a cooling rate of 1×10^{10} K/s) using weighting vector $\boldsymbol{\omega}$ of Cu or Zr trained on Cu-Zr MG system, and then checked the faction of atoms with top 5% non-affine squared displacement ($D^2_{\min}$) upon athermal quasistatic shear of the simulation box to a global strain of 5% after all the Al atoms in the sample are sorted based on SF_i into bins each containing 10% of the atoms. Unfortunately, as shown in Fig. 4.38, no correlation stands out between SF_i and $D^2_{\min}$ for the $Al_{90}Sm_{10}$ MG,

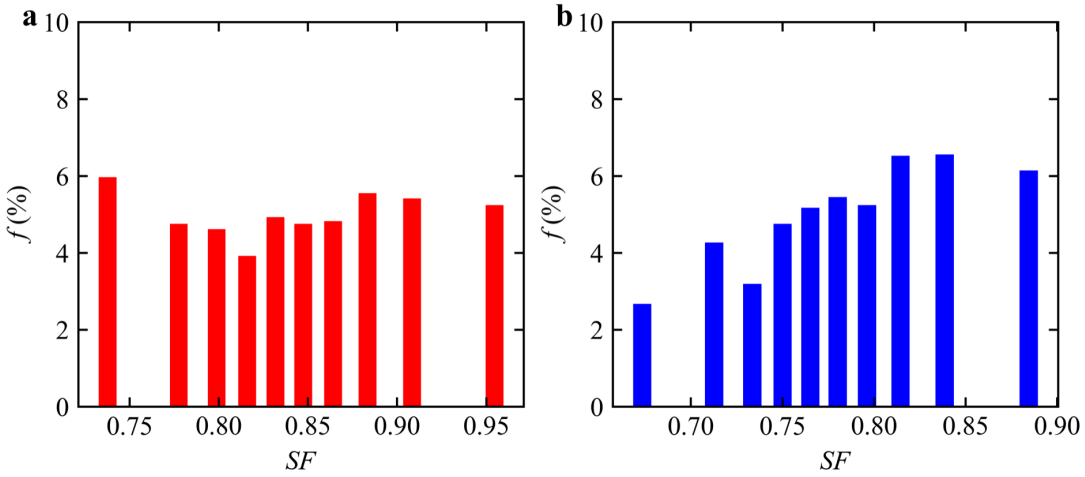

Figure 4.38: Transferability to other MG alloys systems. The bar charts show the faction of atoms with top 5% non-affine squared displacement (D^2_{min}) upon athermal quasistatic shear of the simulation box to a global strain of 5%. All the Al atoms in the sample are sorted based on SF_i, which is obtained using weighting vector ω of Cu (a) or Zr (b) trained on Cu-Zr MG system, into bins each containing 10% of the atoms.

suggesting that the ML models trained on one MG system are not generally applicable to other alloy systems.

Chapter 5

Predicting orientation-dependent plastic susceptibility from static structure in amorphous solids via deep learning

5.1 Introduction

The mechanical response of a crystalline metal to applied stresses can be quantitatively explained by monitoring the evolution of dislocations [2, 186] in the lattice. In stark contrast, amorphous metals do not have such well-defined structural defects, owing to the absence of long-range atomic packing order. As a result, in the static structure of a glass, it remains a grand challenge to identify *a priori* local "defects" that are vulnerable to rearrangements, even when the positions of all atoms are fully known [23, 24, 28, 30, 34]. Over the years, a number of physical parameters have been used to serve as indicators [17–19,26,27,31,45,50,52–55,58,59,61–63,77–79] to forecast local regions as fertile sites for shear transformations. Data-driven models [21, 68, 69, 80] have been put forward as well for the same goal. However, all these attempts have only achieved moderate success: the correlations with the plastic susceptibility of particles/atoms have not been sufficiently strong to predict structure-property relations in glassy solids.

A critical reason for this status quo is that the scalar or rotation-invariant quantities invoked so far are inherently inadequate in capturing the anisotropic response of a local configuration. A given local environment of an atom (particle) can respond quite differently when the externally applied global force is imposed along different orientations [16, 71–73]. Recently, additional

indicators have been invoked to take into account anisotropy in predicting the propensity for plastic activity in two-dimensional (2D) model glasses [71–73]. But it remains unclear how well these new indicators fare in three-dimensional (3D) amorphous solids. Furthermore, these indicators are physical quantities that need to be evaluated with known interparticle interactions, and are hence not based solely on structural information (atomic positions) *per se*.

Recently, deep convolutional neural networks (CNN) have enabled revolutionary breakthroughs in the field of computer vision and pattern recognition [75, 187–189]. Inspired by such successes, here we explore the potential of this deep learning approach via a conversion of local configurations into images. More importantly, we also devise a rotation-variant structure representation, to capture the anisotropic responses of a local configuration and the intrinsic sensitivity to the loading orientation. We will demonstrate that this combination achieves unprecedented accuracy when it is used to separate out particles with high plastic susceptibility from the rest in the sample, unveiling the power of local static structure for predicting orientation-dependent plastic events in both 2D and 3D glasses.

5.2 Atomic structure representation and model architecture

We have developed CNN models in both a 2D binary Lennard-Jones (L-J) glass system [190] and a 3D binary embedded-atom-method (EAM)-based Cu-Zr metallic glass system [141]. To represent the local packing environment of each particle i, we use a new multi-dimensional structural function, termed a Gaussian-weighted spatial density map (SDM). For the 2D model, the SDM of each particle i is defined as

$$\Xi\left(y,x,\beta\right)=\sum\exp\left(-\frac{\left(r_{ij,x}-x\right)^{2}+\left(r_{ij,y}-y\right)^{2}}{2\Delta^{2}}\right), \tag{5.1}$$

where the summation is performed over all particles satisfying these conditions: $\text{species}\left(j\right)\in\beta;\left|r_{ij,x}\right|<r_{c}$ and $\left|r_{ij,y}\right|<r_{c}$, $r_{ij,x}$ and $r_{ij,y}$ are the components along x and y dimensions, respectively, of $\boldsymbol{r}_{ij}$, which is the vector connecting the central particle i with particle j of species β within a cutoff r_c. Particle j may be the central particle when the species of the central particle is that under consideration in the channel. Here $x,y\in[-r_{c}+0.5\Delta,r_{c}-0.5\Delta]$ with an increment of Δ (Δ is a constant), and $\beta\in\{0,1\}$, where 0 represents small (*S*) particles, and 1 large (*L*) ones. We set $r_{c}=5\sigma$ and $\Delta=0.2\sigma$ after trials using many different values (σ is the characteristic length scale parameter in the

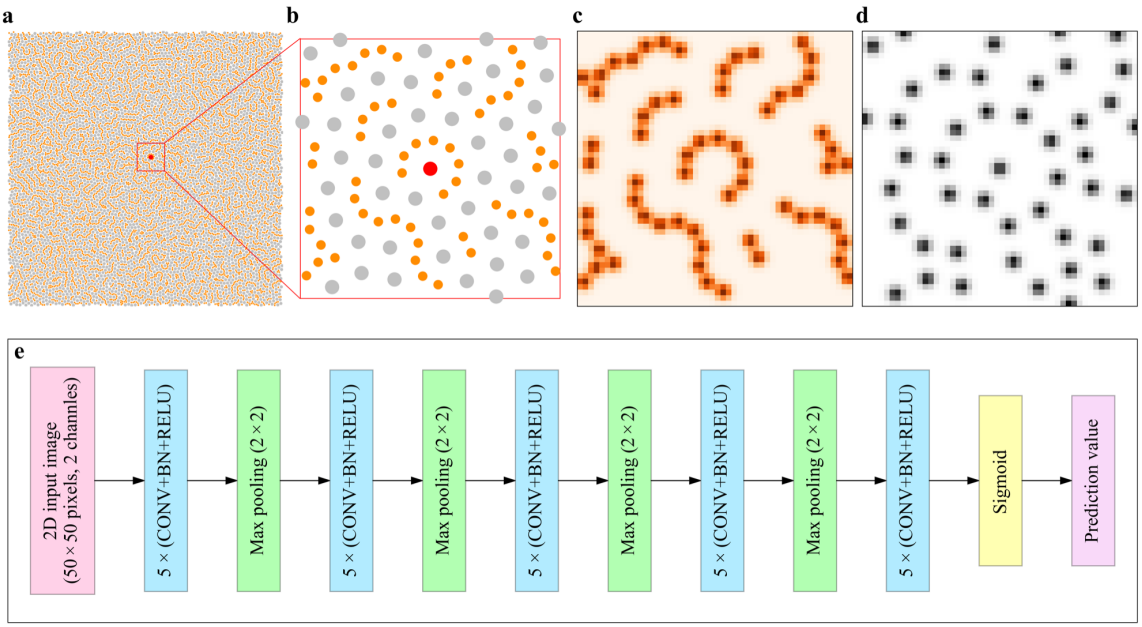

Figure 5.1: Atomic structure representation and model architecture for 2D glasses. (a) Snapshot of a 2D model glass. Orange and silver circles represent small (S) and large (L) particles, respectively. (b) A close-up showing a local configuration around the red particle in (a). (c) and (d) Corresponding spatial density map (SDM) of the S and L particles, respectively. (e) Architecture of the convolutional neural network (CNN) model used for 2D glasses, which contains 25 (5 in each blue box) 2D convolutional (conv.) layers. A 2D max-pooling layer is periodically inserted in-between the successive conv. layers. The last conv. layer is followed by the output layer which is a sigmoid neuron. The corresponding architecture of the CNN model for our 3D model glasses is shown in Fig. 5.2.

potential, see details in Methods, section 5.7.1).

Similarly, for 3D glass systems, the SDM of each atom i is defined as

$$\Xi\left(z,y,x,\beta\right)=\sum\exp\left(-\frac{\left(r_{ij,x}-x\right)^{2}+\left(r_{ij,y}-y\right)^{2}+\left(r_{ij,z}-z\right)^{2}}{2\Delta^{2}}\right), \tag{5.2}$$

here the summation is performed over all particles satisfying these conditions:

species $(j) \in \beta; |r_{ij,x}| < r_c; |r_{ij,y}| < r_c$ and $|r_{ij,z}| < r_c$, and $\beta = 0$ or 1, to represent

Zr and Cu atoms, respectively. Using SDM to represent local configurations can be viewed as projecting the local configurations to 2D (or 3D) grids for different species, which results in a multi-dimensional numerical array, equivalent to a 2D (or 3D) image containing $(2r_c/\Delta)^2$ (or $(2r_c/\Delta)^3$) pixels. Each pixel has channels equal to the number of components in the sample. These images can be used directly as input into the CNN model. For an adequately large r_c, a sufficient number of surrounding particles would be included. And, when Δ is small enough, any tiny variation of particle positions in the local configuration would lead to a corresponding variation in SDM. Therefore, the SDM can faithfully and accurately represent the topological structure feature of a local configuration. In addition, the contribution to the SDM from different species are separated into different channels, taking into account the influence arising from chemical affinity. Fig. 5.1a shows a typical 2D model glass, with a close-up view (a local configuration) in Fig. 5.1b. The SDM of S and L particles corresponding to Fig. 5.1b are shown in Fig. 5.1c and d, respectively, where each image contains 50 $\times$ 50 pixels. The pixels with high intensity (darker color) correspond to the locations of particles. Obviously, the SDM will be different when the local configuration is rotated. In other words, SDM is rotation-variant, which is the key feature we need for predicting orientation-dependent plastic events in amorphous solids.

We then applied the CNN method [75] to each input image to predict the

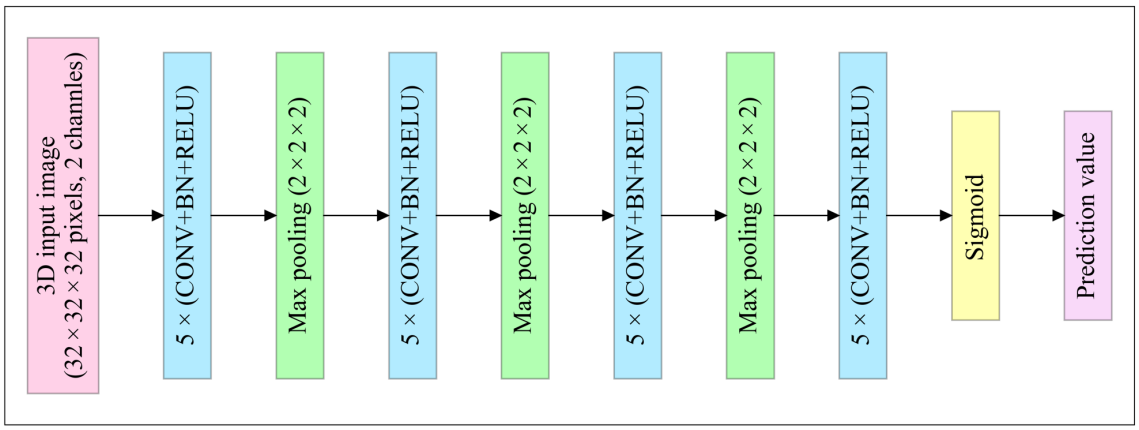

Figure 5.2: The CNN architecture for 3D glasses. The convolutional neural network (CNN) model for the 3D model glasses contains 20 3D convolutional (conv.) layers. A 3D max-pooling layer (green box) is inserted after every 5 conv. layers. The last conv. layer is followed by the output layer which is a sigmoid neuron.

propensity of each particle to experience plastic rearrangement, at different global shear strains when the sample is loaded along a specific orientation. Figure 5.1e illustrates the architecture of the CNN model for the 2D glasses. Specifically, each CNN model contained 25 convolutional (conv.) layers, where filters with a small receptive field of 3 $\times$ 3 were used. Zero-padding was involved in all but the fifth and last conv. layers. Batch normalization (BN) [191] was adopted right after each convolution and before activation with the rectification (ReLU) non-linearity [187]. A max-pooling layer is periodically inserted in-between the 25 successive conv. layers. Max-pooling is performed over a 2 $\times$ 2 pixel window, with a stride of 2. The number of filters is 20 in the first five conv. layers and then doubled after each max-pooling layer. And the last conv. layer is directly followed by the output layer, which is a sigmoid neuron as we

are performing binary classification tasks.

For 3D glasses, $r_c = 9.6\text{Å}$ and $\Delta = 0.6\text{Å}$ were found to produce optimized results (see more detail in Appendix, section 5.8.2, and the resultant input images contain $32 \times 32 \times 32$ pixels. The corresponding CNN model contains 20 conv. layers and 3 max-pooling layers, and both convolution and max-pooling were performed in 3D space (the architecture of the CNN for our 3D glasses is presented in Fig. 5.2). The number of filters in each 3D conv. layer was 60. To accelerate training and avoid shortage of memory, we did not double the filter number after max-pooling. This is not expected to influence significantly the training results, based on our experience with the 2D glasses for which doubling the filter number increased the validation accuracy by less than 1%.

5.3 Structural differences responsible for the anisotropy of local mechanical response

In the literature, most authors quote "free volume" as the structural feature controlling the (local) susceptibility to rearrangement in amorphous solids [26, 35]. However, as will be shown later in this work, no obvious correlation is found, between the susceptibility and local excess volume. There have also been recent observations that atoms with fewer neighboring particles in the nearest neighbor shell, but more in the troughs in between the shells, would

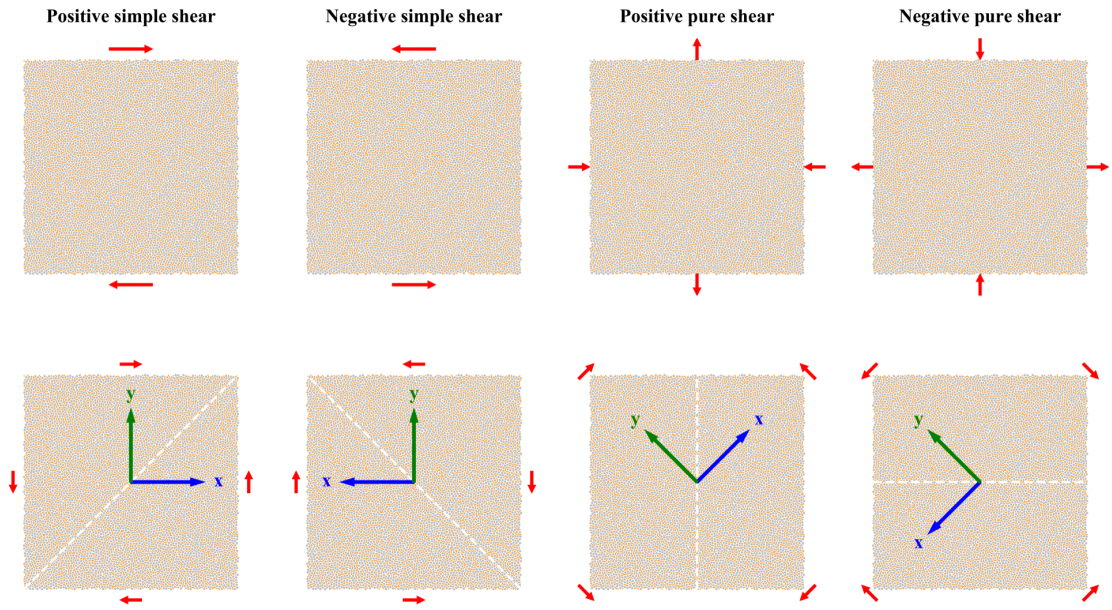

Figure 5.3: Deformation protocols for 2D model glasses. Upper panel: four different loading protocols in simulations; for each case the corresponding effective shear orientation is shown in the lower panel, with an appropriate coordinate system set up to compute the SDM. White dash line marks the macroscopic elongation direction.

be more flexible [21, 80]. However, this does not explain why the same local configuration responds differently to applied global force along different directions. Now that we have converted local configurations into images, let us first examine, from this perspective, if we could identify a critical structure feature responsible for the anisotropic mechanical response. To this end, we seek valuable insight by contrasting the SDMs of particles with extremely high plastic propensity (i.e., the tail end of the high-susceptibility side) versus those on the other end.

We first sheared 5,000 2D glass samples to a shear strain of 3.0% using the

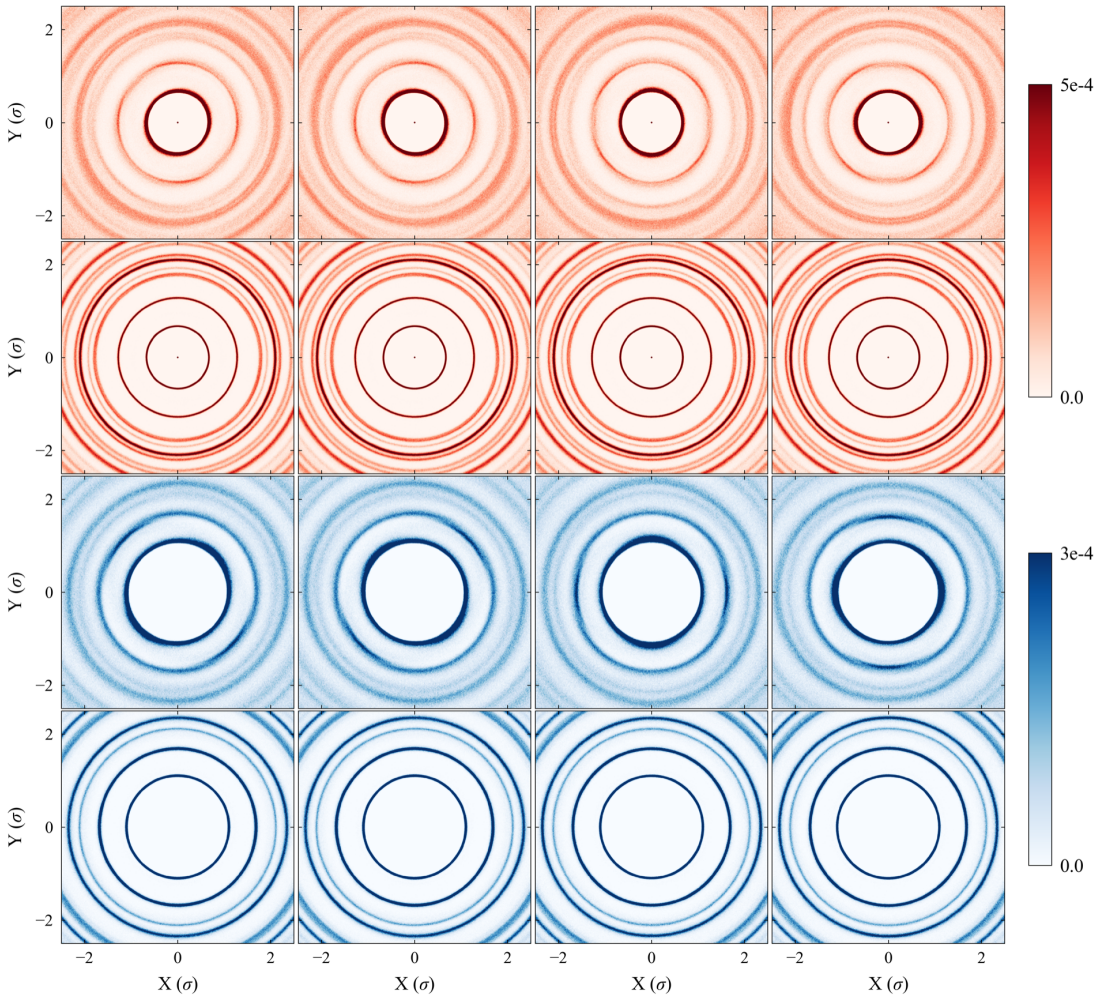

Figure 5.4: SDM of 2D glasses for S particles. Each map is the average of all S particles that have been identified to have extremely large or small D^2_{min} when sheared to 3.0% strain, in 5,000 samples. The image was calculated for these particles in the initial undeformed configurations. The top two rows show the distribution of the S particles in the neighborhood up to medium range: the 1st row for particles with top 0.5% of D^2_{min}, while the 2nd row for those with the lowest 0.5% of D^2_{min}. The bottom two rows are for the surrounding L particles: 3rd row for those with the top 0.5% of D^2_{min}, versus the 4th row with the lowest 0.5%. From left to right, the four columns correspond to the four loading protocols, i.e. positive simple shear, negative simple shear, positive pure shear and negative pure shear.

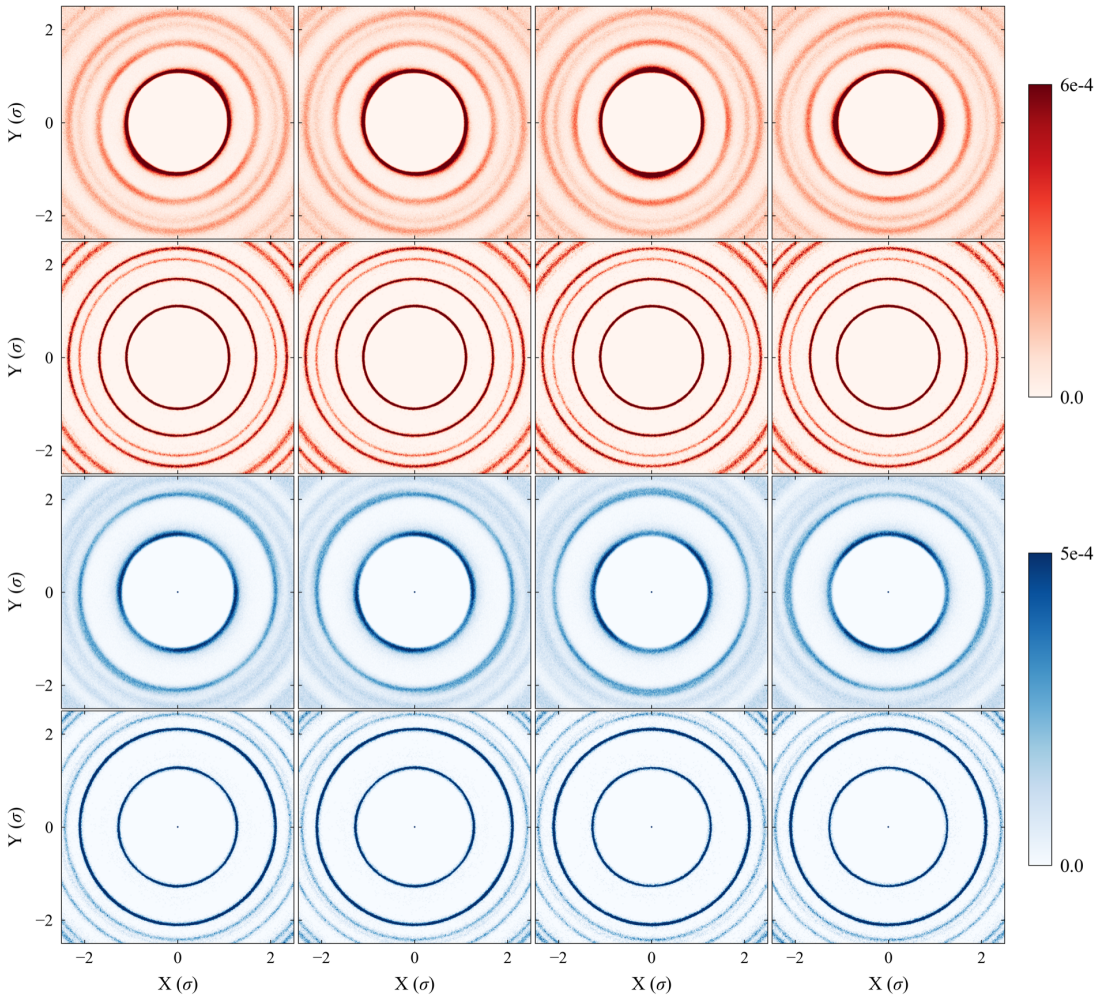

Figure 5.5: SDM of 2D glasses for L particles. Each map is the average of all L particles that have been identified to have extremely large or small D^2_{min} when sheared to 3.0% strain, in 5,000 samples. The image was calculated for these particles in the initial undeformed configurations. The top two rows show the distribution of the S particles in the neighborhood up to medium range: the 1st row for particles with top 0.5% of D^2_{min}, while the 2nd row for those with the lowest 0.5% of D^2_{min}. The bottom two rows are for the surrounding L particles: 3rd row for those with the top 0.5% of D^2_{min}, versus the 4th row with the lowest 0.5%. From left to right, the four columns correspond to the four loading protocols, i.e. positive simple shear, negative simple shear, positive pure shear and negative pure shear.

athermal quasi static (AQS) method [192, 193], such that we can identify all of the particles with extreme (the highest or the lowest 0.5%) non-affine squared displacements ($D^2_{\min}$) [16], for each of the four different loading protocols (positive and negative simple shear, and positive and negative pure shear, see Fig. 5.3). We then went back to the original configurations before deformation, and calculated the SDMs for these two groups of extreme particles that we want to compare. For each group an average SDM was obtained, representing the averaged environment of a representative particle, as shown in the Fig. 5.4 and Fig.5.5. It is interesting to observe that for the highest 0.5% $D^2_{\min}$ (see the 1st and 3rd rows) particle, hereafter referred to as "fertile site", its neighboring shells are more diffuse (wider), and the intensity in the same shell is non-uniform. For the other extreme, the lowest $D^2_{\min}$ particle (shown in the 2nd and 4th rows), each shell is sharper with more uniform intensity. In other words, the images do reveal structural differences between particles with high versus low plastic susceptibility.

This difference in local environment can be appreciated by presenting the SDM in another way, as presented in Fig. 5.6a-h from the standpoint of each S particle (at center). Fig. 5.6a-d are for its S neighbors in the surrounding. In each panel, we subtract the SDM for the center S particles with the lowest 0.5% $D^2_{\min}$ (the 2nd row in Fig. 5.4) from those with the top 0.5% $D^2_{\min}$ (the 1st row in Fig. 5.4). Similarly, Fig. 5.6e-h are for the L neighbors surrounding

an S particle, each panel resulting from the 3rd row in Fig. 5.4 minus the 4th row. The corresponding SDM difference in the L-centric view are provided in Fig. 5.7a-h. As can be seen from these maps, for "fertile sites" the surrounding shells are ellipses. The long axis is parallel to the macroscopic elongation direction ζ - the white dashed line in the map, which is the sum of the unit vector $\hat{\imath}$ (effective shear direction) and $\hat{\eta}$ (normal to the effective shear plane), and the short axis is perpendicular to ζ. In contrast, for particles on the other end of the plastic susceptibility spectrum, their neighboring shells are circles.

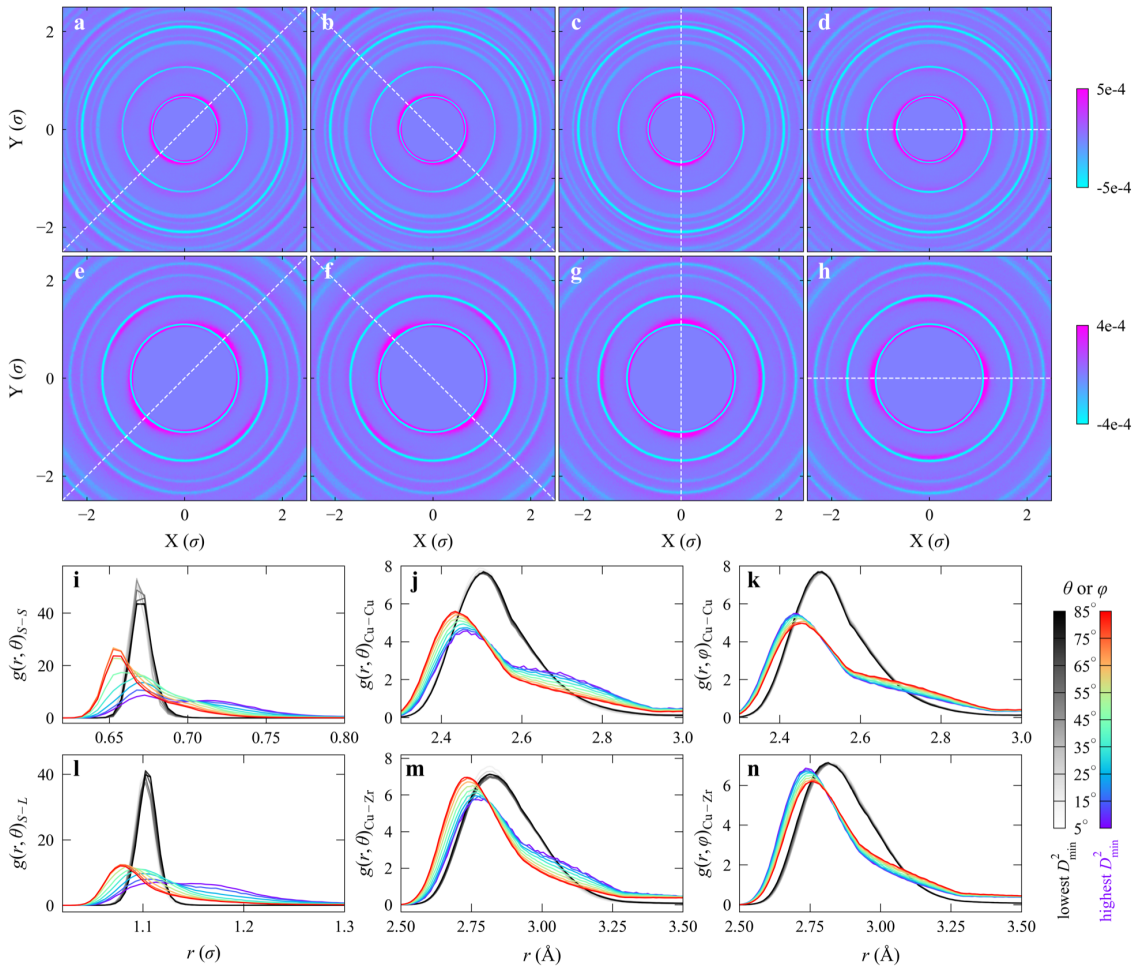

Figure 5.6: Local structural difference between small particles with the highest and those with the lowest plastic susceptibility. (a-d) Difference in SDMs for S particles with extremely high verses low plastic susceptibility in the 2D glass model. See colored scale bar on the right, for the magnitude of the difference, which is calculated using the first row in Fig. 5.4 minus the second row. Each panel maps out the spatial density of surrounding S particles, for one of the four different loading protocols (from left to right: positive simple shear, negative simple shear, positive pure shear and negative pure shear). The white dashed line on each map represents the macroscopic elongation direction, ζ. The corresponding maps for the L particles surrounding the S are shown in (e-h). (i) and (l) show orientational partial (S-centered) pair correlation function $g_\zeta(r,\theta)$, for the S-S and S-L correlation, respectively. Each $g_\zeta(r,\theta)$ curve is an average, over all samples and all loading orientations. For the 3D $Cu_{50}Zr_{50}$ glass, we only show the orientational pair correlation functions for atoms that

showed extreme $D^2_{\min}$ upon straining to 5%. (j) and (m) show Cu-centric $g_{\boldsymbol{\zeta}}(r, \theta)$ curves, for Cu-Cu and Cu-Zr, respectively. And (k) and (n) show Cu-centric $g_{\boldsymbol{\zeta}}(r, \varphi)$ curves, for Cu-Cu and Cu-Zr, respectively. The corresponding figures for L particle as center (2D glass) and Zr atom as center (3D glass) are shown Fig. 5.7.

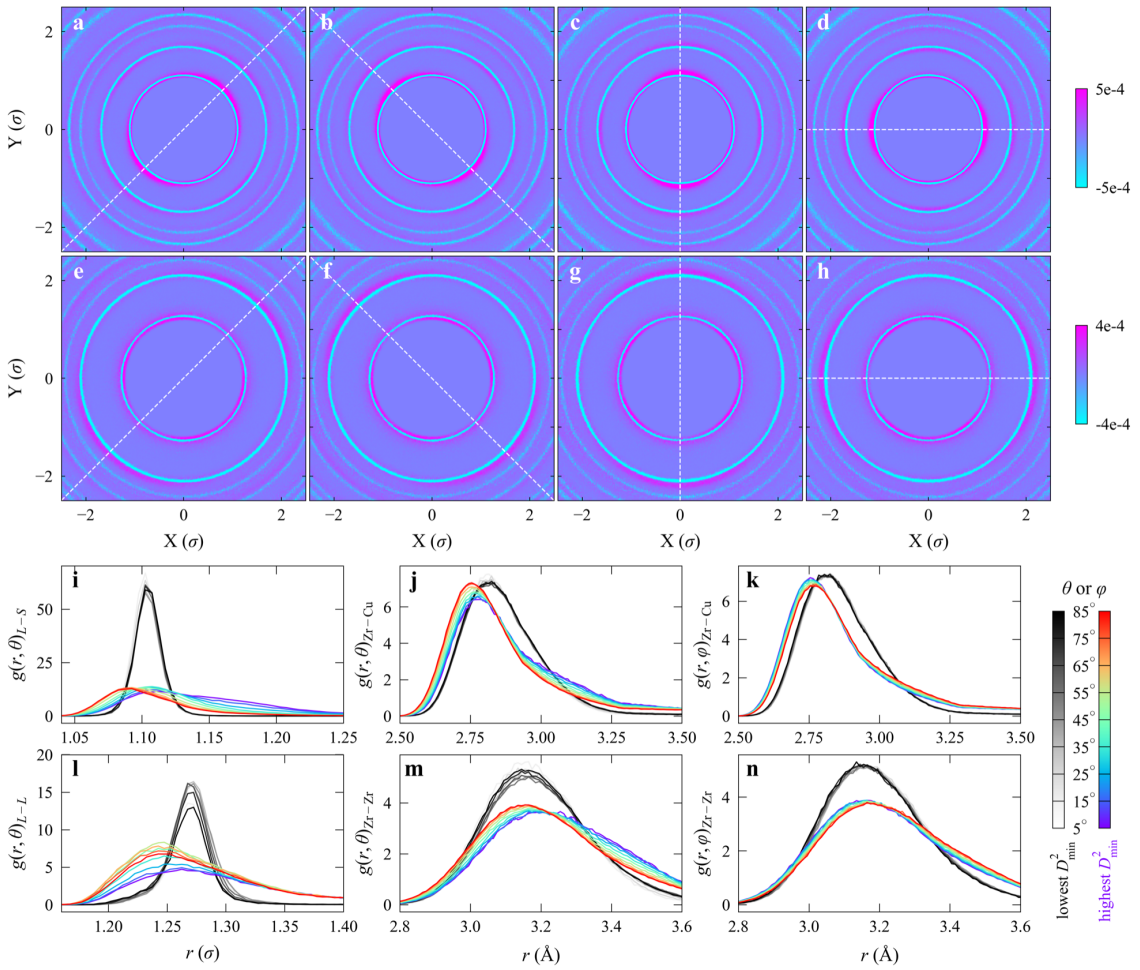

Figure 5.7: Local structural difference between large particles with the highest and those with the lowest plastic susceptibility. (a-d) Difference in SDMs for L particles with extremely high verses low plastic susceptibility in the 2D glass model. See colored scale bar on the right, for the magnitude of the difference, which is calculated using the first row in Fig.5.5 minus the second row. Each panel maps out the spatial density of surrounding S particles, for one of the four different loading protocols (from left to right: positive simple shear, negative simple shear, positive pure shear and negative pure shear). The white dashed line on each map represents the macroscopic elongation direction, ζ. The corresponding maps for the L particles surrounding the L are shown in (e-h). (i) and (l) show orientational partial (L-centered) pair correlation function $g_\zeta(r,\theta)$, for the L-S and L-L correlation, respectively. Each $g_\zeta(r,\theta)$ curve is an average, over all samples and all loading orientations. For the 3D $Cu_{50}Zr_{50}$ glass, we only show the orientational pair correlation functions for atoms that

showed extreme $D^2_{\min}$ upon straining to 5%. (j) and (m) show Zr-centric $g_{\boldsymbol{\zeta}}(r,\theta)$ curves, for Zr-Cu and Zr-Zr, respectively. And (k) and (n) show Zr-centric $g_{\boldsymbol{\zeta}}(r,\varphi)$ curves, for Zr-Cu and Zr-Zr, respectively.

To further understand the structure difference, we also used an orientational pair correlation function, $g_{\boldsymbol{\zeta}}(r,\theta)$, to characterize the local atomic packing environment. The $g_{\boldsymbol{\zeta}}(r,\theta)$ for a single particle i is defined as:

$$g_{\boldsymbol{\zeta},i}(r,\theta)_\beta = \frac{1}{\kappa d f_\beta}\sum_{j=1}^{N_\beta}[\delta(r-r_{ij})\delta(\theta-\theta_{\boldsymbol{\zeta},\boldsymbol{r}_{ij}})], \tag{5.3}$$

where $\theta_{\boldsymbol{\zeta},\boldsymbol{r}_{ij}} = \arccos(|\hat{\boldsymbol{r}}_{ij}\cdot\hat{\boldsymbol{\zeta}}|)$ is the angle between the vector $\boldsymbol{\zeta}$ and $\boldsymbol{r}_{ij}$ and has its values in the range of $[0,\pi/2]$, $r_{ij}=|\boldsymbol{r}_{ij}|$, d is the number density of atoms, f_β is the composition fraction of species β in a sample. For 2D samples, $\kappa = 4r\Delta r\Delta\theta$, and for 3D samples, $\kappa = 4\pi r^2\Delta r[\cos(\theta-0.5\Delta\theta)-\cos(\theta+0.5\Delta\theta)]$. The $g_{\boldsymbol{\zeta}}(r,\theta)$ measures the line density of particles/atoms in the region with radial distance of r from the central atom i, oriented relative to elongation direction $\boldsymbol{\zeta}$ at angle θ (this can be compared with the usual pair correlation function, which can be regarded as the average of orientational correlations over all θ). Again, our goal is to probe the local environment of S (or L) particles identified to exhibit extreme $D^2_{\min}$ in 3.0%-strained 2D samples. In order to accomplish this we went back to the original unsheared sample to calculate the $g_{\boldsymbol{\zeta},i}(r,\theta)$ for these particles of interest. This curve is then averaged over all such S (or L) particles from 5,000 different samples for a given protocol (each sample was sheared 4

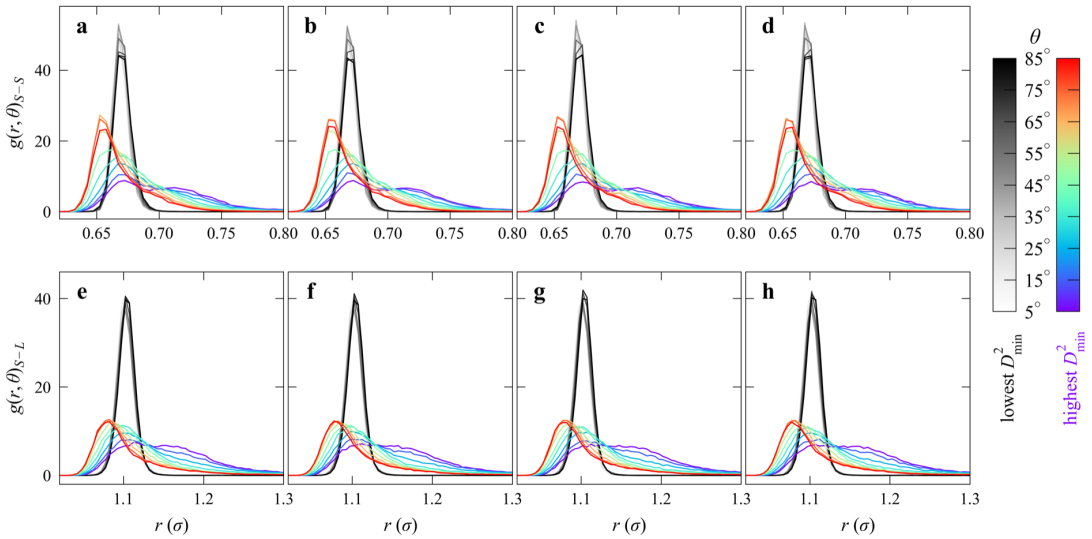

Figure 5.8: The orientational partial pair correlation function $g_\zeta(r,\theta)$ of S particles that showed the top 0.5% $D^2_{\min}$ after being shear strained to 3.0% (colored), compared with that for the lowest 0.5% $D^2_{\min}$ (grey). The upper row is for the neighboring S particles, whereas the lower row is for L particles in the neighborhood. Each curve is the average over all surrounding S (or L) particles from all 5,000 samples. From left to right the columns correspond to positive simple shear, negative simple shear, positive pure shear and negative pure shear, respectively. The (a-d) are similar to each other and are averaged into Fig. 5.6i. And the (e-h) are similar to each other and are averaged into Fig. 5.6l.

times, with the different protocols). The $g_\zeta(r,\theta)$ plots are shown in Fig. 5.8 for S particles and Fig. 5.9 for L particles. The $g_\zeta(r,\theta)$ curves obtained for particles identified in the various loading protocols show little difference; e.g., (a-d) in the Fig. 5.8 are very similar to one another; they were hence averaged to the one shown in Fig. 5.6i.

As seen from these plots, for particles with low plastic susceptibility, the grey curves of $g_\zeta(r,\theta)$ for different θ almost overlap on top of each other, which is consistent with the observation that around each of such particles the neigh-

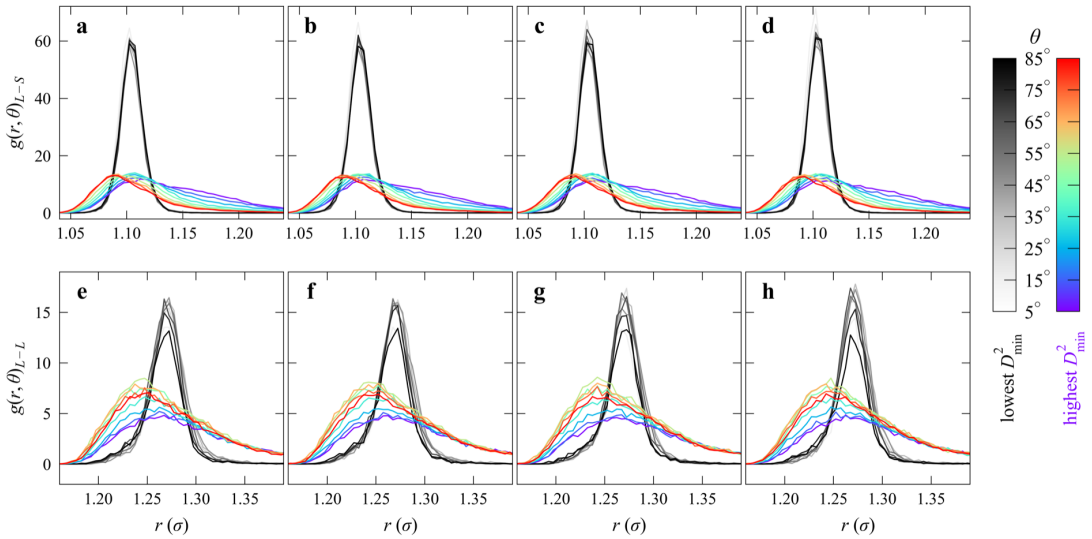

Figure 5.9: The orientational partial pair correlation function $g_{\zeta}(r,\theta)$ of L particles that showed the top 0.5% $D^2_{\min}$ after being shear strained to 3.0% (colored), compared with that for the lowest 0.5% $D^2_{\min}$ (grey). The upper row is for the neighboring S particles, whereas the lower row is for L particles in the neighborhood. Each curve is the average over all surrounding S (or L) particles from all 5,000 samples. From left to right the columns correspond to positive simple shear, negative simple shear, positive pure shear and negative pure shear, respectively. The (a-d) are similar to each other and are averaged into Fig. 5.7i. And the (e-h) are similar to each other and are averaged into Fig. 5.7l.

bors tend to form circularly symmetric shells. In other words, a particle with low plastic susceptibility tends to have almost the same bond length with its n_{th} neighbors. In stark contrast, for fertile-site particles, the curves of $g_{\zeta}(r,\theta)$ at different θ are quite different. Specifically, their neighboring particles with θ close to 0 have longer bond lengths, whereas those with θ closer to $\pi/2$ have shorter bond lengths, see Fig. 5.6i and l. Around L particles with high plastic susceptibility, the distribution of S neighbors (Fig. 5.7i) is similar to that observed in Fig. 5.6i and l, while the distribution of L neighbors changes with

θ mainly in the peak intensity (see Fig. 5.7i), also indicating the asymmetric packing in the surrounding. Note that other peaks at larger radial distance behave similarly, so only the first peaks are compared in the figures. We carried out similar $g_{\boldsymbol{\zeta}}(r,\theta)$ analysis for 3D $Cu_{50}Zr_{50}$ model glasses. As shown in Figs. 5.6 and 5.7 j and m, the structural features are similar to those in 2D glasses.

The analysis based on $g_{\boldsymbol{\zeta}}(r,\theta)$ unveils that a local configuration vulnerable to plastic rearrangement has its longest axis of the elliptical neighboring shells parallel to the elongation direction of global loading. This picks out the softest direction of a 2D local configuration. But for a 3D local configuration under this same condition, there is still one more degree of freedom: the local configuration can rotate arbitrarily around the elongation direction. Additional conditions are therefore needed to identify the softest direction of 3D local configurations, to take into account this angle of rotation. To this end, we employ another orientational pair correlation function, $g_{\boldsymbol{\zeta},i}(r,\varphi)$,

$$g_{\boldsymbol{\zeta},i}(r,\varphi)_\beta = \frac{1}{\kappa df_\beta}\sum_{j=1}^{N_\beta}[\delta(r-r_{ij})\delta(\varphi-\varphi_j)], \tag{5.4}$$

here, we shift the elongation vector $\boldsymbol{\zeta}$ such that it goes through the central atom i of a local configuration and then define a new vector $\boldsymbol{\chi}_j$ for each surrounding atom j of the local configuration. The $\boldsymbol{\chi}_j$ is perpendicular to $\boldsymbol{\zeta}$ and passes through the surrounding atom j of interest. Then φ_j is the angle between $\boldsymbol{\chi}_j$

and the plane ($\boldsymbol{\iota} \times \boldsymbol{\eta}$) defined by the shear direction vector ($\boldsymbol{\iota}$) and the normal vector of shear plane ($\boldsymbol{\eta}$), for each surrounding atom j. Thus, the $g_{\boldsymbol{\zeta},i}(r,\varphi)_\beta$ depicts neighboring shells which pass through the vector $\boldsymbol{\zeta}$ but with different φ relative to the plane of $\boldsymbol{\iota} \times \boldsymbol{\eta}$. When $\varphi = 0$, the shells are in the plane of $\boldsymbol{\iota} \times \boldsymbol{\eta}$, and when $\varphi = \pi/2$, they are perpendicular to the plane of $\boldsymbol{\iota} \times \boldsymbol{\eta}$. Here $\kappa = 8r^2\Delta r\Delta\varphi$, different from that for $g_{\boldsymbol{\zeta}}(r,\theta)$ in equation 5.3.

Figs. 5.6k and n contrast the partial $g_{\boldsymbol{\zeta},i}(r,\varphi)$ of the Cu atoms having the lowest 0.5% $D^2_{\min}$ with those having the 0.5% highest for Cu-Cu and Cu-Zr. The corresponding Zr-centric $g_{\boldsymbol{\zeta},i}(r,\varphi)$ for Zr-Cu and Zr-Zr are shown in Figs. 5.7k and n, respectively. These extreme particles were identified in the 1,500 $Cu_{50}Zr_{50}$ glasses deformed to 5% strain. For the lowest 0.5% $D^2_{\min}$, all partial $g_{\boldsymbol{\zeta},i}(r,\varphi)$ at different φ also overlap with one another, in conjunction with the overlapping partial $g_{\boldsymbol{\zeta},i}(r,\theta)$ at different θ shown in Figs. 5.6j and m and Figs 5.7j and m. These unequivocally confirm that the neighboring shells of particles with lowest plastic susceptibility exhibit spherical symmetry, for the 3D glasses. In other words, the bond lengths in a given shell are very close and the shell is uniformly populated. In contrast, for the fertile sites with the highest 0.5% $D^2_{\min}$, the surrounding particles inside the plane of $\boldsymbol{\iota} \times \boldsymbol{\eta}$ tend to have shorter bond lengths, as seen in all the $g_{\boldsymbol{\zeta},i}(r,\varphi)$ at small φ. Combining this with the insight from Figs. 5.6j and m and Figs. 5.7j and m, a 3D local configuration is expected to emerge as a fertile site when i) the degree of asym-

metry of its atomic packing is sufficiently large; ii) its longest axis is parallel to the elongation direction of the global loading; iii) its orientation around the elongation direction axis is in such a way that the neighboring shell inside the plane of $\boldsymbol{\iota} \times \boldsymbol{\eta}$ coincides with the ellipse having the largest aspect ratio. Putting it another way, in the plane of $\boldsymbol{\iota} \times \boldsymbol{\eta}$, the larger the ratio of the bond length parallel to the elongation direction to that parallel to the contraction direction (the elongation and contraction directions are perpendicular to each other), the higher the susceptibility to plastic rearrangement.

We emphasize here that these features above provide new insight into the difference in local structure, between particles with high versus low plastic susceptibility. To recapitulate, in both the 2D and 3D glasses, for particles with low plastic susceptibility, their neighbors tend to form circular shells with almost uniform intensity (peak height) at different θ and φ. In other words, the bond lengths are very similar for each shell, in which the neighbors uniformly distribute. In contrast, packing tends to be more asymmetric surrounding fertile sites, the neighboring shells are ellipses, each with non-uniform particle distribution. And for a fertile site to be activated upon a particular mechanical loading, the longest and shortest axis of neighboring shells should be parallel to the elongation and contraction directions, respectively. In other words, a fertile site is the most prone to be activated when its surrounding packing along the elongation direction is the loosest and packing along the contraction

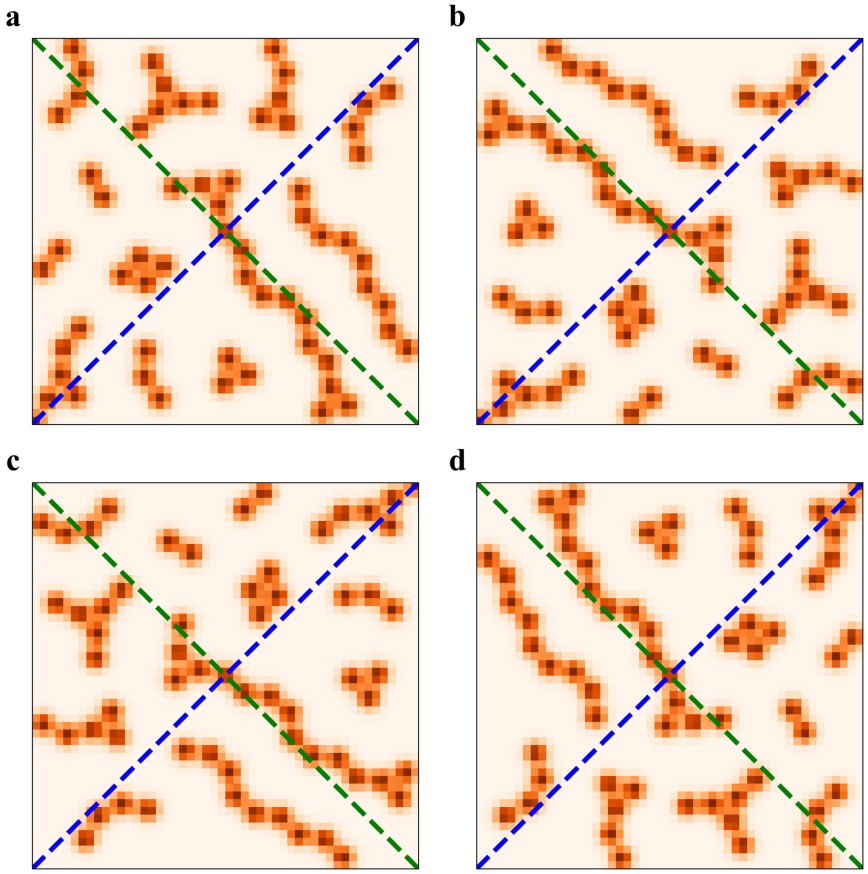

Figure 5.10: Equivalent local configurations based on mirror-symmetries. Here we use the SDMs of species S for a 2D local configuration to illustrate the mirror operations. (a) and (b) are mirrored to each other along macroscopic elongation direction (blue dash line) in the plane of $\iota \times \eta$; (a) and (c) are mirrored to each other along macroscopic contraction direction (green dash line); (a) and (d) will be the same after two mirror operations (along both elongation and contraction lines), which is equivalent to a rotation by 180^{circ} around the center of images. The 4 images can generate another 4 mirrored ones, across the plane of $\iota \times \eta$ for 3D configurations. These mirror operations will not change the packing density of local configurations along elongation or contraction orientations and thus those mirrored configurations are expected to exhibit similar mechanical response, which is confirmed in the Fig. 5.11.

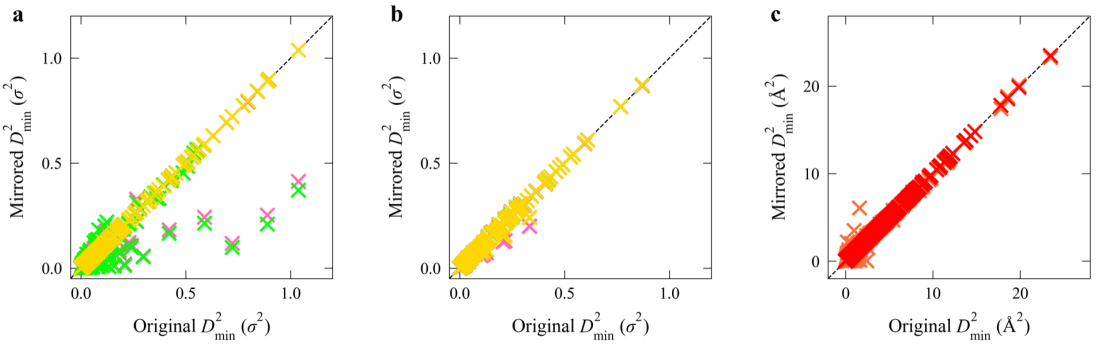

Figure 5.11: Mirrored samples show almost same mechanical response. (a) and (b) are for a 2D glass strained to 2.5% in simple and pure shear, respectively. (c) is for 3D glasses strained to 5.0% in simple shear. Each symbol in the plots represents D^2_{min} of a single particle in one the of 3 (or 7) mirrored samples (see more details about mirror-symmetry in the Fig. 5.10) against that in the original 2D (or 3D) glass. Almost all symbols locate on the diagonal dash lines, suggesting that particles in mirrored samples show almost same mechanical response as those in the original samples.

direction is the densest. These structural differences are responsible for the anisotropy of local mechanical response in amorphous solids.

With these insights in mind, we expect that the mechanical response of a local configuration will not show much difference when one mirrors the local configuration around the plane perpendicular to the plane of $\iota \times \eta$ and containing the vector ζ or the vector perpendicular to ζ, or the plane of $\iota \times \eta$ (see details on these mirror operations in Fig. 5.10), as these mirrors will not change the packing density of local configurations along the elongation or contraction direction. To verify this, we loaded 3 such mirrored configurations of a 2D L-J sample (in both simple and pure shear along a constant loading orientation), and 7 mirrored $Cu_{50}Zr_{50}$ configurations (in simple shear along a constant loading orientation). As expected, D^2_{min} of all particles in those mirrored sam-

ples are indeed almost identical to those in the corresponding original samples, when the strain is well below global yielding, as shown in Fig. 5.11. In training our CNN model (next section), we will augment our training data with these mirror-symmetries. This was found to improve accuracy by $\sim$2%, lending further support to our insight above.

5.4 Training procedure and results

The insight in Fig. 5.6 is useful for our understanding, as it provides a general picture of the main structural features/difference. But there are also other subtle but nontrivial features to be taken into account, when a concrete decision is to be made regarding whether a particular particle has high (or low) susceptibility. As will be demonstrated in the work that follows, deep learning is able to include additional and more subtle information so as to provide such predictive power. And the consistency between the CNN prediction with our expectation based on the insight in Fig. 5.6 will also be confirmed at the end of this subsection. To construct big datasets for the CNN models, we prepared 2D L-J (or 3D $Cu_{50}Zr_{50}$) glasses with constant a cooling time of $10^6\ t_0$ (or effective quench rate of 10^{10} K/s) from the corresponding well-equilibrium liquid. 5,000 (1,500) samples were made, each containing 10,000 (32,000) particles. Each sample was then deformed under 4 (24) different loading protocols (see more details about sample preparation and deformation in Methods section, 5.7). These 2D

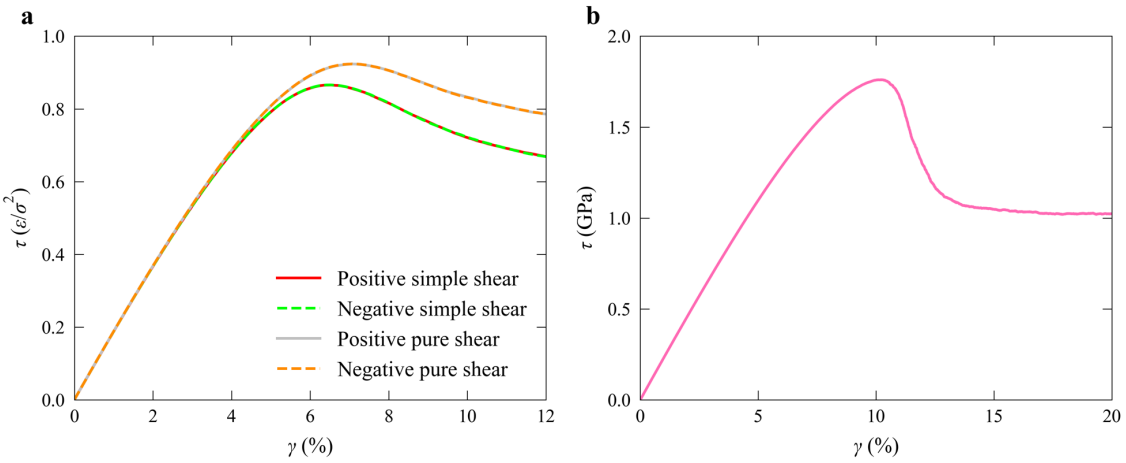

Figure 5.12: (a) Shear stress-strain curves for 2D glasses, averaged over 5,000 post-loading samples for each of the four different protocols. For simple shear, the $\gamma = |\gamma_{xy}|$, the shear stress $\tau = |\tau_{xy}|$, and for pure shear, $\gamma = |\epsilon_{xx} - \epsilon_{yy}|$, and $\tau = \frac{|\sigma_{xx} - \sigma_{yy}|}{2}$. (b) Shear stress-strain curves for $Cu_{50}Zr_{50}$ 3D glass, averaged over 20 samples sheared to large (up to 20%) strains. Each sample was simple-sheared in 24 different orientations and thus the curve is the average of 480 curves.

(3D) glass models were divided into training, validation and test datasets, each containing 4,900 (1,480), 50 (10) and 50 (10) samples, respectively. Since we are interested in identifying particles which will experience extreme (large) plastic rearrangement upon loading, the first step is to do a binary classification task. A particle i is labeled $y_i = 1$ if its $D^2_{\min}$ is higher than a specific threshold and $y_i = 0$ otherwise. Here we use f_{thres} to set the $D^2_{\min}$ threshold at a given shear strain. For example, f_{thres} = 0.5% means that we label particles in the top 0.5% $D^2_{\min}$ group as $y_i = 1$ and the remainder $y_i = 0$. The shear stress-strain curves and cumulative distribution function (CDF) of $D^2_{\min}$ are shown in Figs. 5.12 and 5.13, respectively, for the 2D and 3D glasses. Our training, validation and

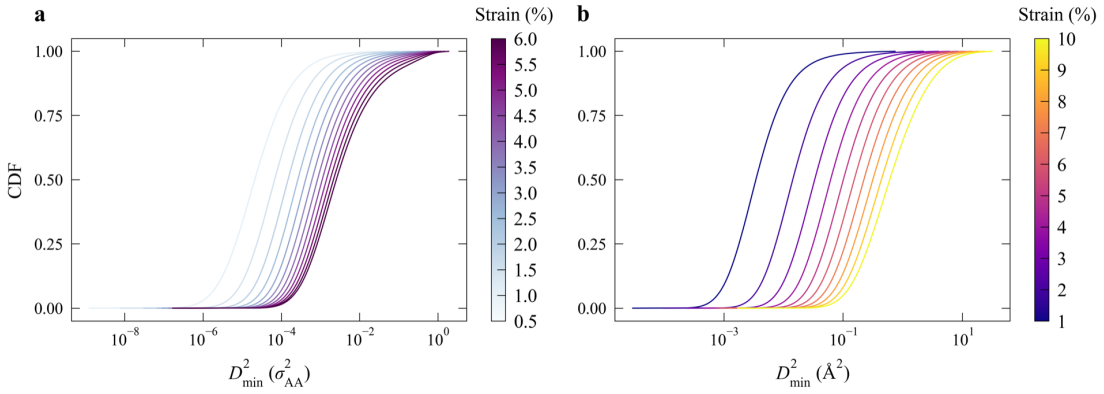

Figure 5.13: The cumulative distribution function (CDF) of $D^2_{\min}$ at different shear strains for 2D glasses (a) and 3D $Cu_{50}Zr_{50}$ MGs (b).

test datasets were balanced, as in each dataset we included all the $y_i = 1$ particles in each sample deformed under each specific deformation protocol, with the same number of $y_i = 0$ particles selected at random from the rest. Note again that the SDM were constructed for particles in the initial undeformed configurations; it is just that these particles were selected based on their $D^2_{\min}$ response upon straining.

Fig. 5.14a and b, for 2D and 3D glasses, respectively, show the predictive accuracy achieved on validation datasets with our CNN method, the graph neural network (GNN) [69] method and linear support vector machine (SVM) [21] method, when differentiating particles/atoms with $y_i = 1$ from those with $y_i = 0$ at different strains with a constant f_{thres} = 0.5%. In what follows, we only quote "accuracy", as our data indicated that the validation accuracy and test accuracy are practically the same. As seen from Fig. 5.14a for the 2D case, CNN exceeds SVM by far in performance, over the entire strain range we consid-

ered; the highest accuracy achieved was as high as 96.27%. This accuracy is very close to the ceiling (see Methods section 5.7.6 for details about the upper bound). Several advantages of CNN make it obviously superior to SVM: i) CNN can capture more complicated relations between static structure and plastic activity compared to linear SVM, as the latter is merely a linear machine learning algorithm; ii) SVM loses some subtle but critical structural information during the conversion from atomic positions to the input features; iii) most importantly, for a given local configuration in different loading directions, we constructed images with different coordinate systems (in which the X axis is parallel to the shear direction (ι) and the Y axis is the normal direction of the shear plane (η). This enabled orientation-dependent predictions, whereas the input features to SVM are rotation-invariant, leading always to the same prediction. We observe that GNN produces slightly lower accuracy compared to the accuracy of our CNN, as shown in Fig. 5.14a. This is not surprising, as GNN used atomic positions directly to construct graphs as input, and in training GNN models we rotated edge vectors for different loading directions, in contrast to the procedure from Ref. [69] (see details in Methods, section 5.7.8). However, the advantage of CNN over GNN is more obvious for larger f_{thres}, Fig. 5.15, and the graph input to GNN cannot be used to provide the insights gained from Fig. 5.6 based on images, the input to CNN.

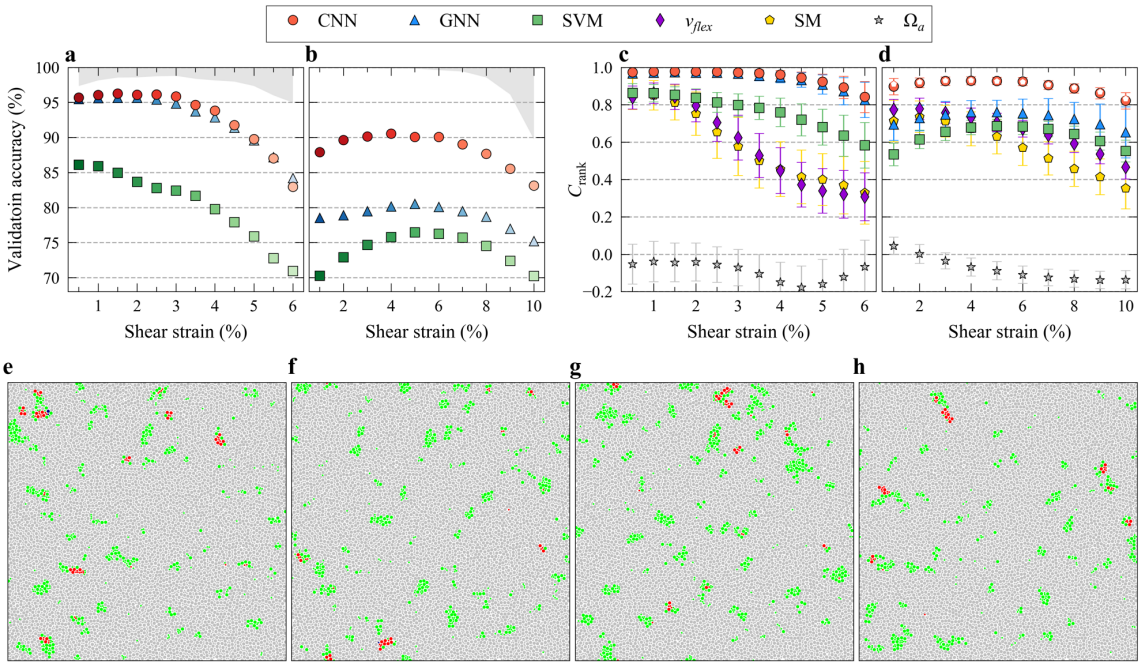

Figure 5.14: Predictive power enabled through deep learning. (a) Accuracy achieved using three different machine learning methods (CNN, GNN and SVM) at different shear strains using a constant f_{thres} of 0.5% for 2D L-J glasses. (b) shows the corresponding results for 3D $Cu_{50}Zr_{50}$) glasses. The lower edge of the region shaded grey is the upper bound, i.e., the ceiling predicted using labels based on new D^2_{min} after conducting another deformation simulation on samples belonging to the test dataset (see more details in Methods section 5.7.6). (c) The cumulative rank correlation (C_{rank}, see text for definitions) between real local plastic response in a sample along a give loading orientation and the plastic susceptibility predicted via each of the six routes, including the three machine learning models and the other three based on physical parameters, i.e., flexibility volume (v_{flex}), soft modes (SM), atomic volume (Ω_a). The corresponding results for the 3D $Cu_{50}Zr_{50}$ glasses are shown in (d). The C_{rank} value are the average for 50 (10) different samples loaded in 4 (24) different loading orientations for 2D (3D) glasses, with the error bar marking the standard deviation. For the 3D glasses, each sample contained 32,000 atoms, although the soft mode analysis was conducted using smaller samples each containing 10,000 atoms. For a fair comparison, CNN was also applied on these smaller samples, as shown with open pentagons (i.e., white pentagons overlapping with red full circles) in (d). (e-h) map out CNN-based prediction results for the same 2D glass but in four different loading protocols (left to right): posi-

tive simple shear, negative simple shear, positive pure shear and negative pure shear. The particles with top 0.5% $D^2_{\min}$ are assumed as fertile sites after the model was loaded to shear strain of 3.0%. On the maps, fertile sites predicted correctly are marked with red color; non-fertile-sites predicted correctly are marked silver while those mislabeled as fertile are marked light green; fertile sites mislabeled as otherwise are marked blue.

When dealing with 3D $Cu_{50}Zr_{50}$ glasses, the GNN method is also superior to SVM, consistent with the observations in Ref. [69]. However, we found that our CNN, as an algorithm with state-of-the-art learning capability, is far more powerful than GNN. This is shown in Fig. 5.14b, over the entire strain range. The highest accuracy achieved with CNN is above 90%, in the strain range from 3 to 6%. Even at a strain of 10% where global yielding occurs (see Fig. 5.12b), the accuracy is still $> 83\%$. This suggests our CNN model may be useful in predicting the location where shear band initiates. This point is beyond the scope of this chapter and will be discussed in next chapter.

One would be naturally curious as to how well our CNN models fare, when compared with the prediction based on a correlation between the propensity for plastic rearrangements of each particle and some previously used physical indicators, such as the participation ratio in soft modes (SM) [19, 54], flexibility volume (v_{flex}) [78], and atomic volume (Ω_a). To allow this comparison, here we evaluate the class probability from CNN and GNN, and the distance to the separation boundary predicted by SVM, to denote the predicted plastic susceptibility of each particle in the samples constructed for the test dataset

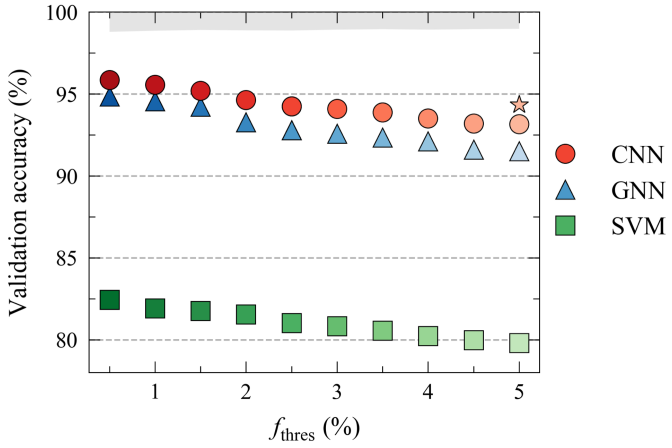

Figure 5.15: Validation accuracy versus f_{thres} for 2D L-J glasses at a constant strain of 3.0%. The shaded region marks the upper bound. Note here that smaller f_{thres} means smaller training datasets for the same number of glass samples. Since both CNN and GNN require large training datasets (see Fig. 5.16) to reach high accuracy, the accuracy at small f_{thres} is expected to be higher if the training dataset size was the same for different f_{thres}. The red star represents the accuracy of 94.28% achieved when the CNN model used 30 conv. layers on images with $r_c = 10.0\sigma$ and $\Delta = 0.2\sigma$. This example of successfully improved CNN accuracy shows again the advantage of CNN, further demonstrating its capability to excel over the GNN model (CNN now performs considerably better when compared with the 91.52% achieved at the same f_{thres} with GNN).

but never involved in the training dataset. Take CNN as an example, the class probability for each input image is a numerical value in the range of $(0, 1)$ provided by the learning algorithm, to represent the probability of having a label of $y_i = 1$ for the input object. For binary classifications, class probability greater than 0.5 predicts $y_i = 1$ and $y_i = 0$ otherwise. Then the plastic susceptibility of each particle can be predicted via one of the six approaches (the three machine learning methods and three physical parameters). Similar as in Ref. [55], we define a cumulative rank correlation (C_{rank}) to compare the power of these six

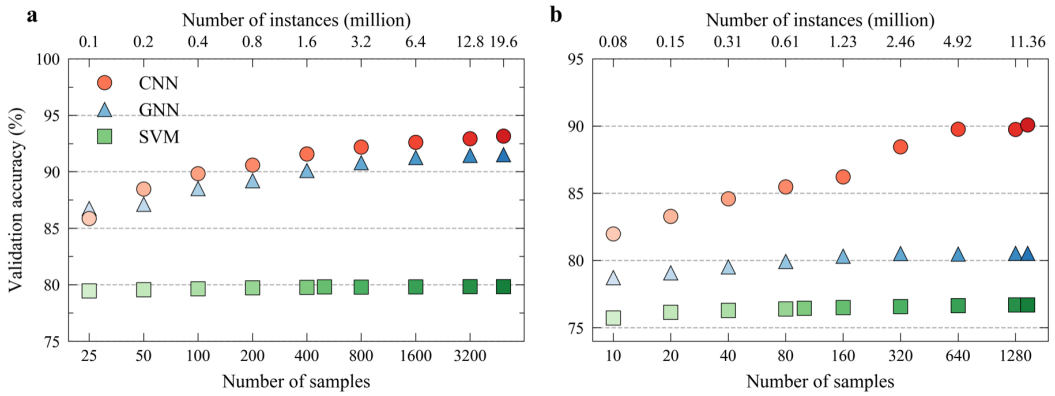

Figure 5.16: The effect of training dataset size on validation accuracy. (a) and (b) are for 2D glasses at shear strain of 3.0% with f_{thres} of 5.0% and 3D $Cu_{50}Zr_{50}$ glasses at shear strain of 5.0% with f_{thres} of 0.5%, respectively. The largest dataset size for the 2D glasses contains 4,900 samples each containing 10,000 particles and sheared in 4 loading orientations, so with f_{thres} of 5.0%, the largest training dataset contained ~19.6 million instances. The largest training dataset size for the 3D glasses contains 1,480 samples each with 32,000 atoms and sheared along 24 loading orientations, so with f_{thres} of 0.5%, the largest dataset contains ~11.36 million instances.

routes in predicting the particles which will have top 0.5% D^2_{min} when a sample is sheared to different strains in a given orientation. As the indicator based on each of the six methods are expected to correlate positively with plastic response, i.e., larger indicator means larger D^2_{min}, here we define

$$C_{\text{rank}} = 2C\bar{D}F(\varrho_i) - 1, \tag{5.5}$$

where ϱ_i is the plastic susceptibility of particle i predicted via one of the six routes, $CDF(\varrho_i)$ is the cumulative distribution function value for ϱ_i, and the bar on top represents averaging $CDF(\varrho_i)$ over all particles with top 0.5% D^2_{min}. The highest (lowest) value of C_{rank} is around 0.995 (-0.995), which means perfect

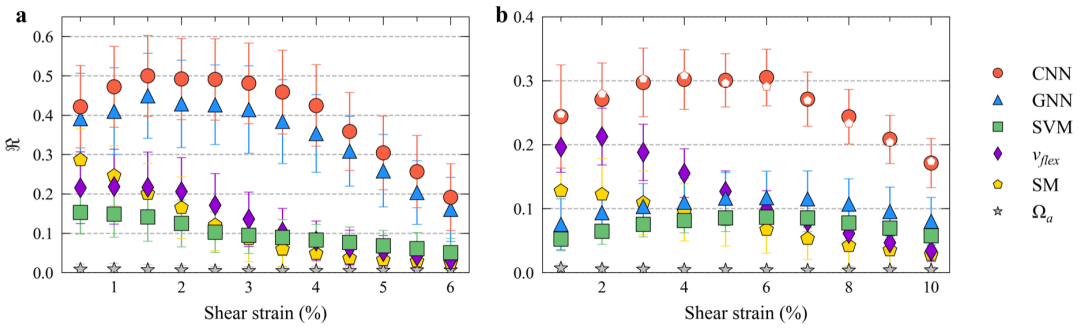

Figure 5.17: Correctly predicted fraction given by the three machine learning models and three physical-indicator-based methods (flexibility volume (v_{flex}), soft modes (SM), atomic volume (Ω_a)): (a) for 2D L-J and (b) for 3D $Cu_{50}Zr_{50}$ glasses, respectively. Here the predictive capability is evaluated in term of $\Re$, which is the overlap ratio given by the number of particles belonging simultaneously to two groups that are intersecting, divided by the number of particles known to have the top 0.5% $D^2_{\min}$. In this context the "intersection" particles are those that belong not only to the group known to have the top 0.5% $D^2_{\min}$, but at the same time also to the group having top 0.5% plastic susceptibility predicted using one of the six methods. As here we only allow a narrow bin of the top 0.5% $D^2_{\min}$, this criterion is the most stringent, arguably to the extreme. The error bars correspond to standard deviation among 50 (10) different samples and 4 (24) different loading protocols for 2D (3D) glasses.For 3D glasses, all predictions used samples each containing 32,000 atoms, except that the soft mode analysis was conducted on 10 different samples each containing 10,000 atoms. For a fair comparison, the CNN analysis was also conducted on the smaller samples (open pentagons in (b)).

correlation (anticorrelation), and $C_{\text{rank}} = 0$ means no correlation.

As seen in Figs. 5.14c and d, the C_{rank} achieved with our CNN method is almost equal to its highest possible value over a wide range of strain for both the 2D and 3D glasses. The worst case is Ω_a, for which C_{rank} is always close to zero across the board, for either the 2D or 3D glasses. For the three data-driven methods, their relative predictive power (the magnitude of C_{rank} follows an order similar to that observed in Figs. 5.14a and b. The CNN prediction

stands out to be the best. Note that the predictive power generally decreases with increasing strain for physical indicators. In this regard, our CNN has a major advantage over other methods at larger strains, which is important for monitoring the correlation between structure and mechanical response of amorphous solids. As soft mode analysis on large 3D samples is too computationally expensive, we used instead $Cu_{50}Zr_{50}$ glasses containing 10,000 atoms. Such smaller samples were also analyzed via CNN, to allow head-to-head comparison (included in 5.14d). In addition, we also used a different and extremely stringent criterion, an overlap ratio, $\Re$, to gauge the fraction of correctly predicted particles. $\Re$ is evaluated by dividing the number of particles belonging simultaneously to two groups that are intersecting (partially overlapping), with the number of particles known to have the top 0.5% $D^2_{\min}$. Here the intersection/overlapping particles are those that fall into not only the group known to have the top 0.5% $D^2_{\min}$, but at the same time also the group having the top 0.5% plastic susceptibility predicted using that particular method/indicator. In the ideal case, the particles predicted to have the top 0.5% plastic susceptibility are expected to be the same particles known to have the top 0.5% $D^2_{\min}$ (i.e., all the particles in that pool). As such, the closer to 1.0 the $\Re$ ratio, the higher the predictive capability. The corresponding results are displayed in Fig. 5.17, which shows a similar trend as in Figs. 5.14c and d. This further confirms the advantage of our CNN method as the most robust of the six, disregarding the

metric adopted to characterize the strength of correlation.

Fig. 5.14e-h show the spatial distribution maps of the CNN prediction for a given 2D glass, each map for one of the four different loading protocols, all at shear strain of 3.0%. We contrast these, in Fig. 5.18, with the corresponding predictions from GNN and SVM models. It is important to observe from Fig. 5.14e-h that our CNN model provides different predictions when the loading direction changes, and almost all of the particles with top 0.5% $D^2_{\min}$ are predicted correctly (red circles on the maps) and very few are predicted incorrectly (blue circles). In other words, almost all true fertile sites are recognized. There are some infertile particles mislabeled as having top 0.5% $D^2_{\min}$ (green circles on the maps). For 2D glass, the GNN prediction is similar to CNN. In stark contrast, SVM gives identical prediction for different loading protocols; as a result, too many particles are falsely predicted as belonging to the top 0.5% $D^2_{\min}$ group (green circles on the maps). There are also some fertile sites that are predicted incorrectly (blue circles).

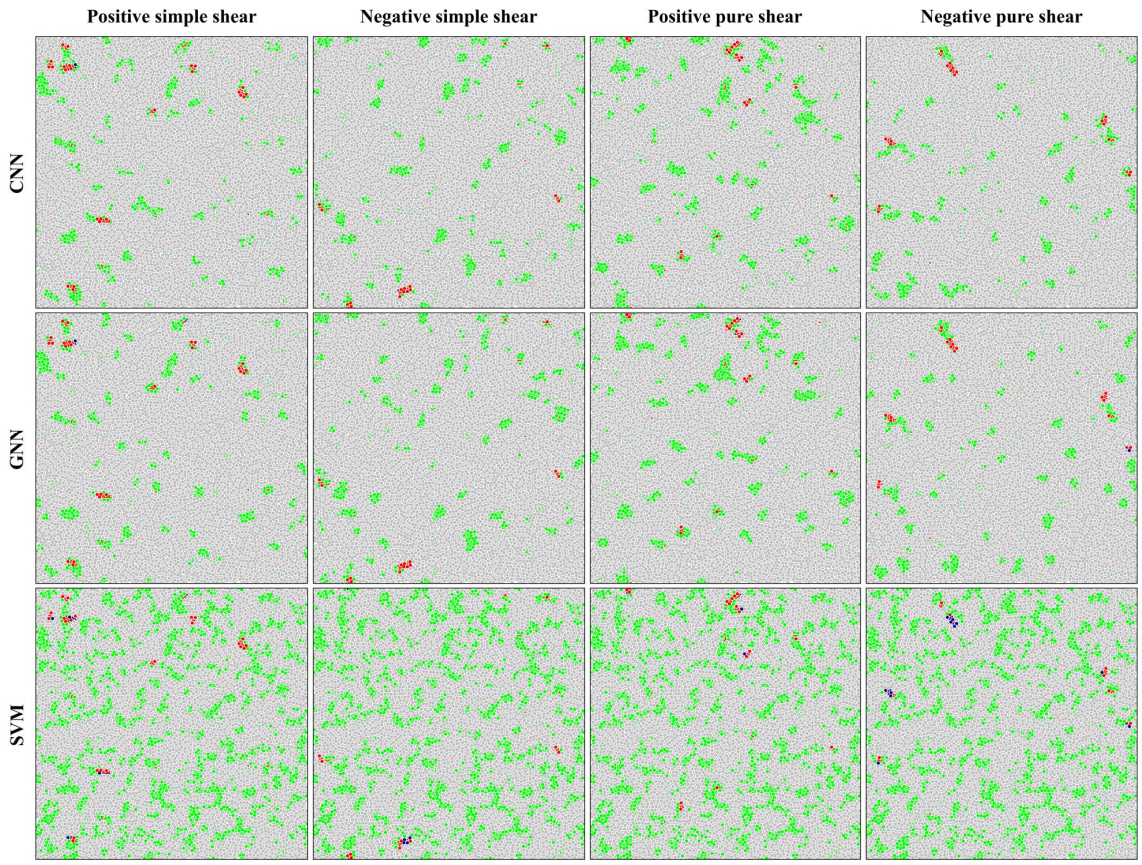

Figure 5.18: Spatial distribution map of prediction results for a given 2D glass sample. The particles with top 0.5% $D^2_{\min}$ are regarded as fertile sites after the model was loaded to shear strain of 3.0%. The results on the upper, middle and lower panels are from CNN, GNN, and SVM models, respectively. From left to right the columns represent four different loading protocols, i.e., positive simple shear, negative simple shear, positive pure shear and negative pure shear, all performed on the same glass. On the maps, fertile sites predicted correctly are marked with red color; non-fertile-sites predicted correctly are marked silver while those mislabeled as fertile are marked light green; fertile sites mislabeled as otherwise are marked blue.

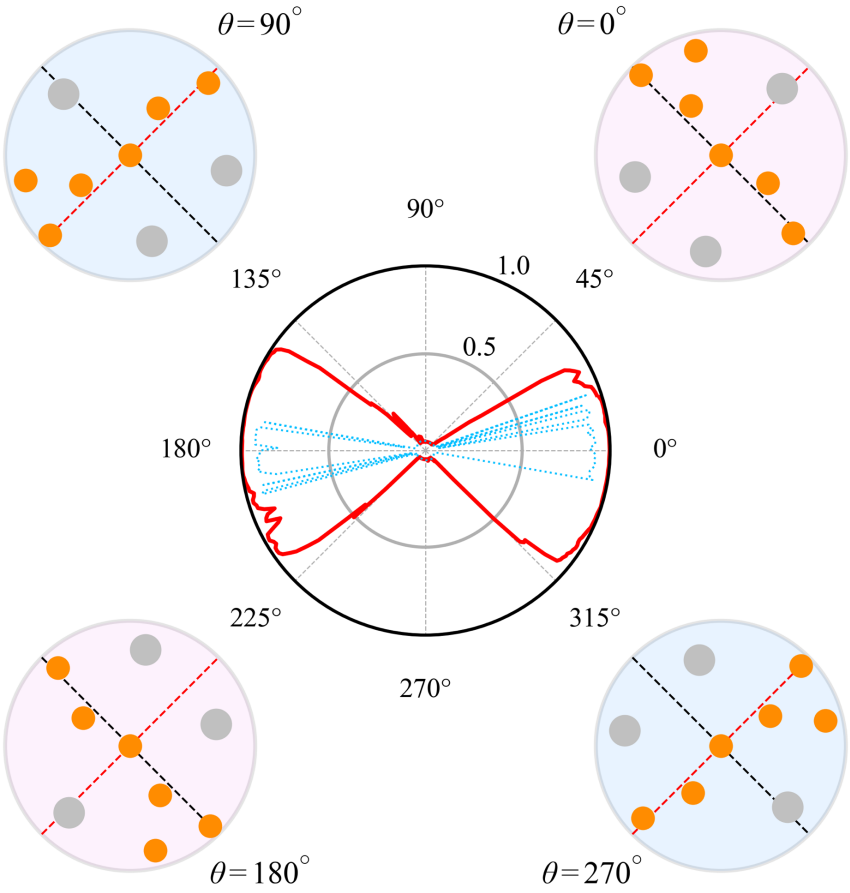

Figure 5.19: The orientation-dependence of CNN-predicted plastic susceptibility for a 2D local configuration. This susceptibility is characterized here by the magnitude of class probability (red solid curve), varying in the range of 0 to 1 (black circle in the center), depending on the rotation angle (θ) of the local configuration relative to the loading orientation (four scenarios during the counter-clockwise rotation at representative angles are displayed). The red and black dashed lines in each snapshot represent the elongation and contraction directions of the global loading, respectively. The blue dotted line in the polar plot represents D^2_{min} of the local configuration at different θ.

To demonstrate that the orientation dependence has been clearly captured, we show in Fig. 5.19 the CNN-predicted plastic susceptibility for a 2D local configuration when it is rotated gradually. In its initial orientation ($\theta = 0°$),

when its loosest and densest packing directions align with the elongation (red dashed line) and contraction (black dashed line) directions of mechanical loading, respectively, CNN predicts the highest plastic susceptibility (class probability very close to 1.0). With the counter-clockwise rotation, these packing directions gradually misalign with the loading ones, and the predicted plastic susceptibility goes down. At $\theta \cong 90^{\circ}$, the loosest packing of the configuration lines up with the contraction direction whereas the densest packing with the elongation direction, class probability drops to a value very close to zero. When θ increases to $\sim 180^{\circ}$, the favorable alignment comes back, such that the plastic susceptibility is predicted to be the highest again. Likewise, the lowest reemerges when $\theta = 270^{\circ}$. This sensitivity to the coupling between the anisotropic local structure and the loading direction demonstrates that, when we feed the images (configurations) into CNN, the algorithm is very good at recognizing this coupling and generating predictions consistent with the insight in Fig. 5.6. The blue dotted line in the polar plot of Fig. 5.19 represents $D^2_{\min}$ of the local configuration at different θ (see Methods, section 5.7.3), which almost matches the CNN prediction. This underscores the benefit and advance enabled by our approach to innovate a new structure representation and combine it with CNN.

5.5 Generalize to different processing history or compositions

Our previous work [80] demonstrated that the SVM models, trained on samples having the same processing history at a single composition, can be generalized to samples with different processing history or at different compositions in the same alloy system. To see if such a generalization is possible with our CNN models, 50 2D samples were quenched over different time periods in the range from 10^0 to 10^6 t_0. For 3D glasses, we also quenched 10 $Cu_{50}Zr_{50}$ samples with effective cooling rates in the range from 10^9 to 10^{13} K/s, and 10 Cu_xZr_{100-x} glasses with different compositions (x = 20, 25, ..., 80) at the same effective cooling rate of 10^{10} K/s. Each of these 2D (3D) samples was sheared using 4 (24) different loading protocols with AQS method. We then constructed test datasets for each processing history and each composition, by selecting all the atoms with $D^2_{\min}$ above a threshold and a same number of atoms randomly from the rest. The accuracy achieved on these datasets, using the CNN model previously trained at a single composition for a particular processing history (see caption and Methods) is presented in Fig. 5.20a-c. We find a very high accuracy across a wide composition range (Fig. 5.20c), especially for samples with slower cooling (Fig. 5.20a and b). For example, for 3D $Cu_{50}Zr_{50}$ quenched at

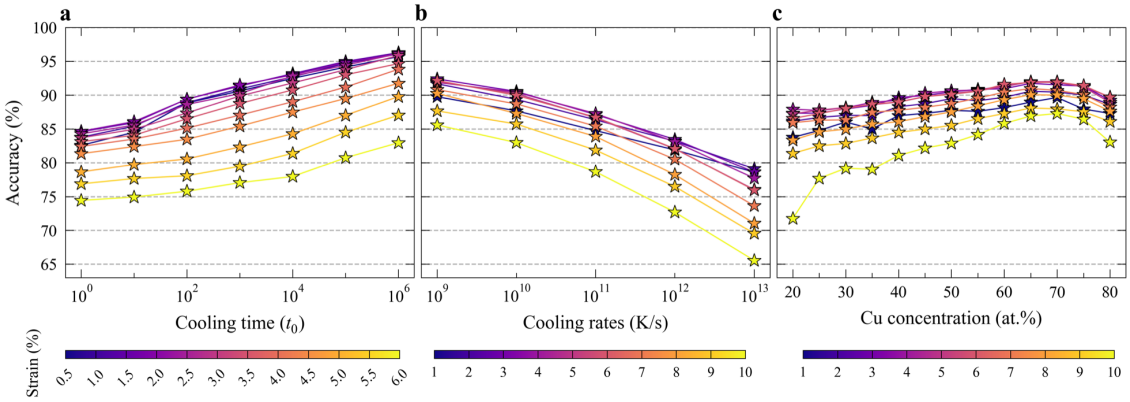

Figure 5.20: The ability of CNN models to generalize. The CNN models were trained on samples at a single composition with one processing history (the 2D glasses at the composition of $N_L : N_S = (1+\sqrt{5}) : 4$, quenched within 10^6 t_0. The 3D $Cu_{50}Zr_{50}$ glasses were quenched at 10^{10} K/s). The accuracy of the models is shown in (a) for 2D glasses quenched with different cooling times, in (b) for $Cu_{50}Zr_{50}$ glasses quenched with different cooling rates, and in (c) for Cu_xZr_{100-x} glasses of different compositions quenched at a constant effective cooling rate of 10^{10} K/s.

cooling rate of 10^9 K/s, the highest accuracy achieved is 92.40%. The decrease in accuracy for faster cooling rate was observed before [42, 55, 71, 80], as the critical structural difference becomes increasingly difficult to distinguish [71]. The more relaxed glasses, on the other hand, have a much smaller population of fertile sites that exhibit larger shear susceptibility, making the recognition easier and prediction more robust.

This transferability of the model offers the desirable applicability to glasses across different compositions and/or different processing history, to compare plastic susceptibility. An example is shown in Fig. 5.21a (for 2D) and b (for 3D). Here the glass structure is generically characterized by the fraction of predicted "$y_i = 1$" particles out of all atoms. This fraction, $f_{py=1}$ (the subscript

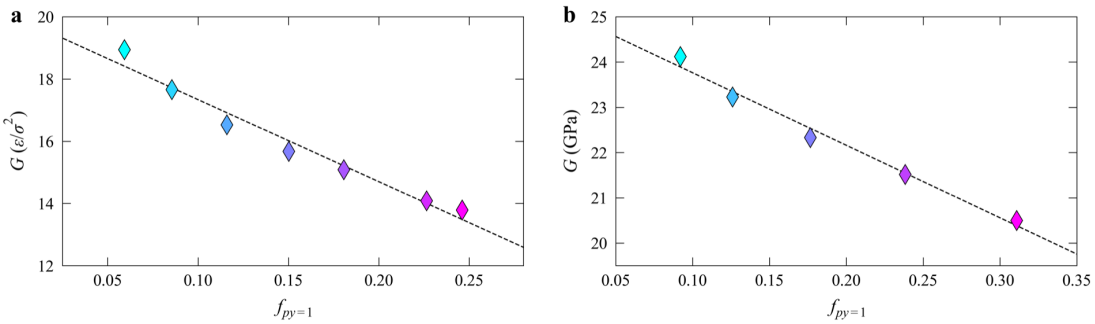

Figure 5.21: Shear modulus (G) versus the CNN-predicted fraction of particles with class probability > 0.5. This fraction is denoted fpy=1 and used as the x axis, for (A) 2D L-J and (B) 3D Cu50Zr50 glass samples with different processing history. Each data point is averaged over 50 (10) samples across 4 (24) loading protocols for 2D (3D) glasses, sheared to a strain of 1% (2%). The dash line serves as a guide to the eye.

means "predicted (labeled) $y = 1$"), is given by the fraction of atoms with class probability > 0.5, and scales almost linearly with the average class probability. These plots reveal a strong correlation between the glass structure and shear modulus (G), found to be robust at any strain as long as it is well below that corresponding to global yielding.

5.6 Summary

Our results presented in this chapter bring about several advances over previous efforts to identify structural "defects" in amorphous solids, i.e., particles that are most prone to rearrangements, in particular shear transformations. First of all, a qualitative but crucial structural difference, in terms of a more non-uniform and asymmetric packing environment, was discovered for

atoms with high plastic susceptibility relative to those with low plastic susceptibility. This difference is found responsible for the anisotropy of local mechanical response in amorphous solids. Our expectation based on this insight, starting from Fig. 5.6, is reflected in the eventual CNN predictions, as highlighted in Fig. 5.19. Second, we achieve unprecedented accuracy in predicting orientation-dependent local mechanical response over a wide range of shear strain, by designing a rotation-variant structure representation coupled with state-of-the-art deep learning algorithm, as highlighted in Fig. 5.14. This unveils the predictive power of the static structure of amorphous solids in forecasting local plastic response. Third, once the optimized CNN model is in hand, all that is needed to predict plastic response is atomic positions, without relying on other knowledge such as interparticle interactions required by previous approaches using parameters based on physical properties. Fourth, we have demonstrated that the CNN models trained on a single glass (with one set of a particular composition and a specific processing history) can be generalized to samples with different processing history or at different compositions in the same alloy system. This is important for probing into the effects of processing procedure or chemical composition on properties, enabling the comparison between different glasses. These four merits open new avenues to the understanding of the structure-property relations in amorphous solids. Finally, we anticipate that our novel structure representation in combination with the

powerful CNN method would find use in the studies of other amorphous matter, beyond metallic glasses.

5.7 Methods

The data used for training and validating deep learning models are from molecular dynamics simulations [180], which are implemented in the LAMMPS package [140].

5.7.1 Preparation of 2D model glasses

2D binary glasses are composed of equal-massed (m) small (S) and large (L) particles which interact via a standard 6-12 Lennard-Jones potential. The full details of the potential are presented elsewhere [190]. We chose our composition such that the ratio between the species is $N_L : N_S = (1+\sqrt{5}) : 4$ to be consistent with previous studies [16,17,55] of this system and each of the sample contains $N = 10,000$ particles. All units will be expressed in terms of m as well as ϵ and σ, the parameters describing the energy and length scale, respectively, of the interparticle interaction. The characteristic time is $t_0 = \sigma\sqrt{m/\epsilon}$. The glass transition temperature T_g of this system is known to be $0.325\epsilon/k_B$ [16, 17, 55], where k_B is the Boltzmann constant. Periodic boundary conditions were imposed on square boxes of linear dimension 98.8045σ. The density of the sys-

tem ($N/L^2 \approx 1.02\sigma^{-2}$) was kept constant. 5,000 2D glass samples were each obtained by continuously decreasing the temperature from a liquid state, well-equilibrated at $1.08T_g$ and quenched to a low-temperature ($0.092T_g$) solid state over a period of $10^6\ t_0$ using a Nose-Hoover thermostat. Then a static relaxation using conjugate gradient algorithm was applied to bring the system to mechanical equilibrium before conducting deformation simulation. Particle positions in this state were used to construct structure representations. Our training, validation and test datasets contained 4,900, 50 and 50 samples, respectively. To demonstrate that the CNN models are valid for the glasses with different processing history, 50 additional samples were quenched from $1.08T_g$ to $0.092T_g$ over different period in the range from $10^5\ t_0$ to $10^0\ t_0$.

5.7.2 Deforming 2D model glasses

Each of the 2D glasses was deformed under four loading conditions (positive and negative simple shear, and positive and negative pure shear) with an athermal quasi static (AQS) method [192, 193]. In positive (negative) simple shear, the applied strain increment was $\Delta\gamma_{xy} = \Delta\gamma$ ($\Delta\gamma_{xy} = -\Delta\gamma$), and in positive (negative) pure shear, the applied strain increments are $\Delta\epsilon_{xx} = -\Delta\epsilon_{yy} = -\Delta\gamma/2$ ($\Delta\epsilon_{xx} = -\Delta\epsilon_{yy} = \Delta\gamma/2$). Here $\Delta\gamma = 10^{-5}$. After each deformation increment, the system was relaxed to its mechanical equilibrium.

5.7.3 Mechanical response of a local 2D configuration at arbitrary orientation

To probe the mechanical response of a local 2D configuration at arbitrary orientation, i.e., the blue dotted curve in the Fig. 5.19, we deleted particles outside the largest circular region from the original square box. Next, we rotated the circular configuration by various angles counter-clockwise, and then conducted simple shear on it with the AQS method. During deformation, the particles in the outer annulus (wall) of width 5σ (two times of potential cutoff) only experience applied affine displacement, i.e., they are not allowed to relax such that the periodic boundary conditions are lost.

5.7.4 Preparation of 3D model glasses

The 3D $Cu_{50}Zr_{50}$ metallic glasses were simulated with an optimized embedded atom method (EAM) potential adopted from Ref. [141]. Each of the 1,500 samples contained 32,000 atoms in a cubic box. After adequate equilibration at 2,000 K, the liquid was first quenched to 1,500 K at a cooling rate of 10^{13} K/s, followed by 10^{12} K/s to 1000 K, then at the desired rate of 10^{10} K/s (effective cooling rate, in the text) to 500 K, and finally at 10^{13} K/s to 50 K in the NPT ensemble using a Nose-Hoover thermostat with zero external pressure. The periodic boundary condition was applied in all three directions. The samples

were then brought to mechanical equilibrium through a static relaxation via a conjugate gradient algorithm. Our training, validation and test datasets for the 3D system contain 1480, 10 and 10 samples, respectively. To demonstrate that the CNN models are valid for glasses with different processing history or at different compositions, 10 $Cu_{50}Zr_{50}$ glasses were also quenched using different effective cooling rates in the range from 10^9 to 10^{13} K/s, and at each different composition (Cu_xZr_{100-x}, x = 20, 25, ..., 80, in step of 5), 10 MG glasses were quenched with an effective cooling rate of 10^{10} K/s.

5.7.5 Deforming 3D model glasses

Before extracting atomic coordinates to construct structure representation and conducting deformation simulation in each of the 24 loading orientations listed in Table 5.1, we rotated each configuration such that the shear direction and the normal direction of the shear plane were parallel to X and Y axis, respectively, of the coordinate system. For some loading orientations, appropriate atom replication was needed after rotation, which is illustrated in Fig. 5.22 and Appendix, section 5.8.5. Each of the 3D glasses was deformed in simple shear along the 24 different loading orientations via an athermal quasi static (AQS) method [192, 193]. After each applied strain increment of $\Delta\gamma_{xy} = 10^{-4}$, the system was relaxed to its mechanical equilibrium. We calculated $D^2_{\min}$ per definition in Ref. [16], implemented in the OVITO package [156].

Table 5.1: The specific shear direction (ι) and the normal direction of the shear plane (η) for the 24 different loading orientations applied on 3D glasses.

#	Shear direction (ι)	Normal direction of shear plane (η)
1	$[1,0,0]$	$[0,1,0]$
2	$[\bar{1},0,0]$	$[0,1,0]$
3	$[1,0,0]$	$[0,0,1]$
4	$[\bar{1},0,0]$	$[0,0,1]$
5	$[0,1,0]$	$[0,0,1]$
6	$[0,\bar{1},0]$	$[0,0,1]$
7	$[1,1,0]$	$[\bar{1},1,0]$
8	$[\bar{1},\bar{1},0]$	$[\bar{1},1,0]$
9	$[1,1,0]$	$[0,0,1]$
10	$[\bar{1},\bar{1},0]$	$[0,0,1]$
11	$[\bar{1},1,0]$	$[0,0,1]$
12	$[1,\bar{1},0]$	$[0,0,1]$
13	$[1,0,1]$	$[\bar{1},0,1]$
14	$[\bar{1},0,\bar{1}]$	$[\bar{1},0,1]$
15	$[1,0,1]$	$[0,1,0]$
16	$[\bar{1},0,\bar{1}]$	$[0,1,0]$
17	$[\bar{1},0,1]$	$[0,1,0]$
18	$[1,0,\bar{1}]$	$[0,1,0]$
19	$[0,1,1]$	$[0,\bar{1},1]$
20	$[0,\bar{1},\bar{1}]$	$[0,\bar{1},1]$
21	$[0,1,1]$	$[1,0,0]$
22	$[0,\bar{1},\bar{1}]$	$[1,0,0]$
23	$[0,\bar{1},1]$	$[1,0,0]$
24	$[0,1,\bar{1}]$	$[1,0,0]$

5.7.6 Upper bound of the prediction accuracy

To assess this ceiling, we make use of the particles from the test dataset, which were already labeled after deformation. Another deformation simulation was then conducted, after shuffling the sequence of all particles, as a new job run on a different computer. The resultant new configuration was used to compute

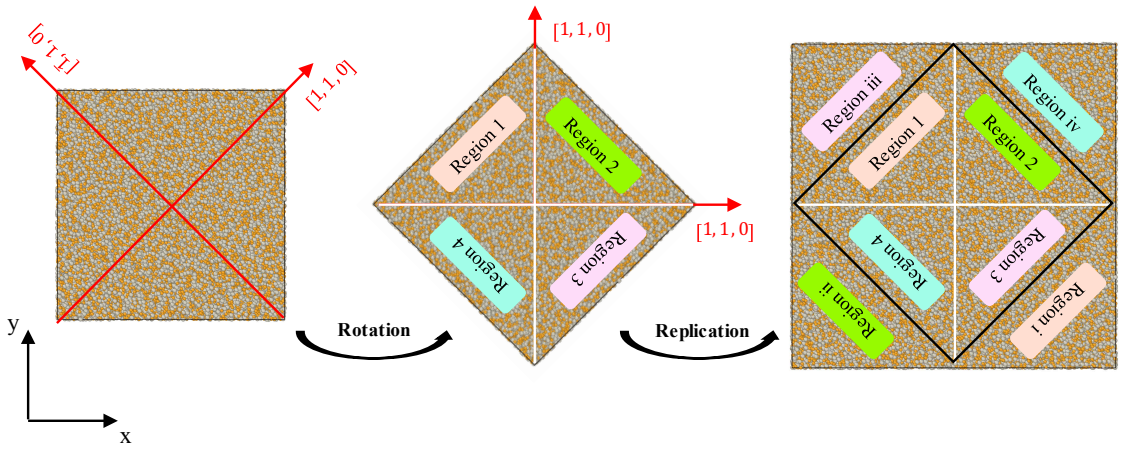

Figure 5.22: Schematic of rotating and replicating configurations in order to deform 3D metallic glasses along desired loading directions.

$D^2_{\min}$ of all the particles, which were labeled again. The number of particles always having the same label, determined based on both the old and the new $D^2_{\min}$, was divided by the total number of particles in the dataset, to give the upper bound of accuracy that can be reached via any method.

5.7.7 Training procedure of CNN models

For the CNN models, we minimized the binary cross-entropy loss between true labels and predicted labels, and used early stopping and selected the model with the highest accuracy in the validation dataset. The learning rate started from 0.001 and was then divided by $\sqrt{10}$ once the validation accuracy plateaued. We chose RMSprop optimizer and mini-batch size of 512 and 64, for the 2D and 3D glasses, respectively. We augmented the training data by applying randomly one of the 4 (or 8) mirror-symmetries to the images of 2D

(or 3D) glasses every time we fed the images into the CNN. The training was implemented in the Tensorflow package [194]. And we conducted distributed deep learning with the Horovod package [195] to accelerate the training for 3D glasses.

5.7.8 GNN methods

We followed the procedure in Ref. [69] to construct graph with edge threshold of 2.0σ (and 4.0Å) for 2D (and 3D) glasses. We used the same GNN architecture as in Ref. [69], except that we activated the output layer with a sigmoid function as we were doing binary classification tasks, and chose n_{rec} = 7 and 6 for 2D and 3D glasses, respectively, according to the optimization results shown in Fig. 5.23. We also tried more neurons in all multilayer perceptors, but this did not further improve the validation accuracy.

For the 2D (3D) samples in both the test and validation datasets, we loaded each sample, and constructed corresponding graph, 4 (24) times, each graph corresponding to one of the 4 (24) loading protocols. And we updated edge vectors of those graphs using relative atomic positions in the new coordinate system, the X and Y axes of which were parallel to the shear direction and the normal of shear plane, respectively, of each specific loading protocol. Atoms were labeled based on the magnitude of D^2_{min}. When evaluating the loss function and accuracy for our GNN models, only the atoms in the test and valida-

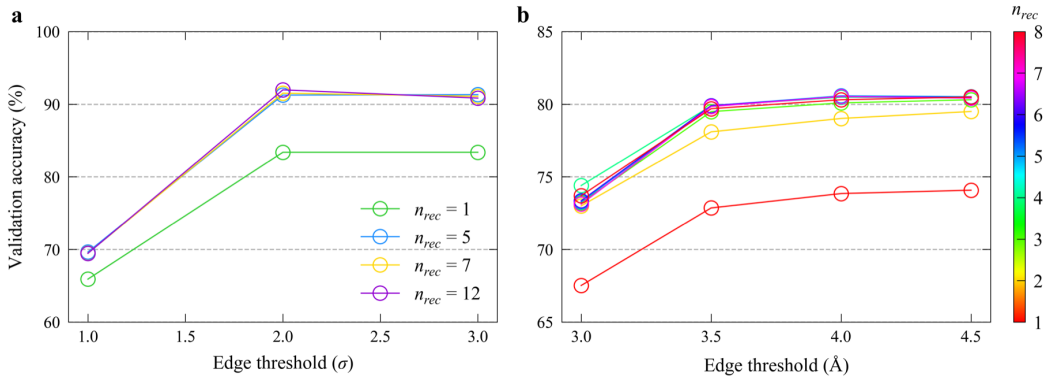

Figure 5.23: Accuracy achieved via GNN, when the hyperparameters are varied, for (a) 2D glasses at strain of 3.0% with f_{thres} of 5.0% and (b) 3D $Cu_{50}Zr_{50}$ glasses at strain of 5.0% with f_{thres} of 0.5%. The edge threshold is varied at a fixed number of unrolls of the network (n_{rec}), and the n_{rec} is varied at a fixed edge threshold.

tion datasets were considered. Therefore, both test and validation datasets for the GNN are exact the same as those for our CNN. For the 2D (3D) samples in training datasets, we constructed only one graph for each sample in order to relieve memory burden and save computation time. However, we took into account all loading directions for each of the 4,900 (1,480) training examples by updating at random their target labels with D^2_{min} from one of the 4 (24) loading protocols and by rotating edge vectors correspondingly every time we fed them (both targets and graphs) to the network (note that in our earlier attempts, we tried to directly construct and load multiple graphs for each training sample, but the results obtained were similar). Also, we augmented the training data by applying randomly one of the 4 (or 8) mirror-symmetries to the edge vectors of graphs of 2D (or 3D) glasses every time we fed the graphs to the GNN. When

optimizing GNN models and evaluating loss function and accuracy, only the atoms in the training datasets were used to enable balanced datasets and a fair comparison with our CNN.

To minimize the binary cross-entropy loss between true labels and predicted labels, similarly to Ref. [69], we used early stopping and selected the model with the highest accuracy on the validation dataset after running enough epochs. We trained the GNN models with a learning rate of 10^{-4}, gradient clipping, Adam optimizer and a Tensorflow implementation.

5.7.9 SVM methods

Same as in Ref. [21], we used the following radial and angular structural functions to construct input features to SVM models:

$$G_{i,\alpha}(r) = \sum_{j\in\alpha, r_{ij}<r_c} \exp(-\frac{(r_{ij}-r)^2}{2\Delta^2}), \tag{5.6}$$

$$\Psi_{i,\alpha,\beta}(\xi,\upsilon,\varpi) = \sum_{j\in\alpha}\sum_{k\in\beta} \exp(-\frac{r_{ij}^2+r_{jk}^2+r_{ik}^2}{\xi^2})(1+\upsilon\cos\theta_{ijk})^{\varpi}, \tag{5.7}$$

where r_{ij} denotes the distance between atom i and j, and α or β denotes the species, θ_{ijk} is the angle between vector $\boldsymbol{r}_{ij}$ and $\boldsymbol{r}_{ik}$, and $r \in [r_0 + 0.5\Delta, r_c)$ with an increment of Δ. We use $r_0 = 0.5\sigma$, $r_c = 5.0\sigma$ and $\Delta = 0.025\sigma$, and $r_0 = 2.0$Å,

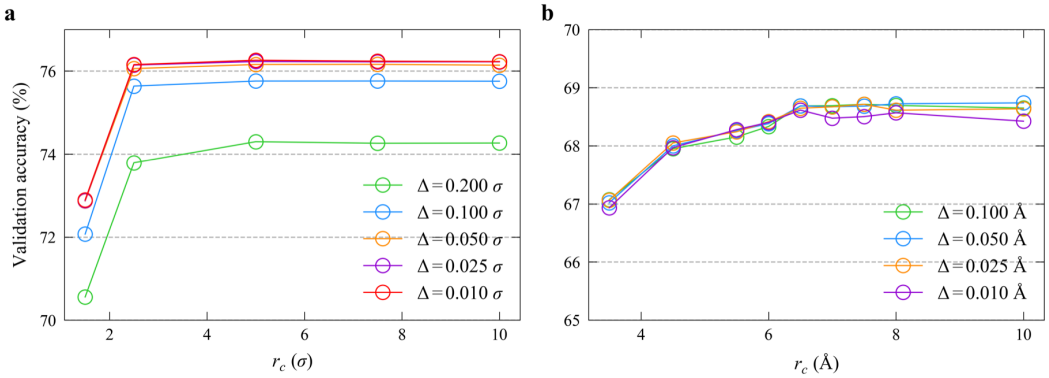

Figure 5.24: Accuracy reached via the SVM models versus r_c and Δ, for (a) 2D glasses at strain of 3.0% with f_{thres} of 5.0%, and (b) 3D $Cu_{50}Zr_{50}$ glasses at strain of 5.0% with f_{thres} of 0.5%. Here the training did not include angular structural functions.

$r_c = 9.6$Å and $\Delta = 0.050$Å for 2D and 3D glasses, respectively, based on the findings in Fig. 5.24. For the parameters in the angular structural functions, similar to Ref. [69], we used $\upsilon \in \{-1, 1\}$, $\varpi \in \{1, 2, 4, 8, 16\}$, and 16 values of ξ equally spaced between 0.75σ and 5.0σ (between 3.0Å and 8.0Å) for 2D (3D) glasses. We tried to use 4, 8, 16, or 32 values for ξ in the give region but found only a weak dependency. We also tried to use exactly the same angular parameters as in the original work [21], but the results came out slightly worse.

We conducted L2-regularized L2-loss support vector classifications with a linear kernel, which were executed in the LIBLINEAR package [170] by solving the primal optimization problem. A regularization parameter of C = 100 was used, as we tried many different values over the range from 10^{-7} to 10^{5} and found only a weak dependency once C was above 10. We also tuned the termination criterion, which did not further improve the accuracy on valida-

Table 5.2: The number of input features and the number of trainable parameters in the various models for 2D L-J glasses.

Model	Number of input features	Number of trainable parameters
SVM	840	841
GNN	∼330,000	70,657
CNN($2r_c/\Delta = 50$, 25 conv. layers)	5,000	5,532,381
CNN($2r_c/\Delta = 100$, 30 conv. layers)	20,000	22,131,101

Table 5.3: The number of input features and the number of trainable parameters in the various models for 3D Cu-Zr glasses.

Model	Number of input features	Number of trainable parameters
SVM	720	721
GNN	∼698,000	70,721
CNN($2r_c/\Delta = 32$, 20 conv. layers)	65,536	1,853,701
CNN($2r_c/\Delta = 50$, 25 conv. layers)	250,000	2,340,601

tion datasets. Note that 500 (100) samples were sufficient to construct training datasets for 2D (3D) glasses, because training the SVM models does not require large datasets, as demonstrated in Fig. 5.16.

Table 5.2 and Table 5.3, for 2D and 3D glasses, respectively, present a summary of the input features and trainable parameters of the three machine learning models.

5.7.10 Calculating the flexibility volume

The flexibility volume is defined as the product of vibrational mean squared displacement (MSD) and atom spacing [78]. We calculated MSD at $0.092T_g$ for

2D glasses and at 50 K for 3D glasses, using the procedure in Ref. [78]. The MSD was averaged over 100 independent runs, all starting from the same configuration but different initial velocities. And the atomic volume is calculated based on Voronoi analysis.

5.7.11 Soft mode analysis

The normal mode analysis of the glasses was carried out by diagonalizing the dynamical matrix of the inherent structure of glasses. The participation fraction of atom i in eigenmode e_ω is $p_i = |\vec{e}_\omega^{\,i}|^2$, where $\vec{e}_\omega^{\,i}$ is the corresponding polarization vector of atom i [142]. Here, p_i was summed over a small fraction of 1% (same as that in Ref. [78] of the lowest-frequency normal modes. p_i measures the involvement of atom i in soft modes.

5.8 Appendix

5.8.1 The choice of $f_{\rm thres}$

We chose $f_{\rm thres}$ = 0.5%, because a previous study [21] found that a higher predictive accuracy can be achieved with a higher $D^2_{\rm min}$ threshold. We confirmed this in Fig. 5.15. The trend for CNN and GNN cannot reflect fully their dependency of accuracy on $f_{\rm thres}$, because large training datasets (see Fig. 5.16) are needed. Here smaller $f_{\rm thres}$ also means smaller training datasets for the same

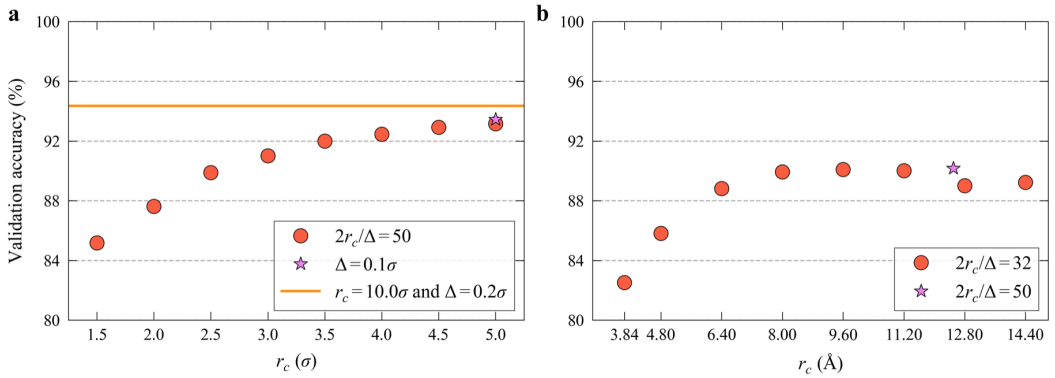

Figure 5.25: Effect of cutoff (r_c) and grid size (Δ) on validation accuracy. (a) 2D glasses at shear strain of 3.0% with f_{thres} of 5.0%. When $r_c = 10.0\sigma$ or $\Delta = 0.1\sigma$, the input images will have 100 $\times$ 100 pixels and thus the corresponding CNN model contains 30 conv. layers. (b) 3D glasses at shear strain of 5.0% with f_{thres} of 0.5%. When $2r_c/\Delta = 50$, the input images will have 50 $\times$ 50 $\times$ 50 pixels and thus the corresponding CNN model contains 25 conv. layers.

number of glass samples. If the training dataset size is the same for different f_{thres}, the accuracy at small f_{thres} is expected to be higher.

5.8.2 The optimization of r_c and Δ for the input features to CNN

During the optimization of CNN models, for 2D glasses we also tried $r_c = 10.0\sigma$ and $\Delta = 0.2\sigma$, or $r_c = 5.0\sigma$ and $\Delta = 0.1\sigma$ with CNN containing 30 conv. layers. We found that the accuracy can increase from 93.16% to 94.28% when using $r_c = 10.0\sigma$, $\Delta = 0.2\sigma$, 30 conv. layers compared to $r_c = 5.0\sigma$, $\Delta = 0.2\sigma$, 25 conv. layers, see Fig. 5.25a. And it is very likely that the accuracy would be higher if there were more training data because the power of deeper CNN models has

to be leveraged with larger training data and, as seen from Fig. 5.16a, validation accuracy did not flatten until the training dataset size increases to ∼19.6 million when training a CNN model containing 25 conv. layers. (Note that for 2D glasses, we did not try 30 conv. layers for f_{thres} =0.5%, because the accuracy achieved with 25 conv. layer is already close to the corresponding ceiling and our training dataset size was only ∼1.96 million when f_{thres} =0.5%, which will not leverage the power of deeper CNN models). For 3D glasses, we tried $r_c = 12.5\text{Å}$ and $\Delta = 0.5\text{Å}$ with CNN containing 25 conv. layers (see Fig. 5.25b), and the possible reasons why it did not improve accuracy significantly are that the current dataset is not big enough and/or a very small mini-batch size of 32 was used due to limited computer memory. These suggest that the accuracy, especially for 3D glasses, can be further improved if more training data and memory are available. However, doubling our current datasets demands huge computation resources. We project that with ever increasing training dataset size the accuracy may approach the upper bound. An example along this line was ResNet [189], which contains more than 100 conv. layers.

5.8.3 The importance of including medium range structural information

We also tried to reduce r_c from its optimized value of 5.0σ (9.6Å) for the 2D (3D) glass, while keeping the same CNN architecture and same ratio of $2r_c/\Delta$. As

shown in Fig. 5.25, the validation accuracy decreases gradually. This demonstrates the importance of including surrounding particles beyond the first nearest neighbor shell in predicting plastic susceptibility, and in particular the environment in the medium range on the order of 1 nm.

5.8.4 Training all species together versus training each species separately

We found that training each species separately could not improve significantly the accuracy achieved for our CNN model, see Fig. 5.26. Although training single species seems more effective, it also means smaller dataset size. In addition, training all species together in a single model is also easier to implement and use.

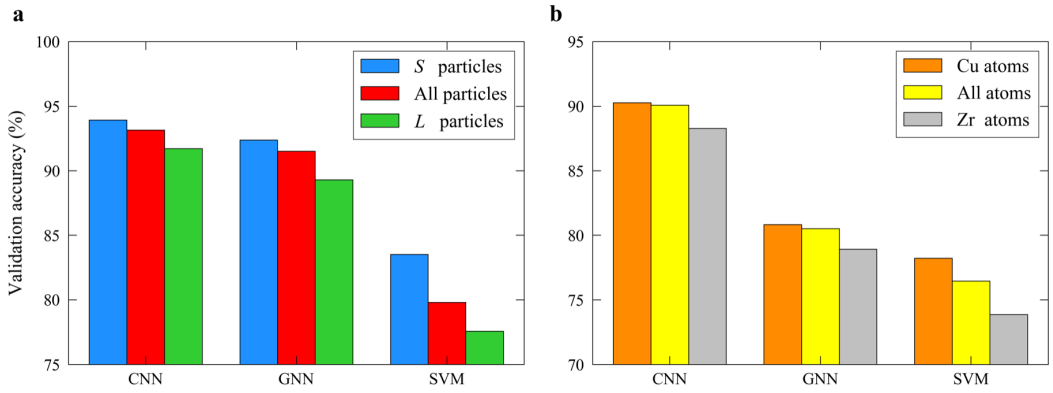

Figure 5.26: Effect on validation accuracy, comparing training each species separately with training all species together. (a) 2D glasses at shear strain of 3.0% with f_{thres} of 5.0%. (b) 3D $Cu_{50}Zr_{50}$ glasses at shear strain of 5.0% with f_{thres} of 0.5%.

5.8.5 Rotating and replicating 3D configurations for shearing along desired loading directions

In the LAMMPS package, the configurations with periodic boundary conditions in all three directions have to be cuboids, of which all the edges are parallel to the axes of the coordinate system. Thus, for the loading orientations of #7-24 listed in Table 5.1, after appropriate rotation such that the shear direction and the normal direction of the shear plane are parallel respectively to X and Y axis of the coordinate system, we have to conduct appropriate replication to perform subsequent deformation simulations. Here we give an example to illustrate our specific operations. As shown in Fig. 5.22, we first rotate the configurations such that $[1,1,0]$ and $[\bar{1},1,0]$ are parallel to the X and Y axis, respectively, of the coordinate system, and then divide the configuration into four regions (Region 1, 2, 3 and 4, as illustrated in Fig. 5.22) and replicate atoms in each region and move these replicated atoms to the corresponding regions i, ii, iii and iv, respectively. This led us to a cuboid cell containing 64,000 atoms, with all edges parallel to $[1,1,0]$, $[\bar{1},1,0]$ or $[0,0,1]$. Finally, we can shear the box in the desired direction (the orientations of #7-12) after appropriate rotation. Similarly, one can rotate the configurations such that $[1,0,1]$ and $[\bar{1},0,1]$ ($[0,1,1]$ and $[0,\bar{1},1]$) are parallel to X and Y axis, respectively, and conduct similar replications and rotations to shear samples along the loading orientations of #13-18 (#19-24).

For all these shear simulations of cuboidal box containing 64,000 atoms, we have confirmed that the D^2_{min} of the replicated atoms is practically the same as that of the original atoms and we select atoms solely from the original atoms to construct training/validating/test datasets.

Chapter 6

Predicting the location of shear band initiation in a metallic glass

6.1 Introduction

The dominant mechanical failure mode in metallic glasses (MGs) is shear banding, a plastic instability that localizes large amounts of shear strain within a narrow region when a MG is deformed [28, 30, 33, 196, 197]. Understanding and controlling the shear banding behavior is of importance for enhancing the ductility of MGs, and thus, shear banding has been a research focus in the MG community over the past few decades [17, 18, 145, 198–208]. However, owing to the disordered structure of MGs and the lack of well-defined topological defects

like dislocations, it remains an open question whether one can identify *a priori* where shear bands will initiate solely based upon their initial undeformed static structure.

Previous research [145, 205] has demonstrated that a shear band is formed by the coalescence of a series of adjacent shear transformation zones (STZs) [16], elementary plastic events that occur under externally applied stresses. One possible conjecture is that one would be able to predict where shear bands initiate in MGs if one were to know which atoms will be involved in STZs under a specific loading condition *a priori* solely from the initial static structure. In chapter 5, we showed that even at 10% strain (around the yielding point) the atoms which will experience extremely large plastic rearrangement can be identified *a priori* with high accuracy solely from the static structure in the initial glassy sample before deformation. This was achieved through the combination of a novel structural representation and a powerful convolutional neural network (CNN). In this chapter, these atoms with high predicted plastic susceptibility (class probability > 0.5) will be referred to as fertile sites for shear transformation, and we will demonstrate that shear bands prefer to initiate around regions with a high density of such fertile sites in simulated $Cu_{50}Zr_{50}$ MGs.

6.2 Initiation sites of shear bands in a MG

It was observed in a recent study [209] that for identical Lennard-Jones glass models, small changes in the deformation protocol, such as the use of different initial random numbers for the thermostat, can change the flow patterns from vertical to horizontal bands, and vice versa. This occurs even though the shear deformation was conducted at very low temperature. From this the authors concluded that the initial undeformed glass sample does not determine whether and where shear bands will form. Rather, they assert that the formation of shear band is linked to stochasticity. We have also observed that the resultant deformation under athermal quasi-static shear (AQS) [192, 193] is not exactly reproducible when the atom sequence in the initial configuration file is changed while keeping all other deformation conditions same. Furthermore, the larger the strain, the larger the difference between simulations with different atom sequences. Therefore, we must first examine if the location at which the shear band initiates is reproducible so long as the MG model is the same and is subjected to the same loading conditions. To this end, we shear the same $Cu_{50}Zr_{50}$ MG consisting of 32,000 atoms quenched at an effective cooling rate of 10^{10} K/s (see method section 6.6 for more details regarding the sample preparation) twice under exactly the same loading condition with the AQS method on the same computer. The only difference between the two defor-

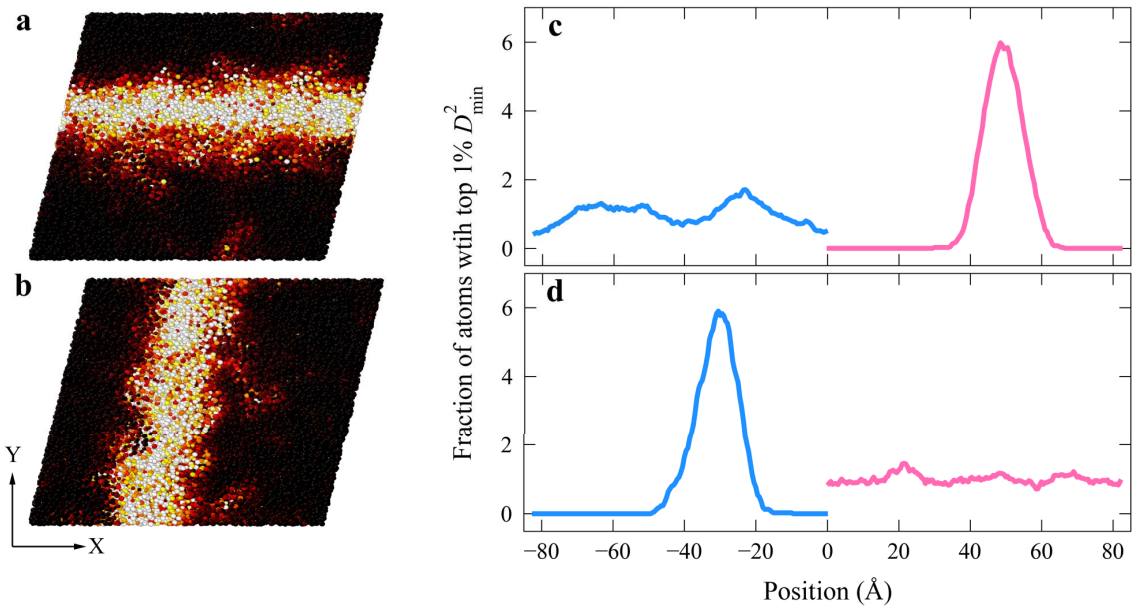

Figure 6.1: Location of shear bands in a MG. (a) and (b) show the colored map of D^2_{min} at strain of 20% after athermal quasistatic shear for a $Cu_{50}Zr_{50}$ MG sample under the same loading condition but from two simulation runs in which the only difference is the atom sequence in the intitial configuration file. On the two maps, bright (dark) color represents large (small) D^2_{min}. (c) and (d) show the distribution of the fraction of atoms with top 1% D^2_{min} for the D^2_{min} field shown in (a) and (b), respectively. The location of the distribution along X axis (blue curve) was multiplied by -1 in order to differentiate it from that of the distribution along Y axis (pink curve).

mation simulations is the atom sequence in the file of the initial undeformed configuration.

Fig. 6.1a and b show the field of deviation from affine displacement (D^2_{min}) [16] at 20% strain for the two simulations. As can been seen from the two D^2_{min} fields, a horizontal shear band (the bright region in Fig. 6.1a, parallel to X axis along the shear direction) formed in one simulation while a vertical shear band (the bright region in Fig. 6.1b, parallel to Y axis perpendicular to the shear direction) formed in another simulation. This suggests that the location of a

shear band is not fully reproducible for the same MG model under athermal conditions. We cannot, however, conclude that the formation of shear bands is fully stochastic. In order to examine the deterministic aspects of shear band formation, we must first introduce a methodology for determining the center position of each shear band.

In our simulations, only one shear band occurs in each sample, so we determine the position of the shear band by calculating the locations of the atoms in the top 1% ($= f_{\text{top}}$) of the D^2_{min} distribution at 20% shear strain. We will refer to these atoms as the "highly deformed atoms." As the shear bands have two possible orientations (horizontal or vertical), the distribution along both X and Y axes are examined. We calculate the fraction of highly deformed atoms within parallelepipeds that have a width along the X axis $\omega_{\text{SB}} = 10\text{Å}$. The length along all other dimensions are equal to that of the simulation box. We will denote the middle point of each parallelepiped aligned with the X axis as x. Similarly, we calculate the fraction of highly deformed atoms along the Y axis at the locations denoted y.

To differentiate the locations along the X and Y axes, the coordinate along X axis was multiplied by -1. Thus for a horizontal shear band, the peak position of the the distribution should be positive while the peak position is negative for a vertical shear band. Fig. 6.1c and d display the distribution of the fraction of highly deformed atoms corresponding to Fig. 6.1a and b, respectively.

Systematically varying the values for both f_{top} and ω_{SB} does not result in large changes in the center position.

6.3 Predicting shear band locations from initial density of fertile sites

If the location of the initiation of a shear band is predictable, deforming the same glassy sample multiple times under identical loading condition should result in repeated shear band initiation at highly correlated locations. To test whether this is the case, we sheared a same $Cu_{50}Zr_{50}$ MG sample 100 times under identical loading condition using the AQS method. Before each simulation run, the atom sequence was reshuffled. The blue curve (right vertical axis) in Fig. 6.2 shows the number of shear bands initiated at each position. Shear bands are observed to initiate predominately around two regions, implying that the shear band location is predictable from initial static structure, and that the strain localization process is not fully stochastic. Based on the reasoning presented in section 6.1, we anticipate that the density of fertile sites (DFS) predicted with the CNN model introduced in chapter 5 should be measurably higher around the two peak positions of the blue curve shown in Fig. 6.2 relative to other regions.

To test this hypothesis, we took an approach similar to that used to deter-

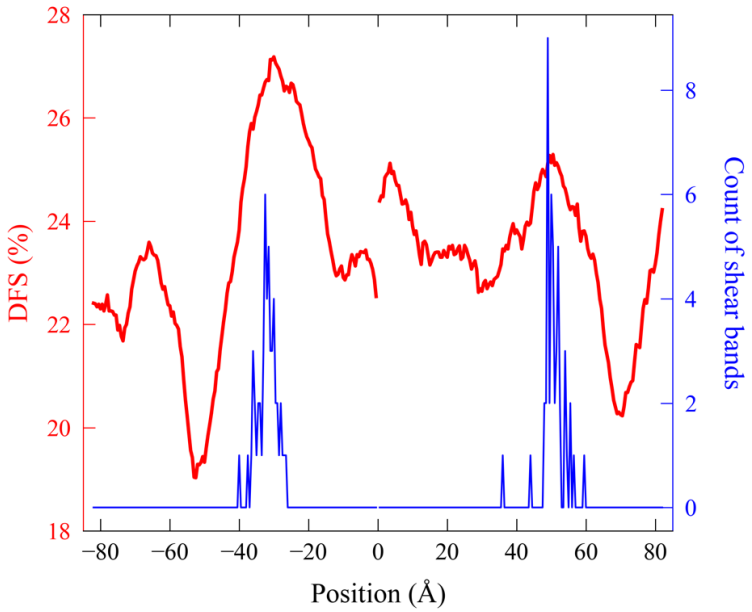

Figure 6.2: Connection between initial distribution of density of fertile sites and final location of a shear band in a $Cu_{50}Zr_{50}$ MG. The red curve (left vertical axis) displays the initial distribution of CNN- predicted density of fertile sites (DFS), and the blue curve (right vertical axis) shows the number of shear bands initiated at each position after shear the same MG 100 times under exactly the same loading condition but with different atom sequence.

mine the center position of shear bands. We calculated the distribution of the DFS in the sample before deformation, i.e., fraction of atoms with class probability > 0.5 in each of the parallelepiped regions. Here we chose a value of 16 $\mathring{\text{A}}$ for ω_{DFS}, the width of the parallelepiped along X (or Y) dimension. The reason why we set $\omega_{\text{DFS}} = 16\mathring{\text{A}}$ will be presented later. The red curve (left vertical axis) in Fig. 6.2 displays the initial distribution of the DFS in the sample. Indeed, the peak positions of the distribution of the DFS closely overlap with the peaks of the blue curve in Fig. 6.2, which is consistent with our expectation and suggests there is strong correlation between initial static structure, i.e. the DFS

predicted with our CNN model, and the sites of shear band initiation in MGs.

6.4 Figure of merit for the correlation

In the preceding section, we showed that the shear band location is potentially predictable solely based on the initial DFS distribution in a MG. In this section, we evaluate the predictive power of this approach by surveying 480 cases. To do this we prepared 20 $Cu_{50}Zr_{50}$ MG samples (not used in the training of our CNN model) and then sheared each of the 20 sample to 20% strain with the AQS method along 24 loading orientations using the strategy introduced in Table 5.1 in chapter 5. For each sample in each loading orientation, we first map out the CNN-predicted DFS along both the X and Y dimensions. Inspired by the methodology introduced in Ref. [72], we then define a parameter γ as a figure of merit, the fraction of locations at which the DFS is lower than or equal to, that at the location of the shear band. If the shear band preferentially initiates in the region having the highest DFS, γ would approach 1.0 for all cases, and the cumulative distribution function $C(\gamma)$ of γ would be a step function: $C(\gamma) = 1$ for $\gamma = 1$ and 0 otherwise. At the other extreme, if there is no correlation between the DFS and the location of shear band initiation, the value of γ should be stochastic and $C(\gamma)$ should be close to a straight line, i.e., the dashed diagonal line in Fig. 6.3a. The resulting $C(\gamma)$ data are denoted by the red curve in Fig. 6.3a, revealing a positive correlation.

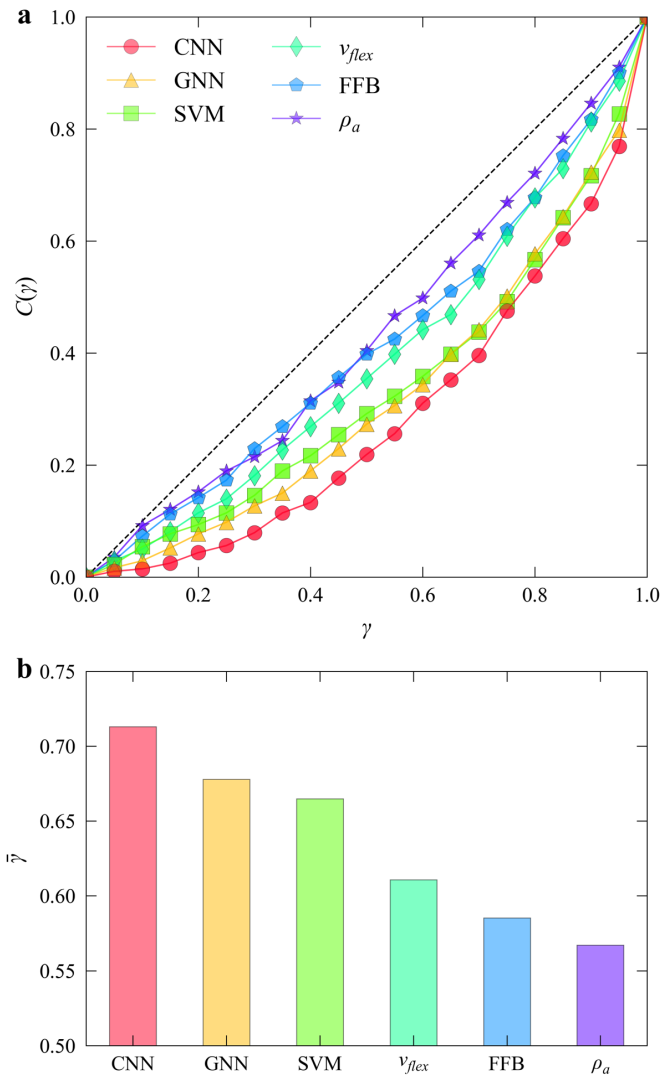

Figure 6.3: Quantifying and comparing the predictive power of different methods in regards to shear band formation. (a) shows the cumulative distribution function $C(\gamma)$ of γ (see text) for the predictions based on six different methods: CNN, graph neural network (GNN), linear support vector machine (SVM), flexibility volume (v_{flex}), five-fold bonds (FFB) and atom density (ρ_a). The diagonal dashed line represents random distribution with no correlation. A perfect prediction would entail $C(\gamma) = 1$ for $\gamma = 1$ and 0 otherwise. (b) shows $\bar{\gamma}$ (arithmetic mean of γ) for the prediction based on the six methods. $\bar{\gamma} = 0.5$ means no predictive power and $\bar{\gamma} = 1.0$ perfect predictive power.

To show the advantage of our CNN-predicted DFS, we compare with predictions based on other data-driven models such as that derived from a graph neural network (GNN) [69], a linear support vector machine (SVM) [21], and three methods based on physical parameters, flexibility volume (v_{flex}) [78], fraction of five-fold bonds (FFB) [61] and the atomic density in the local region (ρ_a, an analog for free volume [26, 43]). These metrics were all previously used in attempts to predict stress-driven shear transformations. Specifically, the fertile sites are defined as those atoms with GNN-predicted class probability $>$ 0.5, or SVM-predicted distance to the separation boundary $>$ 0, or within the top 20% of the values of v_{flex}. For FFB and ρ_a, a lower value is expected to be more favorable for shear band initiation; we therefore modify γ as the fraction of locations at which the density of FFBs or ρ_a is higher than or equal to that in the region where a shear band is initiated. As seen from Fig. 6.3a, the prediction based on our CNN-predicted DFS is superior to those from all the other five methods.

We also can use $\bar{\gamma}$ (the arithmetic mean of γ) to quantify the predictive power for these methods as $\bar{\gamma} = 1.0$ corresponds to perfect prediction and $\bar{\gamma} = 0.5$ would imply no correlation. As seen from the bar chart shown in Fig. 6.3b, the $\bar{\gamma}$ of 0.713 for our CNN-based prediction is the highest.

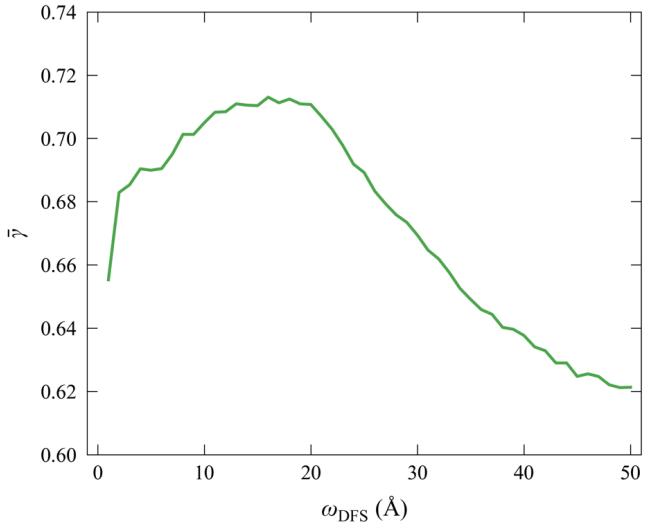

Figure 6.4: The dependency on ω_{DFS} of $\bar{\gamma}$ for our CNN-based prediction.

We tried various values for ω_{DFS} when calculated the DFS and found that when $\omega_{\mathrm{DFS}} = 16\text{Å}$, the $\bar{\gamma}$ is the highest for forecasting the initiation of the 480 shear bands, see Fig. 6.4, which is the reason why we set $\omega_{\mathrm{DFS}} = 16\text{Å}$.

6.5 Summary

In summary, through shearing the same simulated MG sample under the same loading condition using the AQS method and varying atom sequence in the initial configuration, we found that shear bands prefer to initiate around regions with higher CNN-based predicted DFS, although this correlation is not perfect. We defined a figure of merit to quantify the correlation strength between CNN-based predicted DFS and the shear band initiation in the MG samples. We find that this method is superior to the prediction based on a number of

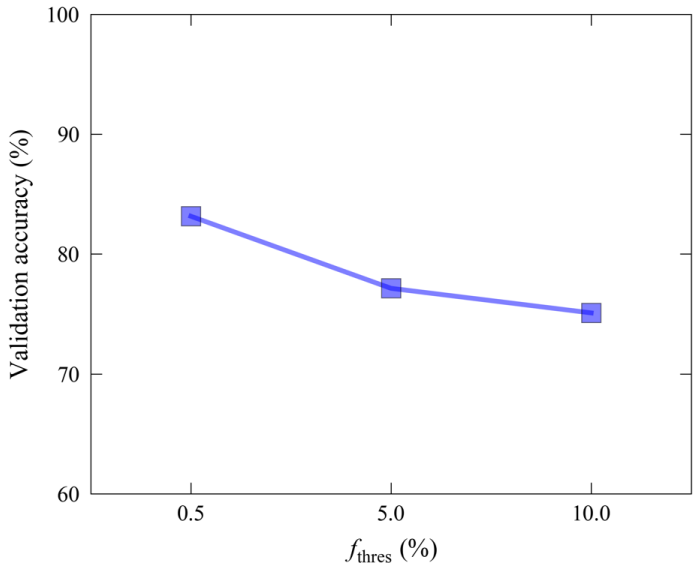

Figure 6.5: The validation accuracy of CNN model trained with various f_{thres}.

other structural indicators suggested previously. To the best of our knowledge, this is the first evidence of correlation between the initial static structure and shear banding behavior in MGs. The demonstrated correlation may be useful to establish robust physical models of plastic behavior in amorphous solids. It also provides some optimism for controlling shear banding behavior and thus optimizing mechanical properties of MGs via the tuning of their initial structural state before deformation.

6.6 Methods

The $Cu_{50}Zr_{50}$ MG samples used in the current work for training, validating and testing CNN and other machine learning models are the same samples used in

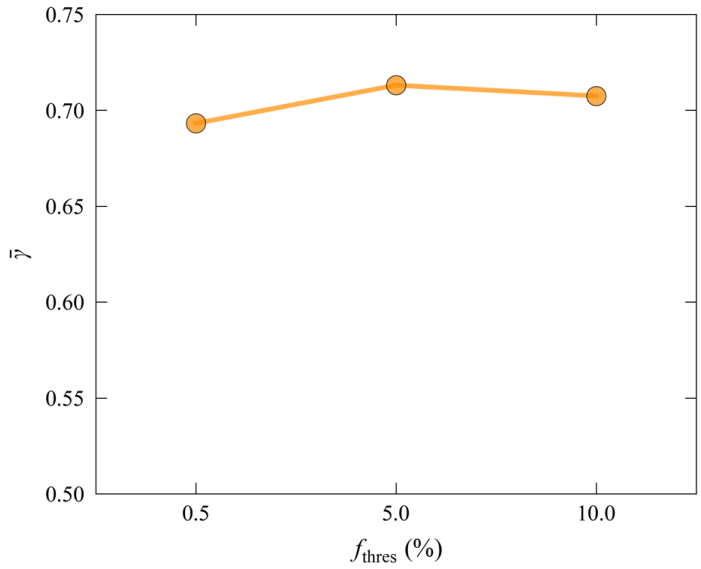

Figure 6.6: The $\bar{\gamma}$ for predicting shear band initiation with the distribution of DFS predicted with CNN model trained with various f_{thres}.

chapter 5. The 20 samples used to predicting shear band initiation were only involved in constructing the validation or test datasets. These 20 sample were never seen in the training stage.

The deformation simulation and the calculation of D^2_{min} also follow the procedure presented in chapter 5. The visualization of D^2_{min} field was performed using the OVITO package [156].

The structural representation and training procedure for all deep or machine learning methods in the current work also follow the procedures detailed in chapter 5. In the main text of this work, the fertile sites were predicted using the CNN, GNN or SVM model, each of which was trained at a strain of 10% with f_{thres} =5.0% based on the results shown in the Figs. 6.5 and 6.6.

The five-fold bonds can be identified after conducting the Voronoi tessellation analysis. And the calculation of flexibility volume is described in chapter 5.

Chapter 7

Conclusion and Outlook

Through systematic analysis of atomistic models of glasses as discussed in this dissertation we have been able to draw some important conclusions regarding the structures of amorphous materials and how these result in their properties. In particular, the strong correlation between flexibility volume and multiple properties of amorphous silicon models as well as the previous work on metallic glasses by Ding *et. al.* [78], suggest that flexibility volume can serve as a universal indicator of the structural state of a glass, applicable across disordered materials with different chemical bonding and atomic packing structures. The flexibility available in the amorphous structure can be used to explain aspects of the plastic flow observed in recent experiments on both metallic glasses and covalently-bonded open network glasses. Based upon this, several feasible ap-

proaches were suggested to tune the degree of flexibility.

This dissertation also details methods capable of revealing the power of *static* structure in predicting properties of amorphous solids using the state-of-the-art machine/deep learning technologies. With the help of linear support vector machine which is a simple machine learning algorithm, we showed that the degree of flexibility of local configurations inside glasses can be evaluated solely from static structural information, i.e., local radial density distribution information, which can be obtained relatively easily. We also achieved the highest accuracy so far in predicting orientation-dependent plastic susceptibility of amorphous solids merely from static structural information, which was realized by designing a new rotation-variant structure representation, in conjunction with convolutional neural network. In addition, the critical structure features responsible for the anisotropy of local mechanical response in glasses was revealed. Finally, it was demonstrated that the location of shear band initiation is predictable from the initial undeformed static structural state of glasses.

Some contents in the chapter 2, 3 and 4 were published on the journals of Physical Review B 2017, Materials Research Letters 2018, and Materials Today 2020, respectively, see Ref. [77, 79, 80]. Some contents presented in chapter 5 are now under review for publication, and related contents in chapter 6 will be submitted soon for publication.

These contributions above are expected to enhance our understanding of structure-property relationships in amorphous solids and to prove useful in searching for amorphous materials with desired performance characteristics. In addition, the deep learning strategy designed in this work is anticipated to be useful in resolving other challenges in materials science and engineering.

Although the achievements presented in this thesis are exciting, there remains much related work to do.

Firstly, the data-driven models established in chapter 4 and 5 are only applicable to glasses at different compositions within the same alloy system. Additional investigation is needed to establish data-driven models applicable to glasses across different compositions across different alloy systems. A more universal data-driven model is desirable as it would enable comparing of properties, such as flexibility or plastic susceptibility, of glasses from different alloy systems.

Secondly, the results discussed here raise the question as to whether it may be possible to establish a robust theory for formulating the mechanical response of amorphous solids based on the plastic susceptibility of each particle in a glass as predicted by a deep learning model. This requires further exploration.

Thirdly, although we achieved unprecedented accuracy in predicting properties of amorphous solids with a deep learning model, so far it is still a grand

challenge to understand how such data-driven models achieve these impressive results. It remains desirable to devise physical models with similar or even higher predictive power for amorphous solids.

This thesis is mainly focused on mechanical properties of amorphous solids and another important property, glass-forming ability, is beyond the scope of this thesis but still warrants extensive investigations. Since the underlying physics that controls glass-forming ability remains elusive, opportunities remain in this area. Advances in understanding the glass transition itself are crucial in searching for materials with high glass-forming ability.

Bibliography

[1] Callister WD. Materials science and engineering an introduction. John Wiley; 2007.

[2] Hirth J, Lothe J. Theory of Dislocations. John Wiley & Sons; 1982.

[3] Taylor Geoffrey Ingram, Quinney H. The latent energy remaining in a metal after cold working. Proceedings of the Royal Society of London Series A, Containing Papers of a Mathematical and Physical Character. 1934;143(849):307–326.

[4] Hall EO. The Deformation and Ageing of Mild Steel: III Discussion of Results. Proc Phys Soc B. 1951;64(9):747–753.

[5] PETCH NJ. The Cleavage Strength of Polycrystals. Journal of the Iron and Steel Institute. 1953;174:25–28.

[6] Ma E, Zhang Z. Reflections from the glass maze. Nature materials. 2011; 10(1):10–11.

[7] Klement W, Willens R, Duwez P. Non-crystalline structure in solidified gold–silicon alloys. Nature. 1960;187(4740):869–870.

[8] Greer A. Metallic glasses. Science. 1995;267(5206):1947–1953.

[9] Johnson WL. Bulk Glass-Forming Metallic Alloys: Science and Technology. MRS Bulletin. 1999;24(10):42–56.

[10] Wang WH, Dong C, Shek CH. Bulk metallic glasses. Materials Science and Engineering: R: Reports. 2004;44(2):45–89.

[11] Schroers J. Bulk Metallic Glasses. Physics today. 2013;66(2):32.

[12] Polk D. Structural model for amorphous silicon and germanium. Journal of Non-Crystalline Solids. 1971;5(5):365–376.

[13] Safarik DJ, Schwarz RB. Elastic constants of amorphous and single-crystal Pd40Cu40P20. Acta Materialia. 2007;55(17):5736–5746.

[14] Wagner H, Bedorf D, Küchemann S, et al. Local elastic properties of a metallic glass. Nature Materials. 2011;10(6):439–442.

[15] Liu YH, Wang D, Nakajima K, et al. Characterization of Nanoscale Mechanical Heterogeneity in a Metallic Glass by Dynamic Force Microscopy. Phys Rev Lett. 2011;106(12):125504.

[16] Falk ML, Langer JS. Dynamics of viscoplastic deformation in amorphous solids. Phys Rev E. 1998;57(6):7192–7205.

[17] Shi Y, Falk ML. Strain Localization and Percolation of Stable Structure in Amorphous Solids. Phys Rev Lett. 2005;95(9):095502.

[18] Shi Y, Falk ML. Atomic-scale simulations of strain localization in three-dimensional model amorphous solids. Phys Rev B. 2006;73(21):214201.

[19] Manning ML, Liu AJ. Vibrational Modes Identify Soft Spots in a Sheared Disordered Packing. Phys Rev Lett. 2011;107(10):108302.

[20] Fan Y, Iwashita T, Egami T. How thermally activated deformation starts in metallic glass. Nature Communications. 2014;5:5083.

[21] Cubuk E, Schoenholz S, Rieser J, et al. Identifying Structural Flow Defects in Disordered Solids Using Machine-Learning Methods. Phys Rev Lett. 2015;114(10):108001.

[22] Cubuk ED, Ivancic RJS, Schoenholz SS, et al. Structure-property relationships from universal signatures of plasticity in disordered solids. Science. 2017;358(6366):1033–1037.

[23] Cheng YQ, Ma E. Atomic-level structure and structure–property relationship in metallic glasses. Progress in Materials Science. 2011; 56(4):379–473.

[24] Ma E. Tuning order in disorder. Nature Materials. 2015;14(6):547–552.

[25] Ma E, Ding J. Tailoring structural inhomogeneities in metallic glasses to enable tensile ductility at room temperature. Materials Today. 2016; 19(10):568–579.

[26] Spaepen F. A microscopic mechanism for steady state inhomogeneous flow in metallic glasses. Acta Metallurgica. 1977;25(4):407–415.

[27] Johnson W, Samwer K. A universal criterion for plastic yielding of metallic glasses with a $(T/T_g)^{2/3}$ temperature dependence. Physical review letters. 2005;95(19):195501.

[28] Schuh CA, Hufnagel TC, Ramamurty U. Mechanical behavior of amorphous alloys. Acta Materialia. 2007;55(12):4067–4109.

[29] Greer AL, Ma E. Bulk Metallic Glasses: At the Cutting Edge of Metals Research. MRS Bulletin. 2007;32(8):611–619.

[30] Greer AL, Cheng YQ, Ma E. Shear bands in metallic glasses. Materials Science and Engineering: R: Reports. 2013;74(4):71–132.

[31] Zylberg J, Lerner E, Bar-Sinai Y, et al. Local thermal energy as a structural indicator in glasses. PNAS. 2017;114(28):7289–7294.

[32] Ding J, Ma E. Computational modeling sheds light on structural evolution in metallic glasses and supercooled liquids. npj Computational Materials. 2017;3(1):9.

[33] Chen M. Mechanical Behavior of Metallic Glasses: Microscopic Understanding of Strength and Ductility. Annual Review of Materials Research. 2008;38(1):445–469.

[34] Hufnagel TC, Schuh CA, Falk ML. Deformation of metallic glasses: Recent developments in theory, simulations, and experiments. Acta Materialia. 2016;109:375–393.

[35] Argon AS. Plastic deformation in metallic glasses. Acta Metallurgica. 1979;27(1):47–58.

[36] Pan D, Inoue A, Sakurai T, et al. Experimental characterization of shear transformation zones for plastic flow of bulk metallic glasses. PNAS. 2008;105(39):14769–14772.

[37] Zhu F, Nguyen HK, Song SX, et al. Intrinsic correlation between β-relaxation and spatial heterogeneity in a metallic glass. Nat Commun. 2016;7(1):1–7.

[38] Zhu F, Hirata A, Liu P, et al. Correlation between Local Structure Order and Spatial Heterogeneity in a Metallic Glass. Phys Rev Lett. 2017; 119(21):215501.

[39] Zhu F, Song S, Reddy KM, et al. Spatial heterogeneity as the structure

feature for structure–property relationship of metallic glasses. Nature Communications. 2018;9(1):3965.

[40] Rodney D, Tanguy A, Vandembroucq D. Modeling the mechanics of amorphous solids at different length scale and time scale. Modelling Simul Mater Sci Eng. 2011;19(8):083001.

[41] Oleinik EF, Mazo MA, Kotelyanskii MI, et al. Plastic Deformation in Disordered Solids: The State of the Art and Unresolved Problems. In: Andrianov IV, Manevich AI, Mikhlin YV, et al., editors. Problems of Nonlinear Mechanics and Physics of Materials. Cham: Springer International Publishing; 2019. Advanced Structured Materials; p. 313–332.

[42] Richard D, Ozawa M, Patinet S, et al. Predicting plasticity in disordered solids from structural indicators. arXiv:200311629 [cond-mat]. 2020;.

[43] Cohen MH, Turnbull D. Molecular Transport in Liquids and Glasses. The Journal of Chemical Physics. 1959;31(5):1164–1169.

[44] Cohen MH, Grest GS. Liquid-glass transition, a free-volume approach. Phys Rev B. 1979;20(3):1077–1098.

[45] Egami T. Atomic level stresses. Progress in Materials Science. 2011; 56(6):637–653.

[46] Widmer-Cooper A, Harrowell P. Free volume cannot explain the spatial

heterogeneity of Debye-Waller factors in a glass-forming binary alloy. Journal of Non-Crystalline Solids. 2006;352(42):5098–5102.

[47] Demkowicz MJ, Argon AS. High-Density Liquidlike Component Facilitates Plastic Flow in a Model Amorphous Silicon System. Phys Rev Lett. 2004;93(2):025505.

[48] Demkowicz MJ, Argon AS. Liquidlike atomic environments act as plasticity carriers in amorphous silicon. Phys Rev B. 2005;72(24):245205.

[49] Demkowicz MJ. Mechanisms of plastic deformation in amorphous silicon by atomistic simulation using the stillinger-weber potential [dissertation]. Massachusetts Institute of Technology; 2005.

[50] Srolovitz D, Maeda K, Vitek V, et al. Structural defects in amorphous solids Statistical analysis of a computer model. Philosophical Magazine A. 1981;44(4):847–866.

[51] Demetriou MD, Harmon JS, Tao M, et al. Cooperative Shear Model for the Rheology of Glass-Forming Metallic Liquids. Phys Rev Lett. 2006; 97(6):065502.

[52] Johnson WL, Demetriou MD, Harmon JS, et al. Rheology and Ultrasonic Properties of Metallic Glass-Forming Liquids: A Potential Energy Landscape Perspective. MRS Bulletin. 2007;32(8):644–650.

[53] Tsamados M, Tanguy A, Goldenberg C, et al. Local elasticity map and plasticity in a model Lennard-Jones glass. Phys Rev E. 2009; 80(2):026112.

[54] Ding J, Patinet S, Falk ML, et al. Soft spots and their structural signature in a metallic glass. PNAS. 2014;111(39):14052–14056.

[55] Patinet S, Vandembroucq D, Falk ML. Connecting Local Yield Stresses with Plastic Activity in Amorphous Solids. Phys Rev Lett. 2016; 117(4):045501.

[56] Badrinarayanan P, Zheng W, Li Q, et al. The glass transition temperature versus the fictive temperature. Journal of Non-Crystalline Solids. 2007;353(26):2603–2612.

[57] Ketkaew J, Chen W, Wang H, et al. Mechanical glass transition revealed by the fracture toughness of metallic glasses. Nature Communications. 2018;9(1):3271.

[58] Xu B, Falk ML, Li J, et al. Predicting Shear Transformation Events in Metallic Glasses. Phys Rev Lett. 2018;120(12):125503.

[59] Liu C, Guan P, Fan Y. Correlating defects density in metallic glasses with the distribution of inherent structures in potential energy landscape. Acta Materialia. 2018;161:295–301.

[60] Ding J, Cheng YQ, Ma E. Full icosahedra dominate local order in $Cu_{64}Zr^{36}$ metallic glass and supercooled liquid. Acta Materialia. 2014; 69:343–354.

[61] Peng HL, Li MZ, Wang WH. Structural Signature of Plastic Deformation in Metallic Glasses. Phys Rev Lett. 2011;106(13):135503.

[62] Peng CX, Şopu D, Song KK, et al. Bond length deviation in CuZr metallic glasses. Phys Rev B. 2017;96(17):174112.

[63] Steinhardt PJ, Nelson DR, Ronchetti M. Bond-orientational order in liquids and glasses. Phys Rev B. 1983;28(2):784–805.

[64] Berthier L, Biroli G, Bouchaud JP, et al. Dynamical heterogeneities in glasses, colloids, and granular media. Vol. 150. OUP Oxford; 2011.

[65] Jordan M, Kleinberg J, Schölkopf B. Information science and statistics. Springer; 2006.

[66] James G, Witten D, Hastie T, et al. An introduction to statistical learning. Vol. 112. Springer; 2013.

[67] Behler J, Parrinello M. Generalized neural-network representation of high-dimensional potential-energy surfaces. Physical review letters. 2007;98(14):146401.

[68] Wang Q, Jain A. A transferable machine-learning framework linking interstice distribution and plastic heterogeneity in metallic glasses. Nature Communications. 2019;10(5537):5537.

[69] Bapst V, Keck T, Grabska-Barwińska A, et al. Unveiling the predictive power of static structure in glassy systems. Nature Physics. 2020; 16(4):448–454.

[70] Battaglia PW, Hamrick JB, Bapst V, et al. Relational inductive biases, deep learning, and graph networks. arXiv preprint arXiv:180601261. 2018;.

[71] Barbot A, Lerbinger M, Hernandez-Garcia A, et al. Local yield stress statistics in model amorphous solids. Phys Rev E. 2018;97(3):033001.

[72] Schwartzman-Nowik Z, Lerner E, Bouchbinder E. Anisotropic structural predictor in glassy materials. Phys Rev E. 2019;99(6):060601.

[73] Xu B, Falk ML, Patinet S, et al. Atomic nonaffinity as a predictor of plasticity in amorphous solids. arXiv:190512035 [cond-mat, physics:physics]. 2020;.

[74] Allen MP, Tildesley DJ. Computer Simulation of Liquids: Second Edition. Oxford University Press; 2017.

[75] LeCun Y, Bengio Y, Hinton G. Deep learning. Nature. 2015; 521(7553):436–444.

[76] Alom MZ, Taha TM, Yakopcic C, et al. The history began from alexnet: A comprehensive survey on deep learning approaches. arXiv preprint arXiv:180301164. 2018;.

[77] Fan Z, Ding J, Li QJ, et al. Correlating the properties of amorphous silicon with its flexibility volume. Phys Rev B. 2017;95(14):144211.

[78] Ding J, Cheng YQ, Sheng H, et al. Universal structural parameter to quantitatively predict metallic glass properties. Nature Communications. 2016;7:13733.

[79] Fan Z, Ding J, Ma E. Making glassy solids ductile at room temperature by imparting flexibility into their amorphous structure. Materials Research Letters. 2018;6(10):570–583.

[80] Fan Z, Ding J, Ma E. Machine learning bridges local static structure with multiple properties in metallic glasses. Materials Today. 2020;40:48–62.

[81] Botu V, Batra R, Chapman J, et al. Machine learning force fields: construction, validation, and outlook. The Journal of Physical Chemistry C. 2017;121(1):511–522.

[82] Unke OT, Chmiela S, Sauceda HE, et al. Machine learning force fields. arXiv preprint arXiv:201007067. 2020;.

[83] Matsumura H, Tachibana H. Amorphous silicon produced by a new thermal chemical vapor deposition method using intermediate species SiF_2. Appl Phys Lett. 1985;47(8):833–835.

[84] Matsumura H. Catalytic chemical vapor deposition (CTC–CVD) method producing high quality hydrogenated amorphous silicon. Japanese journal of applied physics. 1986;25(12A):L949.

[85] Kushner MJ. A model for the discharge kinetics and plasma chemistry during plasma enhanced chemical vapor deposition of amorphous silicon. Journal of Applied Physics. 1988;63(8):2532–2551.

[86] Atwater HA, Brown WL. Grain boundary mediated amorphization in silicon during ion irradiation. Appl Phys Lett. 1990;56(1):30–32.

[87] Roorda S, Sinke WC, Poate JM, et al. Structural relaxation and defect annihilation in pure amorphous silicon. Phys Rev B. 1991;44(8):3702–3725.

[88] Wang YC, Zhang W, Wang LY, et al. In situ TEM study of deformation-induced crystalline-to-amorphous transition in silicon. NPG Asia Materials. 2016;8(7):e291–e291.

[89] Demkowicz MJ, Argon AS. Autocatalytic avalanches of unit inelastic shearing events are the mechanism of plastic deformation in amorphous silicon. Phys Rev B. 2005;72(24):245206.

[90] Yavari AR, Moulec AL, Inoue A, et al. Excess free volume in metallic glasses measured by X-ray diffraction. Acta Materialia. 2005;53(6):1611–1619.

[91] Haxton TK, Liu AJ. Activated Dynamics and Effective Temperature in a Steady State Sheared Glass. Phys Rev Lett. 2007;99(19):195701.

[92] Kumar G, Neibecker P, Liu YH, et al. Critical fictive temperature for plasticity in metallic glasses. Nature Communications. 2013;4:1536.

[93] Guo Y, Morozov A, Schneider D, et al. Ultrastable nanostructured polymer glasses. Nature Materials. 2012;11(4):337–343.

[94] Yu HB, Luo Y, Samwer K. Ultrastable Metallic Glass. Advanced Materials. 2013;25(41):5904–5908.

[95] Xue RJ, Zhao LZ, Shi CL, et al. Enhanced kinetic stability of a bulk metallic glass by high pressure. Appl Phys Lett. 2016;109(22):221904.

[96] Stillinger FH, Weber TA. Computer simulation of local order in condensed phases of silicon. Phys Rev B. 1985;31(8):5262–5271.

[97] Zachariasen WH. The atomic arrangement in glass. J Am Chem Soc. 1932;54(10):3841–3851.

[98] Treacy MMJ, Borisenko KB. The Local Structure of Amorphous Silicon. Science. 2012;335(6071):950–953.

[99] Mousseau N, Lewis LJ. Topology of Amorphous Tetrahedral Semiconductors on Intermediate Length Scales. Phys Rev Lett. 1997;78(8):1484–1487.

[100] Fusco C, Albaret T, Tanguy A. Role of local order in the small-scale plasticity of model amorphous materials. Phys Rev E. 2010;82(6):066116.

[101] Widmer-Cooper A, Harrowell P. Predicting the Long-Time Dynamic Heterogeneity in a Supercooled Liquid on the Basis of Short-Time Heterogeneities. Phys Rev Lett. 2006;96(18):185701.

[102] Tsumuraya K, Ishibashi K, Kusunoki K. Statistics of Voronoi polyhedra in a model silicon glass. Phys Rev B. 1993;47(14):8552–8557.

[103] Malek R, Mousseau N. Dynamics of Lennard-Jones clusters: A characterization of the activation-relaxation technique. Phys Rev E. 2000; 62(6):7723–7728.

[104] Rodney D, Schuh C. Distribution of Thermally Activated Plastic Events in a Flowing Glass. Phys Rev Lett. 2009;102(23):235503.

[105] Zink M, Samwer K, Johnson WL, et al. Plastic deformation of metallic glasses: Size of shear transformation zones from molecular dynamics simulations. Phys Rev B. 2006;73(17):172203.

[106] Albaret T, Tanguy A, Boioli F, et al. Mapping between atomistic simulations and Eshelby inclusions in the shear deformation of an amorphous silicon model. Phys Rev E. 2016;93(5):053002.

[107] Wang WH. The elastic properties, elastic models and elastic perspectives of metallic glasses. Progress in Materials Science. 2012;57(3):487–656.

[108] Buchenau U, Zorn R, Ramos MA. Probing cooperative liquid dynamics with the mean square displacement. Phys Rev E. 2014;90(4):042312.

[109] Reissland JA. The physics of phonons. Wiley-Interscience; 1973.

[110] Caplan PJ, Poindexter EH, Deal BE, et al. ESR centers, interface states, and oxide fixed charge in thermally oxidized silicon wafers. Journal of Applied Physics. 1979;50(9):5847–5854.

[111] van den Hoven GN, Liang ZN, Niesen L, et al. Evidence for vacancies in amorphous silicon. Phys Rev Lett. 1992;68(25):3714–3717.

[112] Pantelides ST. Defects in Amorphous Silicon: A New Perspective. Phys Rev Lett. 1986;57(23):2979–2982.

[113] Maloney CE, Lemaître A. Amorphous systems in athermal, quasistatic shear. Phys Rev E. 2006;74(1):016118.

[114] Kallel H, Mousseau N, Schiettekatte F. Evolution of the Potential-Energy Surface of Amorphous Silicon. Phys Rev Lett. 2010;105(4):045503.

[115] Theodorou DN, Suter UW. Detailed molecular structure of a vinyl polymer glass. Macromolecules. 1985;18(7):1467–1478.

[116] Warren BE, Biscce J. The Structure of Silica Glass by X-Ray Diffraction Studies. Journal of the American Ceramic Society. 1938;21(2):49–54.

[117] Tanaka H. Bond orientational order in liquids: Towards a unified description of water-like anomalies, liquid-liquid transition, glass transition, and crystallization. The European Physical Journal E. 2012; 35(10):113.

[118] Bouchbinder E, Langer JS, Procaccia I. Athermal shear-transformation-zone theory of amorphous plastic deformation. I. Basic principles. Phys Rev E. 2007;75(3):036107.

[119] Tanguy A, Mantisi B, Tsamados M. Vibrational modes as a predictor for plasticity in a model glass. EPL. 2010;90(1):16004.

[120] Chen K, Manning ML, Yunker PJ, et al. Measurement of Correlations between Low-Frequency Vibrational Modes and Particle Rear-

rangements in Quasi-Two-Dimensional Colloidal Glasses. Phys Rev Lett. 2011;107(10):108301.

[121] Inoue A, Shen B, Koshiba H, et al. Cobalt-based bulk glassy alloy with ultrahigh strength and soft magnetic properties. Nature Materials. 2003; 2(10):661.

[122] Duan G, Wiest A, Lind ML, et al. Bulk Metallic Glass with Benchmark Thermoplastic Processability. Adv Mater. 2007;19(23):4272–4275.

[123] Zberg B, Uggowitzer PJ, Löffler JF. MgZnCa glasses without clinically observable hydrogen evolution for biodegradable implants. Nature Materials. 2009;8(11):887.

[124] Staebler DL, Wronski CR. Reversible conductivity changes in discharge-produced amorphous Si. Appl Phys Lett. 1977;31(4):292–294.

[125] Lin Y, Battaglia C, Boccard M, et al. Amorphous Si Thin Film Based Photocathodes with High Photovoltage for Efficient Hydrogen Production. Nano Lett. 2013;13(11):5615–5618.

[126] Sun BA, Wang WH. The fracture of bulk metallic glasses. Progress in Materials Science. 2015;74:211–307.

[127] Guo H, Yan PF, Wang YB, et al. Tensile ductility and necking of metallic glass. Nature Materials. 2007;6(10):735.

[128] Sehgal J, Ito S. Brittleness of glass. Journal of Non-Crystalline Solids. 1999;253(1):126–132.

[129] Tian L, Cheng YQ, Shan ZW, et al. Approaching the ideal elastic limit of metallic glasses. Nature Communications. 2012;3:609.

[130] Tian L, Shan ZW, Ma E. Ductile necking behavior of nanoscale metallic glasses under uniaxial tension at room temperature. Acta Materialia. 2013;61(13):4823–4830.

[131] Magagnosc DJ, Ehrbar R, Kumar G, et al. Tunable Tensile Ductility in Metallic Glasses. Scientific Reports. 2013;3:1096.

[132] Chen DZ, Jang D, Guan KM, et al. Nanometallic Glasses: Size Reduction Brings Ductility, Surface State Drives Its Extent. Nano Lett. 2013; 13(9):4462–4468.

[133] Raghavan R, Boopathy K, Ghisleni R, et al. Ion irradiation enhances the mechanical performance of metallic glasses. Scripta Materialia. 2010; 62(7):462–465.

[134] Thompson Rachel L, Wang Yongqiang, Greer Julia R. Irradiation Enhances Strength and Deformability of Nano-Architected Metallic Glass. Advanced Engineering Materials. 2018;0(0):1701055.

[135] Liontas R, Jafary-Zadeh M, Zeng Q, et al. Substantial tensile ductility

in sputtered Zr-Ni-Al nano-sized metallic glass. Acta Materialia. 2016; 118:270–285.

[136] Zheng K, Wang C, Cheng YQ, et al. Electron-beam-assisted superplastic shaping of nanoscale amorphous silica. Nature Communications. 2010; 1:24.

[137] Mott NF. The viscosity of vitreous silicon dioxide. Philosophical Magazine B. 1987;56(2):257–262.

[138] Spaepen F. Metallic glasses: Must shear bands be hot? Nature Materials. 2006;5(1):7–8.

[139] Kirkpatrick TR, Thirumalai D, Wolynes PG. Scaling concepts for the dynamics of viscous liquids near an ideal glassy state. Phys Rev A. 1989; 40(2):1045–1054.

[140] Plimpton S. Fast Parallel Algorithms for Short-Range Molecular Dynamics. Journal of Computational Physics. 1995;117(1):1–19.

[141] Cheng YQ, Ma E, Sheng HW. Atomic Level Structure in Multicomponent Bulk Metallic Glass. Phys Rev Lett. 2009;102(24):245501.

[142] Widmer-Cooper A, Perry H, Harrowell P, et al. Irreversible reorganization in a supercooled liquid originates from localized soft modes. Nature Physics. 2008;4(9):711–715.

[143] Widmer-Cooper A, Perry H, Harrowell P, et al. Localized soft modes and the supercooled liquid's irreversible passage through its configuration space. The Journal of Chemical Physics. 2009;131(19):194508.

[144] Mosayebi M, Ilg P, Widmer-Cooper A, et al. Soft Modes and Nonaffine Rearrangements in the Inherent Structures of Supercooled Liquids. Phys Rev Lett. 2014;112(10):105503.

[145] Cao AJ, Cheng YQ, Ma E. Structural processes that initiate shear localization in metallic glass. Acta Materialia. 2009;57(17):5146–5155.

[146] Albe K, Ritter Y, Sopu D. Enhancing the plasticity of metallic glasses: Shear band formation, nanocomposites and nanoglasses investigated by molecular dynamics simulations. Mechanics of Materials. 2013;67:94–103.

[147] Xiao Q, Huang L, Shi Y. Suppression of shear banding in amorphous ZrCuAl nanopillars by irradiation. Journal of Applied Physics. 2013; 113(8):083514.

[148] Avchaciov KA, Ritter Y, Djurabekova F, et al. Effect of ion irradiation on structural properties of $Cu_{64}Zr_{36}$ metallic glass. Nuclear Instruments and Methods in Physics Research Section B: Beam Interactions with Materials and Atoms. 2014;341:22–26.

[149] Talati M, Albaret T, Tanguy A. Atomistic simulations of elastic and plastic properties in amorphous silicon. EPL. 2009;86(6):66005.

[150] Holland D, Marder M. Ideal Brittle Fracture of Silicon Studied with Molecular Dynamics. Phys Rev Lett. 1998;80(4):746–749.

[151] Holland D, Marder M. Erratum: Ideal Brittle Fracture of Silicon Studied with Molecular Dynamics. Phys Rev Lett. 1998;81(18):4029–4029.

[152] Sundararaman S, Huang L, Ispas S, et al. New optimization scheme to obtain interaction potentials for oxide glasses. The Journal of Chemical Physics. 2018;148(19):194504.

[153] Ziegler JF, Biersack JP. The Stopping and Range of Ions in Matter. In: Treatise on Heavy-Ion Science. Springer, Boston, MA; 1985. p. 93–129.

[154] Wootton A, Thomas B, Harrowell P. Radiation-induced densification in amorphous silica: A computer simulation study. The Journal of Chemical Physics. 2001;115(7):3336–3341.

[155] Shimizu F, Ogata S, Li J. Theory of Shear Banding in Metallic Glasses and Molecular Dynamics Calculations. Mater Trans. 2007;48(11):2923–2927.

[156] Stukowski A. Visualization and analysis of atomistic simulation data

with OVITO—the Open Visualization Tool. Modelling Simul Mater Sci Eng. 2010;18(1):015012.

[157] Egerton RF, Li P, Malac M. Radiation damage in the TEM and SEM. Micron. 2004;35(6):399–409.

[158] Hu YC, Guan PF, Li MZ, et al. Unveiling atomic-scale features of inherent heterogeneity in metallic glass by molecular dynamics simulations. Phys Rev B. 2016;93(21):214202.

[159] Ritter Y, Sopu D, Gleiter H, et al. Structure, stability and mechanical properties of internal interfaces in $Cu_{64}Zr_{36}$ nanoglasses studied by MD simulations. Acta Materialia. 2011;59(17):6588–6593.

[160] Sopu D, Albe K. Influence of grain size and composition, topology and excess free volume on the deformation behavior of Cu–Zr nanoglasses. Beilstein Journal of Nanotechnology. 2015;6(1):537–545.

[161] Sopu D, Ritter Y, Gleiter H, et al. Deformation behavior of bulk and nanostructured metallic glasses studied via molecular dynamics simulations. Phys Rev B. 2011;83(10):100202.

[162] Pan J, Wang YX, Guo Q, et al. Extreme rejuvenation and softening in a bulk metallic glass. Nature Communications. 2018;9(1):560.

[163] Sun Y, Concustell A, Greer AL. Thermomechanical processing of metallic

glasses: extending the range of the glassy state. Nature Reviews Materials. 2016;1(9):16039.

[164] Ketov SV, Sun YH, Nachum S, et al. Rejuvenation of metallic glasses by non-affine thermal strain. Nature. 2015;524(7564):200–203.

[165] Schoenholz SS, Cubuk ED, Sussman DM, et al. A structural approach to relaxation in glassy liquids. Nature Physics. 2016;12(5):469–471.

[166] Candelier R, Widmer-Cooper A, Kummerfeld JK, et al. Spatiotemporal hierarchy of relaxation events, dynamical heterogeneities, and structural reorganization in a supercooled liquid. Physical review letters. 2010; 105(13):135702.

[167] Smessaert A, Rottler J. Distribution of local relaxation events in an aging three-dimensional glass: Spatiotemporal correlation and dynamical heterogeneity. Physical Review E. 2013;88(2):022314.

[168] Landes FP, Biroli G, Dauchot O, et al. Attractive versus truncated repulsive supercooled liquids: The dynamics is encoded in the pair correlation function. Phys Rev E. 2020;101(1):010602.

[169] Egami T, Billinge SJL. Underneath the Bragg Peaks: Structural Analysis of Complex Materials. Newnes; 2012.

[170] Fan RE, Chang KW, Hsieh CJ, et al. LIBLINEAR: A Library for Large

Linear Classification. Journal of Machine Learning Research. 2008; 9(Aug):1871–1874.

[171] Grigera TS, Martín-Mayor V, Parisi G, et al. Phonon interpretation of the 'boson peak' in supercooled liquids. Nature. 2003;422(6929):289–292.

[172] Shintani H, Tanaka H. Universal link between the boson peak and transverse phonons in glass. Nature Mater. 2008;7(11):870–877.

[173] Jakse N, Nassour A, Pasturel A. Structural and dynamic origin of the boson peak in a Cu-Zr metallic glass. Phys Rev B. 2012;85(17):174201.

[174] Brink T, Koch L, Albe K. Structural origins of the boson peak in metals: From high-entropy alloys to metallic glasses. Phys Rev B. 2016; 94(22):224203.

[175] Giuntoli A, Leporini D. Boson Peak Decouples from Elasticity in Glasses with Low Connectivity. Phys Rev Lett. 2018;121(18):185502.

[176] Yang J, Wang YJ, Ma E, et al. Structural Parameter of Orientational Order to Predict the Boson Vibrational Anomaly in Glasses. Phys Rev Lett. 2019;122(1):015501.

[177] Baggioli M, Zaccone A. Universal Origin of Boson Peak Vibrational Anomalies in Ordered Crystals and in Amorphous Materials. Phys Rev Lett. 2019;122(14):145501.

[178] Bünz J, Brink T, Tsuchiya K, et al. Low Temperature Heat Capacity of a Severely Deformed Metallic Glass. Phys Rev Lett. 2014;112(13):135501.

[179] Egami T. Understanding the properties and structure of metallic glasses at the atomic level. JOM. 2010;62(2):70–75.

[180] Brooks CL. Computer simulation of liquids. J Solution Chem. 1989; 18(1):99–99.

[181] Cheng YQ, Ma E. Configurational dependence of elastic modulus of metallic glass. Phys Rev B. 2009;80(6):064104.

[182] Widmer-Cooper A, Harrowell P, Fynewever H. How reproducible are dynamic heterogeneities in a supercooled liquid? Physical review letters. 2004;93(13):135701.

[183] Cancès E, Legoll F, Marinica MC, et al. Some improvements of the activation-relaxation technique method for finding transition pathways on potential energy surfaces. J Chem Phys. 2009;130(11):114711.

[184] Dickey J, Paskin A. Computer Simulation of the Lattice Dynamics of Solids. Phys Rev. 1969;188(3):1407–1418.

[185] Mendelev M, Zhang F, Ye Z, et al. Development of interatomic potentials appropriate for simulation of devitrification of al90sm10 alloy.

Modelling and Simulation in Materials Science and Engineering. 2015; 23(4):045013.

[186] Cottrell AH. The Mechanical Properties of Matter. Wiley; 1964.

[187] Krizhevsky A, Sutskever I, Hinton GE. ImageNet Classification with Deep Convolutional Neural Networks. In: Pereira F, Burges CJC, Bottou L, et al., editors. Advances in Neural Information Processing Systems 25. Curran Associates, Inc.; 2012. p. 1097–1105.

[188] Simonyan K, Zisserman A. Very Deep Convolutional Networks for Large-Scale Image Recognition. arXiv:14091556 [cs]. 2015;.

[189] He K, Zhang X, Ren S, et al. Deep residual learning for image recognition. In: Proceedings of the IEEE conference on computer vision and pattern recognition; 2016. p. 770–778.

[190] Lançon F, Billard L, Chaudhari P. Thermodynamical Properties of a Two-Dimensional Quasi-Crystal from Molecular Dynamics Calculations. EPL. 1986;2(8):625–629.

[191] Ioffe S, Szegedy C. Batch Normalization: Accelerating Deep Network Training by Reducing Internal Covariate Shift. arXiv:150203167 [cs]. 2015;.

[192] Malandro DL, Lacks DJ. Molecular-Level Mechanical Instabilities and

Enhanced Self-Diffusion in Flowing Liquids. Phys Rev Lett. 1998; 81(25):5576–5579.

[193] Maloney C, Lemaître A. Universal Breakdown of Elasticity at the Onset of Material Failure. Phys Rev Lett. 2004;93(19):195501.

[194] Abadi M, Barham P, Chen J, et al. TensorFlow: A System for Large-Scale Machine Learning; 2016. p. 265–283.

[195] Sergeev A, Del Balso M. Horovod: fast and easy distributed deep learning in TensorFlow. arXiv:180205799 [cs, stat]. 2018;.

[196] Yavari AR, Lewandowski JJ, Eckert J. Mechanical Properties of Bulk Metallic Glasses. MRS Bulletin. 2007;32(8):635–638.

[197] Trexler MM, Thadhani NN. Mechanical properties of bulk metallic glasses. Progress in Materials Science. 2010;55(8):759–839.

[198] Wright WJ, Hufnagel TC, Nix WD. Free volume coalescence and void formation in shear bands in metallic glass. Journal of Applied Physics. 2003;93(3):1432–1437.

[199] Li J, Spaepen F, Hufnagel TC. Nanometre-scale defects in shear bands in a metallic glass. Philosophical Magazine A. 2002;82(13):2623–2630.

[200] Jiang WH, Pinkerton FE, Atzmon M. Mechanical behavior of shear

bands and the effect of their relaxation in a rolled amorphous Al-based alloy. Acta Materialia. 2005;53(12):3469–3477.

[201] Lee JY, Han KH, Park JM, et al. Deformation and evolution of shear bands under compressive loading in bulk metallic glasses. Acta Materialia. 2006;54(19):5271–5279.

[202] Lewandowski JJ, Greer AL. Temperature rise at shear bands in metallic glasses. Nature Materials. 2006;5(1):15–18.

[203] Packard CE, Schuh CA. Initiation of shear bands near a stress concentration in metallic glass. Acta Materialia. 2007;55(16):5348–5358.

[204] Shi Y, Katz MB, Li H, et al. Evaluation of the Disorder Temperature and Free-Volume Formalisms via Simulations of Shear Banding in Amorphous Solids. Phys Rev Lett. 2007;98(18):185505.

[205] Şopu D, Stukowski A, Stoica M, et al. Atomic-Level Processes of Shear Band Nucleation in Metallic Glasses. Physical review letters. 2017; 119(19):195503.

[206] Alix-Williams DD, Falk ML. Shear band broadening in simulated glasses. Phys Rev E. 2018;98(5):053002.

[207] Liu C, Ikeda Y, Maaß R. Strain-dependent shear-band structure in a Zr-based bulk metallic glass. Scripta Materialia. 2021;190:75–79.

[208] Şopu D, Moitzi F, Mousseau N, et al. An atomic-level perspective of shear band formation and interaction in monolithic metallic glasses. Applied Materials Today. 2020;21:100828.

[209] Golkia M, Shrivastav GP, Chaudhuri P, et al. Flow heterogeneities in supercooled liquids and glasses under shear. Phys Rev E. 2020; 102(2):023002.

Vita

Zhao Fan was born in Jinshi, China on January 10, 1991. He entered Taiyuan Institute of Technology in 2009 and received his B.S. degree in Mechanical Engineering in 2013. He continued his graduate study in Prof. Zhaoping Lu's group at University of Science and Technology Beijing, and obtained his M.S. degree in Materials Science and Engineering in January 2016. He joined Prof. Evan Ma's group at Johns Hopkins University in January 2016 and worked on the project of "Structure-property relationships in amorphous solids via atomic simulations and machine learning". After Prof. Evan Ma retired in July 2020, Prof. Michael Falk was guiding him to finish the thesis. He will graduate in December 2020 with Ph.D. degree in Materials Science and Engineering.